Control of Teleoperation Systems for Beating-Heart Surgery

by

Lingbo Cheng

A thesis submitted in partial fulfillment of the requirements for the degree of

Doctor of Philosophy

in

Control Systems

Department of Electrical and Computer Engineering
University of Alberta

Abstract

Cardiovascular disease is one of the leading causes of death worldwide. Conventional extra- and intra-cardiac surgeries need the heart to be arrested and involve connecting the patient to a cardiopulmonary bypass (CPB) machine. However, arrested-heart surgery has adverse effects such as risk of long-term cognitive loss and stroke. Different from arrested-heart surgery, beating-heart surgery could eliminate such negative effects of CPB by allowing the heart to beat normally and could also enable intraoperative evaluation of the heart tissue motion, which is critical to the assessment of reconstructive heart operations. Beating-heart surgery, however, introduces serious challenges for the surgeons due to the heart's fast motions. To facilitate beating-heart surgery, minimize the risks of tool-tissue collision and tissue injury, and ensure haptic feedback to the surgeon precludes oscillatory tool-tissue interaction forces, a robot-assisted system is necessary for beating-heart surgery. If the robot-assisted system can move a surgical tool in synchrony with the target heart tissue while the heart beats freely, the oscillatory forces between the surgical tool and heart tissue will be small, giving a feeling of making contact with an idle heart to the human operator (surgeon).

This thesis presents a study of robot-assisted master-slave teleoperation systems for beating-heart surgery. The objective is to develop a telerobotic system to simultaneously compensate for the beating heart's motion and provide the human operator with a non-oscillatory force feedback, which will give him/her a feeling of operating on an "arrested" heart. To this end, in Chapter 3, a bilateral-impedance-controlled telerobotic system is proposed to help perform

surgical tasks without stopping the heart by designing two reference impedance models for the master and slave robots. The efficacy of the proposed teleoperation system is assessed through experiments for 1-DOF (degree of freedom) and 3-DOF heart motions, respectively.

Inspired by the bilateral impedance control method, a switched-impedance control method is proposed and implemented for telerobotic beating-heart surgery in Chapter 4. This method involves two switched reference impedance models for the master and slave robots to achieve both motion compensation and non-oscillatory force feedback during slave-heart interaction. Both the switched reference impedance models and their parameters are different from the previous method. The main advantage of this method over the one presented in Chapter 3 is that during slave-heart interaction, the human operator can feel the stiffness of the heart tissue through the master robot.

In Chapters 5 and 6, the robot impedance control method is then combined with ultrasound imaging-based control algorithms to achieve the ideal behaviors. Similarly, to provide the human operator with non-oscillatory force feedback, a reference impedance model is designed for the master robot. Moreover, the synchronization of the slave robot with heart motion is attained by employing ultrasound imaging to measure the heart tissue position. Issues including slow sampling rate and time delay caused by ultrasound imaging are addressed by a cubic polynomial interpolation and a heart motion predictor, respectively. Additionally, two heart motion predictors: the extended Kalman filter (EKF) in Chapter 5 and the recurrent neural network (NN) predictor in Chapter 6 are designed. The ability of the systems with two heart motion predictors is evaluated experimentally. It is demonstrated that the motion compensation and force feedback using a NN predictor performs better than using an EKF predictor for a teleoperation system in beating-heart surgery.

In Chapter 7, the impedance control method is used for haptic-enabled surgical training and cooperation in beating-heart surgery. A multi-user shared control architecture is developed, and a multilateral impedance-controlled strategy is employed for this architecture. The desired objectives of the proposed system are a) providing position guidance to the trainees during training procedure, b) providing force feedback to all human operators (trainer and trainees) regardless of their levels of authority over the slave robot, c) motion compensation for the heart's motion, and d) reflecting only the non-oscillatory force portion of the slave-heart tissue interaction force to all human operators. To this end, virtual fixtures and a dominance factor are introduced, and a reference impedance model with adjusted parameters is designed for each master or slave robot. The proposed impedance-based control methodology is evaluated experimentally, and its feasibility is demonstrated successfully.

Preface

This thesis is based on the research presented in the following papers. The research project, of which this thesis is a part, received research ethics approval from the University of Alberta Research Ethics Board under project "Measuring user performance in controlling a robot through a user interface," No. Pro00055825.

My contribution to each chapter is summarized. In general, I was responsible for most of the work including experiment design, data collection and analysis, and manuscript preparation. My supervisor, Dr. Mahdi Tavakoli, provided overall guidance in the research including experimental design and valuable suggestions/discussions. Dr. Mahdi Tavakoli was involved in the editing of the resulting manuscripts and thesis chapters.

This thesis is divided into 8 chapters. **Chapter** 1 presents the motivation and objectives of this project and summarized the thesis organization and contributions.

Chapter 2 is based on the book chapter: B. Fallahi, L. Cheng and M. Tavakoli, "State Observation and Feedback Control in Robotic Systems for Therapy and Surgery," in Control System Design of Bio-Robotics and Bio-Mechatronic with Advanced Applications, Elsevier, 2019. I completed the literature review of the second part of the book chapter (related to beating-heart surgery), performed experiments and prepared the initial draft of the second part of the book chapter. Dr. Fallahi contributed to the first part of the book chapter (related to soft-tissue needle insertion). All co-authors contributed to the revisions of the manuscript.

Chapter 3 is based on the following two papers (listed in the order of appearance in the text):

1. L. Cheng, M. Sharifi, M. Tavakoli, "Towards Robot-Assisted Anchor Deployment in Beating-Heart Mitral Valve Surgery," The International Journal of Medical Robotics and Computer Assisted Surgery, vol. 14, no. 3, pp. e1900, 2018. Dr. Sharifi and I designed the research.

I performed all experiments, analyzed the data and prepared the initial draft of the manuscript. All co-authors contributed to the interpretation of the data and further editing of the manuscript.

2. L. Cheng, J. Fong, M. Tavakoli, "Semi-Autonomous Surgical Robot Control for Beating-Heart Surgery," IEEE 15th International Conference on Automation Science and Engineering, Vancouver, Canada, 2019. I designed the research, performed all experiments, analyzed the data and prepared the initial draft of the manuscript. Mr. Fong provided technical support for using velocity control of the Motoman SIA-5F robot. All co-authors contributed to the interpretation of the data and further editing of the manuscript.

Chapter 4 is based on the paper: L. Cheng and M. Tavakoli, "Switched-Impedance Control of Surgical Robots in Teleoperated Beating-Heart Surgery," Journal of Medical Robotics Research, vol. 3, no. 3, pp. 1841003(1-15), 2018. I designed the research, performed all experiments, analyzed the data and prepared the initial draft of the manuscript. Dr. Tavakoli contributed to the interpretation of the data and revision of the manuscript.

Chapter 5 is based on the following paper: L. Cheng and M. Tavakoli, "Ultrasound Image Guidance and Robot Impedance Control for Beating-Heart Surgery," Control Engineering Practice (A Journal of IFAC), vol. 81, pp. 9-17, 2018. I designed the research, performed all experiments, analyzed the data and drafted the manuscript. Dr. Tavakoli contributed to the interpretation of the data and revision of the manuscript.

Chapter 6 is based on the following two papers (listed in the order of appearance in the text):

1. L. Cheng and M. Tavakoli, "Neural-Network-Based Heart Motion Prediction for Ultrasound-Guided Beating-Heart Surgery," IEEE 15th International Conference on Automation Science and Engineering, Vancouver, Canada, 2019.

2. L. Cheng and M. Tavakoli, "Neural Network-based Physiological Organ Motion Prediction and Robot Impedance Control for Teleoperated Beating-Heart Surgery," Journal of Medical Robotics Research, 2019, in preparation for submission.

I designed the research, performed all experiments, analyzed the data and drafted the manuscript. Dr. Tavakoli contributed to the interpretation of the data and revision of the manuscript.

Chapter 7 is based on the following paper: L. Cheng and M. Tavakoli, "A Multilateral Impedance-Controlled System for Haptics-Enabled Surgical Training and Cooperation in Beating-Heart Surgery," International Journal of Intelligent Robotics and Applications, 2019, 1-12. I designed the research, performed all experiments, analyzed the data and drafted the manuscript. Dr. Tavakoli contributed to the interpretation of the data and revision of the manuscript.

The final chapter, **Chapter** 8, concludes the thesis and describes future directions of this project.

Dedication

To my dearest parents and brother:

Thank you for the love, care, understanding and support you have given me throughout this journey and for always showing concern to keep myself from getting off track. Without your unselfish love and unconditional support, I would never be who I am today.

Acknowledgements

Content

List of Tables

List of Figures

Abbreviations

AFM	Average Force Applied on the Master Robot
AFS	Average Force Applied on the Simulated Heart
AMC	Automatic Motion Compensation
CPB	Cardiopulmonary Bypass
DFR	Direct Force Reflection
DOF	Degree of freedom
ECG	Electrocardiogram
EKF	Extended Kalman Filter
GPC	Generalized Predictive Control
MAE	Mean Absolute Error
MASE	Mean Absolute Synchronization Error
MLP	Multilayer Perceptron
NAR	Nonlinear Autoregressive Model
NN	Neural Network
PID	Proportional Integral Derivative Control
PSD	Power Spectral Densities
POI	Point of interest
RMSE	Root Mean Square Error
RNN	Recurrent Neural Network
US	Ultrasound

Symbols

$\mathbf{f}_e$	Vector of slave-heart interaction forces
$\mathbf{f}_h$	Vector of human-master interaction forces
$\mathbf{f}_{v_i}$	Vector of virtual force generated by a virtual fixture
$\mathbf{K}_m$, $\mathbf{C}_m$, $\mathbf{M}_m$	Vectors of stiffness, damping, and mass of the master impedance model
$\mathbf{K}_s$, $\mathbf{C}_s$, $\mathbf{M}_s$	Vectors of stiffness, damping, and mass of the slave impedance model
$\mathbf{K}_p$, $\mathbf{K}_f$	Vectors of position and force scaling factors
$\mathbf{K}_{p_m}$, $\mathbf{K}_{i_m}$, $\mathbf{K}_{d_m}$	Coefficients for the proportional, integral, and derivative terms of PID for the master robot
$\mathbf{K}_{p_s}$, $\mathbf{K}_{i_s}$, $\mathbf{K}_{d_s}$	Coefficients for the proportional, integral, and derivative terms of PID for the slave robot
M_m^v, C_m^v, K_m^v	Impedance characteristics of the virtual fixture model
$\boldsymbol{\mu}_m$, $\boldsymbol{\mu}_s$, $\boldsymbol{\tau}_m$, $\boldsymbol{\tau}_s$	Vectors of control signals for the master and slave robots
$\mathbf{x}_m$, $\mathbf{x}_s$	Vectors of positions of the master and slave robots
$\mathbf{x}_{ref_m}$, $\mathbf{x}_{ref_s}$	Vectors of reference positions for the master and slave robots
$\mathbf{x}_e$	Vector of beating-heart position
x_e	Beating-heart position
X_d^d	Slowly sampled and delayed robot-heart distance
x_d^d	Delayed robot-heart distance with a fast sampling rate
x_e^d	Delayed beating heart position with a fast sampling rate
x_s^d	Delayed slave robot potion with a fast sampling rate
α_i	Dominance factor
β	Force scaling factor
$\mathbf{Z}_m$, $\mathbf{Z}_s$	Vector of damping ratios of the impedance models for the robots
ζ_{m_i}, ζ_{s_i}	Damping ratios of the impedance models for the robots in i-axis

$\mathbf{\Omega}_{n_m}$, $\mathbf{\Omega}_{n_s}$	Vector of natural frequencies of the impedance models for the robots
$\omega_{n_{m_i}}$, $\omega_{n_{s_i}}$	Natural frequencies of the impedance models for the robots in i-axis
ω_h	Frequency of heartbeat motion
ω_r	Frequency of respiratory motion
$\lambda_{1,m}$, $\lambda_{2,m}$	Positive constant parameters guarantee the stability of sliding surface for the master
$\lambda_{1,s}$, $\lambda_{2,s}$	Positive constant parameters guarantee the stability of sliding surface for the slave
$\mathbf{W}_m$	Positive definite matrix for the master
$\mathbf{W}_s$	Positive definite matrix for the slave

Chapter 1

Introduction

1.1 Motivation

In recent years, robotic systems have been employed for surgery, where a human operator (surgeon) interacts with a master robot to perform a desired task on the target tissue by a surgical tool mounted on a slave robot [1], [2]. As cardiovascular disease is one of the leading causes of death worldwide [3], considerable attention has been paid to the research on robot-assisted system for cardiac surgery. Master-slave teleoperation systems can be used to perform extra- and intra-cardiac surgeries while the heart is arrested [4]. However, arrested-heart surgery has adverse effects due to using cardiopulmonary bypass (CPB) [5]–[9]. There is a major risk of morbidity following CPB due to the systemic inflammatory response associated with increased cytokine production and complement activation that can result in neurologic dysfunction in adults and neurodevelopmental dysfunction in children [7]–[9]. Moreover, arrested-heart surgery can increase the risk of stroke and lead to long-term cognitive loss [5], [10]. In contrast, beating-heart surgery could eliminate such negative effects of CPB by allowing the heart to beat normally [11] and also enables intraoperative evaluation of the heart tissue motion, which is critical to the assessment of reconstructive heart operations, particularly for mitral valve surgery [12]. Considering the significant

1

benefits for both patients and surgeons of the beating-heart intra-cardiac surgery, this promising technology has drawn more and more attention and study.

Beating-heart surgery, however, is challenging due to the need for heart tissue motion compensation during the surgical operation in order to minimize the risks of tool-tissue collision and tissue injury. Directly operating on the beating-heart tissue introduces significant challenges for the human operator as the fast motion of the heart requires the human operator to take care of the motion compensation manually. It is very easy for the human operator to feel fatigued during the procedure. To overcome this obstacle, a mechanical heart stabilizer was originally proposed to minimize the motion of the heart. This heart stabilizer cannot stop the heart motion completely but minimizes motion in a localized area on the exterior surface of the beating heart. In other words, the risks of tool-tissue collision and tissue injury still highly exist, and this device is only suitable for certain extra-cardiac surgeries.

To facilitate beating-heart surgery, minimize the risks of tool-tissue collision and tissue injury, a robot-assisted system is necessary for beating-heart surgery. If the robotic system could move a surgical tool in synchrony with the target tissue while the heart beats, the human operator could then perform the surgical procedure as if the beating heart were stationary.

1.2 Objectives

The most prominent challenge to be addressed for beating-heart surgery is the rapid motions of the heart whose movement velocity and acceleration are approximately 210 mm/s and 3800 mm/s^2, respectively [13]. Manual tool position compensation according to the heart motion will not only lead to the human operator's fatigue and exhaustion but also increase the risks of tool-tissue collision and tissue injury. Therefore, one main objective for the robot-assisted system for beating-heart surgery is motion compensation for the beating heart's motion. By controlling the motion of the robot-assisted system, the surgical tool attached to

the end of the robot-assisted system can comply with the motion of the beating-heart tissue, so that to realize automatically compensate for the beating heart's motion.

In addition, the employment of the robot-assisted system introduces another issue of haptic feedback to the human operator. Haptic feedback during a surgical operation is critical for the human operator to be able to accurately execute the surgical tasks especially in beating heart surgeries involving tissue cutting and sewing, dissection, grasping, etc. During the operation of such surgical tasks, the tool-tissue interaction forces should be within a safe range to avoid potential tissue injury. As the human operator manipulates the robot-assisted system instead of directly manipulating the surgical tool, appropriate tool-tissue interaction force feedback is necessary especially for master-slave teleoperation systems. This thesis will focus on designing master-slave teleoperation robot-assisted beating-heart surgical systems which could provide haptic feedback to the human operators and the reason will be described in detail in Section 2.1.

Teleoperation beating-heart surgery involves two phases: "No contact with the heart" and "contact with the heart" as far as the slave robot is concerned. First, when there is no contact between the slave robot and the heart tissue, the slave robot should precisely mimic the motion of the master robot, which is being manipulated by the human operator. It should be noted that compared to the fast motion of the beating heart, the motion of the human operator/master robot has a relatively low frequency. Second, when contact occurs, the slave robot should compensate for the fast movements of the beating heart while following the commands of the human operator as much as possible. In other words, as the slave robot follows the human operator's motions, it should also synchronize its motion to that of the beating heart. Based on that, the slave-heart interaction force has two frequency components – a low frequency corresponding to the human operator's motion commands and a high frequency corresponding to the beating heart motion. As far as the force feedback about the slave-heart interaction to the human operator is concerned, there is a need to only reflect the low-frequency component of slave-heart interaction force, which is caused by the motion of

human operator. The high-frequency component of it (quasi-periodic heartbeat-induced forces) is due to any residual mismatch between the heart motion and the slave robot motion and also due to the internal inertia of the force sensor (which makes it register a sinusoidal force when the sensor undergoes an oscillatory motion even under no contact). In other words, the force feedback perceived by the human operator should be the non-oscillatory low-frequency portion of the tool-tissue interaction force to reduce the human operator's fatigue and exhaustion.

Therefore, this teleoperation system guarantees that the slave robot implements rapid compensation for the beating heart's motion and the master robot reflects non-oscillatory portion of slave-tissue interaction forces to the human operator. In this way, the operator does not need to synchronize the master robot's motion with the moving heart's motion manually, which would have been a daunting task. In a word, to minimize the risks of tool-tissue collision and tissue injury, a robot-assisted system enabling to automatically provide compensation for the fast heart's motion and reflect non-oscillatory haptic forces to the human operator is needed.

1.3 Thesis Organization

The structure of this thesis is organized as follows:

Chapter 1 Introduction: Discusses the motivation, objectives, organization, and contributions of this thesis.

Chapter 2 Literature Review: Introduces the general surgical systems and measurements and feedbacks for robot-assisted beating-heart surgery, discusses previously proposed control solutions for heart motion compensation and haptic feedback and describes the technical challenges of the control of robot-assisted teleoperation systems for beating-heart surgery.

Chapter 3 Bilateral Impedance Control: Proposes a teleoperation bilateral impedance control method for robot-assisted beating-heart surgery, including two reference impedance models design, parameter adjustments, controller design, and 1-degree of freedom (DOF) and 3-DOF experimental evaluations.

Chapter 4 Switched Impedance Control: Proposes a novel switched-bilateral impedance control method for robot-assisted beating-heart surgery, including design of two switched-reference impedance models, parameter adjustments, controller design, and simulation and experimental evaluations.

Chapter 5 Ultrasound Image Guidance and Robot Impedance Control: Combines the robot impedance control method with ultrasound image-based control algorithms for robot-assisted beating-heart surgery, dealing with problems of ultrasound image processing, heart motion upsampling, and extended Kalman filter (EKF)-based heart motion prediction.

Chapter 6 Neural Network-based Physiological Organ Motion Prediction: Proposes a neural network (NN)-based heart motion predictor for time delay compensation caused by ultrasound image acquisition and processing and combines it with the robot impedance control method for robot-assisted beating-heart surgery.

Chapter 7 Multilateral Impedance Control for Surgical Training and Cooperation: Describes the development and evaluation of an impedance-controlled multi-master/single-slave telerobotic system for haptics-enabled surgical training and cooperation in beating-heart surgery.

Chapter 8 Summary and Future Directions: Concludes the thesis and describes future directions of this project.

1.4 Thesis Contributions

This thesis presents a study of the robot-assisted master-slave teleoperation systems for beating-heart surgery to automatically provide compensation for the beating heart's motion and reflect non-oscillatory haptic forces to the human operator.

In Chapter 3, a bilateral-impedance-controlled master-slave telerobotic system is proposed to help perform anchor deployment for mitral valve annuloplasty without stopping the heart [14]. The main advantage of this method is that the impedance models' responses can be modulated such that they generate desired responses by varying the parameters and/or structure of the impedance models. This advantage makes the ideal behaviors (motion compensation and non-oscillatory haptic feedback) much easier to achieve. The efficacy of the proposed teleoperation system is assessed through experiments for 1-DOF [14] and 3-DOF [15], respectively. Due to the flexibility of the designed reference impedance model for the slave robot, this method is more suitable for surgeries that require less tool-tissue interaction forces such as mitral valve annuloplasty, blunt resection, ablation, etc.

In Chapter 4, a switched-impedance control method is proposed and implemented for telerobotic beating-heart surgery [16]. This method involves two switched reference impedance models for the master and slave robots to achieve two desired objectives. The main advantage of this method over the one presented in Chapter 3 is that during slave-heart interaction, the human operator can feel the same stiffness of the heart tissue through the master robot, and the slave robot can synchronize its motions with the heart's motion and follow the commands of the human operator as closely as possible to execute the desired surgical task. Therefore, this method is more suitable for surgeries which require larger execute forces on the heart tissue such as tissue cutting, suturing, penetration, etc.

In Chapter 5 and 6, the robot impedance control method is combined with ultrasound imaging-based control algorithms to achieve the ideal behaviors of a robot-assisted system for beating-heart surgery. Similarly, to make the human operator perform the surgical

procedure as if the beating heart is stationary, a reference impedance model is designed for the master robot. The ultrasound imaging is used to capture the position of the point of interest (POI) on the heart tissue. The slave robot is controlled to synchronize its motions with the heart's (POI) motion and follow the commands of the human operator. However, ultrasound image acquisition and processing introduce non-negligible time delay to the system. To address this issue, an EKF-based heart motion predictor [17] and a NN-based heart motion predictor [18] are designed in Chapter 5 and 6, respectively. The ability of the systems with the two heart motion predictors is evaluated experimentally.

In Chapter 7, the impedance control method is used for haptic-enabled surgical training and cooperation in beating-heart surgery [19]. Multi-user shared control architecture is developed, and a multilateral impedance-controlled strategy is employed for this architecture. Besides the two desired objectives for robot-assisted beating-heart surgery, two more objectives of the proposed system are described as follows: (a) providing position guidance to the trainees during the training procedure, (b) providing force feedback to all human operators (trainer and trainees) regardless of their levels of authority over the slave robot. To this end, virtual fixtures and a dominance factor are introduced, and a reference impedance model with adjusted parameters is designed for each master or slave robot. The proposed impedance-based control methodology is evaluated experimentally, and its feasibility is demonstrated successfully.

Chapter 2

Literature Review

This chapter[1] presents an overview of the state-of-the-art research relevant to this project. Section 2.1 provides the surgical systems for beating-heart surgery. Section 2.2 discusses the various measurements and feedbacks for the robot-assisted beating-heart surgical systems. Section 2.3 presents the control methods to achieve the desired objectives shown in Section 1.2.

2.1 Surgical Systems

Depending on the intended surgical procedures, several robot-assisted surgical systems have been developed, which can be mainly categorized into two groups based on the interaction modes with the human operator [20]: hand-held surgical robotic systems and teleoperation surgical robotic systems.

Hand-held surgical systems require the human operator to hold the surgical system directly, which includes an actuator and a surgical tool attached at the end of the system so

---

[1]Portions of this chapter were published as B. Fallahi, L. Cheng and M. Tavakoli, "State Observation and Feedback Control in Robotic Systems for Therapy and Surgery," in *Control System Design of Bio-Robotics and Bio-Mechatronic with Advanced Applications*. Elsevier, 2019. [108]

that the surgical tool can move with respect to the handle [13], [21], [22] (Fig. 2.1a). Different from the hand-held surgical systems, a teleoperation surgical system involves a master robot that provides position and/or force commands and a slave robot that receives those commands and executes tasks on the heart tissue [23], [24]. These systems have been shown to offer lots of advantages such as dexterity, fine and remote manipulation capability, and haptic feedback capability for the human operator. The da Vinci surgical robotic system [25] (Fig. 2.1b) by Intuitive Surgical Inc. is one of the most prominent commercial teleoperation surgical systems.

<div align="center">(a)   (b)</div>
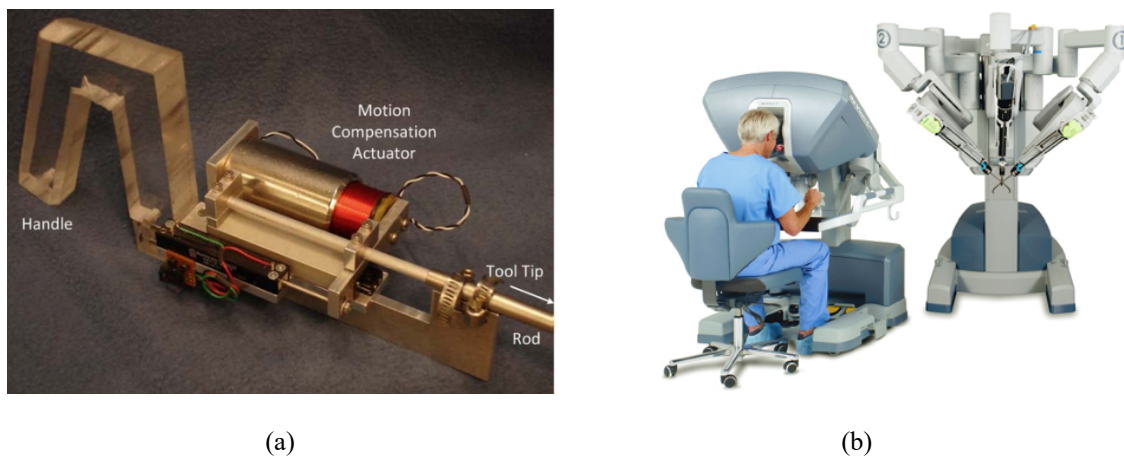
Figure 2.1. Surgical systems for beating-heart surgery. (a) Hand-held surgical system [21], (b) teleoperation surgical system da Vinci (Intuitive Surgical, Mountain View, CA).

Teleoperation surgical systems can be divided into two categories depending on their features. In a unilateral teleoperation system, the human operator loses the sense of touch. In contrast, in a bilateral teleoperation system, the human operator can feel the interaction force between the slave robot and what it is touching, enabling the human operator to efficiently manipulate the master robot to provide appropriate commands. As during the operation of specific surgical tasks, the tool-tissue interaction forces should be within a safety range to avoid potential tissue injury, haptic feedback is significant for the human operator to be able to accurately execute the surgical tasks especially in beating heart surgeries involving tissue

cutting and sewing, dissection, grasping, etc. Therefore, this thesis will focus on designing master-slave teleoperated robot-assisted beating-heart surgical systems which could provide haptic feedback to the human operators.

Moreover, the robot-assisted surgical systems can be categorized into rigid and flexible surgical robots based on the dexterity of the surgical robots. Conventional surgical tools used in robot-assist systems for cardiac surgeries are short and rigid. Surgical tools like scissors, forceps, and graspers are usually mounted on the end of the systems to perform surgical tasks. However, during intravascular interventions and minimally invasive surgeries, the dexterity of surgical robots can be enhanced by using flexible, thin and lightweight surgical tools such as catheters while also reducing trauma, which is a benefit for post-operative recovery [26]. These flexible surgical tools can be combined with the above robot-assisted systems to perform intended surgical procedures. However, the control of a mechatronics-assisted system with the link and joint flexibility is quite challenging. In this project, the transparency of a teleoperation system with a flexible surgical robot was analysized [27]. As this part of work is limited to simulation and not extended to beating-heart surgery, the methodology and analysis results are presented in Appendix A.

2.2 Measurements and Feedbacks

To address the issue of beating heart motion compensation, several types of sensors have been used to capture the position of the heart, so that the human operator perceives visual feedback of the surgical site through sensors, and the robotic surgical instruments tracks the beating-heart's motion by utilizing the measured heart positions.

In [28], Nakamura et al. adopt one color camera to provide colorful visual feedback and one monochrome high-speed camera to measure the heart position. The human operator utilized the guidance of those two cameras to demonstrate automatic tracking of a point on the heart that was lit by laser. In [29]–[31], Ginhoux et al. measured the 2-DOF cardiac motions by using a 500-Hz camera to avoid aliasing. In [32]–[34], the authors extended 2-

DOF position tracking to 3-DOF position tracking using a stereo camera system. In addition, the high-speed camera has been employed in other literatures about beating-heart surgery as well [35]–[38]. These sensors provided real-time and accurate position information to compensate for the rapid movement of the beating heart. However, high-speed cameras can only visualize the outer surface of the heart and are not appropriate for surgeries performed inside the heart.

In [39], a pair of X-ray cameras and an infrared tracking system were combined to obtain the positions of the internal markers attached to the heart tissue. Similarly, in [40], the authors used an infrared tracker system to locate the 3-DOF positions of the heart. These methods require passive markers attached on the point of interest of the heart tissue, which may be affected during tool-tissue interaction and further operations.

Another common sensor used for guiding intracardiac beating heart repairs is ultrasound (US) machine. Yuen et al. developed a 3-DOF US-guided motion compensation system for beating-heart mitral valve repair [21], [41]. Kesner et al. applied a robotic catheter system combining US guidance and force control to perform cardiac tissue ablation [42]. In [17], [43]–[45], the authors developed a master-slave teleoperation system and combined US images with various controllers to compensate for the beating heart's motion. The acquisition and processing of US images cause a large time delay, which needs to be compensated for via control.

In addition to various image-based sensors, non-image-based sensors such as force sensors and sonomicrometry crystals are proposed to solve the problem of motion compensation and/or haptic feedback. In [46]–[50], the authors utilized force sensors to compensate for the physiological motion by controlling the contact forces to track the desired ones. These methods were assumed that the surgical robot has somehow been initially controlled to come into contact with the heart tissue, and the control goals are maintaining contact between the tool and the tissue. In [51], [52], the authors used sonomicrometry crystals to track the beating-heart motion in real time and generalized adaptive predictors to

11

predict the heart's motion. By putting six and one sonomicrometry crystals under and on the surface of the heart, the electrocardiogram (ECG) biological signals of the heart surface can be measured based on the transmission and reception of US signals. This technique is feasible as the heart position can be captured through blood, although the calculation is complex and time-consuming.

2.3 Control Methods

Various position-, force-, and impedance-based control methods have been proposed for enabling tool-tissue motion compensation for beating-heart surgery and non-oscillatory haptic feedback in teleoperation systems.

2.3.1 Position-based Control Methods

The position-based controllers need the current beating-heart's position and can be classified into predictive feedforward controllers and predictive feedback controllers. Predictive feedforward controllers use the heart's position as the set point to move the surgical tools. Predictive feedback controllers not only need the heart's current position but also take the tracking error into account.

In [52], Bebek and Cavusoglu proposed a control algorithm based on the previous quasiperiodic heart motions which are ECG signals detected through sonomicrometry crystals. In [21], the authors collected the heart positions from US images, and employed an EKF to compensate the time delay caused by image acquisition and processing. This method took advantage of the quasi-periodicity of the heart motion and modeled the heart motion as a time-varying Fourier series. Many of the predictive feedforward controllers are used for hand-held systems.

To further compensate for the position tracking errors, predictive feedback controllers are used. In [23], the authors developed a teleoperation system and proposed a feedback controller with a modified Smith predictor to ensure the distance between the surgical tool

and the heart at desired values as commanded by the human operator's hand position. In [43], the authors presented three different Smith-predictor-based feedback controllers to tackle issues such as time delays, different measurement rates, and unregistered sensor data.

2.3.2 Force-based Control Methods

Force control methods are benefit for applications that require contact such as heart biopsy with controlled depth. Considering the process of tool-tissue interaction in robot-assisted beating-heart surgery, precisely applying forces on the beating-heart tissue and enabling the surgical robot to comply with the beating-heart's motion simultaneously is important. Therefore, several force control methods were proposed.

Moreira et al. [46], [47] proposed a force control method using active observer based on a viscoelastic interaction model to compensate for the physiological motion. Dominici and Cortesao achieved motion compensation by designing a cascade model predictive control architecture with a Kalman active observer [48], [49], and a double active observer architecture [50]. These systems use similar feedback controllers. In addition, Yuen [53] and Kesner [42], [54] separately combined the US image guidance with a force controller incorporating a feed-forward term containing the estimated motion of the beating heart. These methods incorparated position control and force control to achieve beating-heart motion compensation.

Much of the above work focuses on hand-held systems instead of teleoperation systems which are possible to enable haptic feedback to the human operator. Haptic feedback during a surgical operation is significant for the human operator to be able to accurately execute the surgical tasks especially in beating-heart surgeries involving tissue cutting and sewing, grasping, dissection [55], etc. During the operation of such surgical tasks, the tool-tissue interaction forces should be within a safety range to avoid potential tissue injury. To enable the human operator to perceive appropriate haptic feedback under contact, bilateral teleoperation systems were studied. As discussed above, the issue of oscillatory haptic

13

feedback caused by force sensor inertia should be considered. For instance, in [36], Nakajima et al. performed haptic feedback using an acceleration-based bilateral control system. In [56], the authors developed a force feedback control system for bimanual telerobotic surgery using the da Vinci surgical system (Intuitive Surgical Inc.).

2.3.3 Impedance-based Control Methods

Most successful applications of robot-assisted surgical systems to date have been performed based on position or force control, in which the surgical robot is treated essentially as an isolated system. However, in robot-assisted beating-heart surgeries, control of the dynamic behavior between the surgical robot and the beating-heart tissue is also required. Given the beating-heart contains inertial objects, the surgical robot and the beating-heart can be expressed as an impedance and admittance, respectively [57], [58]. Generally, the beating-heart can be regarded as a source of "disturbances" to the surgical robot, and the "disturbance response" of the surgical robot can be modulated to control the dynamic behavior between the surgical robot and the beating-heart tissue by varying the parameters and/or structure of the impedance. In [59], the authors proposed an adaptive control architecture based on model reference adaptive control to solve the 3D physiological motion compensation in beating heart surgery. The main advantage of impedance-based control system is the desired performance can be achieved via appropriate parameter adjustment of the reference impedance models without any measurement or estimation of the beating-heart's motion.

Following the lead from prior work, in this thesis, we present several reference-impedance-model-based master-slave teleoperation systems to achieve the following objectives during slave-heart interaction (Fig. 2.2): (a) the slave robot should synchronize its motions with the heart's motion to execute specific surgical tasks, and (b) to avoid the induced motion phenomenon [60], the human operator should only feel what one would feel when directly working on an arrested heart. The second objective means that the quasi-periodic heartbeat-induced forces caused by the residual mismatch between the robot and the heart motions and by the slave-mounted force sensor's internal inertia (which makes it

register a sinusoidal force when the sensor undergoes an oscillatory motion) should not be transmitted to the operator.

In this thesis, the communication delay is not considered because long-distance telesurgery of the beating heart is not the goal. The purpose of the telerobotics-assisted surgical system is to enable motion compensation and non-oscillatory haptic feedback during beating-heart surgery while allowing the human operator to operate from a user console.
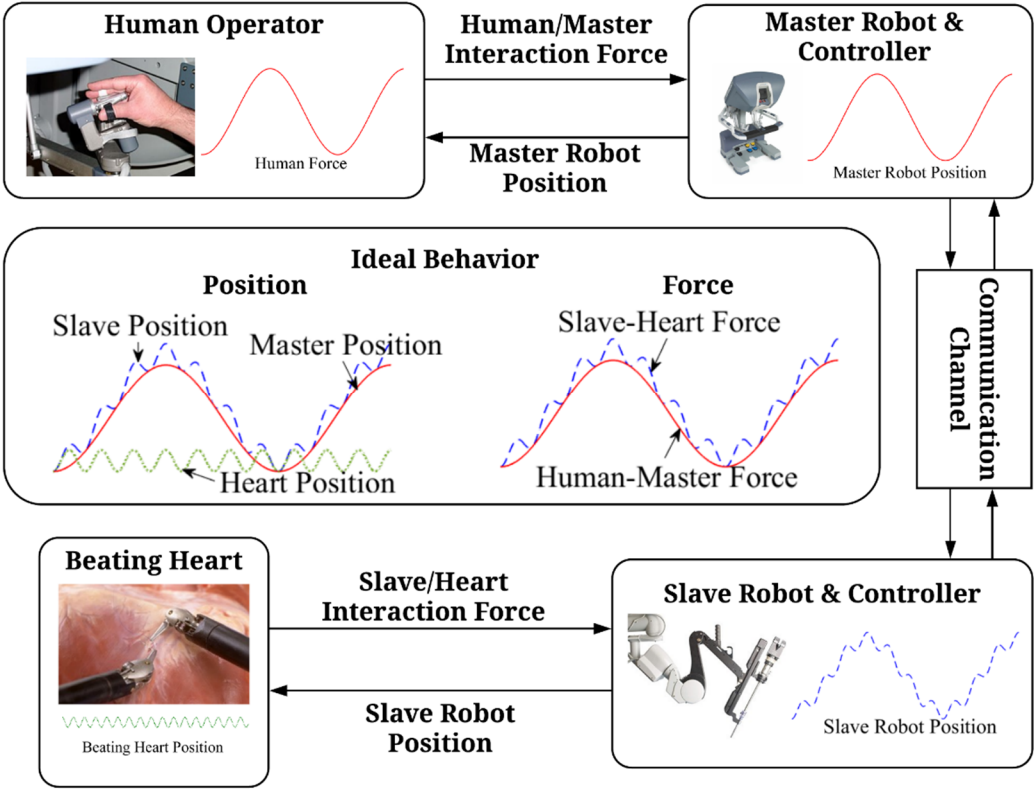
Figure 2.2. The ideal teleoperation system and the ideal behaviors of position and force for beating-heart surgery. The desired position-tracking performance is shown in the left part of the ideal behavior block. To graphically identify the noncontact and contact cases, the heart's position (dotted green line) is shown to have an offset from the initial positions of the master (solid red line) and slave (dashed blue line) robots' end-effectors. When the dotted

green line is above the latter two lines, it means there is no contact, and the master and the slave have the same trajectory; otherwise, contact has been made, and the slave robot is to follow the master's commands and compensates for the heart's oscillatory motion. The desired force performance is shown in the right part of the ideal behavior block. When there is no contact, the slave-heart interaction force (dashed red line) stays at zero; while when contact, it should be similar to the human-master interaction force (solid black line).

Chapter 3

Bilateral Impedance Control

This chapter[2] will discuss the design and development process for a bilateral impedance-controlled master-slave telerobotic system for beating-heart surgery to implement rapid compensation for the beating heart's motion and reflect the non-oscillatory portion of salve-heart tissue interaction force on the human operator's hand as haptic feedback. The designed reference impedance models for the master and slave robots and their parameters adjustments and robot controllers are presented in section 3.2. The efficacy of the proposed strategy and developed system is assessed through experiments for 1-DOF and 3-DOF, respectively.

3.1 Telerobotic System

The goal of a robot-assisted teleoperation system for beating-heart surgery is to simultaneously make the slave robot compensate for the heart motion and ensure the human operator to perceive non-oscillatory haptic feedback. To achieve the desired behaviors, the

---

[2]Portions of this chapter were published in "L. Cheng, M. Sharifi, M. Tavakoli, "Towards Robot-Assisted Anchor Deployment in Beating-Heart Mitral Valve Surgery," *The International Journal of Medical Robotics and Computer Assisted Surgery*, vol. 14, no. 3, pp. e1900, 2018." [14] and in "L. Cheng, J. Fong, M. Tavakoli, "Semi-Autonomous Surgical Robot Control for Beating-Heart Surgery," *IEEE 15th International Conference on Automation Science and Engineering*, Vancouver, Canada, 2019." [15]

block diagram of the developed bilateral impedance-controlled teleoperation system is shown in Figure 3.1. In Figure 3.1, $\mathbf{f}_h$ is the interaction force vector between the master robot and the human operator, and $\mathbf{f}_e$ is the interaction force vector between the slave robot and the beating heart. They are measured directly through two force sensors. In the developed system, a thin rigid surgical tool is mounted on the end of the slave robot, where a force sensor attached. Considering the volume of the force sensor, in realistic surgery the thin and long surgical tool will be inserted into the heart through a suture on the exterior heart wall and leave the force sensor outside the body.
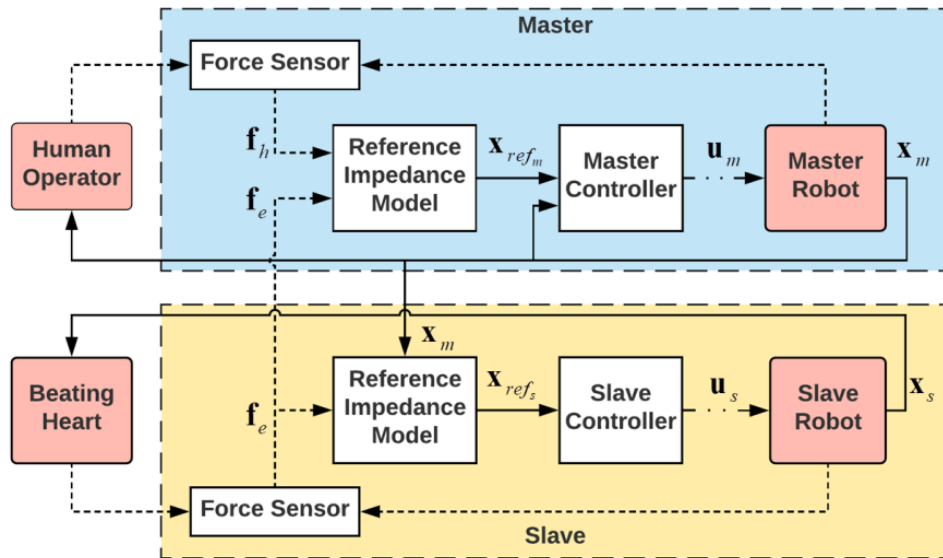
Figure 3.1. The bilateral impedance-controlled teleoperation system. The solid lines indicate the position transfer paths. The dashed lines indicate the force transfer paths. The dash-dotted lines are control signals.

In addition, $\mathbf{x}_{ref_m}$ and $\mathbf{x}_{ref_s}$ are the desired position vectors for the master and slave robots, which are generated by the reference impedance models for the respective robot. Note

that $\mathbf{x}_m$ and $\mathbf{x}_s$ are the actual position vectors of the master and slave robots, respectively. The controllers receive the position errors between the desired positions generated by the reference models and the actual positions read from the robots and then output torque vectors $\mathbf{\mu}_m$ and $\mathbf{\mu}_s$ to the robots.

3.2 Bilateral Impedance Control

3.2.1 Reference Impedance Models

The reference impedance model for the master robot in Cartesian coordinates includes the human-master interaction force, the scaled slave-heart interaction force, and the desired master response trajectory. The relationships can be expressed as

$$\mathbf{M}_m \ddot{\mathbf{x}}_{ref_m} + \mathbf{C}_m \dot{\mathbf{x}}_{ref_m} + \mathbf{K}_m \mathbf{x}_{ref_m} = \mathbf{f}_h - \mathbf{K}_f \mathbf{f}_e \tag{3.1}$$

where $\mathbf{K}_m$, $\mathbf{C}_m$, $\mathbf{M}_m$ are the virtual stiffness, damping and mass 3-by-3 diagonal matrices of the master impedance model. Here, $\mathbf{x}_{ref_m}$ is the position response of the master impedance model, $\mathbf{f}_h \in \mathbb{R}^{3 \times 1}$ and $\mathbf{f}_e \in \mathbb{R}^{3 \times 1}$ are the interaction force between the human operator and the master robot and the interaction force between the slave robot and the heart tissue, respectively. Also, $\mathbf{K}_f$ is a diagonal matrix of the force scaling factor. The interaction forces ($\mathbf{f}_h \in \mathbb{R}^{3 \times 1}$, $\mathbf{f}_e \in \mathbb{R}^{3 \times 1}$) and the desired master response ($\mathbf{x}_{ref_m} \in \mathbb{R}^{3 \times 1}$) are vectors.

Equivalently, the transfer function of (3.1) in each axis can be written as a second order function with a damping ratio ζ_{m_i} and a natural frequency $\omega_{n_{m_i}}$

$$Z_{m_i} = \frac{1}{m_{m_i} s^2 + c_{m_i} s + k_{m_i}} = \frac{\omega_{n_{m_i}}^2}{k_{m_i}(s^2 + 2\zeta_{m_i}\omega_{n_{m_i}} s + \omega_{n_{m_i}}^2)} \tag{3.2}$$

19

where $\zeta_{m_i} = \dfrac{c_{m_i}}{2\sqrt{m_{m_i} k_{m_i}}}$ and $\omega_{n_{m_i}} = \sqrt{\dfrac{k_{m_i}}{m_{m_i}}}$. Note that, $i = x,\ y,\ z$ for the x-, y-, z-axis, respectively. Matrix $\mathbf{M}_m = \mathrm{diag}(\omega_{n_{m_x}}, \omega_{n_{m_y}}, \omega_{n_{m_z}})$, $\mathbf{C}_m = \mathrm{diag}(c_{m_x}, c_{m_y}, c_{m_z})$, $\mathbf{K}_m = \mathrm{diag}(k_{m_x}, k_{m_y}, k_{m_z})$, $\mathbf{Z}_m = \mathrm{diag}(\zeta_{m_x}, \zeta_{m_y}, \zeta_{m_z})$, and $\mathbf{\Omega}_{n_m} = \mathrm{diag}(\omega_{n_{m_x}}, \omega_{n_{m_y}}, \omega_{n_{m_z}})$. In the following, only matrices $\mathbf{K}_m$, $\mathbf{Z}_m$, and $\mathbf{\Omega}_{n_m}$ will be adjusted.

The reference impedance model for the slave robot is concerned with the slave-heart interaction force and the desired slave impedance model's response deviation from the trajectory of the master robot. It can be expressed as

$$\mathbf{M}_s \ddot{\tilde{\mathbf{x}}}_{ref_s} + \mathbf{C}_s \dot{\tilde{\mathbf{x}}}_{ref_s} + \mathbf{K}_s \tilde{\mathbf{x}}_{ref_s} = -\mathbf{f}_e \tag{3.3}$$

Where $\tilde{\mathbf{x}}_{ref_s} = \mathbf{x}_{ref_s} - \mathbf{K}_\mathrm{p} \mathbf{x}_m$, and $\mathbf{K}_\mathrm{p}$ is a matrix of the position scaling factor. Here, $\mathbf{x}_m \in \mathbb{R}^{3\times 1}$ is the Cartesian position vector of the master robot's end-effector, and $\mathbf{x}_{ref_s}$ is the position of the slave impedance model. Also, $\mathbf{K}_s$, $\mathbf{C}_s$, $\mathbf{M}_s$ are the virtual stiffness, damping and mass diagonal matrices of the slave impedance model.

The transfer function of (3.3) in each axis is

$$Z_{s_i} = \frac{1}{m_{s_i} s^2 + c_{s_i} s + k_{s_i}} = \frac{\omega_{n_{s_i}}^2}{k_{s_i}(s^2 + 2\zeta_{s_i} \omega_{n_{s_i}} s + \omega_{n_{s_i}}^2)} \tag{3.4}$$

where $\zeta_{s_i} = \dfrac{c_{s_i}}{2\sqrt{m_{s_i} k_{s_i}}}$ and $\omega_{n_{s_i}} = \sqrt{\dfrac{k_{s_i}}{m_{s_i}}}$. Also, $i = x,\ y,\ z$ for the x-, y-, z-axis, respectively. The matrices that need to be adjusted are $\mathbf{K}_s = \mathrm{diag}(k_{s_x}, k_{s_y}, k_{s_z})$, $\mathbf{Z}_s = \mathrm{diag}(\zeta_{s_x}, \zeta_{s_y}, \zeta_{s_z})$, and $\mathbf{\Omega}_{n_s} = \mathrm{diag}(\omega_{n_{s_x}}, \omega_{n_{s_y}}, \omega_{n_{s_z}})$.

The reference impedance models for slave and master robots are stable second-order differential equations when the impedance parameters are set as positive. In order to make the telerobotic system have motion compensation for the fast beating heart's motion, the most crucial procedure is parameter adjustment for the two reference impedance models for the master and slave robots.

3.2.2 Parameter Adjustments

The parameter adjustments for the reference impedance models mainly rely on the frequency ranges of the moving organ motions induced by respiratory and heartbeat. In this section, a general description about the parameter adjustments is presented to show how the developed telerobotic system can achieve motion compensation and non-oscillatory force feedback simultaneously. More detail parameter adjustments guidance and analysis will be presented in Section 3.3 and 3.4 according to specific heart motion sequences and applications.

The master impedance model (3.1) should be designed to provide feedback of the non-oscillatory part of the slave-heart tissue interaction force for the human operator and not to reflect the oscillatory motion to the human operator's hand so that to avoid fatigue and exhaustion, which means $(\mathbf{f}_h - \mathbf{K}_\mathrm{f} \mathbf{f}_e) \to \mathbf{0}$ when the high frequency of the slave/heart interaction force $(\mathbf{f}_e)$ has been filtered. To achieve this static force reflecting performance, the stiffness parameter, $\mathbf{K}_m$, of the master impedance model should be chosen small, and the natural frequency of the master impedance model should be much lower than that of the beating heart ω_h, that is $\mathbf{\Omega}_{n_m}$ should have a low natural frequency. In addition, in order to get a fast behavior in response to the harmonic physiological force of the human operator, the damping ratio of the master impedance model in each direction is chosen to be 0.7.

The slave impedance model (3.3) should be adjusted such that the slave robot complies with the physiological force and/or the disturbance of beating heart during the procedure of tracking the scaled master robot's trajectory, that is the flexibility of the slave

21

robot is the deviation from the master trajectory ($\tilde{\mathbf{x}}_{ref_s} = \mathbf{x}_{ref_s} - \mathbf{K}_\mathrm{p}\mathbf{x}_m$) based on the magnitude of the slave/heart interaction force. It should be noticed that the values of the slave impedance parameters can neither be too small nor too large, because too small values will lead to a super flexible slave robot that it cannot apply enough forces to the heart and too large values will make the slave robot very rigid that the motion compensation will not be accurate. Therefore, the stiffness value of the slave impedance model ($\mathbf{K}_s$) should be adjusted to be moderate. Similarly, to get a fast behavior in response to the harmonic physiological force of the heart, the damping ratio of the slave impedance model in each direction is chosen to be 0.7. The natural frequency of the impedance model should be greater than the frequency of the beating heart, that is $\mathbf{\Omega}_{n_s}$ should have a high natural frequency.

The designed reference impedance models for the master and slave robots can be used for teleoperation systems to execute surgical tasks on the beating-heart tissue. In Section 3.3 and 3.4, two teleoperation systems are developed to perform 1-DOF and 3-DOF surgical tasks, respectively.

3.3 1-DOF Physiological Organ Motion Compensation

In this Section, the developed system is validated in a specific simulated surgical task — anchor deployment for mitral valve annuloplasty, which undergoes rapid translational motions primarily along one axis [61]. As the mitral valve annulus has a predominantly uniaxial motion trajectory, in the experiments the simulated surgical task is simplified to 1-DOF task.

Every year, 300,000 people worldwide undergo open heart surgery for mitral valve repair [62]. When the two leaflets normally involved in sealing the mitral valve do not coaptate properly, a reconstructive procedure called mitral valve annuloplasty may be used to address this problem. This surgery involves implanting an annuloplasty ring onto the mitral valve using several anchors; pulling a string that goes through the ring pulls the leaflets

22

together to facilitate coaptation and aid to reshape the mitral valve [63], [64], and it has better durability and reliability than ringless repairs, except recurrent regurgitation not resulting in reoperation may occur [65]. To enable the performing of this particular surgical task when the heart is beating, a motion compensation system is needed. The instruments used for mitral valve annuloplasty involve two parts (Figure 3.2). One instrument is the annuloplasty ring holder. The other one is the anchor driver mounted on the end of the slave robot. The anchor driver is a thin rigid tube and deploys anchors that secure the stiff ring to the annulus to reshape it. To reach the interior heart tissue, both instruments are inserted into the left atrium through a suture on the exterior heart wall [61]. In the experiments, for the sake of brevity, we simulated the procedure of anchor deployment using a phantom tissue that undergoes movements similar to that of a beating heart. In the following, a detailed description of the parameter adjustment guideline is presented, and then an evaluation in terms of safely interacting with a moving organ is implemented in a water tank.
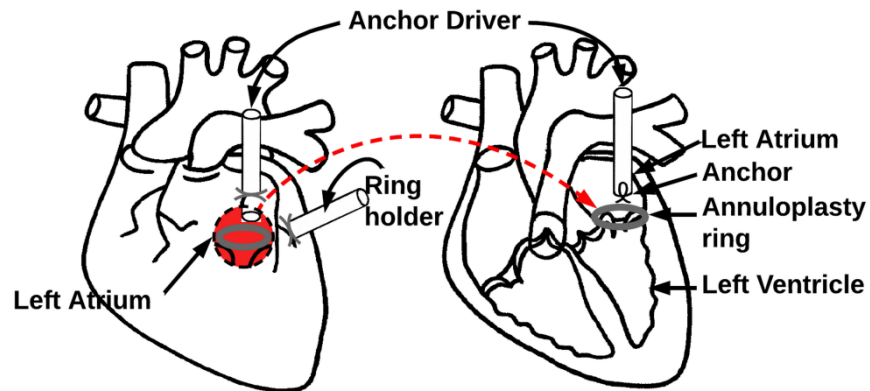
Figure 3.2. Diagram of proposed mitral valve annuloplasty procedure.

To enable the performing of anchor deployment when the heart is beating, a motion compensation system such as the one shown in Figure 3.3 is needed. To begin, the human operator should use one of his/her hands to control a telerobotic system, which includes a master and a slave robot to bring an anchor driver attached to the end-effector of slave robot close to the beating-heart tissue. Once the anchor driver and the heart tissue contact, the

23

human operator could use his/her other hand to execute the anchor deployment. All of these are guided by US images provided to the human operator.
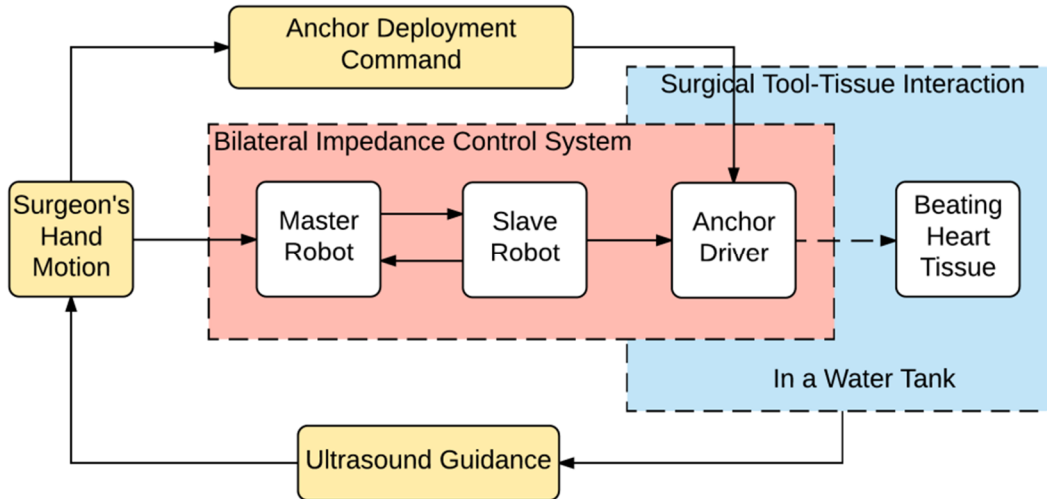
Figure 3.3. Motion compensation system for simulated mitral valve annuloplasty procedure.

In this section, the two bilateral impedance controllers for the master and slave robots are used to compensate for the beating heart motion to improve the success rate of deploying anchors and minimize the risk of tool-tissue collision and tissue injury. The concepts of the two defined reference impedance models (3.1) and (3.3) are schematically expressed in Figure 3.4. The reference impedance model for the master robot (3.1) provides the human operator the non-oscillatory slave-tissue interaction force feedback, and the reference impedance model for the slave robot (3.3) determines the flexibility of the surgical tool attached to the end of the slave robot with respect to the master robot's trajectory in response to the slave-tissue interaction forces.
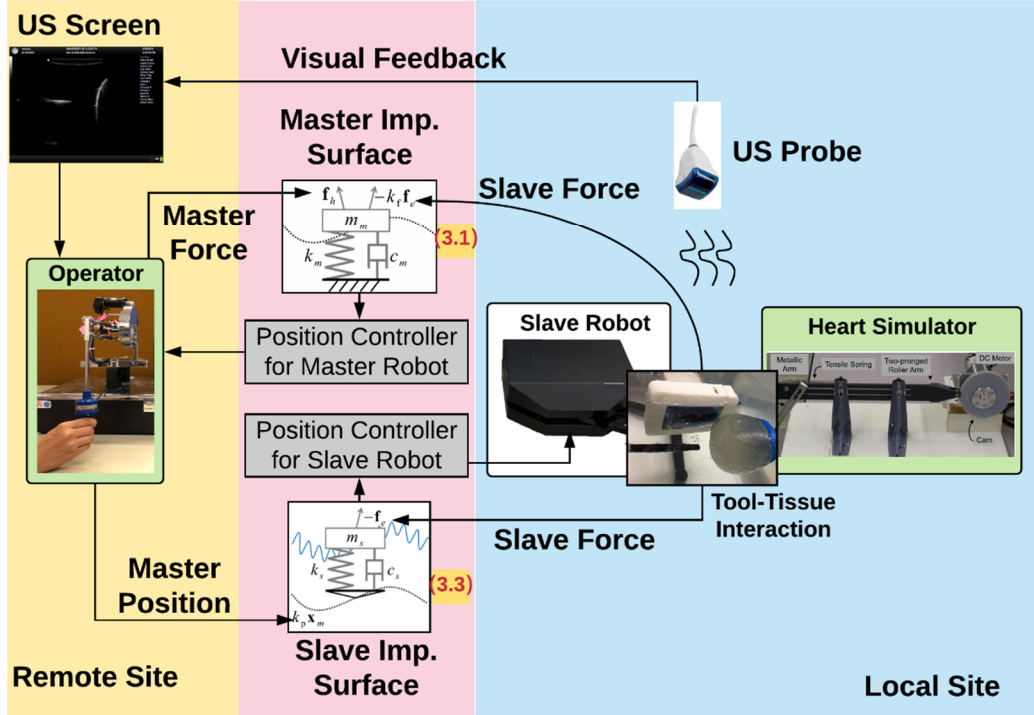
Figure 3.4. The concepts of master and slave reference impedance models in the proposed bilateral controller for robotic surgery systems.

3.3.1 Experimental setup

The experimental setup employs a Phantom Premium 1.5A robot (Geomagic Inc., Wilmington, MA, USA) with three DOFs as the master robot and a Quanser planar robot (Quanser Consulting Inc., Markham, ON, Canada) with two DOFs as the slave robot (Figure 3.5a). To measure the applied interaction forces of the human operator and the heart tissue, the Phantom Premium and Quanser robots are respectively equipped with a 6-axis 50M31 force/torque sensor (JR3 Inc., Woodland, CA, USA) and a 6-axis Gamma force/torque sensor (ATI Industrial Automation, Apex, NC, USA), respectively. An US scanner (SonixTouch from Ultrasonix, Richmond, BC, Canada) is used by the operator to see the surgical tool and

the simulated heart, both of which are submerged in water to represent the presence of blood inside the heart's chamber.

The red dashed box in Figure 3.5a, which is magnified in Figure 3.5b, includes a handheld anchor deployment device, a simulated moving heart tissue, a surgical tool, and the US probe. The anchor driver is inserted into a 16-gauge blunt needle (OD 1.651mm) and fixed on the end-effector of the slave robot. By pressing the button of the anchor driver, an anchor can be pushed out from the surgical tool tip. The heart tissue is simulated by an artificial plastisol-based tissue made of soft plastic that is visible under US. This tissue is attached to a custom-built mechanical cam which produces peak-to-peak amplitude of 9 mm and has a fundamental frequency of 64 bpm to simulate the beating heart motion which temporally matched to an ECG signal [24]. These instruments are placed in a tank with water. To verify the results of automated heart tissue tracking by the slave robot, real-time position measurement of the beating-heart simulator was collected from a potentiometer. The position of the US probe is adjusted such that the motions of surgical tool tip and the heart tissue are both visible to the human operator (Figure 3.6).
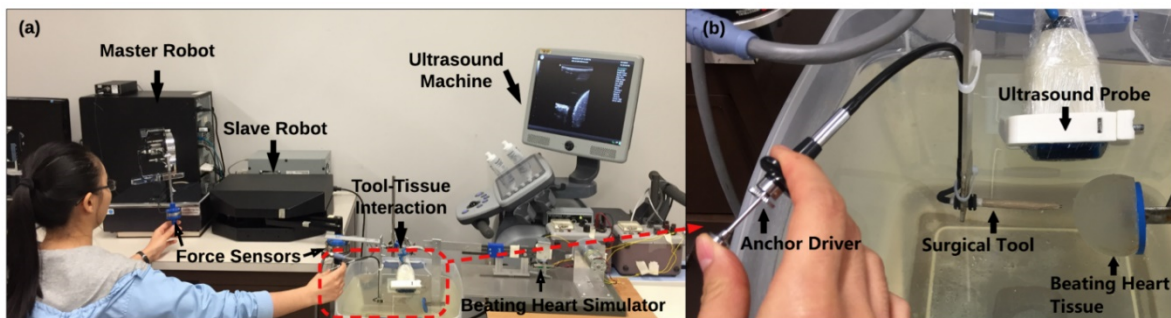
Figure 3.5. Experimental setup. (a) Master, slave and heart simulator and (b) tool-tissue interaction.
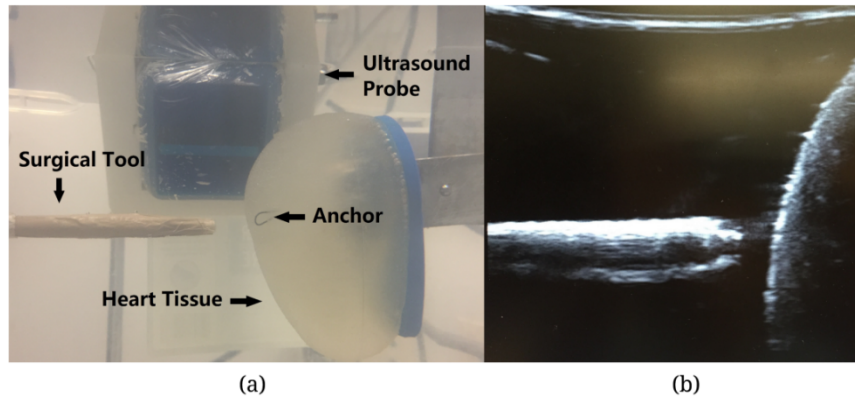
Figure 3.6. (a) Underwater view of the surgical tool and heart tissue, and (b) their US image.

1) Heart Motion

For mitral valve annuloplasty, as the heart tissue undergoes rapid translational motions primarily along one axis, a mechanical beating-heart simulator with 1-DOF motion is used in the experiments. The built beating-heart simulator utilized a mechanical cam to convert the rotational movement of a DC motor into linear movement. The custom-built mechanical cam produces peak-to-peak amplitude of 9 mm and its speed and torque can be controlled by the DC motor (DC Gearmotor 6331K33 from McMaster-Carr, Aurora, OH, USA). In this experiment, the fundamental frequency of the mechanical cam was chosen to be 64 bpm to simulate the beating heart motion which temporally matched to an ECG signal. The quasi-periodic 1-DOF heart motion signals with the respective power spectral densities (PSD) are shown in Figure 3.7. Observable dominant peaks are at $\omega_h = 7.04$ rad/sec, which correspond to heartbeat motion. This dominant frequency will be used to adjust the parameters of the reference impedance models.
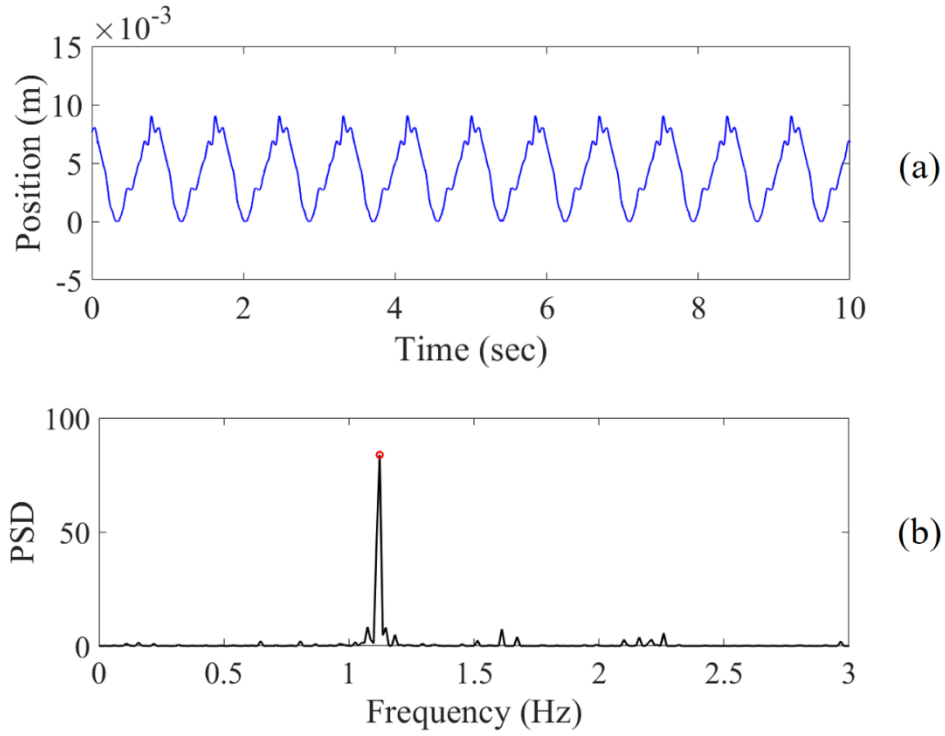
Figure 3.7. 1-DOF position of the heart simulator. (a) The motion of the customized heart simulator. (b) The power spectral density (PSD) analysis of the heart beats.

2) Parameters Tuning

According to Section 3.2.2, the matrices that need to be tuned are $\mathbf{K}_m$, $\mathbf{Z}_m$, and $\mathbf{\Omega}_{n_m}$ and $\mathbf{K}_s$, $\mathbf{Z}_s$, and $\mathbf{\Omega}_{n_s}$. As the task is 1-DOF, the parameters tuning guidance shown below is in one direction. Please note, the impedance parameters are set as positive so that the reference impedance models are stable second-order differential equations.

The reference impedance model (3.1) should be designed to achieve $(f_h - k_f f_e) \to 0$ when the high frequency of the slave-heart interaction force has been filtered to avoid possible exhaustion caused by the refection of the oscillatory slave-heart interaction force to

the human operator. Therefore, the stiffness parameter, k_m, of the impedance model should be chosen small, and the natural frequency of the model should be much lower than that of the beating-heart ω_h which has a range of 6.28 ~ 10.68 rad/sec; that is $\omega_{n_m} = \sqrt{k_m/m_m}$ should have a low natural frequency ($\omega_{n_m} \leq 0.6$ rad/sec $<< \omega_h$) [66]. Also, the damping ratio of the impedance model ($\zeta_m = c_m/2\sqrt{m_m k_m}$) is chosen to be 0.7 so that to get a fast behavior in response to the harmonic physiological force of the human operator.

It should be noted that the proposed strategy can be used for a large range of irregular heart rates. For example, if the irregular heart motion has a rate not less than 2 rad/sec, the oscillatory portion of the tool-tissue interaction force will barely be perceived by the human operator given the adjusted ω_{n_m}. To be more specific, Figure 3.8 implies that when $\omega_{n_m} << \omega_h$, the high-frequency oscillatory force portion of f_e can be significantly filtered. Moreover, based on the slope (-40 dB/decade) in the Bode diagram of Fig. 5, the amplitude of the master impedance model's response with respect to the amplitude of the high-frequency portion of the slave-heart interaction force (F_e^h) is $\left| X_{ref_m}^h \right| < (\omega_{n_m}/\omega_h)^2 \left| k_f F_e^h / k_m \right|$. It can be seen that a small ω_{n_m} will lead to small amplitude of the master impedance model's response with respect to high-frequency inputs. In the experiments, ω_{n_m} is chosen to be 0.5 rad/sec, so when ω_h is not less than 2 rad/sec, the magnitude of master impedance response with respect to the oscillatory tool-tissue interaction forces will be reduced to $\left| X_{ref_m}^h \right| < 0.0625 \left| k_f F_e^h / k_m \right|$.
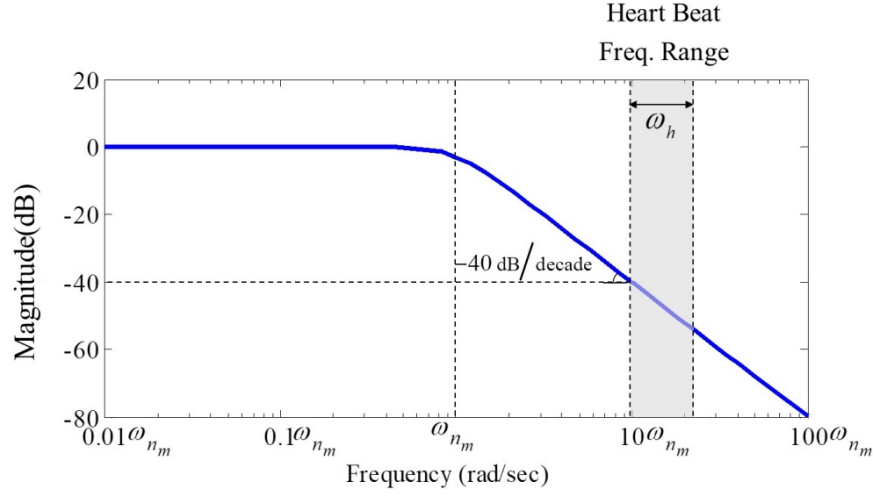
Figure 3.8. The Bode diagram of the reference impedance model for the master robot.
This imedance model has a natural frequency of ω_{n_m} and damping ratio of 0.7 for filtration
of the high-frequency oscillatory portion of the slave-heart interaction force.

The slave impedance model (3.3) should be adjusted such that the slave robot
complies with the physiological force and/or the disturbance of beating heart during the
procedure of tracking the scaled master robot's trajectory. The flexibility of the slave
impedance model leads to the deviation from the master trajectory ($\tilde{x}_{ref_s} = x_{ref_s} - k_p x_m$),
which is suitable for compliance with the heart's oscillatory motion. However, the values of
the slave impedance parameters can neither be too small nor too large, because too small
values will lead to a super flexible slave robot that it cannot apply enough forces to the heart
and too large values will make the slave robot very rigid that the motion compensation will
not be accurate. Therefore, the stiffness value of the slave impedance model (k_s) should be
adjusted to be moderate. The exact stiffness can be tuned by trial and error according to
specific task and the used slave robot. Also, the natural frequency of (3.3) (ω_{n_s}) should be
several times greater than the higher rate of the physiological motion ($\omega_{n_s} \gg \omega_h$). Figure 3.9

shows that when $\omega_{n_s} \gg \omega_h$, the magnitude of the slave impedance model's response (deviation response $\tilde{x}_{ref_s}$) will be maximum and its phase will be the same as that of the input forces (f_e). Similarly, ζ_s is chosen to be 0.7.
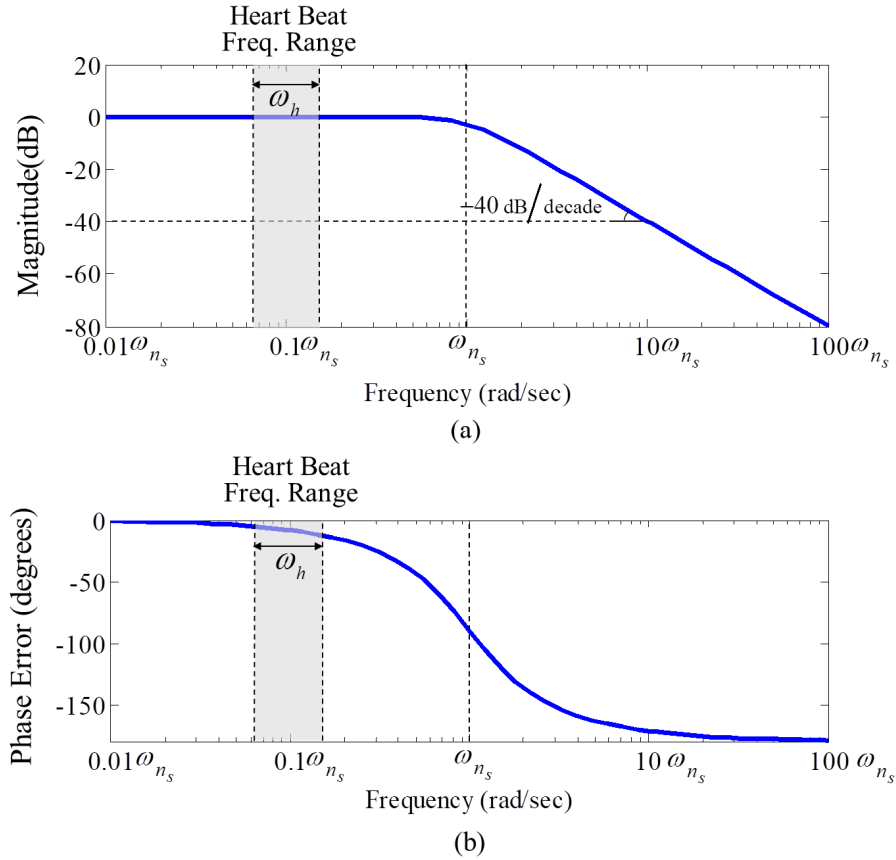
Figure 3.9. The Bode diagram of the reference impedance model for the slave robot. This impedance model has a natural frequency of ω_{n_s} and damping ratio of 0.7 for a fast and compliant response to the oscillatory slave-heart interaction forces. (a) and (b) show the magnitude and phase error, respectively.

31

For the above purposes, the adjusted parameters of the two impedance models are listed in Table 3.1.

Table 3.1. Parameter adjustments of master and slave impedance models

CHARACTERISTIC	Master Impedance Adjustment	Slave Impedance Adjustment
Stiffness	$k_m = 5$ N/m	$k_s = 100$ N/m
Damping Ratio	$\zeta_m = 0.7$	$\zeta_s = 0.7$
Natural Frequency	$\omega_{n_m} = 0.5$ rad/sec	$\omega_{n_s} = 50$ rad/sec
Damping and Mass	$m_m = 20$ kg, $c_m = 14$ Ns/m	$m_s = 0.04$ kg, $c_s = 2.8$ Ns/m
Scaling Factor	$k_f = 1$	$k_p = 1$

3) Controllers

In order to make the master and slave robots track the desired position perfectly, a nonlinear bilateral adaptive impedance controller was designed for each of them, respectively. In a nonlinear master-slave teleoperation system with master position x_m and slave position x_s, the dynamics of the master and slave in the Cartesian space are [67]

$$\mathbf{M}_{\mathbf{x},m}(\boldsymbol{\theta}_m)\ddot{\mathbf{x}}_m + \mathbf{C}_{\mathbf{x},m}(\boldsymbol{\theta}_m,\dot{\boldsymbol{\theta}}_m)\dot{\mathbf{x}}_m + \mathbf{G}_{\mathbf{x},m}(\boldsymbol{\theta}_m) + \mathbf{F}_{\mathbf{x},m}(\dot{\boldsymbol{\theta}}_m) = \mathbf{f}_h + \mathbf{f}_m \tag{3.5}$$

$$\mathbf{M}_{\mathbf{x},s}(\boldsymbol{\theta}_s)\ddot{\mathbf{x}}_s + \mathbf{C}_{\mathbf{x},s}(\boldsymbol{\theta}_s,\dot{\boldsymbol{\theta}}_s)\dot{\mathbf{x}}_s + \mathbf{G}_{\mathbf{x},s}(\boldsymbol{\theta}_s) + \mathbf{F}_{\mathbf{x},s}(\dot{\boldsymbol{\theta}}_s) = \mathbf{f}_s - \mathbf{f}_e \tag{3.6}$$

where $\boldsymbol{\theta}_i$ is the joint angle of the robot's end-effector, $\mathbf{f}_i$ is the control torque of the robot, and $\mathbf{M}_{\mathbf{x},i}(\boldsymbol{\theta}_i)$, $\mathbf{C}_{\mathbf{x},i}(\boldsymbol{\theta}_i,\dot{\boldsymbol{\theta}}_i)$, $\mathbf{G}_{\mathbf{x},i}(\boldsymbol{\theta}_i)$ and $\mathbf{F}_{\mathbf{x},i}(\dot{\boldsymbol{\theta}}_i)$ are the inertia matrix, the centrifugal and Coriolis term, the gravity term, and the friction torque, respectively. Note that $i=m$ for the master and $i=s$ for the slave.

The kinematic transformations between the Cartesian space and the joint space are expressed as

$$\mathbf{x}_i = \mathbf{\Omega}_i(\mathbf{\theta}_i), \ \dot{\mathbf{x}}_i = \mathbf{J}_i(\mathbf{\theta}_i)\dot{\mathbf{\theta}}_i, \ \ddot{\mathbf{x}}_i = \mathbf{J}_i(\mathbf{\theta}_i)\ddot{\mathbf{\theta}}_i + \dot{\mathbf{J}}_i(\mathbf{\theta}_i)\dot{\mathbf{\theta}}_i \tag{3.7}$$

where $\mathbf{J}_i(\mathbf{\theta}_i) = d\mathbf{\Omega}_i(\mathbf{\theta}_i)/d\mathbf{\theta}_i$ is the Jacobian matrix.

The matrices have the following properties [68]:

Property 1. The matrix $\mathbf{M}_{\mathbf{x},i}(\mathbf{\theta}_i)$ is symmetric and positive definite.

Property 2. $\dot{\mathbf{M}}_{\mathbf{x},i}(\mathbf{\theta}_i) - 2\mathbf{C}_{\mathbf{x},i}(\mathbf{\theta}_i, \dot{\mathbf{\theta}}_i)$ is skew symmetric.

Property 3. The left hand of (3.5) and (3.6) can be linearly parameterized

$$\mathbf{M}_{\mathbf{x},i}(\mathbf{\theta}_i)\mathbf{\Psi}_{1,i} + \mathbf{C}_{\mathbf{x},i}(\mathbf{\theta}_i, \dot{\mathbf{\theta}}_i)\mathbf{\Psi}_{2,i} + \mathbf{G}_{\mathbf{x},i}(\mathbf{\theta}_i) + \mathbf{F}_{\mathbf{x},i}(\dot{\mathbf{\theta}}_i) = \mathbf{Y}_{\mathbf{x},i}(\mathbf{\Psi}_{1,i}, \mathbf{\Psi}_{2,i}, \mathbf{\theta}_i, \dot{\mathbf{\theta}}_i)\hat{\mathbf{\theta}}_{\mathbf{x},i} \tag{3.8}$$

where $\hat{\mathbf{\theta}}_{\mathbf{x},i}$ is the vector of unknown parameters of the robot, and the regressor matrix $\mathbf{Y}_{\mathbf{x},i}$ contains known functions in the Cartesian space. The known vectors $\mathbf{\Psi}_{1,i}$ and $\mathbf{\Psi}_{2,i}$ are chosen according to the application.

In order to realize the responses tracking of the above two reference impedance models for the master and slave robots respectively, two nonlinear bilateral adaptive impedance control laws [69], [70] in Cartesian space are designed and expressed as

$$\mathbf{f}_m = -\lambda_{1,m}\hat{\mathbf{M}}_{\mathbf{x},m}\mathbf{s}_m + \hat{\mathbf{M}}_{\mathbf{x},m}\ddot{\mathbf{x}}_{r,m} + \hat{\mathbf{C}}_{\mathbf{x},m}\dot{\mathbf{x}}_{r,m} + \hat{\mathbf{G}}_{\mathbf{x},m} + \hat{\mathbf{F}}_{\mathbf{x},m} - \mathbf{f}_h \tag{3.9}$$

$$\mathbf{f}_s = -\lambda_{1,s}\hat{\mathbf{M}}_{\mathbf{x},s}\mathbf{s}_s + \hat{\mathbf{M}}_{\mathbf{x},s}\ddot{\mathbf{x}}_{r,s} + \hat{\mathbf{C}}_{\mathbf{x},s}\dot{\mathbf{x}}_{r,s} + \hat{\mathbf{G}}_{\mathbf{x},s} + \hat{\mathbf{F}}_{\mathbf{x},s} + \mathbf{f}_e \tag{3.10}$$

where $\mathbf{s}_i = \dot{\tilde{\mathbf{x}}}_i + \lambda_{2,i}\tilde{\mathbf{x}}_i$ is the designed sliding surface, $\dot{\mathbf{x}}_{r,i} = \dot{\mathbf{x}}_{ref_i} - \lambda_{2,i}\tilde{\mathbf{x}}_i$ is defined as the reference velocity for the robot, $\tilde{\mathbf{x}}_i = \mathbf{x}_i - \mathbf{x}_{ref_i}$ is the position tracking error of the robot. Here, $\lambda_{1,i}$ and $\lambda_{2,i}$ are positive constant parameters guarantee the stability of sliding surfaces (i.e. $\tilde{\mathbf{x}}_i \rightarrow 0$ as $\mathbf{s}_i \rightarrow 0$). The accent $\wedge$ denotes the estimated and updated values of matrices, vectors and scalars. Also, $\hat{\mathbf{M}}_{\mathbf{x},i}$, $\hat{\mathbf{C}}_{\mathbf{x},i}$, $\hat{\mathbf{G}}_{\mathbf{x},i}$ and $\hat{\mathbf{F}}_{\mathbf{x},i}$ are the estimated inertia matrix, Coriolis and centrifugal vector, gravity vector and friction vector, respectively. Also, based on (3.3), $\mathbf{x}_{ref_s} = \mathbf{x}_m + \tilde{\mathbf{x}}_{ref_s}$, $\dot{\mathbf{x}}_{ref_s} = \dot{\mathbf{x}}_m + \dot{\tilde{\mathbf{x}}}_{ref_s}$, and $\ddot{\mathbf{x}}_{ref_s} = \ddot{\mathbf{x}}_m + \ddot{\tilde{\mathbf{x}}}_{ref_s}$. Since a direct measurement of the master robot acceleration is challenging, it is estimated as

$$\ddot{\mathbf{x}}_{m_{est}} \simeq \frac{1}{m_m}(\mathbf{f}_h - k_f\mathbf{f}_e) - \frac{c_m}{m_m}\dot{\mathbf{x}}_m - \frac{k_m}{m_m}(\mathbf{x}_m - \mathbf{x}_0) \tag{3.11}$$

Equations (3.9) and (3.10) can be rewrite using Property 3, the linear parameterization

$$\mathbf{f}_m = \hat{\mathbf{M}}_{\mathbf{x},m}(-\lambda_{1,m}\mathbf{s}_m + \ddot{\mathbf{x}}_{r,m}) + \hat{\mathbf{C}}_{\mathbf{x},m}\dot{\mathbf{x}}_{r,m} + \hat{\mathbf{G}}_{\mathbf{x},m} + \hat{\mathbf{F}}_{\mathbf{x},m} - \mathbf{f}_h = \mathbf{Y}_{\mathbf{x},m}\hat{\boldsymbol{\theta}}_{\mathbf{x},m} - \mathbf{f}_h \tag{3.12}$$

$$\mathbf{f}_s = \hat{\mathbf{M}}_{\mathbf{x},s}(-\lambda_{1,s}\mathbf{s}_s + \ddot{\mathbf{x}}_{r,s}) + \hat{\mathbf{C}}_{\mathbf{x},s}\dot{\mathbf{x}}_{r,s} + \hat{\mathbf{G}}_{\mathbf{x},s} + \hat{\mathbf{F}}_{\mathbf{x},s} + \mathbf{f}_e = \mathbf{Y}_{\mathbf{x},s}\hat{\boldsymbol{\theta}}_{\mathbf{x},s} + \mathbf{f}_e \tag{3.13}$$

The closed-loop dynamics of the master and slave robots using the above bilateral adaptive impedance controller are expressed as

$$\mathbf{M}_{\mathbf{x},m}(\dot{\mathbf{s}}_m + \lambda_{1,m}\mathbf{s}_m) + \mathbf{C}_{\mathbf{x},m}\mathbf{s}_m = \mathbf{Y}_{\mathbf{x},m}\tilde{\boldsymbol{\theta}}_{\mathbf{x},m} \tag{3.14}$$

$$\mathbf{M}_{\mathbf{x},s}(\dot{\mathbf{s}}_s + \lambda_{1,s}\mathbf{s}_s) + \mathbf{C}_{\mathbf{x},s}\mathbf{s}_s = \mathbf{Y}_{\mathbf{x},s}\tilde{\boldsymbol{\theta}}_{\mathbf{x},s} \tag{3.15}$$

where $\tilde{\boldsymbol{\theta}}_{\mathbf{x},i} = \hat{\boldsymbol{\theta}}_{\mathbf{x},i} - \boldsymbol{\theta}_{\mathbf{x},i}$ is the estimation error of robot dynamic parameter vector.

To further prove the stability of the system and the tracking convergence of the robots' trajectories, a positive definite Lyapunov function candidate is used

$$V(t) = \frac{1}{2}\left(\mathbf{s}_m^T \mathbf{M}_{\mathbf{x},m}\mathbf{s}_m + \tilde{\boldsymbol{\theta}}_{\mathbf{x},m}^T \mathbf{W}_m^{-1}\tilde{\boldsymbol{\theta}}_{\mathbf{x},m} + \mathbf{s}_s^T \mathbf{M}_{\mathbf{x},s}\mathbf{s}_s + \tilde{\boldsymbol{\theta}}_{\mathbf{x},s}^T \mathbf{W}_s^{-1}\tilde{\boldsymbol{\theta}}_{\mathbf{x},s}\right) \tag{3.16}$$

where $\mathbf{M}_{\mathbf{x},i}$ and $\mathbf{W}_i$ are positive definite matrices.

On the basis of the second property of robot dynamics, and by combining (3.14), (3.15) with (3.16), the time derivative of $V(t)$ is obtained as

$$\dot{V}(t) = \left(-\lambda_{1,m}\mathbf{s}_m^T \mathbf{M}_{\mathbf{x},m}\mathbf{s}_m - \lambda_{1,s}\mathbf{s}_s^T \mathbf{M}_{\mathbf{x},s}\mathbf{s}_s\right) + \left(\mathbf{s}_m^T \mathbf{Y}_{\mathbf{x},m}\tilde{\boldsymbol{\theta}}_{\mathbf{x},m} + \dot{\tilde{\boldsymbol{\theta}}}_{\mathbf{x},m}^T \mathbf{W}_m^{-1}\tilde{\boldsymbol{\theta}}_{\mathbf{x},m} + \mathbf{s}_s^T \mathbf{Y}_{\mathbf{x},s}\tilde{\boldsymbol{\theta}}_{\mathbf{x},s} + \dot{\tilde{\boldsymbol{\theta}}}_{\mathbf{x},s}^T \mathbf{W}_s^{-1}\tilde{\boldsymbol{\theta}}_{\mathbf{x},s}\right)$$
$$\tag{3.17}$$

The adaptation laws for updating the estimated parameters of the system are defined as

$$\dot{\hat{\boldsymbol{\theta}}}_{\mathbf{x},m} = -\mathbf{W}_m^T \mathbf{Y}_{\mathbf{x},m}^T \mathbf{s}_m^T, \quad \dot{\hat{\boldsymbol{\theta}}}_{\mathbf{x},s} = -\mathbf{W}_s^T \mathbf{Y}_{\mathbf{x},s}^T \mathbf{s}_s^T \tag{3.18}$$

Then, $\dot{V}(t)$ can be simplified to

$$\dot{V}(t) = -\lambda_{1,m}\mathbf{s}_m^T \mathbf{M}_{\mathbf{x},m}\mathbf{s}_m - \lambda_{1,s}\mathbf{s}_s^T \mathbf{M}_{\mathbf{x},s}\mathbf{s}_s \leq 0 \tag{3.19}$$

The second order time derivative of $V(t)$ is found as

$$\ddot{V}(t) = -\lambda_{1,m}\mathbf{s}_m^T \dot{\mathbf{M}}_{\mathbf{x},m}\mathbf{s}_m - 2\lambda_{1,m}\mathbf{s}_m^T \mathbf{M}_{\mathbf{x},m}\dot{\mathbf{s}}_m - \lambda_{1,s}\mathbf{s}_s^T \dot{\mathbf{M}}_{\mathbf{x},s}\mathbf{s}_s - 2\lambda_{1,s}\mathbf{s}_s^T \mathbf{M}_{\mathbf{x},s}\dot{\mathbf{s}}_s \tag{3.20}$$

As $\mathbf{s}_i$, $\dot{\mathbf{s}}_i$, $\mathbf{M}_{\mathbf{x},i}$, and $\dot{\mathbf{M}}_{\mathbf{x},i}$ are all bounded, thus $\ddot{V}(t)$ is bounded. Using Barbalat's lemma [67], it is proved that $\mathbf{s}_i \to 0$ and consequently $\tilde{\mathbf{x}}_i \to 0 (\mathbf{x}_i \to \mathbf{x}_{ref_i})$ as $t \to \infty$. As a result, the control strategy makes the system stable and ensures the master and slave robots track

the corresponding impedance models' responses. The parameters used in the control laws and the adaptation laws are shown in Table 3.2 based on the experimental adjustment.

Table 3.2. Parameters of the control laws and adaptation laws

Control Laws	Adaptation Laws
$\lambda_{1,m} = 50, \lambda_{2,m} = 0.14$	$\mathbf{W}_m = 2\mathbf{I}$
$\lambda_{1,s} = 420, \lambda_{2,s} = 0.14$	$\mathbf{W}_s = 32\mathbf{I}$

3.3.2 Experimental protocal

We had 8 participants (4 males and 4 females) deploy anchors into the moving heart tissue under the guidance of US images with and without robotic motion compensation. All the participants who were not surgeons ages 22-32. Specifically, the former condition uses the proposed bilateral adaptive controller and the latter uses a regular direct force reflection (DFR) teleoperation controller [71], which reflects the entire slave-heart tissue contact force to the master robot and requires the human operator to take care of the motion compensation manually. The experimental setup for the two cases is the same. The only difference between the two cases is the control method. Different from the proposed semi-autonomous control method, for the case without motion compensation, the operator must synchronize the slave robot with the heart motion manually and perform task on the heart tissue; that is, the simulated surgical operation is fully manual.

For a successful anchor deployment task, each participant should insert the anchor into the heart tissue firmly to a depth of at least 5 mm (the length of the anchor is 10 mm). Moreover, as safety is a very important consideration when using robots in beating-heart surgery, in order to not harm the heart tissue, the anchor deployment forces should not exceed 2 N [21]. When the deployment force is greater than 2 N, the trial will be treated as a failure.

The experiments include two steps: training and test. To begin, each participant was allowed to deploy anchors three times with motion compensation. Then, they practiced repeating the task without motion compensation until they got used to the device. After that, 10 trials with and without motion compensation were completed by each participant.

For each participant and each trial, several performance metrics are calculated (Table 3.3). Here, it should be noted that the contact duration is defined as the time when the slave-heart tissue interaction force is greater than 0.4 N. Also, three time-related metrics are considered: synchronization time, stapling time, and total completion time. During tool-tissue contact, a mean absolute synchronization error can be calculated to reflect the tissue deformation and motion compensation accuracy. Another important metric is the maximum force applied by the operator. A related key matric is the maximum force applied on tissue, which directly reflects the risk of tissue injury. Based on this force, the excess force rate can be obtained. The success rate is calculated to reflect both successful anchor deployment and non-excessive force application.

3.3.3 Experimental results

The results of performance metrics are listed in Table 3.4 with respect to two cases (with and without motion compensation). To compare the results of the two cases, a paired two-sided t-test [72] was used to obtain the probability of the null hypothesis for the trials under different conditions as each participant performed two trials for cases with motion compensation and without motion compensation. A p-value of less than 0.05 was considered statistically significant.

Table 3.3. Performance metrics

Performance Metric	Related to	Description	Function
Synchronization Time	Trial	The time from the beginning to the contact start	Viability and complexity
Stapling Time	Trial	The time from the contact start to stapling	
Total Completion Time	Trial	The sum of synchronization time and stapling time for a trial	
Mean Absolute Synchronization Error	Trial	$\text{MAPE} = \frac{1}{n}\sum_{i=1}^{n}|e_i|$, where e_i is the position error between surgical tool tip and the heart tissue, n is the samples number of contact duration	Tissue deformation and motion compensation accuracy
Maximum Force by Operator on Master	Trial	The maximum force of operator applied on the master during the contact	Complexity
Maximum Force by Slave on Tissue	Trial	The maximum slave/heart interaction force during the contact	Safety of the system
Excess Force Rate	Operator	The rate of anchor deployment force being greater than 2 N	Safety of the device-tissue interaction instrument
Anchor Deployment Rate	Operator	The rate of deploying anchors with a depth greater than 5 mm	Anchor deployment accuracy
Success Rate	Operator	The rate of successfully deploying anchors while applying forces less than 2 N on tissue	Success rate of the anchor deployment system

Table 3.4. Experimental Results

Robot-assisted motion compensation		Yes	No	P-value
Time	Synchronization Time (s)	8.32±2.68	11.34±2.90	0.0041
	Stapling Time (s)	5.94±2.12	7.58±3.49	0.0824
	Total Completion Time (s)	14.26±2.00	18.92±5.81	0.0019
Position and Force	Mean Absolute Synchronization Error (mm)	1.73±0.32	2.42±1.67	0.0151
	Maximum Force by Operator on Master (N)	1.03±0.35	1.54±0.78	0.0004
	Maximum Force by Slave on Tissue (N)	1.38±0.34	1.60±0.67	0.0313
Rate	Excess Force Rate (%)	7.5±10.35	25±25.63	0.0875
	Anchor Deployment Rate (%)	92.5±10.35	60±18.52	0.0034
	Success Rate (%)	85±9.26	42.5±16.69	0.0011

1) Operating Time

With robotic stabilization, the system provided a mean instrument synchronization time that was roughly 30% less than that measured for the case of no motion compensation. The mean total completion time using the proposed motion compensation system was much less compared to the other case, and the standard deviation was reduced by 66%. A statistically significant difference between the means of total completion times was apparent using a two-sided t-test ($p = 0.0019$).

2) Position and Force Results

Providing no compensation, the mean and standard deviation of mean absolute synchronization error was 2.42 ± 1.67 mm (mean $\pm$ std. error). However, by providing motion compensation, these values were reduced to 1.73 ± 0.32 mm. The two-sided t-test shows that there was a clear difference between the two position errors ($p = 0.0151$).

Averaged across all trials, manual contact with the tissue yielded operator's maximum forces on the master of 1.54 ± 0.78 N. The proposed method of impedance control reduced these to 1.03 ± 0.35 N with clear statistical significance in a two-sided t-test ($p = 0.0004$). Additionally, the two-sided t-test also shows a significant difference with respect to not providing compensation between male and female ($p = 0.0048$), but not with respect to providing compensation ($p = 0.0863$). These values present that compared to male, female participants may have been more careful and gentler in terms of manually compensating for the heart motion with reductions of mean and standard deviation by 35% and 46%, respectively (male $= 1.86 \pm 0.89$ N, female $= 1.21 \pm 0.48$ N).

The maximum force by the slave on tissue in each trial for each participant was recorded (see Figure 3.10a). The excess force rate for each participant was presented in Figure 3.10b. Motion compensated anchor driving provided a mean excess force rate that was roughly 70% less than that observed without motion compensation. When providing motion compensation, there was no significant difference between male and female with respect to the maximum force by slave on tissue ($p = 0.8464$). However, providing no compensation, there was a statistically significant difference with a probability of 0.0042 (male $= 1.89 \pm 0.73$ N, female $= 1.32 \pm 0.48$ N).
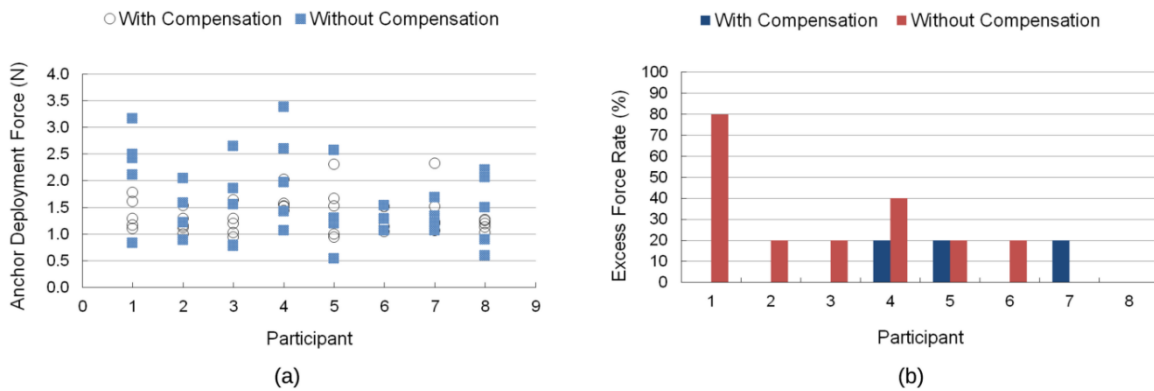
Figure 3.10. The maximum forces on tissue. (a) The maximum forces applied on tissue of each trial for each participant, and (b) the excess force rate for each participant.

For the case of no motion compensation, the oscillatory interaction force of slave-heart tissue will be directly reflected to the master robot, which means once the contact occurs, the operator feels the whole haptic feedback coming from the moving tissue. For this case, there are two tricks can be used to complete the surgery. Operator 1 tried to apply large forces to the master robot during the contact, which introduced large interaction forces, small amplitudes of slave robot's position, and big tissue deformations (Figure 3.11a). Another trick for the operator was manually compensating the motion of the beating simulator, which operator could be realized by attempting to move the master robot back and forth synchronously with the tissue (Figure 3.11b). Comparatively, Figure 3.12 shows the results of interaction forces and positions with motion compensation.
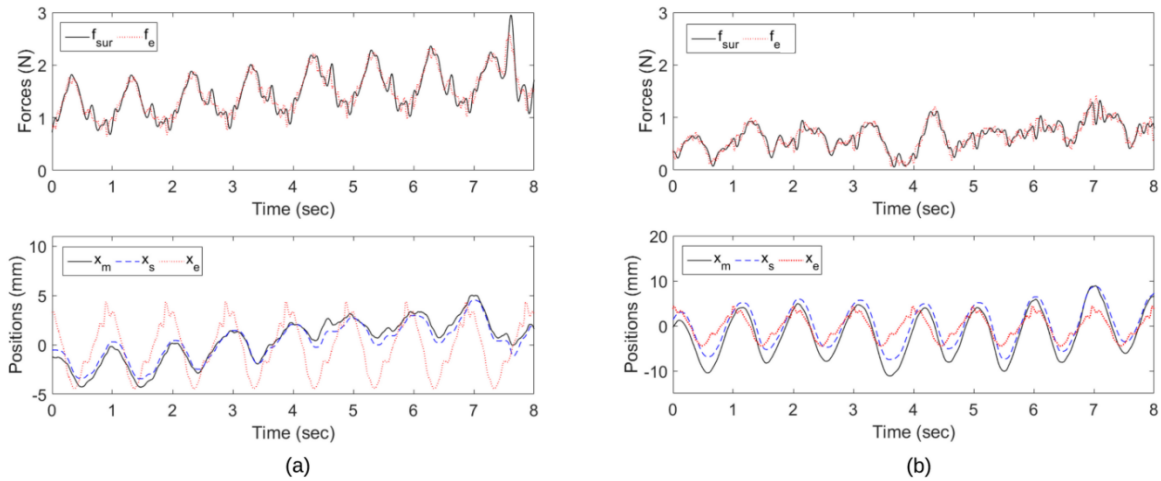
Figure 3.11. Contact forces and positions under no motion compensation. (a) Results when the operator applies a large force, and (b) results when the operator applies a small force. Here, f_{sur} (f_h, upper solid line) is the operator-master interaction force, f_e (upper dotted line) is the slave-heart interaction force, x_m (below solid line) is the position of the master robot, x_s (below dashed line) is the position of the slave robot, x_e (below dotted line) is the position of the heart tissue.
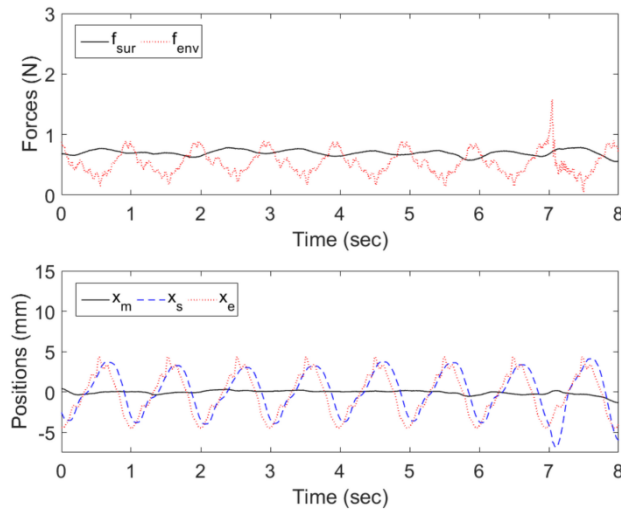
Figure 3.12. Contact forces and positions with the motion compensation.

3) Excess Force Rate and Success Rate

With motion compensation, the anchor deployment rate was 92.5% and the excess force rate was 7.5% of the trials, yielding the final success rate of anchor deployment to be 85%. Without compensation, the anchor deployment rate was 60% and the excess force rate was 25%, and the final success rate of anchor deployment reduced to 42.5%. The anchor deployment rate and success rate are given in Figure 3.13. The t-test p-value, 0.0011, promises a statistically significant difference between the means of success rates.

In addition, a two-sided t-test was used again to compare the success rates for male and female, and the result shows that there was not a significant difference with respect to the success rate with compensation ($p = 0.1817$), but there was with respect to the case of without compensation ($p = 0.0154$).
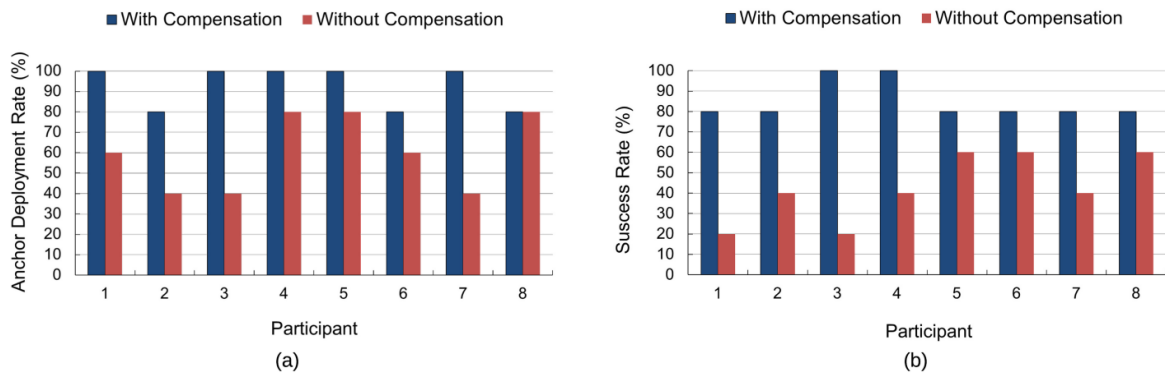
Figure 3.13. The anchor deployment rate and the success rate for each participant. (a) The anchor deployment rate, and (b) the success rates considering the excessive force.

3.3.4 Discussions

Results from the study of operating time demonstrate that using the proposed robotic motion compensation system the participant can be much faster to adapt the heart's rapid motion and do the anchor deployment task so that decrease the possibility of operator's fatigue during the procedure. Reduced possibility of tool-tissue collision and tissue injury was achieved when providing motion compensation by comparing the maximum forces applied on tissue under two cases. Figure 3.10a shows that the forces with motion compensation are generally smaller and more consistent compared to those without compensation, which means that the maximum force by slave on tissue is much easier to be controlled and kept within 2 N when providing motion compensation.

Providing no motion compensation, some operators applied large forces to hold the master robot relatively firmly (Figure 3.11a), but obviously the risk of tissue injury would be very high, and the position and force metrics would be large as well. Some others tried to manually compensate the motion of the beating simulator to decrease the possibility of excessive interaction force (Figure 3.11b), but it would also reduce the success rate of anchor deployment as the contact was not tight enough. Moreover, by manually making

43

compensation, the operator needs more time to complete the task and it is much easier to be exhausted. The two tricks imply a trade-off between the high success rate and the safety of surgery. Without motion compensation, the operator needed to pay more attention to the forces applied to the master robot, causing the procedure to become time-consuming, high-risk, and with low success rate.

When the surgical tool contacted the tissue under motion compensation case, the oscillatory force of the moving tissue was filtered and only a stable baseline contact force was reflected to the operator (Figure 3.12). To control the surgical tool tip to perform an accurate motion tracking and improve the success rate of anchor deployment, the operator could just apply a small stable force to the master robot to keep the surgical tool in a tight contact with the tissue surface. The small position deviation between the surgical tool tip and the tissue during this tight contact was caused by the tissue deformation. Generally, with compensation, the operator was more easily able to perform the task, and the interaction forces were more likely to be kept within 2 N as the force and position of the operator were all non-oscillatory.

In all the force control experiments, the operator expressed greater confidence in instrument manipulation on the beating mitral annulus, making the impedance controller also subjectively better than the regular DFR teleoperation controller. These findings suggest that the stabilization of the force reflected to the operator is an effective aid to the operator for beating heart mitral annuloplasty.

Additionally, there is another interesting result should be noted that the motion compensation strategy has an advantage in terms of reducing the significant difference between the male and female with respect to the applied maximum forces by slave on tissue and the success rate of anchor deployment. One possible reason is that maybe the female operator is more scrupulous and better at controlling forces when there is motion compensation.

Previous research has shown that motion tracking of intracardiac beating-heart tissue by the surgical robot is feasible [13], [73], [74]. However, much of these work used a hand-held device for surgery instead of utilizing a teleoperation system, which poses additional challenges due to the dynamical interferences of the master and slave robot (i.e., any lack of "transparency" of the master-slave teleoperation system makes motion compensation and robot operation harder than the case where the master and the slave are unified into one hand-held device). Moreover, the above US image-based methods would result in an accurate motion tracking of the heart tissue by the surgical robot as long as the surgical tool tip and the heart tissue did not make contact. During interactions with the surgical tool, the tissue deformation makes it difficult to extract the tool and tissue position based on US images.

For this reason, other researchers have proposed methods using force control to implement motion compensation [55], [75], [76]. Hara et al. [77] and Kempf et al. [78] showed that repetitive control methods based on force are well suited for quasi-periodic servoing tasks. Ginhoux et al. [29] and Bebek and Cavusoglu [79] successively proposed using a force-based model predictive controller to improve motion tracking accuracy. While the tracking performances are good, past work did not incorporate haptic feedback to the human operator. Kitagawa et al. show that with the addition of force feedback, both accuracy and repeatability of the forces improve [76]. Moreover, force feedback would help to decrease tissue damages and prevent undesirable trauma [26].

In this proposed strategy, the developed system can not only feedback the non-oscillatory slave-heart tissue interaction force to the human operator but also make compensation for the rapid heart's motion. This system does not need the sensor for the tool-tissue interaction force to be placed inside the body. It also does not require any heart motion prediction, observation and/or learning, making it easy to implement. Nevertheless, there are still several aspects to be improved. Future work may involve extending the motion compensation technology to multi-DOF cardiac surgeries and exploring the system's potential uses in other forms of beating heart procedure that may require complex tissue

trajectory tracking, such as pericardiectomy, myocardial injury suture, catheter ablation, and so on. In addition, the fixed parameters of the impedance models during the experiments can be designed to be variable to increase the robustness of the system.

3.4 3-DOF Physiological Organ Motion Compensation

The bilateral impedance control system is also suitable for 3-DOF robotic tracking of the complex physiological organ motion introduced by respiration and heartbeat in cardiac surgery. The semi-autonomous surgical system includes a slave surgical robot which can compensate for the physiological organ motion automatically and a master robot (user interface) which is manipulated by the human operator to provide task commands to the surgical robot. With no need for organ motion prediction, observation or learning, the proposed impedance control method for the surgical robot only needs the frequency range of the physiological motion to synchronize the surgical instrument with the organ motion automatically. A usability study emulating the motion requirements of tissue ablation is carried out. Experimental results are presented to show the effectiveness of the proposed method by comparing the results to the manual compensation method.

3.4.1 Experimental setup

Experiments are implemented with motion compensation (the proposed strategy) and without motion compensation (the DFR haptic teleoperation control [20]). The task requires a prolonged contact with the heart surface to evaluate the performance of position tracking and force feedback. The experimental results and a usability study emulating the motion requirements of tissue ablation are presented in Section 3.4.2 and 3.4.3, respectively.

The experiment employs a 3-DOF Phantom Premium 1.5A robot (Geomagic Inc., Wilmington, MA, USA) equipped with a 6-DOF 50M31 force/torque sensor (JR3 Inc., Woodland, CA, USA) as the master robot and a Motoman SIA-5F (Yaskawa America, Inc., Miamisburg, OH, USA) 7-DOF serial manipulator equipped with a 6-DOF ATI Gamma Net

force/torque sensor (ATI Industrial Automation, Inc., Apex, NC, USA) as the slave robot (Figure 3.14a).

The developed semi-autonomous surgical robot control system for beating-heart surgery utilizes an impedance-controlled teleoperation framework (Figure 3.14b) which includes a master robot in the local site and a slave robot in the remote site to achieve the desired objectives. Two reference impedance models for the master and slave robots, respectively, are designed, and the results for a 3D task to be done on a simulated heart undergoing a 3D motion are presented. The 3D motion trajectory of the simulated heart was extracted from a real heart's motion (courtesy of the authors of [81] who provided us with the data). A 7-DOF Motoman SIA5F robot with significant dynamics, which is more similar to a real surgical robot, is used as the slave robot.
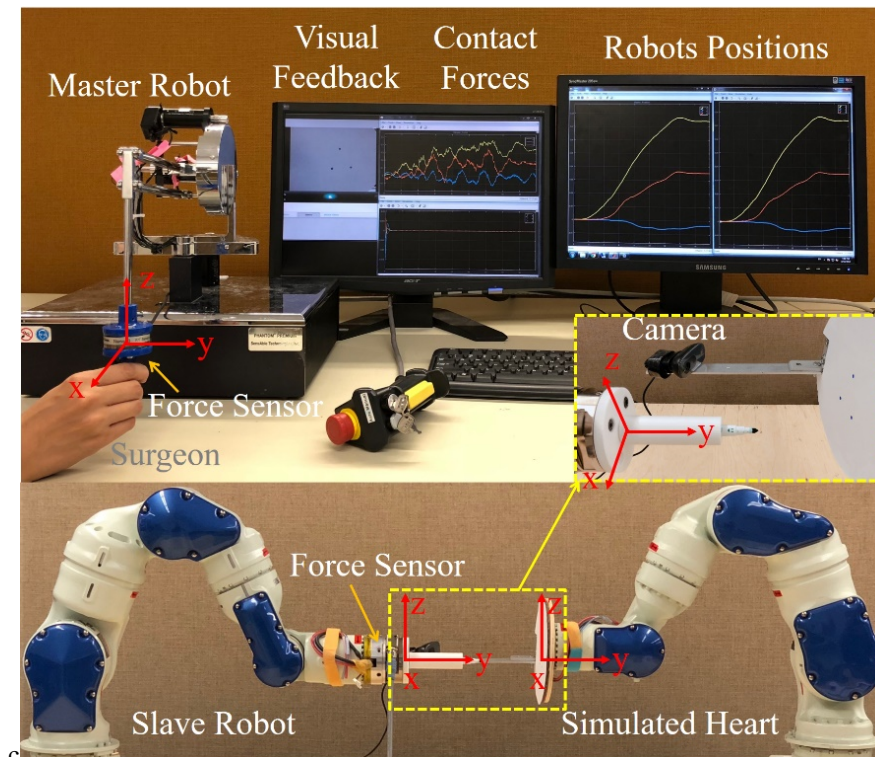
(a)
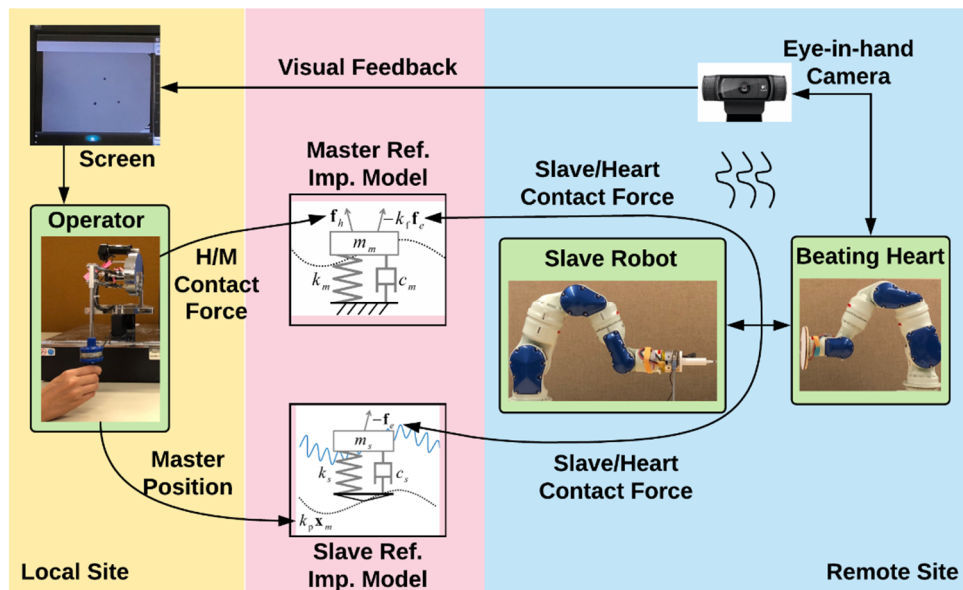
(b)

Figure 3.14. (a) Experimental setup for 3-DOF physiological organ motion compensation. (b) A schematic of the proposed semi-autonomous surgical robot control system for beating-heart surgery. The human operator manipulates the master robot in the local site and provides position commands for the slave robot in the remote site. Two 7-DOF Motoman SIA5F robots are used as the slave robot and the simulated beating heart, respectively. H/M contact force is the abbreviation of human-master contact force. An eye-in-hand configuration for the camera and the beating heart simulator is used to accomplish visual stabilization. In realistic beating-heart surgery, visual stabilization when displaying images of the beating heart to the human operator is an important issue. It should not only compensate for the heart's motion but should also compensate for tissue deformations. As this research focuses on motion compensation and force feedback, visual stabilization is accomplished by using an eye-in-hand configuration for the camera and the heart simulator instead of using the existing 3D tracking algorithms. The camera can obtain a stabilized view of the beating heart by moving with the heart.

The encoder positions of the master and slave robots were transformed into end-effector positions and recorded. The beating-heart is simulated by another Motoman manipulator attached with a flat interface (a soft tissue phantom) and a camera to provide visual stabilization. The simulated heart tissue is made having a stiffness of 200 N/m to imitate the real heart tissue [80]. The whole system of the heart simulator was controlled to have a 3-DOF movement by giving the recorded heart position signals as shown in Figure 3.15 (described below in detail). The QUARC software (Quanser Consulting Inc., Markham, ON, Canada) is used as a real-time control environment to implement the proposed method with a sampling rate of 1 kHz. The 3-DOF heart position signals were interpolated from its inherent measurement rate which is 25 Hz to the sampling rate of 1 kHz. The MATLAB/SIMULINK program includes the master robot controller, the reference impedance models for the master and slave robots, and the UDP blocks to communicate between the Simulink based models and the C++ based velocity controller for the slave robot.

1) Heart Motion

The motion of beating-heart surface is primarily induced by respiratory and heartbeat motions with different frequency ranges. In the section, the 3-DOF heart positions were measured offline from a stereo video of *in vivo* porcine heart by vision tracking [81]. The stereo video recorded image sequence of a totally endoscopic coronary artery bypass graft from a da Vinci (Intuitive Surgical, CA) surgical platform [32]. The quasi-periodic 3-DOF heart motion signals with the respective PSD are shown in Figure 3.15 Observable dominant peaks are at $\omega_r = 1.07$, $\omega_h = 5.22$, and $2\omega_h = 10.43$ rad/sec, which correspond to respiratory motion, heartbeat motion, and the first harmonic of the heartbeat motion, respectively. These dominant frequencies will be used to adjust the parameters of the reference impedance models.
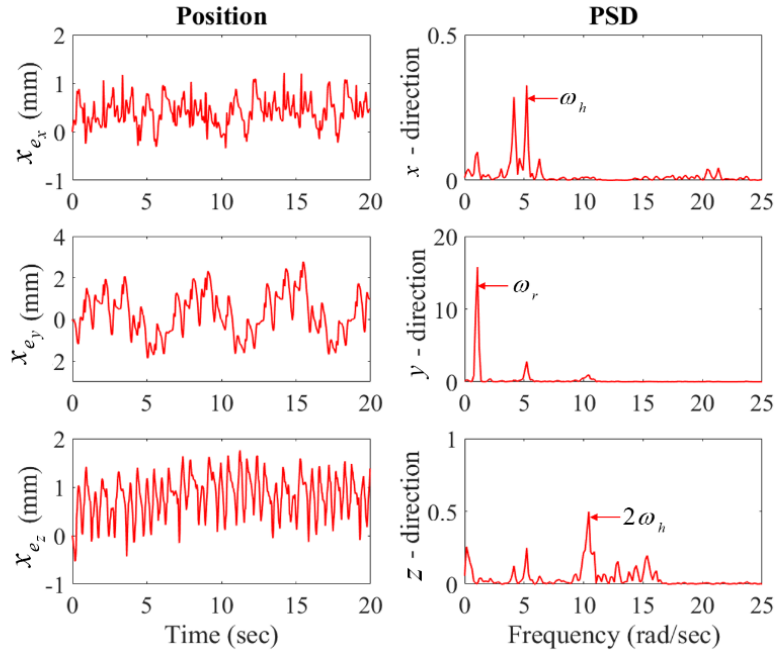
Figure 3.15. 3-DOF physiological heart motion. It is measured from an in vivo porcine heart stereo video which recorded image sequence of a totally endoscopic coronary artery bypass graft from a da Vinci (Intuitive Surgical, CA) surgical platform and its power spectral density (PSD) analysis.

2) Parameters Tuning

According to Section 3.2.2, the matrices that need to be tuned are $\mathbf{K}_m$, $\mathbf{Z}_m$, $\mathbf{\Omega}_{n_m}$, and $\mathbf{K}_s$, $\mathbf{Z}_s$, $\mathbf{\Omega}_{n_s}$. For the sake of brevity, the parameters tuning guidance shown below is in one direction. The subscript $i = x, y, z$ for the x-, y-, z-axis, respectively.

The reference impedance model for the master robot (3.1) aims to avoid possible fatigue and exhaustion caused by the oscillatory slave-heart interaction force feedback to the human operator. It means that the high frequency of the slave-heart interaction force should

50

be filtered to achieve $(f_{h_i} - k_{f_i} f_{e_i}) \to 0$. To satisfy this condition, the stiffness of model (3.1) (k_{m_i}) should be chosen small, and the natural frequency of (3.2) ($\omega_{n_{m_i}}$) should be several times smaller than the lower rate of the physiological motion; that is, $\omega_{n_{m_i}} \ll \omega_r$ (Figure 3.16a). Also, to get a fast behaviour in response to the harmonic physiological force of the human operator, ζ_{m_i} is chosen to be 0.7.

The goal of the slave impedance model (3.3) is to make the slave robot comply with the physiological force and motion during tool-tissue interaction. Based on (3.3), the flexibility of the slave robot, which can neither be too small nor too large, is the deviation from the scaled master trajectory ($\tilde{x}_{ref_{s_i}} = x_{ref_{s_i}} - k_{p_i} x_{m_i}$). If the slave robot is too flexible, it cannot apply enough forces on the heart surface to perform tasks. If the slave robot is too rigid, the motion compensation cannot be achieved. Therefore, the stiffness value of the slave impedance model (k_{s_i}) should be adjusted to be moderate. The exact stiffness can be tuned by trial and error according to specific task and the used slave robot. Also, the natural frequency of (3.5) ($\omega_{n_{s_i}}$) should be several times greater than the higher rate of the physiological motion ($\omega_{n_{s_i}} \gg \omega_h$) (Figure 3.16b). Similarly, ζ_{s_i} is chosen to be 0.7.

It is worth noting that the flexibility of the slave robot may reduce the traditional definition of transparency of the system, but it is vital for heart motion compensation. For specific cardiac procedures such as tissue ablation, reducing the risk of tissue damage while maintaining a steady contact with the heart is important, and there is little need for the slave robot to track the exact master robot's trajectory. It is more important to synchronize the surgical instrument with the moving tissue and keep the contact force at a safe level than to synchronize the surgical instrument with the operator's hand. When there is no contact between the beating heart and the slave robot, the slave robot will track the exact scaled position of the master robot and the transparency of the system is good. Therefore, the trade-

off between the transparency and the flexibility of the system makes the proposed strategy and parameter tuning guidelines more suitable for applications that need low and constant contact forces during beating-heart interventions. The parameters of the impedance models are listed in Table 3.5.
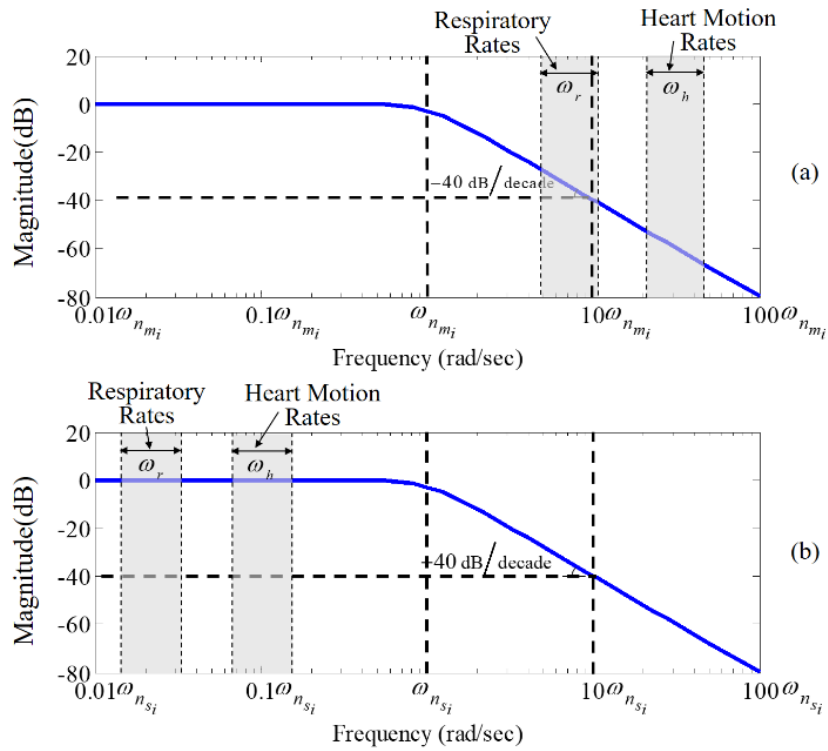
Figure 3.16. Bode diagrams in one direction of (a) the master reference impedance model and (b) the slave reference impedance model.

Table 3.5. Parameters of the reference impedance models

Impedance Model (1)	Impedance Model (3)
$\mathbf{K}_m = \text{diag}(7.2, 2.7, 5)$ N/m	$\mathbf{K}_s = \text{diag}(125, 160, 250)$ N/m
$\mathbf{Z}_m = 0.7\,\mathbf{I}_{3\times3}$	$\mathbf{Z}_s = 0.7\,\mathbf{I}_{3\times3}$
$\mathbf{\Omega}_{n_m} = \text{diag}(0.6, 0.3, 0.5)$ rad/sec	$\mathbf{\Omega}_{n_s} = \text{diag}(25, 40, 50)$ rad/sec
$\mathbf{K}_f = \mathbf{I}_{3\times3}$	$\mathbf{K}_p = \mathbf{I}_{3\times3}$

3) Controllers

To track the ideal responses of the two reference impedance models for the master and slave robots, a proportional- integral-derivative (PID) controller is employed for the master robot and tuned based on the dynamics of the master robot. The position controller makes sure the master robot tracks the desired positions calculated from the reference impedance model for the master robot, which is given in (3.21). In Figure 3.1, the control variables $\mathbf{\mu}_m(t)$ is determined by the weighted sum

$$\mathbf{\tau}_m(t) = \mathbf{K}_{p_m} \mathbf{e}_m(t) + \mathbf{K}_{i_m} \int_0^t \mathbf{e}_m(\tau)d\tau + \mathbf{K}_{d_m} \frac{d\mathbf{e}_m(t)}{dt} \tag{3.21}$$

where $\mathbf{e}_m(t) = \mathbf{x}_{ref_m}(t) - \mathbf{x}_m(t)$. Also, $\mathbf{K}_{p_m}$, $\mathbf{K}_{i_m}$, and $\mathbf{K}_{d_m}$, all non-negative values, denote the coefficients for the proportional, integral, and derivative terms, respectively. In the experiments, the proportional, integral, and derivative terms are set as $\mathbf{K}_{p_m} = 1000\,\mathbf{I}_{3\times3}$, $\mathbf{K}_{i_m} = 200\,\mathbf{I}_{3\times3}$, and $\mathbf{K}_{d_m} = \mathbf{I}_{3\times3}$. Control of the slave robot is performed through a velocity controller as opposed to a position controller.

It is worth noting that the procedure explained above entails using the desired impedance surfaces (3.1) and (3.3) in an admittance control framework where based on measurements of contact forces $\mathbf{f}_h$ and $\mathbf{f}_e$, a desired position for the master robot and a desired velocity for the slave robot are calculated and fed to respective position and velocity controllers [82]. Alternatively, we could have implemented an impedance controller on the slave robot for generating torque commands to ensure that (3.3) holds. However, in this case, the inverse dynamics of the slave robot would be required but they are unavailable due to the complexity in estimating the dynamics of the 7-DOF Motoman robot.

3.4.2 Experimental results

The performance of the developed system is evaluated by calculating the mean absolute synchronization error (MASE) in 3D, $\text{MASE} = \frac{1}{n}\sum_{i=1}^{n}|e_i|$, where e_i is the position error in 3D between the surgical tool tip and its desired position when contact occurs, n is the samples number of contact duration. The contact between the slave robot and the heart tissue is detected based on the slave-heart interaction force. When no motion compensation provided, the desired trajectory is defined to be the heart position as the human operator is conducted to manually synchronize the slave robot with the heart motion and try to remain in contact on the surface of the heart. When motion compensation provided, the desired position for the slave robot is defined as the combined trajectory of the master robot and the heart. The experiments are carried out for 100 s. The first and last $\sim$ 10 s of the 100 s are used for the slave robot to approach and leave the heart. The position results are shown in Table 3.6. In addition, the average force applied by the human operator on the master robot (AFM) in 3D and the average force applied by the slave robot on the simulated heart (AFS) in 3D are calculated and presented in Table 3.6 as well.

Table 3.6. Experimental Results

Motion Compensation	Yes	No
MASE (mm)	**0.959**	**2.373**
AFM (N)	1.021 $\pm$ **0.079**	0.290 $\pm$ **0.189**
AFS (N)	**0.791** $\pm$ 0.181	**0.290** $\pm$ 0.189

As can be seen in Table 3.6, with motion compensation, the MASE is 0.959 mm which is much lower than the values when motion compensation is not provided (2.373 mm). It is worth noting that the MASE is higher than the value presented in [23]. However, this

comparison is not appropriate as the experimental systems are totally different. In addition, in [23], the slave robot did not contact the simulated heart tissue, which further indicates that the two experiments are not suitable for comparison. Moreover, taking into consideration the significant dynamic of the surgical robot, this position tracking result is satisfied for now. Also, with motion compensation, the standard deviation of AFM (0.079 N) is much lower than the standard deviation of AFS (0.181 N), which means the force perceived by the human operator is steadier and the oscillatory portion of slave-heart contact forces is filtered out perfectly. Without motion compensation, as the slave-heart contact force is directly reflected to the human operator, the means and standard deviations of AFM and AFS are the same. Moreover, it is worth noting that the mean value of AFM with motion compensation (1.021 N) is higher than that without motion compensation (0.29 N). It is because that without motion compensation the human operator must manually synchronize the slave robot with the heart motion which results in contact discontinuity during operation as the slave robot has a high risk of bouncing off the heart surface.

Figure 3.17 shows the actual slave robot positions and its desired trajectories in 3D for the cases with and without motion compensation. The right vertical axis of Figure 3.17 is the position tracking error for each direction and each case. As can be seen more clearly in Figure 3.17, the position tracking errors shown in Figure 3.17b are much smaller than the errors shown in Figure 3.17a, which demonstrates that the motion compensation performance improves significantly by using the proposed semi-autonomous surgical robot control system.

Contact force results for each case in 3D are shown in Figure 3.18. All three axes of the robots demonstrated similar performance. In Figure 3.18a, as the slave-heart contact force is directly reflected to the human operator, the force perceived by the human operator and the slave-heart contact force are the same. Due to the manual motion compensation and contact discontinuity, both are oscillatory and very low. In Figure 3.18b, the slave-heart contact force in each direction (blue dashed line) is always positive and higher than that in

Figure 3.18a, which means the tool-heart contact is constant although the amplitude of the oscillatory portion of the slave-heart contact force still high. Also, in Figure 3.18b, the human-master contact forces (red solid line) are much steadier than the slave-heart contact forces as their oscillatory portions are filtered out by using the proposed method.

To further explore the difference between the two cases, the position and force results of the master robot in the y-axis for each case are presented in Figure 3.19. With motion compensation, both position and force of the human operator are relatively steady which provides the human operator a feeling of operating on an 'arrested' heart.
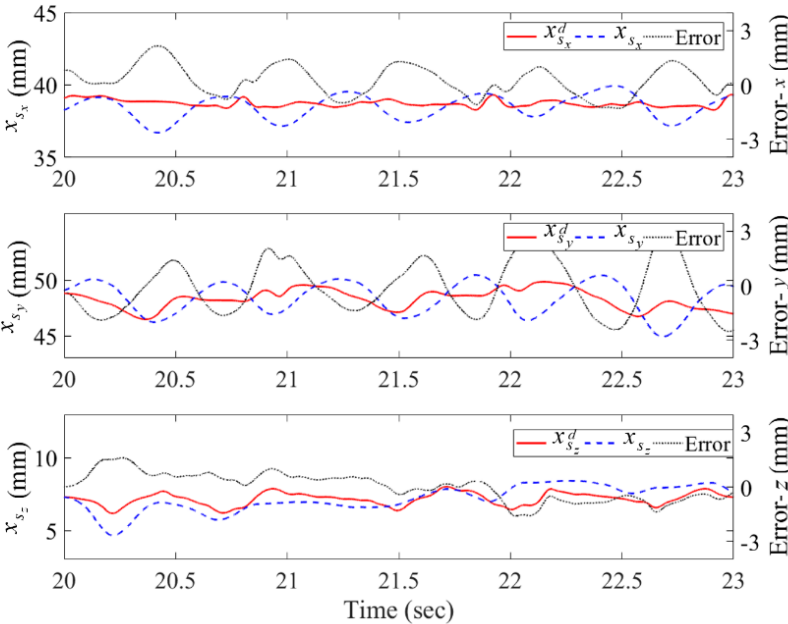
(a)
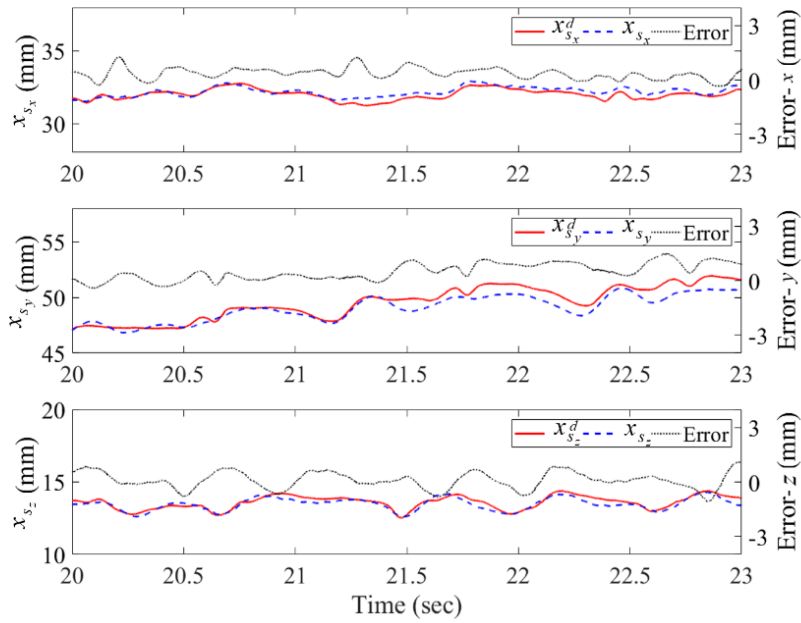
(b)

Figure 3.17. Results of the slave robot 3-DOF position. The 3-DOF positions involve the slave robot's real (blue dashed line, x_{s_i}) and desired (red solid line, $x_{s_i}^d$) trajectories and tracking error (black dotted line) for the cases (a) without motion compensation and (b) with motion compensation. Subscripts $i = x, y, z$ are the three axes, respectively.

(a)

(b)

58
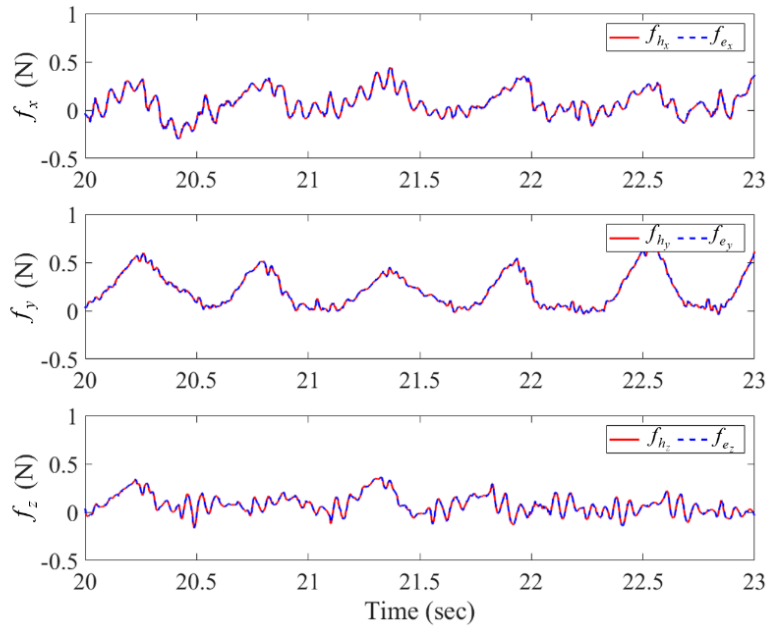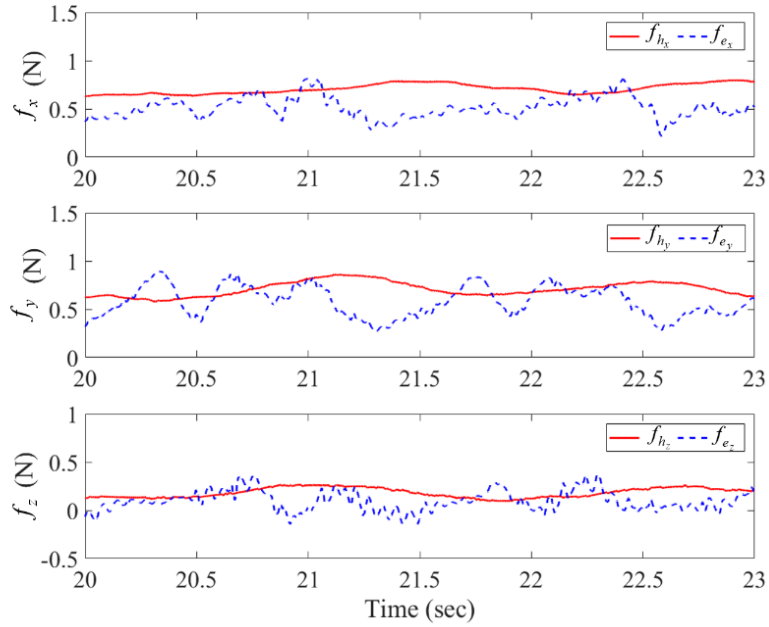
Figure 3.18. Results of the interaction forces. The results include the interaction forces of the master (red solid line, f_{h_i}) and slave (blue dashed line, f_{e_i}) robots in 3D for the cases (a) without motion compensation and (b) with motion compensation. Subscripts $i = x, y, z$ are the three axes, respectively.
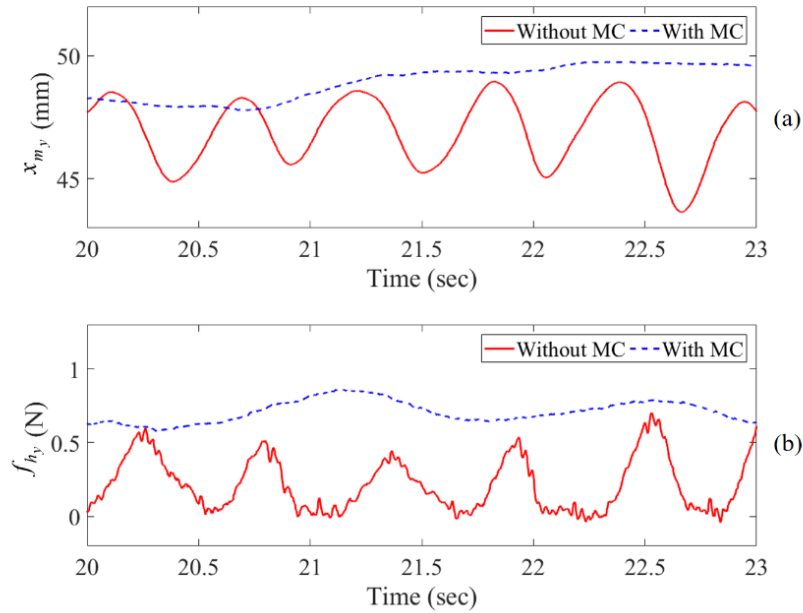
Figure 3.19. (a) Positions and (b) forces of the master robot in the *y*-axis for the two cases. Legend MC is the abbreviation of motion compensation.

3.4.3 Usability Study

The usability study emulates the motion requirements of tissue ablation, which needs a prolonged contact with the heart surface. The task simulating this is to draw a triangle with sides that are 4 cm long on the surface of the simulated heart. The task starts at the left bottom of the triangle and proceeds in the clockwise direction. This study is completed with and without motion compensation by one user (the thesis author). For each case, experiments are

59

repeated five times. During the experiments, the user is conducted to draw continuous and straight lines and at the same time to finish the task as soon as possible.

Figure 3.20 shows representative drawn triangle results for the two cases. Based on the results shown in Table 3.6 and Figure 3.18, it can be concluded that with motion compensation the master position will be steadier than the slave position, while without motion compensation, the master position will be the same as the slave position. Thus, the motion commands of the human operator for the two cases are not shown in Figure 3.20. With motion compensation (Figure 3.20a), the drawn lines are more continuous and straighter than the without motion compensation (Figure 3.20b). The latter has break points and is fragmented. Under motion compensation, task completion times (56.38 ± 4.33s) are shorter than without motion compensation (77.09 ± 4.72s) by as much as 25%. The t-test p-value, 0.026, ensures a statistically significant difference between the task completion times under two cases (significance corresponds to $p < 0.05$). The results of usability study present the dominant advantage of the proposed control system over the DFR system. Although the triangle is drawn on a plane, considering the 3-DOF motion of the heart surface (the plane), the task is 3 DOF.

(a)   (b)
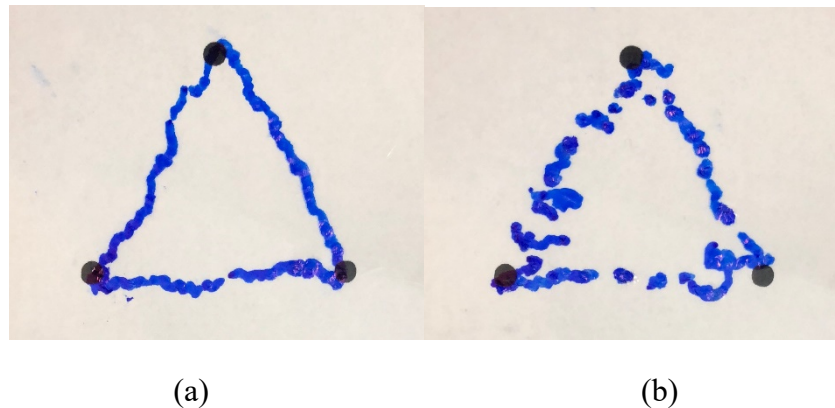
Figure 3.20. Triangle results. (a) With motion compensation. (b) Without motion compensation.

3.4.4 Discussions

The experimental position results show that the position tracking performance of the slave robot improves significantly when using the proposed semi-autonomous surgical robot control system. When there is no motion compensation (as can be seen in Figure 3.17a and Figure 3.19a), manually compensating for the complex 3-DOF heart motion is not accurate or comfortable for the human operator. In this case, the human operator needs not only compensate for the heart motion but also perform task on the heart tissue, which requires high focus and is very easy to cause fatigue. On the contrary, with motion compensation, the MASE is roughly 60% less than that the case without motion compensation. The slave robot complies with the heart motion automatically and the human operator (shown in Figure 3.19a) only provides position commands to the slave robot and does not need to move back and forth to mimic the heart motion, which is more convenient for the operator to implement surgical tasks.

The force results also demonstrate that the force feedback to the human operator is non-oscillatory by using the proposed method. When using DFR method, in order to reduce the tool-tissue collision and tissue injury, the human operator in the experiments pays more attention to motion compensation but constant contact which is more challenging. This leads to contact discontinuity as the slave robot can easily be bounced off the heart surface. When using the proposed method, the slave robot can be easily controlled to stay in constant contact with the heart surface because the human operator only needs to focus on the contact task regardless of the fast motion of the heart. The designed reference impedance model for the master robot guarantees the force feedback to the human operator is relatively steady.

The proposed reference impedance models for the master and slave robots build on the work presented in Section 3.3 and extend the 1-DOF task on a simulated heart undergoing a 1-DOF motion to a 3-DOF task on a simulated heart undergoing a real 3-DOF heart motion. Relative to the past work, the main contributions of this parper are therefore as follows: (a) Considering a more complicated 3-DOF physiological heart motion (includes breathing

motion and heartbeat motion) instead of the simulated 1-DOF heart motion generated by a custom-built mechanical cam is used for motion compensation, (b) using a 7-DOF Motoman SIA5F robot with significant dynamics, which is more similar to a real surgical robot, is used as the slave robot, whereas in Section 3.3, a haptic device with negligible dynamics was used as the slave robot, (c) investigating whether the parameters of the slave impedance model can be tuned to the appropriate values given the significant dynamics of the Motoman SIA5F robot (in our previous work the parameters of the slave impedance model could be freely adjusted anywhere from near zero to infinity), (d) using a different controller for the slave robot, 7-DOF Motoman SIA5F robot, which requires movements to be performed through a velocity controller as opposed to a position controller for haptic devices, and (e) considering a 3-DOF task is performed in the usability study to emulate the motion requirements of tissue ablation, while in the previous work only a 1-DOF anchor deployment was performed. The contributions of this experiments lay the foundation for the future implementation of even more complex experiments using more actual surgical robotic systems. Furthermore, the proposed system is suitable for cardiac procedures in the presence arrythmia, which is quite challenging for motion prediction methods.

3.5 Concluding Remarks

This chapter developed a bilateral impedance-controlled telerobotic system for beating-heart surgery. The proposed method only uses the measured interaction forces without any need for vision-based heart motion estimation, active observer or motion prediction to compensate for the beating-heart motion automatically and provide the human operator with a feeling of operating on an arrested heart simultaneously.

This chapter has demonstrated the viability and superiority of the developed system performing 1-DOF and 3-DOF simulated surgical tasks. The 1-DOF task is performing beating-heart anchor deployment for mitral valve annuloplasty under the guidance of US images. This system has been shown reduce operation time, increase safety to the heart tissue,

achieve lower and more stable force application by the operator, and obtain high success rate of deploying anchors. The telerobotic system with an anchor driver attached to the slave robot's end-effector reduced the excess force application rate by 70% and increased the success rate of anchor deployment by 100% compared to manual attempts. The motion compensation instrument also decreased the task completion time (from the operation start to stapling) by 22% and reduced the mean absolute synchronization error by 30%. Low and stable operator forces were achieved when compared to the case of without compensation.

The proposed system is used for 3-DOF physiological motion compensation as well. The experimental evaluations demonstrated that the proposed method could be used in the robot with significant dynamics and achieve accurate performance for surgical applications that need low and constant contact forces during beating-heart interventions. Future work may involve exploring the system's potential uses in forms of beating-heart procedures. Due to the flexibility of the designed reference impedance model for the slave robot, this method is more suitable for surgeries that require less tool-tissue interaction forces such as mitral valve annuloplasty, blunt resection, ablation, etc.

Chapter 4

Switched Impedance Control

4.1 Introduction

In this chapter[3], a switched impedance-controlled teleoperation system is proposed to achieve two objectives in noncontact and contact situations as far as interaction between the slave robot and the beating heart is concerned. The main advantage of this method over the one presented in Chapter 3 is that during slave-heart interaction, the human operator can feel the same stiffness of the heart tissue through the master robot, and the slave robot can synchronize its motions with the heart's motion and follow the commands of the human operator as closely as possible to execute the desired surgical task. Therefore, this method is more suitable for surgeries which require larger execute forces on the heart tissue such as tissue cutting, suturing, penetration, etc.

Teleoperation beating-heart surgery involves two phases: No contact with the heart and contact with the heart as far as the slave robot is concerned. Contact detection can be achieved based on the slave-tissue interaction force, which can be measured by a force sensor mounted on the end-effector of the slave robot. Theoretically, if the slave-tissue interaction force equals zero,

---

[3]Portions of this chapter were published in "L. Cheng and M. Tavakoli, "Switched-Impedance Control of Surgical Robots in Teleoperated Beating-Heart Surgery," *Journal of Medical Robotics Research*, vol. 3, no. 3, pp. 1841003(1-15), 2018." [16]

the slave robot has not contacted the heart; otherwise, it has. When there is no contact between the beating heart and the slave robot, which happens when the human operator is either not doing anything or trying to manipulate the master robot such that the slave robot gets closer to or farther from the heart surface, the slave robot should simply follow the (possibly scaled) trajectory of the master robot. When the slave robot is in contact with the beating heart, there are two requirements. First, to avoid the induced motion phenomenon [60], the human operator should only feel what one would feel when directly working on an arrested heart. This means the quasi-periodic heartbeat-induced forces caused by the residual mismatch between the robot and the heart motions and by the slave-mounted force sensor's internal inertia should not be transmitted to the operator. Second, the slave robot should synchronize its motions with the heart's motion *and* follow the commands of the human operator as closely as possible to execute the desired surgical task.

The rest of this chapter is organized as follows. Section 4.2 introduces the switched impedance-controlled telerobotic system including the developed system architecture, reference impedance models, adjustment guidelines for the model parameters, and controllers used in the system. Section 4.3 describes the validation protocol. Section 4.4 and 4.5 present the simulation and experimental results, respectively. Finally, the concluding remarks are given in Section 4.6.

4.2 Switched Impedance Models

To achieve the desired behaviors described above, the detailed model developments, parameter tuning, and controller design are presented below. Transmitting the force and position information of the master and slave robots through the communication channel, two switched-reference impedance models for the master and slave robots are proposed. The reference impedance models generate reference positions for the two robots, which are then sent to the master and slave position controllers (Figure 4.1).
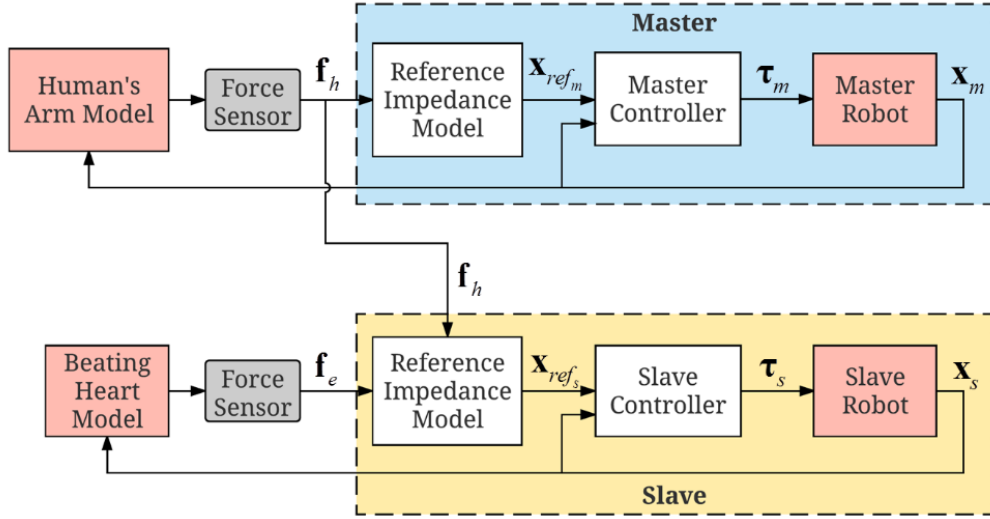
Figure 4.1. The switched impedance control system. Here, $\mathbf{f}_h$ is the interaction force between the master and the operator, and $\mathbf{f}_e$ is the interaction force between the slave and the beating heart. They are measured directly through two force sensors. Also, $\mathbf{x}_{ref_m}$ and $\mathbf{x}_{ref_s}$ are the desired positions for the master and slave robots, which are generated by the reference impedance models for the respective robot. Note that, $\mathbf{x}_m$ and $\mathbf{x}_s$ are the actual positions of the master and slave robots, respectively. The controllers receive the position errors between the desired positions generated by the reference models and the actual positions read from the robots, and then output torques $\boldsymbol{\tau}_m$ and $\boldsymbol{\tau}_s$ to the robots. The position of the beating heart is indicated by $\mathbf{x}_e$. The initial point of beating heart position is set when the slave robot is far away from the heart, and meanwhile the heart is closest to the slave robot.

4.2.1 Reference impedance models

The reference impedance model of the master robot expresses a dynamical relationship between the operator-master interaction force and the difference between the master impedance model's response (which is the desired position for the master robot) and a varying initial trajectory $\mathbf{x}_{ini_m}$ as

66

$$m_m \ddot{\mathbf{x}}_{ref_m} + c_m \dot{\mathbf{x}}_{ref_m} + k_m \tilde{\mathbf{x}}_{ref_m} = \mathbf{f}_h$$

$$\tilde{\mathbf{x}}_{ref_m} = \mathbf{x}_{ref_m} - \mathbf{x}_{ini_m}, \text{where} \begin{cases} \mathbf{x}_{ini_m} = 0 \ , \ \text{when } \mathbf{f}_e = 0 \\ \mathbf{x}_{ini_m} = \mathbf{x}_{m_0}, \text{when } \mathbf{f}_e \neq 0 \end{cases} \tag{4.1}$$

In the above, m_m, c_m, k_m are the mass, damping and virtual stiffness parameters of the master impedance model. Here, $\mathbf{x}_{ini_m}$ is the initial position for the master robot. When there is no contact between the slave robot and the tissue ($\mathbf{f}_e = 0$), $\mathbf{x}_{ini_m}$ equals 0; when contact occurs ($\mathbf{f}_e \neq 0$), $\mathbf{x}_{ini_m}$ is chosen to be $\mathbf{x}_{m_0}$, which is the master robot position when the slave robot first makes contact with the beating heart. Note that, $\mathbf{x}_{ini_m}$ is set according to the above to ensure $\mathbf{x}_m$ continuously increase during the transition between noncontact and contact cases, as the impedance parameters of model (4.1) will be changed according to the absence or presence of contact.

The reference impedance model for the slave robot is defined as a dynamical relationship between a force summation (involving the scaled human-master interaction force and the slave-heart interaction force) and the slave robot's position as

$$m_s \ddot{\mathbf{x}}_{ref_s} + c_s \dot{\mathbf{x}}_{ref_s} + k_s \tilde{\mathbf{x}}_{ref_s} = k_f \mathbf{f}_h - \mathbf{f}_e$$

$$\tilde{\mathbf{x}}_{ref_s} = \mathbf{x}_{ref_s} - \mathbf{x}_{ini_s}, \text{where} \begin{cases} \mathbf{x}_{ini_s} = 0 \ , \ \text{when } \mathbf{f}_e = 0 \\ \mathbf{x}_{ini_s} = \mathbf{x}_{s_0}, \text{when } \mathbf{f}_e \neq 0 \end{cases} \tag{4.2}$$

Here, k_f is a force scaling factor. Also, m_s, c_s, k_s are the mass, damping and virtual stiffness parameters of the slave impedance model. Similar to $\mathbf{x}_{ini_m}$, the initial position $\mathbf{x}_{ini_s}$ should be reset as the parameters of the slave impedance model will be changed depending on the absence or presence of contact. Note that, $\mathbf{x}_{s_0}$ is the slave robot's position when the slave robot first contacts the beating heart.

The reference impedance models for the master and slave robots are stable second-order differential equations when the impedance parameters are set to be positive. The stability

characteristic of reference impedance models enhances the patient safety during the robot-assisted surgery. To achieve motion compensation and non-oscillatory force feedback during slave-heart interaction, the parameters for the two impedance models should be adjusted appropriately. Instead of tuning all these parameters directly, damping ratios and natural frequencies of the models are used to adjust the impedance models.

The damping ratios of the two models can be expressed as $\zeta_m = c_m / 2\sqrt{m_m k_m}$ and $\zeta_s = c_s / 2\sqrt{m_s k_s}$, which describe how oscillations decay after an input. In order to ensure the impedance model (4.1) and (4.2) have fast behaviors in response to the force inputs and small overshoots in response to the step force inputs, the damping ratios are both set as 0.7.

The natural frequencies (the cut-off frequency for damping ratio equals 0.7) of the two impedance models are given by $\omega_{n_m} = \sqrt{k_m / m_m}$ and $\omega_{n_s} = \sqrt{k_s / m_s}$. For the purpose of disturbance rejection and compliance with heart's motion, different ω_{n_m} and ω_{n_s} should be chosen according to the absence or presence of contact between the slave robot and the heart. In addition, the stiffness values of the two models k_m and k_s need to be designed first, so that the mass and damping parameters can be obtained from the natural frequencies and the damping ratios. Therefore, the parameters need to be adjusted below are only stiffness and natural frequency.

4.2.2 Parameter Adjustments

1) Adjustment of impedance models for no contact case

For the case of no contact, the slave robot should follow the (possibly scaled) trajectory of the master robot. To achieve this objective, the parameters of the two impedance models for the master and slave robots should be proportional to one another (i.e., $k_{m1} = k_p k_{s1}$, $\zeta_{n_{m1}} = \zeta_{n_{s1}}$, $\omega_{n_{m1}} = \omega_{n_{s1}}$), which will lead to a scaled position tracking ($\mathbf{x}_{ref_{m1}} = k_p \mathbf{x}_{ref_{s1}}$). Here, k_p is a position scaling factor, which equals $1/k_f$ and can be set to be unity for simplicity.

In reality, when there is no contact, the human operator should only sense the master robot's dynamics and should be able to perceive the switch between noncontact and contact. To realize these, for the noncontact case, both the master and the slave impedances are chosen as a small value (Known damping ratio and natural frequency, $k_{m1} = k_{s1} \approx 0$).

Moreover, for the purpose of avoiding the uncontrollable hand tremor of the human operator ($\omega_t = 6 \sim 12$ Hz $= 37.68 \sim 75.36$ rad/sec), and taking the low-frequency motion of the human hand ($\omega_o = 0.05 \sim 0.2$ rad/sec) into consideration, the natural frequencies are designed to be chosen within a small range (i.e. $10\omega_o \leq \omega_{n_{m1}} (= \omega_{n_{s1}}) \leq 0.1\omega_t$). Specifically, in the following section, when there is no contact, $\omega_{n_{m1}}$ and $\omega_{n_{s1}}$ are set to be 1 rad/sec.

2) Adjustment of impedance models for contact case

When the slave robot makes contact with the beating heart tissue, the human operator's force affects both the master and the slave impedance models. In the slave impedance model (4.2), to guarantee the scaled human-master interaction force to be as similar as the slave-heart interaction force, the impedance for the slave robot should be adjusted to be very small (i.e., $k_{s2} \approx 0$). Then the left side of (4.2) becomes small due to the boundedness of $\mathbf{x}_{ref_{s2}}$, $\dot{\mathbf{x}}_{ref_{s2}}$ and $\ddot{\mathbf{x}}_{ref_{s2}}$, and accordingly, the right side of this equation will be small as well ($(k_{\mathrm{f}}\mathbf{f}_h - \mathbf{f}_e) \rightarrow 0$). Therefore, the slave robot will compensate for the heart's motion and follow the scaled position of the master robot ($\mathbf{X}_s \rightarrow ((k_{\mathrm{f}} Z_{m2} / Z_e)\mathbf{X}_m + \mathbf{X}_e)$, where $\mathbf{X}$ is the Laplace transform of the position, Z_{m2} and Z_e are the impedances of the master model and the beating heart), as $(k_{\mathrm{f}}\mathbf{F}_h - \mathbf{F}_e) = (k_{\mathrm{f}} Z_{m2}\mathbf{X}_{ref_{m2}} - Z_e(\mathbf{X}_s - \mathbf{X}_e)) \rightarrow 0$.

Additionally, the slave impedance model (4.2) should comply with the slave-heart interaction force. Therefore, the natural frequency is selected several times greater than the range of beating heart frequency ($\omega_{n_{s2}} \gg \omega_h$ ($\omega_h = 6.28 \sim 10.68$ rad/sec)). Particularly, the natural

frequency of the slave impedance model under contact case is set to be 50 rad/sec in the following section.

In the master impedance model (4.1), the natural frequency is set to be the same as that for the noncontact case ($\omega_{n_{m2}}$ = 1 rad/sec) to filter the high-frequency component. Therefore, the only varying parameter of the master impedance model is the stiffness (k_{m2}). As the slave-heart interaction force is approximately equal to the scaled human-master interaction force, the human operator should exert appropriate forces to the slave impedance model (4.2). For this purpose, k_{m2} should be adjusted appropriately. If it is set to be a very small value, in order to apply a desired force to the slave robot, the human operator has to move the master robot through a large distance, which may be beyond the workspace for the master robot. To the contrary, if k_{m2} is chosen to be very large, the master robot will become too rigid to be manipulated; that is, a tiny movement of the master robot will generate a pretty large force.

Based on that, generally, k_{m2} can be set to be the same as the stiffness of the tissue target (k_e), so that the human operator will have the sense of directly operating on the environment – specifically, a seemingly "arrested" heart. The slave robot will follow the trajectories of the master robot and the heart ($\mathbf{x}_s \rightarrow (k_f\mathbf{x}_m + \mathbf{x}_e)$, as $Z_{m2} \approx Z_e$. Nevertheless, if the stiffness of the tissue target is not able to be measured in advance, k_{m2} can be chosen from the range of the stiffness for the soft organs, 100-300 N/m [83], [84]. By tuning the force scaling factor, k_f, the force applied by the human operator to the slave impedance model (4.2) can be adjusted to be in the desired range.

It is reasonable to tune the force scaling factor instead of the workspace of the master robot to adjust the applied force to the slave robot, as for cases that require small slave-heart interaction forces the force scaling factor can reduce the tissue injury caused by accident. According to the absence or presence of contact between the slave robot and the heart, the objectives and parameter adjustment guidelines for the impedance models are summarized in Table 4.1.

70

Table 4.1. Objectives and parameter adjustment guidelines for impedance models

Parameters	No contact		Contact	
	Master	**Slave**	**Master**	**Slave**
Objective	$\mathbf{f}_h \approx 0$, $\mathbf{x}_m = \mathbf{x}_s$		$\mathbf{x}_s \approx (k_f \mathbf{x}_m + \mathbf{x}_e)$, $k_f \mathbf{f}_h = \mathbf{f}_e$	
Stiffness	$k_{m1} = k_{s1} \approx 0$ To simulate master robot's dynamics		$k_{m2} \approx k_e$ To provide sense of operating on an idle heart	$k_{s2} \approx 0$ To guarantee $k_f \mathbf{f}_h = \mathbf{f}_e$
Natural Frequency (rad/sed)	$\omega_{n_{m1}} = \omega_{n_{s1}} = \omega_{n_{m2}} = 1$ To reduce hand tremor and comply with the force $\mathbf{f}_h$			$\omega_{n_{s2}} = 50$ To comply with the force $\mathbf{f}_e$
Damping ratio	$\zeta_{m1} = \zeta_{s1} = \zeta_{m2} = \zeta_{s2} = 0.7$ To ensure model (4.1) and (4.2) have fast behaviors in response to the force inputs and small overshoots in response to the step force inputs			
Mass and damping	Calculate from $\omega_{n_m} = \sqrt{k_m / m_m}$, $\zeta_m = c_m / 2\sqrt{m_m k_m}$ $\omega_{n_s} = \sqrt{k_s / m_s}$, $\zeta_s = c_s / 2\sqrt{m_s k_s}$			

To track the ideal responses of the two reference impedance models for the master and slave robots, two PID controllers are employed and tuned based on the dynamics of the master and slave robots. These position controllers make sure the master and slave robots track the desired positions calculated from the reference impedance models for the respective robots, which are given in (4.1) and (4.2), respectively. In Figure 4.1, the control variables $\tau_m(t)$ and $\tau_s(t)$ are determined by two weighted sums, respectively

$$\tau_m(t) = K_{P_m} \mathbf{e}_m(t) + K_{i_m} \int_0^t \mathbf{e}_m(\tau) d\tau + K_{d_m} \frac{d\mathbf{e}_m(t)}{dt} \tag{4.3}$$

$$\tau_s(t) = K_{p_s} \mathbf{e}_s(t) + K_{i_s} \int_0^t \mathbf{e}_s(\tau) d\tau + K_{d_s} \frac{d\mathbf{e}_s(t)}{dt} \tag{4.4}$$

71

where $\mathbf{e}_i(t) = \mathbf{x}_{ref_i}(t) - \mathbf{x}_i(t)$. Here, the subscript $i = m$ for the master and $i = s$ for the slave. Also, K_{p_i}, K_{I_i}, and K_{d_i}, all non-negative values, denote the coefficients for the proportional, integral, and derivative terms, respectively.

4.3 Testing Protocal

To validate the proposed telerobotic framework, two scenarios amenable to two surgical tasks including mitral valve annuloplasty (MVA) [74], and soft tissue cutting (STC) [85], [86] are tested in both simulations and experiments. A user study involving a line drawing task, which is similar to tissue cutting, is conducted in experiments.

4.3.1 Surgical tasks

The two surgical tasks considered in this chapter require different tool-tissue contact forces. Based on this, the two scenarios are designed to achieve the desired contact forces of the tasks by tuning the model parameters. The requirements of contact forces for specific surgical tasks are described below.

In mitral valve annuloplasty, the surgical tool should compensate for the heart's fast motions to allow the human operator to easily deploy anchors into the moving annulus. In [74], Yuen provided the required contact forces of 2~3 N to deploy anchors firmly into the annulus, and emphasized that forces must stay below 5.5 N to avoid tissue damage.

In soft tissue cutting, the maximum cutting force indicates the required force for the blade to cut into the tissue. The authors in [85] and [86] studied the tissue cutting process of excised organs and showed the cutting force increased linearly in terms of magnitude as the tissue deformed; the cutting force peak was found to be greater than 3~4 N.

4.3.1 Protocol

To apply appropriate forces to the target tissue during surgery and avoid tissue damage, a simple way allowed by (4.2) in the proposed framework is to roughly fix the master-human interaction force, $\mathbf{f}_h$, and tune the force scaling factor, k_f. For instance, if $\mathbf{f}_h$ is around 3~4 N, the force scaling factor for the two aforementioned tasks can be set at 0.63, and 1, respectively, to obtain the corresponding desired range for the contact force between the surgical tool and tissue. Therefore, the two surgical scenarios are designed as shown in Table 4.2.

Table 4.2. Surgical scenarios

Surgical scenario	1	2
Surgical tasks	MVA	STC
Desired contact force (N)	2~3	>3~4
$\mathbf{f}_h$ during slave-heart contact (N)	3~4	
Force scaling factor	0.63	1

In simulations, both the human arm and the beating heart will be modeled mathematically. A harmonic function will be used to simulate the exogenous input force of the human arm, and produce a harmonic master-human interaction force with a maximum magnitude of ~ 4 N.

In the experiments, an actual human operator can actively maintain the master-human interaction force at any level. To clearly present the force tracking performance during contact, the operator is instructed to hold the surgical instrument against the tissue with 2 N of force for ~15s followed by 3-4 N for ~15s, and then with 2 N for ~15s.

It is worth noting that the desired contact forces for the two surgical scenarios should be examined in the direction normal to the tissue plane [13]. In the experimental user study, where the motions of the robots contain 2 DOFs (degree of freedoms), this needs to be taken into account too. Detailed information with regard to the user study is presented in Section 4.5.2.

4.4 Simulations

A teleoperation system is modeled and simulated in MATLAB/SIMULINK. In the simulations, two PHANToM Premium 1.5A robots with 3-DOF (shown in Figure 4.2) are modeled to play the role of the master and slave robots. As the two tasks are single-DOF, only simulation along the x-axis of each PHANToM robot is presented.

Spatial and Tool Frames
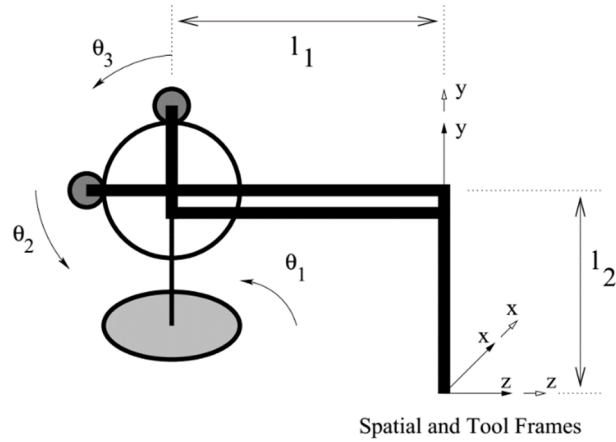
Figure 4.2. Zero configuration of PHANToM (adapted from [87]).

In terms of modeling, the experimentally identified transfer function model for the PHANToM at the center of the workspace along the x-axis is expressed as [87]

$$\frac{x}{f} = \frac{1}{s_2} \frac{s^2 + 5.716s + 9.201 \times 10^4}{3.329 \times 10^{-6} s^2 + 0.001226s + 1.536} \tag{4.5}$$

It has been shown that this linear model closely approximates the low-frequency behavior (up to about 200 Hz) of the robot dynamics [87].

The interaction force between the master and the operator, $\mathbf{f}_h$, and the interaction force between the slave and the environment, $\mathbf{f}_e$, can be experimentally measured by force sensors.

74

Alternatively, in simulations, $\mathbf{f}_h$ and $\mathbf{f}_e$ will be calculated based on the dynamic models for the operator and the beating heart, respectively. The dynamics are assumed to be the following two second-order linear time invariant (LTI) models [69], [88]:

$$\mathbf{f}_h = \mathbf{f}_h^* - (m_h \ddot{\mathbf{x}}_m + c_h \dot{\mathbf{x}}_m + k_h \mathbf{x}_m) \tag{4.6}$$

$$\mathbf{f}_e = m_e \ddot{\tilde{\mathbf{x}}}_s + c_e \dot{\tilde{\mathbf{x}}}_s + k_e \tilde{\mathbf{x}}_s \tag{4.7}$$

Here, $\mathbf{f}_h^*$ is the exogenous input force of the human operator generated by the muscles, and $\tilde{\mathbf{x}}_s = (\mathbf{x}_s - \mathbf{x}_e)$ is the relative displacement between the slave robot and the beating heart. Also, m_h, m_e, c_h, c_e, k_h, k_e are the mass, damping, and stiffness parameters of the operator arm and the heart tissue, respectively.

The exogenous input force of the human operator and the oscillatory motion of the beating heart along the x-axis are simulated, respectively, as

$$f_h^* = 5 - 5\cos(0.05\pi t) \tag{4.8}$$

$$x_e = -0.005\cos(7.5\,t) + 0.005 \tag{4.9}$$

The parameters of the operator and the heart models, based on [83], [89], are shown in Table 4.3. Based on the adjustment guidelines presented in Section 4.2.2 and the scaling factors for the position and force described in Section 4.3, the parameters of the master and slave impedance models for contact and noncontact cases are shown in Table 4.3. The PID controllers for the master and slave robots used in simulations are the same for both robots. The parameters of the controllers are chosen to be $K_\mathrm{p} = 125$, $K_\mathrm{i} = 9.21$, $K_\mathrm{d} = 0.0103$.

It should be mentioned that in simulations, as there is no force sensor to directly measure the contact force, contact will be detected based on position. To simulate the cases of non-contact and contact, the heart position was set to have an offset from the initial position of the slave robot.

Once the position of the slave exceeded this offset, contact occurred. Based on this, each trial was divided into three steps: approach the heart, make contact with the heart, and break contact with the heart. The first and third phases belong to the noncontact case. Additionally, to further simulate the realistic force sensor noise, the calculated force signals were corrupted by an additive zero-mean Gaussian noise with variance of 0.005 N.

For the first scenario, the mean absolute errors (MAEs) of the master and the slave positions with respect to their corresponding reference positions calculated using (4.1) and (4.2) were 8.25×10^{-10} m and 2.76×10^{-8} m, respectively. For the second scenario, the MAEs between the real positions of the robots and their reference positions were 8.32×10^{-10} m and 3.40×10^{-8} m, respectively. These demonstrate the designed controllers achieved position tracking successfully.

Table 4.3 Model parameters of the human operator's arm, the beating heart, the master robot and the slave robot

Parameters	Human Operator	Beating Heart	Noncontact		Contact	
			Master Z_{m1}	Slave Z_{s1}	Master Z_{m2}	Slave Z_{m2}
Stiffness (N/m)	$k_h = 300$	$k_e = 200$	$k_{m1} = 10$	$k_{s1} = 10$	$k_{m2} = 200$	$k_{s2} = 10$
Mass (kg)	$m_h = 3.25$	$m_e = 0.25$	$m_{m1} = 10$	$m_{s1} = 10$	$m_{m2} = 200$	$m_{s2} = 0.004$
Damping (Ns/m)	$c_h = 20$	$c_e = 4.5$	$c_{m1} = 14$	$c_{s1} = 14$	$c_{m2} = 280$	$c_{s2} = 0.28$

Figure 4.3 shows the positions of the master and slave robots for the two surgical scenarios. It can be seen that when the slave robot was near the heart, the non-contact and contact cases alternatively occurred because of the movement of the heart. To reduce the number of repetitive switching, when the slave robot was near the heart, both the impedances of the master and slave models were increased continuously from $Z_{m1}(Z_{s1})$ to Z_{m2}. If the scaled human-master

interaction force were greater than the slave-heart interaction force, based on model (4.2) the switch would stop. Otherwise, the slave robot would be pushed back, and repetitive switching would go on. In Figure 4.3, for both scenarios, switching appeared during the transitions between contact case and non-contact case. However, large force scaling factor resulted in large human-master interaction force, which leaded to less switching and small motion amplitude of the master robot. The zoomed-up transitions clearly showed that the contacts between the slave robot and the heart were weak.

For the sake of following calculations, the contact period was defined as the slave robot made firm contact with the heart, that is, no switching occurred during the contact period. The rest periods were treated as non-contact case. During non-contact periods, the position tracking MAEs between the slave robot and the master robot for the two scenarios were 2.64×10^{-4} m and 1.31×10^{-4} m, respectively.

When the slave robot made contact with the heart, to obtain the dominant frequencies associated with the heartbeat and human arm's motions, a fast Fourier transform (FFT) with a Hamming window was applied to the slave robot position. In Figure 4.3a, the high-frequency component of the slave robot position (HFCS) had amplitude of 4.67 mm that was 93.4% of the beating heart's motion amplitude (5mm). The low-frequency component of the slave robot position (LFCS) had an amplitude of 3.92 mm, that was 109% of the scaled amplitude of the human operator motion (note that $k_f x_m = 3.58$ mm). The results for the other scenario incorporating the first one was summarized in Table 4.4.

The MAEs between the slave robot position and the summation of the scaled master robot position and the beating heart position for two tasks were 1.73 mm, and 1.17 mm, respectively, which are satisfactorily small given that the main criteria for task success were defined in terms of applying the required force levels on tissue.

Table 4.4. Position-tracking results in simulations

Surgical scenario		1	2
High frequency amplitude	HFCS (mm)	4.67	4.76
	Heart motion (mm)	5	5
	Ratio	93.4%	95.2%
Low frequency amplitude	LFCS (mm)	3.92	7.75
	Scaled human motion (mm)	3.58	7.26
	Ratio	109%	107%

(a)   (b)
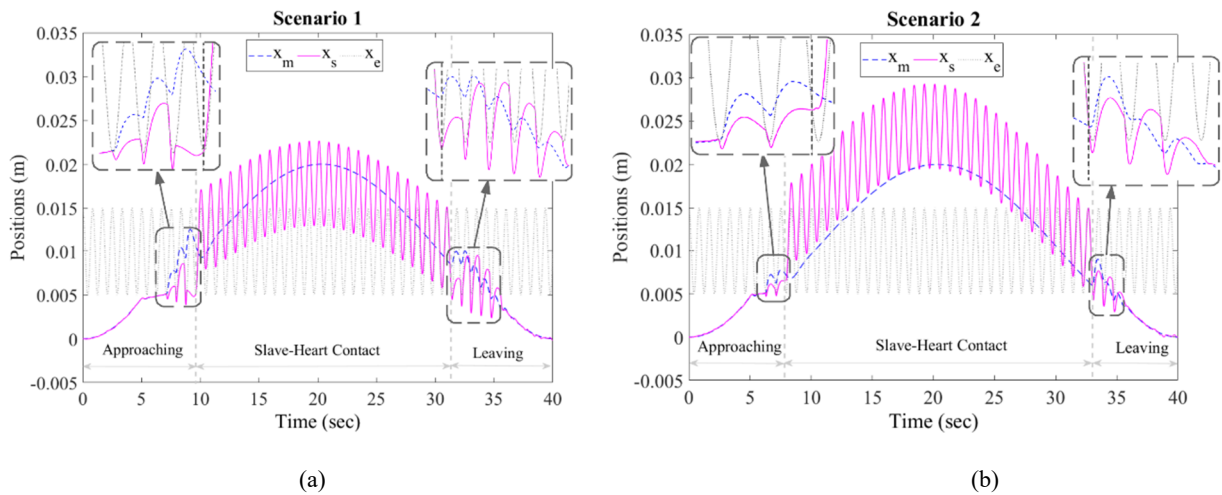
Figure 4.3. Simulated position-tracking performance. The positions of the master and slave robots for surgical scenario amenable to task: (a) mitral valve annuloplasty, and (b) soft tissue cutting. The dashed blue line and the solid pink line denote the real positions of the master and slave robots, respectively. The trajectory of the heart tissue is presented by the dotted gray line.

Figure 4.4 shows the force performance. The scaled human-master interaction forces were approximately equal to the slave-heart interaction forces with MAEs between them of 0.12 N, and 0.15 N during contact period for the two surgical scenarios, respectively. Moreover, the zoomed-up transitions between contact and non-contact cases show that the contact for scenario 1 is weaker than that for scenario 2. It is because small force scaling factor leads to small scaled human-master

78

interaction force. If this force were smaller than the slave-heart interaction force, the slave robot would be rebounded.

(a)   (b)
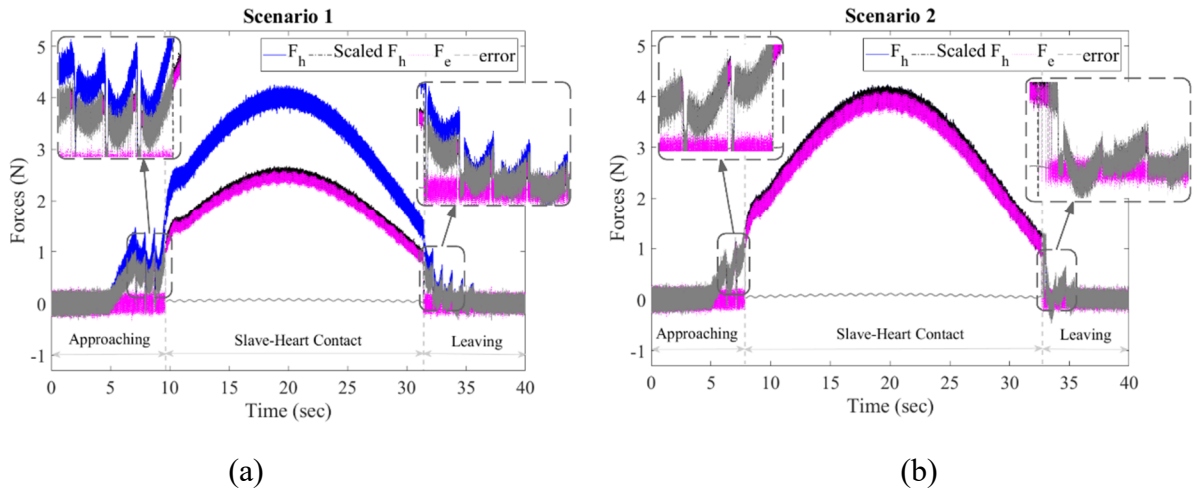
Figure 4.4. Interaction force results. The simulated human-master interaction force (solid blue line) plotted versus the simulated slave-heart interaction force (dotted pink line) for surgical scenario amenable to task: (a) mitral valve annuloplasty, and (b) soft tissue cutting. In addition, the scaled-down human-master contact forces (dash-dotted black line) and force errors between the scaled human-master interaction force and the slave-heart interaction force (dashed black line) are presented as well.

4.5 Experiments

Following the successful simulation study, experiments are performed with a teleoperation robotic system. The experimental setup employs a 3-DOF Phantom Premium 1.5A robot (Geomagic Inc., Wilmington, MA, USA) as the master robot and a 2-DOF Quanser planar robot (Quanser Consulting Inc., Markham, ON, Canada) as the slave robot (Figure 4.5). To measure the applied interaction forces of the human operator and the heart tissue, the Phantom Premium and Quanser robots are respectively equipped with a 6-axis 50M31 force/torque sensor (JR3 Inc., Woodland, CA, USA) and a 6-axis Gamma force/torque sensor (ATI Industrial Automation, Apex, NC, USA),

respectively. The beating heart is simulated by an artificial plastisol-based tissue attached to a custom-built mechanical cam which produces peak-to-peak amplitude of 9 mm and has a fundamental frequency of 64 bpm (1.07 Hz) to simulate the beating-heart's motion which temporally matched to an ECG signal [24]. To simplify the analysis, the motion direction of the heart simulator is adjusted to be the same as the x direction of the robots. As mentioned before, the positions and forces presented in Section 4.5.1 (1-DOF scenarios corresponding to the two surgical tasks) are along the x direction, and in Section 4.5.2 (2-DOF user study) are along x and y directions.
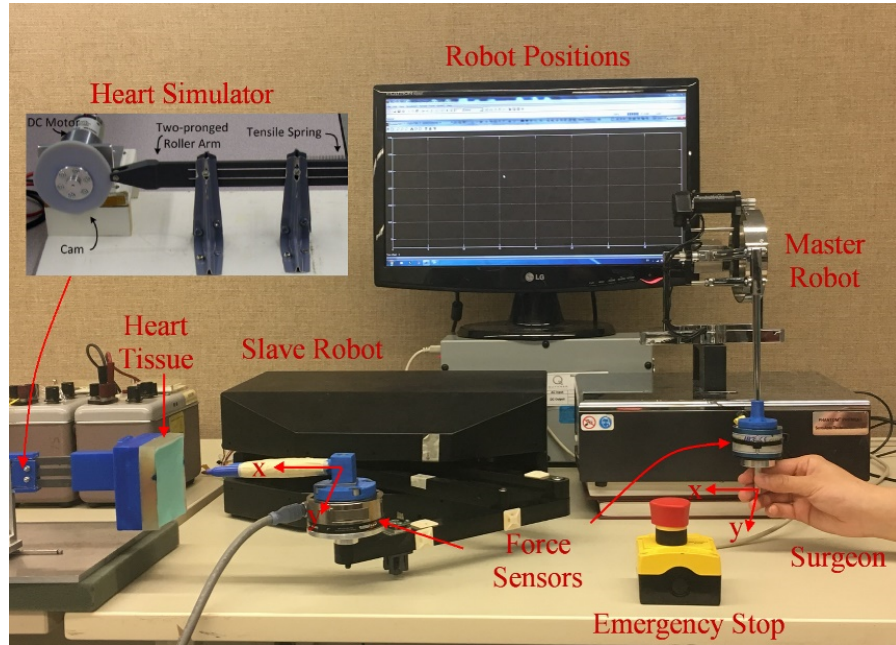
Figure 4.5. Experimental setup.

Unlike the simulations, in the experiments the stiffness of the heart tissue is unknown, so the impedance parameters for the master robot during contact are arbitrarily set to be $k_{m2} = 300$ N/m, $m_{m2} = 300$ kg, and $c_{m2} = 420$ Ns/m. The parameters for the slave impedance model during contact are set at $k_{s2} = 50$ N/m, $m_{s2} = 0.02$ kg, and $c_{s2} = 1.4$ Ns/m. The parameters of PID controllers for the master robot are $K_{P_m} = 1000$, $K_{i_m} = 200$, $K_{d_m} = 1$. The PID controller

parameters for the slave robot are $K_{p_s} = 1000$, $K_{i_s} = 0$, $K_{d_s} = 20$. Note that the master and slave robots are not identical in the experiments as they were in the simulations.

4.5.1 Surgical scenarios validation

Testing indicated that in the x direction, a threshold of 0.3 N for the slave-heart interaction force was appropriate to detect the contact state surgical tool and tissue. Based on this force threshold, each trial was divided into three steps as well: approach the heart, make contact with the heart, and break contact with the heart.

The position-tracking performances for two different surgical scenarios are shown in Figure 4.6. The MAEs between the master robot position and its reference position generated by the impedance model (4.1) for two scenarios were 0.54 mm, and 0.44 mm, respectively. The MAEs between the slave robot position and its reference position generated by the impedance model (4.2) for the two surgical scenarios were 0.47 mm, and 0.64 mm, respectively. The above MAEs were calculated across the two phases of approaching, making contact with, and breaking contact with the heart.

In Figure 4.6a, by applying FFT to the position data of the slave robot for contact case, the high-frequency component had an amplitude of 3.96 mm, which was 88% of the amplitude of the heart's motion (4.5 mm), and the amplitude of the low-frequency component was 2.37 mm, which was 75% of the scaled master motion amplitude (note that $k_f x_m = 3.16$ mm). Section 4.2.2 presented the slave robot would comply with the heart's motion and follow the theoretically scaled position of the master robot ($\mathbf{X}_s \rightarrow (\mathbf{X}_e + (k_f Z_{m2} / Z_e)\mathbf{X}_m)$). However, the experimental results show that only 75% of $k_f x_m$ was transmitted to the slave robot, which means the ratio of Z_{m2} / Z_e was less than 1. In other words, the artificial tissue used in the experiments is more rigid than the stiffness of the master robot (300 N/m). More results about the two surgical scenarios are shown in Table 4.5.

In summary, the results in Figure 4.6 demonstrate that (a) the local position controllers used in the system guarantee the robots follow their corresponding reference impedance positions, (b) when the slave robot is getting close to or is leaving the tissue, the master and slave robots have very similar positions, and most importantly (c) when the slave robot makes contact with the tissue, the slave robot successfully complies with the fast oscillatory motions of the tissue while following the (scaled) position of the master robot as closely as possible.

Table 4.5. Position-tracking results in expeiments

Surgical scenario		1	2
High frequency amplitude	HFCS (mm)	3.96	4.12
	Heart motion (mm)	4.5	4.5
	Ratio	88%	93.6%
Low frequency amplitude	LFCS (mm)	2.37	4.98
	Scaled human motion (mm)	3.16	6.07
	Ratio	75%	82%

In addition, the transitions between non-contact and contact are zoomed-in in Figure 4.6 as well. Similarly, in order to obtain steady slave-tissue contact and avoid chattering during interaction, the human operator should exert relatively a large force to make the scaled-down human-master interaction force that is greater than the slave-heart interaction force. Once the slave-heart interaction force was kept greater than the force threshold of 0.3 N, the switch would stop. The transitions shown in Figure 4.6 for the two scenarios demonstrate that the larger the force scaling factor is the less the number of repetitive switching will be.

Figure 4.7 demonstrates the performance of non-oscillatory haptic perception for each scenario. Based on the reference impedance model for the slave robot (4.2), when slave robot made contact with the tissue, the scaled-down human-master interaction force was transmitted to model (4.2). The MAEs between the scaled human-master interaction force and the slave-tissue interaction force for the two surgical scenarios were 0.33 N, and 0.36 N, respectively. The zoomed-

in parts in Figure 4.7 demonstrate that large slave-heart contact force reduces the number of repetitive switching between contact and non-contact cases when the slave robot is close to the heart.

These experimental results in Figure 4.6 and Figure 4.7 suggest that the proposed switched-impedance control based telerobotic system achieves position-tracking and non-oscillatory tactility simultaneously even when the slave is making contact with the beating heart. In addition, regarding the two specific scenarios, by choosing an appropriate force scaling factor, the ideal behaviors of position and force are achieved.

(a)   (b)
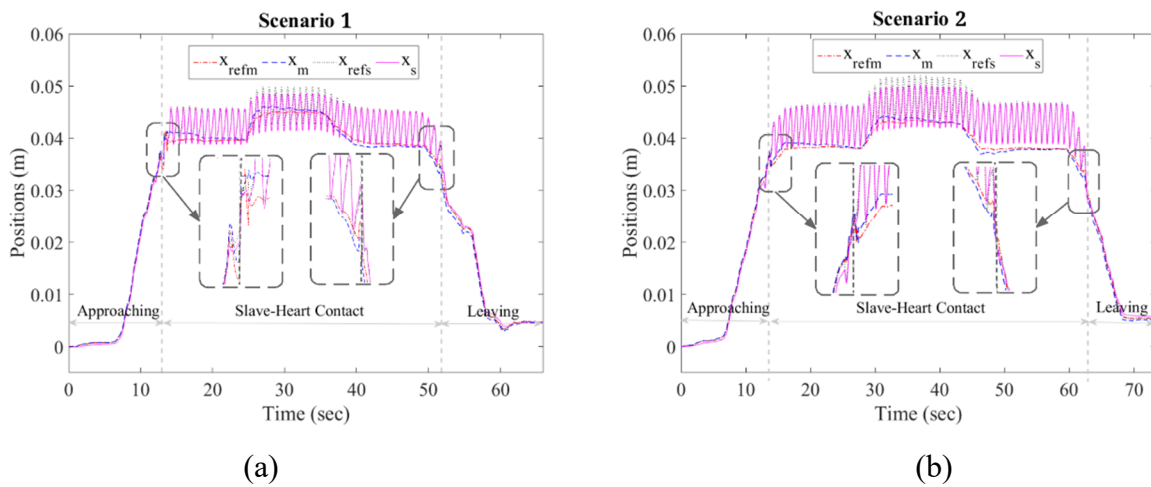
Figure 4.6. Experimental position-tracking performance of the master and slave robots for surgical scenario amenable to task: (a) mitral valve annuloplasty, and (b) soft tissue cutting. The reference positions and the actual positions of the master and slave robots are presented. The dash-dotted red line and the dotted black line denote the reference positions of the master and slave robots, respectively. The dashed blue line and the solid pink line denote the actual positions of the master and slave robots, respectively.
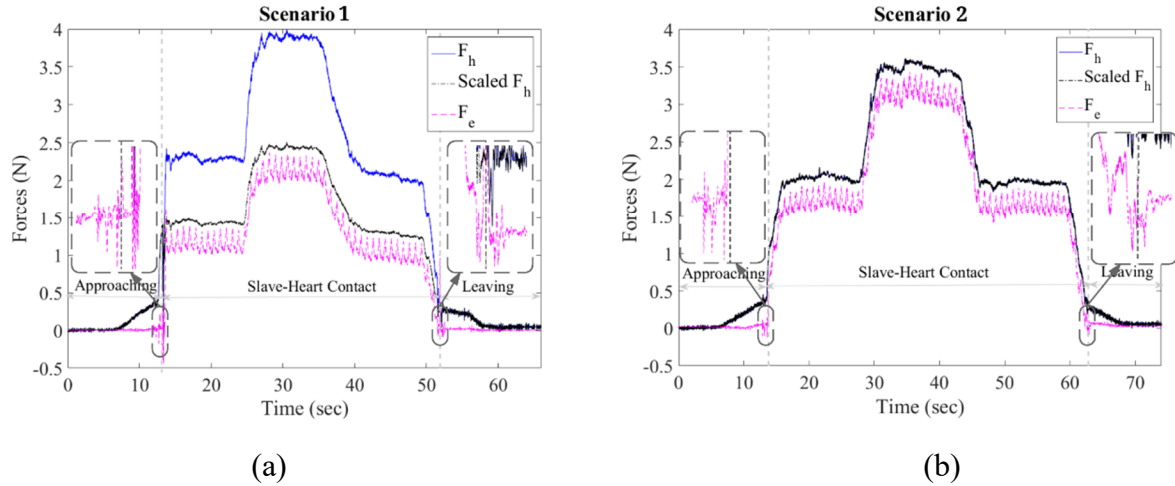
Figure 4.7. The interaction force results. The experimental human-master interaction force (solid blue line) plotted versus the experimental slave-heart interaction force (dashed pink line) for surgical scenario amenable to task: (a) mitral valve annuloplasty, and (b) soft tissue cutting. The scaled human-master interaction forces (dash-dotted black line) are also presented.

4.5.2 User study

The user study presented here was selected to emulate the motion requirements of cutting tissue. It involves drawing a line on the surface of the mock beating heart by using a marker mounted on the end of the slave robotic arm.

In this study, the simulated heart is moving back and forth along the x direction. The participant commands the slave robot to approach the tissue surface by manipulating the master robot. After the slave robot makes contact with the tissue, the participant commands the slave robot to draw a solid legible line along the robot's y direction for ~ 3 cm. To record the results, for each trial a paper is stuck to the surface of the mechanical beating heart simulator (on top of the soft plastisol tissue to still recreate the soft heart tissue). The process requires a prolonged contact with the surface while the contact forces should not be too large to cause damage to the tissue. This task is completed with motion compensation (the proposed strategy) and without motion compensation (simple DFR haptic teleoperation control).

84

The task included 5 participants (4 females and 1 male). The participants aged 20-30 and were graduate student volunteers. Each participant trained with and without motion compensation until he/she got used to the system. Then, 10 trials in which each participant alternated between with and without motion compensation cases were completed.

The results of line drawing time and break points number are listed in Table 4.6 with respect to the two cases (with and without motion compensation). To compare the results of the two cases, a paired two-sided *t-test* was used to obtain the probability of the null hypothesis for the 10 trials. Data are shown as means ± standard derivations. Means were considered significantly different if P < 0.05.

Table 4.6. Experimental results of time and break points

Motion Compensation	Yes	No	P-value
Drawing Time (s)	18.67 ± 2.74	25.20 ± 2.45	< 0.0001
Number of Break Points	0.68 ± 0.90	4.24 ± 1.83	< 0.0001

With motion compensation, the mean drawing time was 26% less than the time measured without motion compensation. The mean and standard deviation of the break points number were reduced sharply when providing motion compensation. The P-values indicate that there was a significant difference between providing and not providing compensation with respect to the drawing time and the number of break points.

In addition, considering all the trials of the 5 participants, the means and standard deviations of the force by operator on master robot and the force by slave robot on tissue with and without compensation are shown in Table 4.7. Providing no compensation, the two standard deviations of forces were roughly 10 times and 2 times, respectively, greater than those measured when provided compensation. In addition, when there was no motion compensation provided, the human-master interaction forces were generally smaller than those provided compensation. It is

85

because participants usually did not apply large forces to the master robot to avoid unexpected tool-tissue collision. If the human-master contact force were too large, it was more likely to puncture the paper.

When there was no motion compensation provided, the user had to make compensation manually as well as attempted to draw a solid line along the perpendicular direction. It was not easy for the user to achieve the two objectives simultaneously. Figure 4.8 shows the drawn lines without motion compensation, which include lots of break points. In Figure 4.9, the robot positions and the interaction forces in both x and y directions are presented. It can be seen that in the x direction, the motion synchronization was difficult for the human operator to achieve and the slave-heart interaction force level was hard to control. In the y direction, both the positions and the forces have oscillatory motions with small amplitudes, which appeared due to tissue deformation and friction.

Table 4.7. Experimental results of forces

Motion Compensation	Yes	No
Force by Operator on Master in x direction (N)	1.84 ± 0.05	1.57 ± 0.48
Force by Slave on Tissue in x direction (N)	1.41 ± 0.22	1.55 ± 0.53
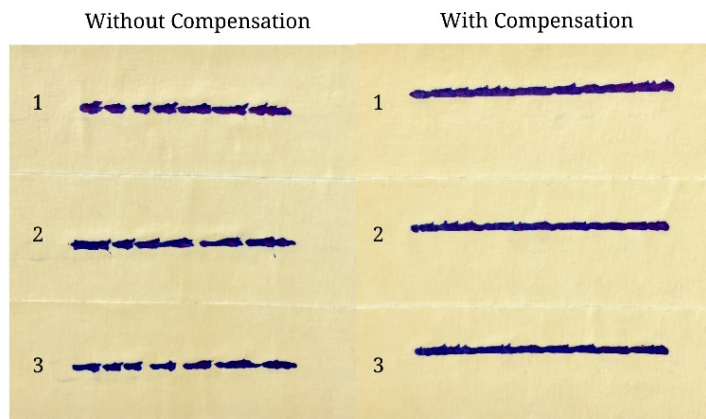
Figure 4.8. Comparison of line results.

When motion compensation was provided, it was easier for the user to draw a solid line along the direction perpendicular to the movement direction. The lines shown in Figure 4.8 with compensation demonstrate that the proposed method achieves better results. The positions of the master robot in both x and y directions do not include the oscillatory motions of the slave robot (Figure 4.10). In the x direction, the slave robot successfully synchronizes its movement with the moving heart's motion, and the human-master interaction force provides the user a steady contact force. This steady force was simultaneously transmitted to the slave robot, which made the control of the slave-heart contact force easily. In the y direction, the positions and forces of the slave robot were both oscillatory due to unexpected tissue deformation and friction. Similarly, these oscillatory behaviors did not influence the frequencies of the positions and forces of the master robot.

4.6 Concluding Remarks

This chapter demonstrated the effectiveness of the proposed switched-impedance controlled master-slave teleoperation system, which is designed to both implement fast compensation for the beating heart's motion and apply accurate interaction force to the heart tissue to perform surgical tasks on or inside the heart. The desired behavior was achieved in the proposed system by switching the parameters of two reference impedance models for the master and slave robots. When the slave robot does not make contact with the beating heart, the slave robot closely follows the motion commands of the human operator given to the master robot. *Once contact occurs, the slave robot complies with the combined motion of the master robot and the beating heart and enables the human operator to perceive non-oscillatory interaction force that is akin to a sense of operating on a seemingly idle heart.* Results of both simulations and experiments for two surgical scenarios suggest that the proposed telerobotic system achieves the stated goals. In addition, the user study of line drawing demonstrates that the proposed switched impedance control strategy offers timesaving, perfect lines, and easy control of the slave-heart interaction force compared to the case without motion compensation.
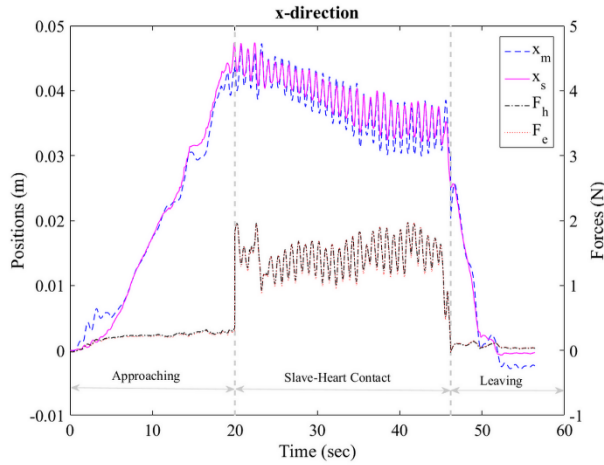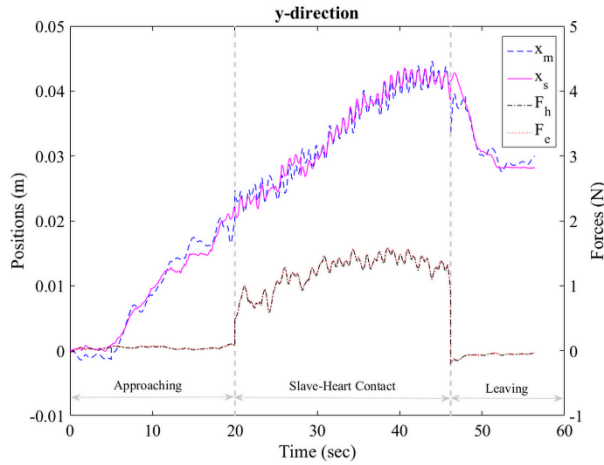
Figure 4.9. Position and force results when no motion compensation provided. (a) Robot positions and interaction forces without motion compensation in the x direction. (b) Robot positions and interaction forces without motion compensation in the y direction. The dashed blue line is the position of the master robot. The solid pink line is the position of the slave robot. The dash-dotted black line shows the human-master interaction force. The dotted red line indicates the slave-heart interaction force.
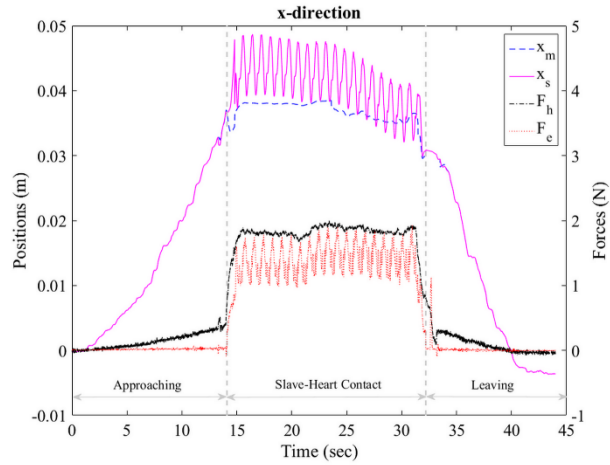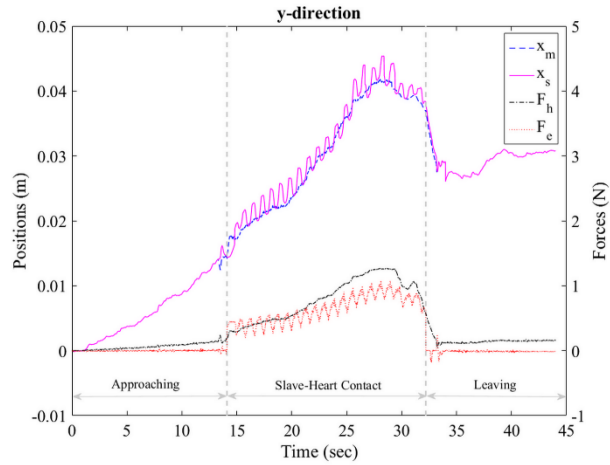
Figure 4.10. Position and force results when motion compensation provided. (a) Robot positions and interaction forces with motion compensation in the x direction. (b) Robot positions and interaction forces with motion compensation in the y direction. The dashed blue line is the position of the master robot. The solid pink line indicates the position of the slave robot. The dash-dotted black line is the human-master interaction force. The dotted red line shows the slave-heart interaction force.

Chapter 5

Ultrasound Image Guidance and Robot

Impedance Control

5.1 Introduction

In Chapter 3, two reference impedance models were designed for the master and slave robots. By adjusting the parameters for the impedance models, the slave robot followed the position commands of the human operator when there was no contact between surgical tool and tissue and was able to comply with the beating heart's motion during the tool-tissue interaction. However, the trade-off between the flexibility of the slave robot and the force applied to the heart tissue restricts the system's widespread applications. Besides, as the slave robot only compensates for the fast heart's motion during contact, it would be difficult for the human operator to control the slave robot to accurately reach the specific point on the surface of the heart tissue, especially for complicated surgeries. In this chapter[4], to simultaneously achieve motion compensation for the slave robot and non-oscillatory haptic feedback on the master robot, an US image-based position controller for the slave robot and an impedance controller for the master robot are proposed for

---

[4]Portions of this chapter were published in "L. Cheng and M. Tavakoli, "Ultrasound Image Guidance and Robot Impedance Control for Beating-Heart Surgery," *Control Engineering Practice (A Journal of IFAC)*, vol. 81, pp. 9-17, 2018." [17]

telerobotic beating-heart surgery (Figure 5.1). The US imaging is used to provide visual feedback and measure the beating heart position which is transmitted to the slave robot to make motion compensation. The impedance model for the master robot is used to provide the human operator with non-oscillatory force feedback during tool-tissue interaction. The chapter is organized as follows. Section 5.1 introduces the developed system for telerobotic beating-heart surgeries. Section 5.2 presents the motion compensation algorithms for the slave robot using US images. Section 5.3 presents the algorithm for non-oscillatory haptic feedback through the master robot. Section 5.4 shows the experimental results. Finally, Section 5.5 concludes the chapter.
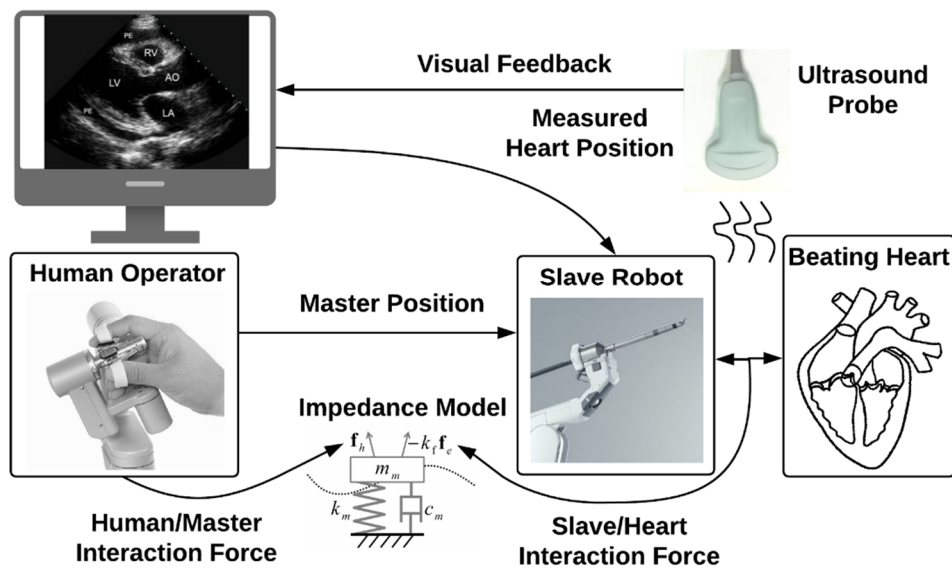
Figure 5.1. System concept of the proposal. The US imaging is used to compensate for the fast heart motion, and the impedance model for the master robot is proposed to achieve non-oscillatory haptic feedback.

The developed telerobotic beating-heart surgical system to simultaneously achieve heartbeat motion compensation and haptic feedback is shown in Figure 5.2.

In the portion of slave block diagram, an US imaging machine is used to obtain the position of the beating heart $\mathbf{x}_e$. The summed position of the master robot $\mathbf{x}_m$ and the heart $\mathbf{x}_e$ is transmitted

to the slave robot as a reference signal $\mathbf{x}_r(=\mathbf{x}_m+\mathbf{x}_e)$. And then a generalized predictive controller (GPC) is used to guarantee the position of the slave robot $\mathbf{x}_s$ follows its reference trajectory $\mathbf{x}_r$. In the portion of the master block diagram, the interaction force between the human operator and the master robot $\mathbf{f}_h$, and the interaction force between the heart tissue and the slave robot $\mathbf{f}_e$ are transmitted directly to a reference impedance model, which will be discussed later can filter out the high-frequency portion of $\mathbf{f}_e$ and achieve $\mathbf{f}_h$ equals the filtered $\mathbf{f}_e$. The impedance model generates a reference position $\mathbf{x}_{ref_m}$ for the master robot to follow.

To implement heartbeat motion compensation and non-oscillatory haptic feedback using the proposed system, there are three main problems need to be addressed:

1) *US imaging issues: slow sampling rate and time delay.* US machines have slow frame rates typically between 20 to 60 Hz. The force sensor, however, generally has a fast sampling rate, which is more than 1000 Hz. To unify the sampling rate of the system, the position data collected at the low sampling rate of the US images should be upsampled first. In addition, the time delay caused by image acquisition and processing is not negligible and must be compensated for. To address this time delay, an extended Kalman filter (EKF) is used to predict the measured heart position.

2) *Motion compensation controller.* The slave robot is designed to follow the summation of the human operator's position commands and the upsampled current heart motion. As the beating-heart motion is quasi-periodic, the future input and output signals to the slave robot can be calculated by assuming the human operator's motion is very slow. The calculated future input and output values can be taken advantage of by the controller to obtain the optimal control signal to the slave robot. Specifically, GPC is chosen to calculate the control signal over a given horizon into the future.

3) *Master robot impedance control.* To guarantee that the human operator mostly perceives the slave-heart interaction forces with little feedback from the oscillatory forces through a reference impedance model, the key is to appropriately adjust the parameters of the impedance model used for the master robot.
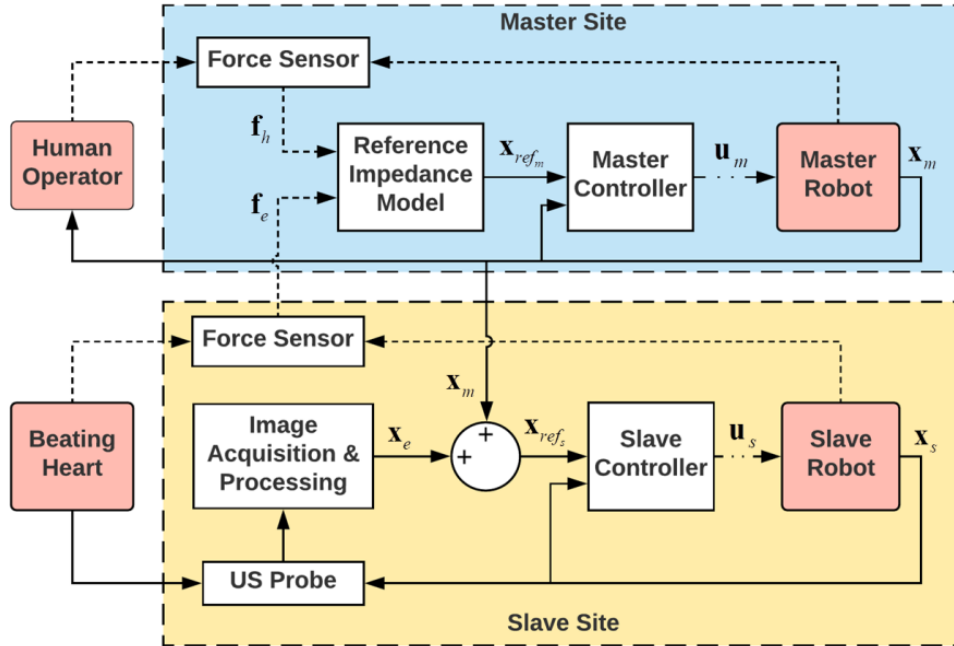
Figure 5.2. The teleoperation system with US image guidance and robot impedance control. The solid lines indicate the position transfer paths. The dashed lines indicate the force transfer paths. The dash-dotted lines are control signals.

5.2 Slave Robot: Motion Compensation

For the sake of brevity and clarity, subsequent algorithms presented in this section will focus on the direction of the major component of heart motion. Multi-degree of freedom applications can be achieved by adjusting one axis of the slave robot frame along the direction of heart motion.

The motion compensation system is shown in Figure 5.3. The designed heartbeat synchronization method requires the slave robot to follow the combined trajectory of the master robot and the beating heart. The beating-heart position can be calculated based on the position of the slave robot and the measured robot-heart distance by US machine along the surgical tool's axis. Due to the time delay caused by image acquisition and processing, the system includes two classes of data: real-time data (shown by black lines) and delayed data (shown by gray lines). The

real-time positions of the master and slave robots are measured by two position sensors mounted on the robots. The measured robot-heart distance X_d^d by US images is delayed data because US image acquisition and processing are needed for that measurement.
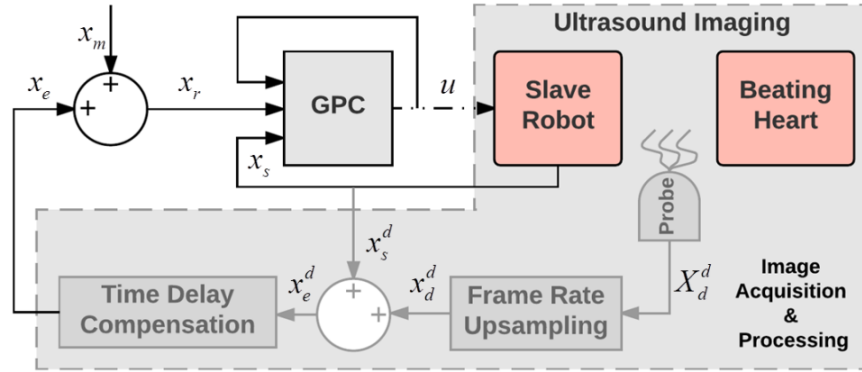
Figure 5.3. Motion compensation control system. Here, X_d^d indicates the measured robot-heart distance by US machine, which is slowly sampled and delayed. Also, x_d^d, x_s^d, and x_e^d are the robot-heart distance, slave robot potion, and beating heart position with a fast sampling rate, respectively. The superscript d indicates the data is delayed. The predicted beating heart position is indicated by x_e , which has both high sampling rate and no delay.

Since that the direction of x_s is set the same as the direction of the beating heart, the measured robot-heart distance X_d^d is converted to the slave robot's frame by converting it from pixels into mm. As the low sampling rate of the US image, the measured robot-heart distance X_d^d needs to be upsampled to the system control sampling rate first. And then the delayed upsampled heart position x_e^d can be obtained by delaying the position of the slave robot x_s^d and adding it to the upsampled robot-heart distance x_d^d.

To compensate for the non-negligible time delay, a predictive filter is used to predict the current heart position. In addition, a GPC is designed to obtain the control signal to the slave robot.

5.2.1 Image processing

The slow sampled robot-heart distance X_d^d can be measured directly from each US image. In the following experiments, a long and thin surgical tool is mounted on the end of the slave robot to perform specific tasks. For this case, the robot-heart distance is actually the distance between the surgical tool tip and the heart tissue. To begin, each original acquired image (Figure 5.4 a) is converted to black and white (Figure 5.4b) by choosing a binary threshold of 0.3. Then, a $3{\times}3$ Sobel edge detection algorithm [90] is used to obtain the edge points of each binary image, and a Hough transform [91] is used to identify the longest line as the detected surgical tool. By extending this line through the surgical tool, there is an intersection of the line and the edge of the heart tissue; this intersection is the point of interest (POI) considered as the heart position. Figure 5.4c shows the detected edges of the surgical tool and heart tissue as well as the identified longest line and its extension. The points of surgical tool tip and POI presented in Figure 5.4d provide the robot-heart distance X_d^d. When the surgical tool tip makes contact with the heart tissue, the robot-heart distance is assumed to be zero.

5.2.2 Data upsampling and prediction

To begin, the measured robot-heart distance X_d^d under lower sampling rate ΔT is upsampled to a higher sampling rate Δt by using cubic interpolation. Consider the data points X_{d0}^d and X_{d1}^d and assume that the n points need to be added between the two data points. A third-degree polynomial, $f(i) = ai^3 + bi^2 + ci + d, i \in (0,1/(n{+}1), 2/(n{+}1), \cdots, 1)$, can be interpolated on the interval $[0,1]$. The four coefficients are given by

$$a = 2f(0) - 2f(1) + f'(0) + f'(1)$$

$$b = -3f(0) + 3f(1) - 2f'(0) - f'(1)$$

$$c = f'(0)$$

$$d = f(0) \tag{5.1}$$

where $f(0) = X_{d0}^d$, $f(1) = X_{d1}^d$, and $f'(0)$ and $f'(1)$ are the slopes at points X_{d0}^d and X_{d1}^d. As the calculation of $f'(1)$ requires another slowly sampled point X_{d2}^d, the total interpolation increases a processing delay of $(2n+1)\Delta t$.
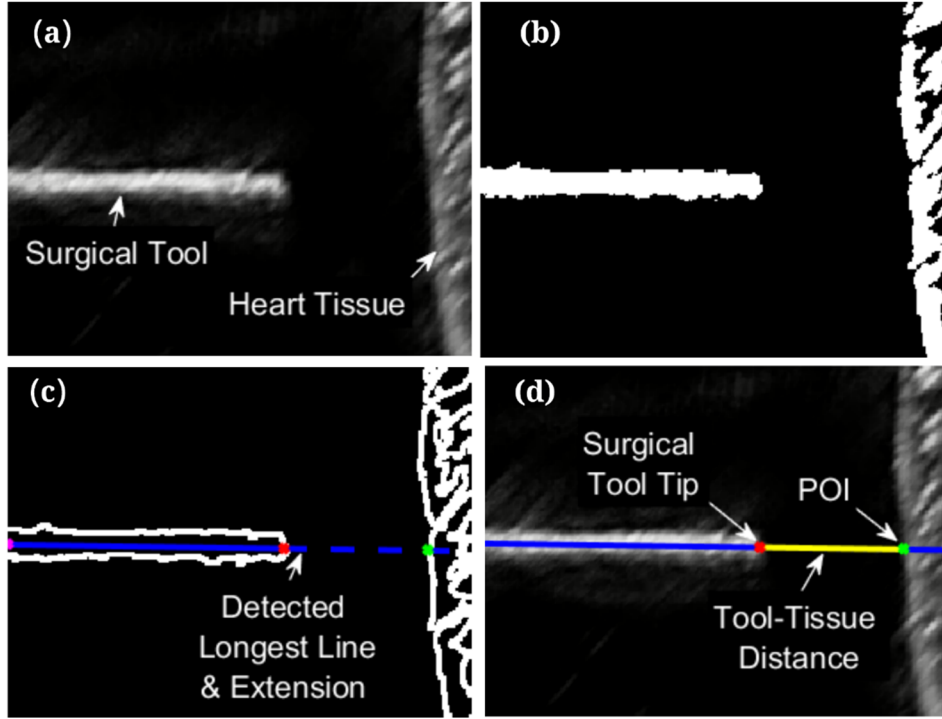
Figure 5.4. Image processing results. (a) The original image. (b) The converted binary image. (c) The image edges and the identified longest line and its extension using Hough transform. (d) The detected robot-heart distance between tool tip and POI in the original image.

To take advantage of the quasi-periodicity of the heart motion, the delayed upsampled heart position x_e^d is calculated by delaying the position of the slave robot and adding it to the upsampled robot-heart distance x_d^d. The delayed quasi- periodic heart position x_e^d is modeled as a time-varying Fourier series and predicted by an EKF [92] to compensate for the time delay. The state space model is expressed as

$$\mathbf{x}(t + \Delta t) = \mathbf{A}(\Delta t)\mathbf{x}(t) + \boldsymbol{\mu}(t)$$

$$x_e^d(t) = h(\mathbf{x}(t)) + v(t) \tag{5.2}$$

In the above, $h(\mathbf{x}(t)) = c(t) + \sum_{i=1}^{m} r_i(t) \sin \theta_i(t) = c(t) + \sum_{i=1}^{m} r_i(t) \sin\left(i \int_0^t \omega(\tau) d\tau + \phi_i(t)\right)$ is the Fourier series of the heart motion, $c(t)$ indicates an offset from the minimum quasi-periodic heart motion to its mean value. Here, $\mathbf{x}(t) \triangleq [c(t), r_i(t), \omega(t), \theta_i(t)]^{\mathrm{T}}$, $i \in (1, 2, \cdots, m)$, is the state vector. The first $m + 2$ state variables and $\phi_i(t)$ are assumed to evolve through random walk. Also, $\boldsymbol{\mu}(t) \sim \mathcal{N}(\mathbf{0}, \mathbf{Q})$ and $v(t) \sim \mathcal{N}(0, R)$ are the process and measurement noises, respectively.

The state transition model is

$$\mathbf{A}(\Delta t) = \begin{bmatrix} \mathbf{I}_{m+1} & & & & & & \mathbf{0} \\ & 1 & & & & & \\ & \Delta t & 1 & & & & \\ \mathbf{0} & 2\Delta t & 0 & 1 & & & \\ & \vdots & & & \ddots & & \\ & m\Delta t & 0 & 0 & \cdots & 1 \end{bmatrix}.$$

The Kalman filter is a recursive estimator. It uses the estimated state from the previous time step $\hat{\mathbf{x}}(t|t)$ and the 'current' heart position measurement $x_e^d(t + \Delta t)$ to compute the estimate for the 'current' state $\hat{\mathbf{x}}(t + \Delta t|t + \Delta t)$. To begin, the predicted state estimate and estimate covariance are expressed as

$$\hat{\mathbf{x}}(t + \Delta t|t) = \mathbf{A}(\Delta t)\hat{\mathbf{x}}(t|t) \tag{5.3}$$

$$\mathbf{P}(t + \Delta t|t) = \mathbf{A}\mathbf{P}(t|t)\mathbf{A}^{\mathrm{T}} + \mathbf{Q} \tag{5.4}$$

To obtain the optimal state estimate $\hat{\mathbf{x}}(t + \Delta t|t + \Delta t)$, a Kalman gain $\mathbf{K}$ is needed and given by

$$\mathbf{K} = (\mathbf{H}\mathbf{P}(t + \Delta t|t)\mathbf{H}^{\mathrm{T}} + R)^{-1}\mathbf{P}(t + \Delta t|t)\mathbf{H}^{\mathrm{T}} \tag{5.5}$$

Here, $\mathbf{H}^{\mathrm{T}}(\Delta t) = \left(\frac{\partial h}{\partial \mathbf{x}}\right)^{\mathrm{T}}\bigg|_{\hat{\mathbf{x}}(t + \Delta t|t) = \mathbf{A}(\Delta t)\hat{\mathbf{x}}(t|t)}$

97

$$
= \begin{bmatrix}
1 \\
\sin \hat{\theta}_1(t + \Delta t | t) \\
\vdots \\
\sin \hat{\theta}_m(t + \Delta t | t) \\
0 \\
\hat{r}_1(\Delta t | t) \cos \hat{\theta}_1(t + \Delta t | t) \\
\vdots \\
\hat{r}_m(\Delta t | t) \cos \hat{\theta}_m(t + \Delta t | t)
\end{bmatrix}.
$$

The formulas for the updated state estimate and estimate covariance are as follows

$$
\hat{\mathbf{x}}(t + \Delta t | t + \Delta t) = \mathbf{K}(x_e^d(t + \Delta t) - h(\hat{\mathbf{x}}(t + \Delta t | t))) + \hat{\mathbf{x}}(t + \Delta t | t) \tag{5.6}
$$

$$
\mathbf{P}(t + \Delta t | t + \Delta t) = (\mathbf{I} - \mathbf{K}\mathbf{H})\mathbf{P}(t + \Delta t | t) \tag{5.7}
$$

It should be noted that the state estimate $\hat{\mathbf{x}}(t + \Delta t | t + \Delta t)$ has a time delay. To overcome this delay, j future points ahead are predicted, and the state vector $\hat{\mathbf{x}}(t + \Delta t | t + \Delta t)$ is propagated ahead j time steps as

$$
\hat{\mathbf{x}}(t + (j + 1)\Delta t) = \mathbf{A}^j(\Delta t)\hat{\mathbf{x}}(t + \Delta t | t + \Delta t) \tag{5.8}
$$

The predicted heart position at $t + \Delta t$ can be calculated by

$$
x_e(t + \Delta t) = h(\hat{\mathbf{x}}(t + (j + 1)\Delta t)) \tag{5.9}
$$

5.2.3 Real-time position tracking

With the upsampled and predicted heart motion, the slave robot can be controlled with GPC [93] to follow the human operator's motions and synchronize with the beating-heart motion by taking advantage of the future input and output values. A linear or linearized dynamical model of the slave robot (a single-input single-output plant) is required to estimate the future outputs. Specifically, a multi-DOF nonlinear robot dynamics can be linearized by taking into consideration the fact that the robot moves around a setpoint in a considered task. A controlled auto-regressive integrated moving average (CARIMA) model is used to describe the slave robot dynamics

$$A(z^{-1})x_s(t) = z^{-D}B(z^{-1})u(t - \Delta t) + C(z^{-1})\frac{e(t)}{\Delta}, \text{ with } \Delta = 1 - z^{-1} \tag{5.10}$$

In the above, $u(t)$ and $x_s(t)$ are the control and output sequences of the slave robot and $e(t)$ is a zero-mean white noise. In addition, D is the dead time of the system, and A, B, and C are three polynomials of orders n_a, n_b and n_c in the backward shift operator z^{-1}, respectively

$$A(z^{-1}) = 1 + a_1 z^{-1} + a_2 z^{-2} + \cdots + a_{n_a} z^{-n_a}$$

$$B(z^{-1}) = b_0 + b_1 z^{-1} + b_2 z^{-2} + \cdots + b_{n_b} z^{-n_b}$$

$$C(z^{-1}) = 1 + c_1 z^{-1} + c_2 z^{-2} + \cdots + c_{n_c} z^{-n_c} \tag{5.11}$$

For simplicity, $C(z^{-1})$ is chosen to be 1 for the consideration of white noise case. The cost function needs to be minimized is given by

$$J(N_1, N_2, N_u) = \sum_{k=N_1}^{N_2} \delta(k)[\hat{x}_s(t + k\Delta t|t) - \omega(t + k\Delta t)]^2 + \sum_{k=1}^{N_u} \lambda(k)[\Delta u(t + (k-1)\Delta t)]^2$$

$$\tag{5.12}$$

where $\hat{x}_s(t + k\Delta t|t)$ is a k step ahead prediction of the system output, $\omega(t + k\Delta t)$ is the future reference trajectory for the system, and $\Delta u(t + (k-1)\Delta t)$ is the change of the control signal. In the above, N_1 and N_2 are the minima and maximum prediction horizons, and N_u is the control horizon. Also, $\delta(k)$ and $\lambda(k)$ are two weighting factors.

The goal of this cost function is to drive the future system output $\hat{x}_s(t + k\Delta t|t)$ close to the reference value $\omega(t + k\Delta t)$ and meanwhile to minimize the change of the control signal $\Delta u(t + (k-1)\Delta t)$. Note that $\omega(t + k\Delta t)$ is approximated from the current system output $x_s(t)$ towards the known reference $x_r(t + k\Delta t)$ by means of the first-order system

$$\omega(t) = x_s(t),$$

$$\omega(t + k\Delta t) = \alpha\omega(t + (k-1)\Delta t) + (1 - \alpha)x_r(t + k\Delta t), \, k \in (1, 2, \cdots, (N_1 - N_2 + 1)) \tag{5.13}$$

where $x_r = x_e + x_m$. Here, $x_e(t + k\Delta t)$ can be obtained from the predicted heart motion by EKF. Note that $x_m(t + k\Delta t)$ is approximately equal to $x_m(t)$ by assuming the human operator moves very slowly.

To estimate the future system output $\hat{x}_s(t + k\Delta t|t)$, the following Diophantine equation is considered:

$$1 = E_k(z^{-1})\Delta A(z^{-1}) + z^{-k}F_k(z^{-1}) \tag{5.14}$$

Here, E_k and F_k are two unique polynomials of orders $k - 1$ and n_a, respectively.

Multiplying (5.11) by $\Delta E_k(z^{-1})z^k$ and considering (5.14), it can be obtained that

$$x_s(t + k\Delta t) = E_k(z^{-1})B(z^{-1})\Delta u(t + (k - d - 1)\Delta t) + F_k(z^{-1}) x_s(t) + E_k(z^{-1}) e(t + k\Delta t) \tag{5.15}$$

As the degree of E_k is $k - 1$, the noise terms $E_k(z^{-1}) e(t + k\Delta t)$ are all in the future. Assuming their values are zero, the future system output $\hat{x}_s(t + k\Delta t|t)$ can be obtained as

$$\hat{x}_s(t + k\Delta t|t) = G_k(z^{-1})\Delta u(t + (k - d - 1)\Delta t) + F_k(z^{-1}) x_s(t) \tag{5.16}$$

where $G_k = E_k B = g_0 + g_1 z^{-1} + \cdots + g_k z^{-(n_b + k - 1)}$.

The prediction of $\sum_{k = N_1}^{N_2} \hat{x}_s(t + k\Delta t|t)$ can be obtained by considering

$$\mathbf{x}_s = \underbrace{\mathbf{F}(z^{-1})y(t) + \mathbf{G'}(z^{-1})\Delta u(t - \Delta t)}_{\text{past}} + \underbrace{\mathbf{Gu}}_{\text{future}} = \underbrace{\mathbf{f}}_{\text{past}} + \underbrace{\mathbf{Gu}}_{\text{future}} \tag{5.17}$$

where $\mathbf{x}_s = \begin{bmatrix} \hat{x}_s(t + N_1\Delta t) \\ \hat{x}_s(t + (N_1 + 1)\Delta t) \\ \vdots \\ \hat{x}_s(t + N_2\Delta t) \end{bmatrix}$, $\mathbf{F}(z^{-1}) = \begin{bmatrix} F_{N_1}(z^{-1}) \\ F_{N_1+1}(z^{-1}) \\ \vdots \\ F_{N_2}(z^{-1}) \end{bmatrix}$,

$$\mathbf{G'}(z^{-1}) = \begin{bmatrix} (G_{N_1}(z^{-1}) - g_0)z \\ (G_{N_1+1}(z^{-1}) - g_0 - g_1 z^{-1})z^2 \\ \vdots \\ (G_{N_2}(z^{-1}) - g_0 - g_1 z^{-1} - \cdots - g_{N_2-N_1} z^{-(N_2-N_1)})z^{N_2-N_1+1} \end{bmatrix},$$

$$\mathbf{G} = \begin{bmatrix} g_0 & 0 & \cdots & 0 \\ g_1 & g_0 & \cdots & 0 \\ \vdots & \vdots & \ddots & \vdots \\ g_{N_2-N_1} & g_{N_2-N_1-1} & \cdots & g_0 \end{bmatrix}, \quad \mathbf{u} = \begin{bmatrix} \Delta u(t) \\ \Delta u(t+\Delta t) \\ \vdots \\ \Delta u(t+(N_2-N_1)\Delta t) \end{bmatrix}.$$

The cost function can be written as

$$J = (\mathbf{f} + \mathbf{G}\mathbf{u} - \boldsymbol{\omega})^{\mathrm{T}}(\mathbf{f} + \mathbf{G}\mathbf{u} - \boldsymbol{\omega}) + \lambda \mathbf{u}^{\mathrm{T}}\mathbf{u} \qquad (5.18)$$

where $\boldsymbol{\omega} = \begin{bmatrix} \omega(t+N_1\Delta t) \\ \omega(t+(N_1+1)\Delta t) \\ \vdots \\ \omega(t+N_2\Delta t) \end{bmatrix}$.

By minimize (5.18), $\Delta u(t)$ can be calculated

$$\Delta u(t) = \mathbf{K}(\boldsymbol{\omega} - \mathbf{f}) \qquad (5.19)$$

where $\mathbf{K}$ is the first row of matrix $(\mathbf{G}^{\mathrm{T}}\mathbf{G} + \lambda\mathbf{I})^{-1}\mathbf{G}^{\mathrm{T}}$.

5.3 Master Robot: Non-oscillatory Force Feedback

The reference impedance model for the master robot is designed the same as shown in (3.1). Its parameters are chosen the same as those listed in the second column of Table 3.1. For the sake of brevity, the uncertainties of the system dynamics are not considered here. A detailed nonlinear robust adaptive impedance controller used for parametric and non-parametric uncertainties of the system is presented in [94]. In the chapter, a PID controller is used to guarantee the position of the master robot x_m to follow the reference trajectory x_{ref_m}. The PID controllers for the master robot

of $K_{\mathrm{p}_m} = 1000$, $K_{\mathrm{i}_m} = 200$, $K_{\mathrm{d}_m} = 1$ and for the slave robot of $K_{\mathrm{p}_s} = 1000$, $K_{\mathrm{i}_s} = 0$, $K_{\mathrm{d}_s} = 20$ are used to guarantee the robot positions follow their corresponding desired trajectories.

5.4 Experiments

5.4.1 Experimental setup

The experimental setup employs a Phantom Premium 1.5A robot (Geomagic Inc., Wilmington, MA, USA) as the master robot and a Quanser robot (Quanser Consulting Inc., Markham, ON, Canada) as the slave robot (Figure 5.5). To measure the applied interaction forces of the human operator and the heart tissue, the master and slave robots are respectively equipped with a 50M31 force/torque sensor (JR3 Inc., Woodland, CA, USA) and a Gamma force/torque sensor (ATI Industrial Automation, Apex, NC, USA).

A 6MHz 4dl14-5/38 linear 4D transducer connected to a SonixTouch US scanner (SonixTouch from Ultrasonix, Richmond, BC, Canada) is used as the image sensor to detect the positions of the surgical tool and the simulated heart, both of which are submerged in a water tank to represent the presence of blood inside the heart chamber. The US scanner has a low frame rate of 25 Hz. The depth of the images was 5.5 cm. The 2D US images were collected from the US scanner using a DVI2USB 3.0 frame grabber (Epiphan, Ottawa, ON, Canada). The entire image acquisition, transmission, and processing delay is 180 ms.

The heart tissue is simulated by an artificial plastisol-based tissue made of soft plastic that is visible under US. This tissue is attached to a custom-built mechanical cam which produces a peak-to-peak amplitude of 9 mm and has a fundamental frequency of 64 bpm to simulate the beating-heart motion which temporally matched to an ECG signal (Bowthorpe et al. 2014a). To verify the automated heart tissue tracking results, real-time position measurement of the beating-heart simulator was collected from a potentiometer (LP-75FP-5K from Midori America Corp., Fullerton, CA, USA). The system was controlled to perform at 1000 Hz under US guidance with the help of the interpolation algorithm.
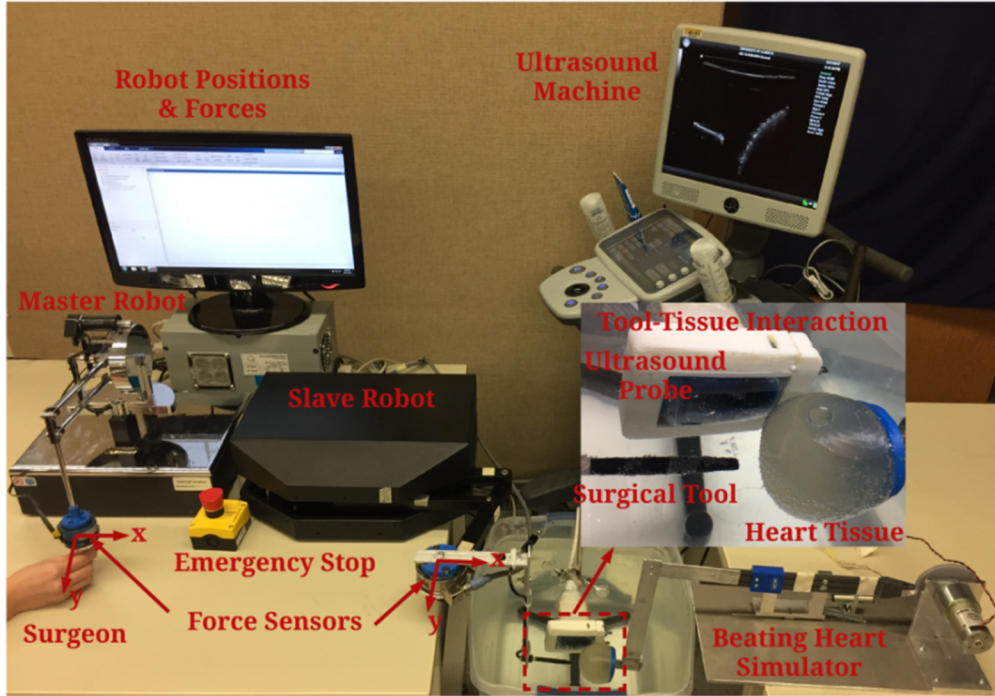
Figure 5.5. Experimental setup.

To implement the GPC system, as the heart motion is simplified to be 1 DOF, only the dynamics of the slave joints that are responsible for the translation of the surgical tool along its axis (*x*-axis) are considered. A simplified transfer function model for the slave robot along the *x*-axis is identified using Matlab®. The slave robot's transfer function between the input force and the output position along *x*-axis can be expressed as

$$\frac{x}{F}(z^{-1})=z^{-D}\frac{4.09+16.01z^{-1}+3.977z^{-2}}{1-1.974z^{-1}+0.974z^{-2}}\times10^{-4} \tag{5.21}$$

Considering the system was controlled to perform at 1 KHz, the effect of discretization on the slave robot controller performance is too small to be ignored. The parameters used in the above algorithms and controllers which were obtained by trial and error during the experiments are shown in Table 5.1.

Table 5.1. Experimental Parameters

Algorithms	Parameters Information		
	Symbol	*Definition*	*Value*
EKF	m	Harmonics number of heart motion	8
	$\mathbf{Q}$	Process noise covariance matrix	$\mathrm{diag}[0.0001_{1\times(2m+2)}]$
	R	Measurement noise covariance	0.01
	$\mathbf{P}(t_0\vert t_0)$	Initial estimate covariance matrix	$\mathrm{diag}[0.001,\frac{0.1}{1},\frac{0.1}{2},\cdots,$ $\frac{0.1}{m}, 0.1, 0.2_{1\times m}]$
GPC	$\lambda(k)$	Weighting factor	0.00003
	$\delta(k)$	Weighting factor	1
	D	Dead time	2
	N_1	Minimum prediction horizon	3
	N_2	Maximum prediction horizon	7
	N_u	Control horizon	5
Imp. model	ω_{n_m}	Natural frequency of impedance model	0.5 rad/sec
	k_m	Stiffness	4 N/m
	m_m	Mass	16 kg
	c_m	Damping	11.2 Ns/m
	k_f	Force scaling factor	1
PID	K_p	Proportional coefficient	1000
	K_i	Integral coefficient	200
	K_d	Derivative coefficient	1

5.4.2 Experimental results

The surgical tasks in the experiments are that human operator teleoperated a slave robot to get close to, make contact with, and break contact with the simulated beating heart tissue. To verify the advantages of the proposed method compared with conventional methods, the surgical task was implemented using three methods, respectively. The first method uses a regular DFR teleoperation controller without automatic motion compensation (AMC) [95]. This method reflects the entire slave-heart interaction force to the human operator and requires the human operator to perform motion compensation manually. The second method added AMC to the first method; thus,

the force reflected to the human operator contains an oscillatory portion. The last method is the proposed strategy, which has both motion compensation and non-oscillatory force feedback.

Figure 5.6 shows the actual master and slave positions and forces in the *x*-direction for the DFR teleoperation system without AMC. As seen in Figure 5.6, the slave robot tracks both the position and force of the master robot during the entire operation. However, the tracking of the beating heart motion is poor as the human operator must manually compensate for the heart motion. It is very difficult for the human operator to control the oscillatory motion of the slave robot from the master site quickly enough to match the beating heart motion. Moreover, the oscillatory human-master interaction force suggests that the human operator receives unsteady haptic feedback, which makes it more challenging to synchronize the motion of the slave robot along with the beating heart motion.
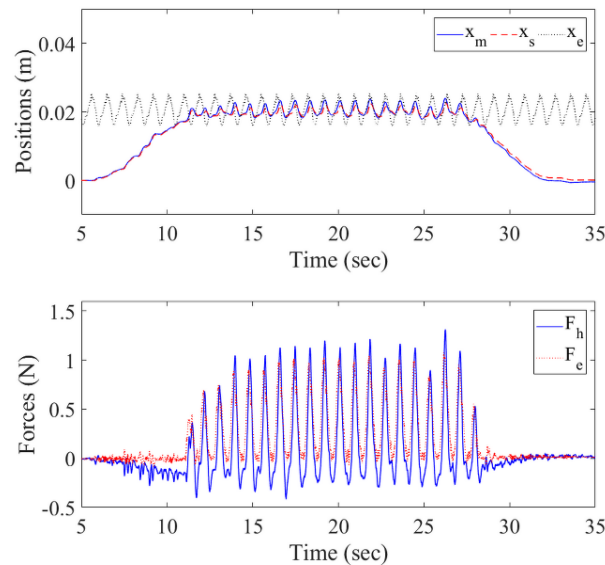
Figure 5.6. Position and force results for the DFR teleoperation system without AMC. In the upper position figure, the blue solid line is the position of the master robot/human operator, the red dashed line is the position of the slave robot, and the gray dotted line is the position of the heart. In the below force figure, the blue solid line is the human-master interaction force, and the red dotted line is the slave-tissue interaction force.

105

Figure 5.7 illustrates the positions and forces for the DFR teleoperation system with AMC. In this case, the slave robot is controlled to track the combined trajectory of the master robot and the heart using the proposed slave robot control scheme in Section 5.2. As the motion compensation is automatically achieved through the control scheme, the human operator only needs to maneuver the master robot to control the slave robot towards the heart tissue. The position tracking result is much better in this case than that in the first case. Nevertheless, the haptic feedback to the human operator is still oscillatory. Meanwhile, an oscillatory motion with small amplitude remains in the master robot position due to the poor quality of haptic feedback.
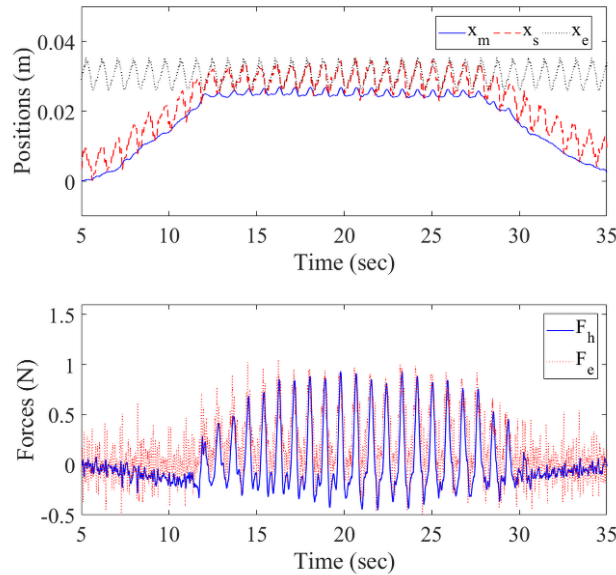
Figure 5.7. Position and force results for the DFR teleoperation system with AMC. In the upper position figure, the blue solid line is the position of the master robot/human operator, the red dashed line is the position of the slave robot, and the gray dotted line is the position of the heart. In the below force figure, the blue solid line is the human-master interaction force, and the red dotted line is the slave-tissue interaction force.

Using the proposed control schemes for both the master and slave robots, the results of the positions and forces are shown in Figure 5.8. As seen in Figure 5.8, the slave robot tracks the

summed position of the human operator and the beating heart, and the position tracking result is significantly better than that in the first method. In addition, both the position and force of the master robot are much steadier as the oscillatory portions have been filtered using the proposed impedance model for the master robot. In this case, the human operator is able to operate on a beating heart without manual compensation, and at the same time, have a sense of operation on a seemingly idle heart.
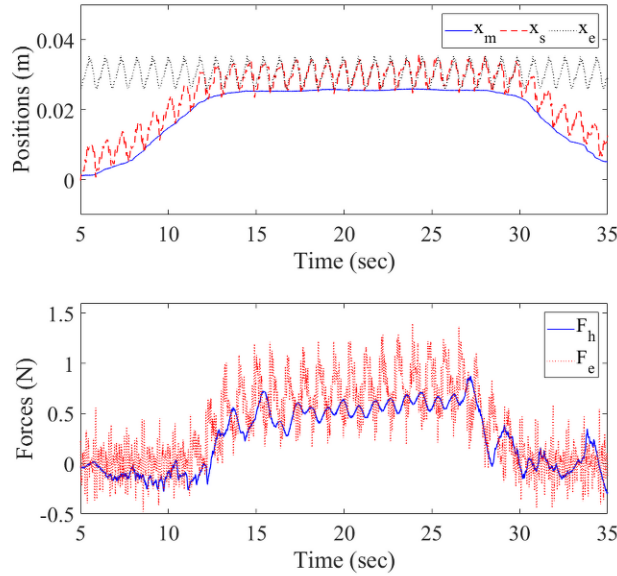
Figure 5.8. Position and force results for the proposed teleoperation system. In the upper position figure, the blue solid line is the position of the master robot/human operator, the red dashed line is the position of the slave robot, and the gray dotted line is the position of the heart. In the below force figure, the blue solid line is the human-master interaction force, and the red dotted line is the slave-tissue interaction force.

In this chapter, as the purpose of it is to show the feasibility of the proposed method, three different cases are considered to present their results and discussions. In the future research, more experimental results may be presented by altering different beating rates, tissue stiffness, and impedance adjustment to show the relationships among them.

107

5.5 Concluding Remarks

An US image-based position controller for the slave robot and an impedance controller for the master robot are proposed for a telerobotic beating-heart surgical system to simultaneously achieve motion compensation for the slave robot and non-oscillatory haptic feedback on the master robot. The validity of the proposed method was implemented through experiments, which demonstrated that the presented method could be used in teleoperation beating heart surgeries and achieve safer and accuracy performance. Future work will involve exploring the system's use in actual beating heart procedures.

Chapter 6

Neural Network-based Physiological Organ Motion Prediction

In this chapter[5], a neural network (NN)-based heart motion prediction method is proposed for US-guided beating-heart surgery to compensate for time delays caused by US image acquisition and processing. Such image processing is needed for tracking heart tissue in US images, which is itself a requirement for beating-heart surgery. In Section 6.2, a NN-based heart motion predictor is presented. Specifically, once the heart tissue is tracked in US images, a recurrent neural network (RNN) is employed to learn how to predict the motion of the tracked heart motion in order to compensate for the delays introduced in the initial US image processing step. To verify the feasibility of predicting both simple and complex heart motions, the NN is tested with two types of heart motion data: (a) fixed heart rate and maximum amplitude, and (b) varying heart rate and maximum amplitude. Also, the NN was tested with different prediction horizons and showed effectiveness for both small and large delays. The heart motion prediction results using NN are

---

[5]Portions of this chapter were published in "L. Cheng and M. Tavakoli, "Neural-Network-Based Heart Motion Prediction for Ultrasound-Guided Beating-Heart Surgery," *IEEE 15th International Conference on Automation Science and Engineering*, Vancouver, Canada, 2019." [18] and in "L. Cheng and M. Tavakoli, "Neural Network-based Physiological Organ Motion Prediction and Robot Impedance Control for Teleoperated Beating-Heart Surgery," *Journal of Medical Robotics Research*, 2019, in preparation."

compared to the results using an EKF algorithm. Using NN, the mean absolute error and the root mean squared error between the predicted and the tracked heart motions are roughly 60% smaller than those achieved by using the EKF. Moreover, the NN can predict the heart position up to 1000 ms in advance, which significantly exceeds the typical US image acquisition/processing delays for this application (160 ms in our tests). Overall, the NN predictor shows significant advantages (higher accuracy and longer prediction horizon) compared to the EKF predictor. In Section 6.4, the NN-based heart motion predictor is combined with the robotic impedance control, which is similar to the control strategy for a teleoperation system presented in Chapter 5, to achieve the desired objectives for beating-heart surgery.

6.1 Introduction

As discussed in Chapter 5, the position of a POI on the heart can be obtained from US images [42], [96] and be used to control on the surgical robot so that it follows the motion of the heart. However, the time delay caused by US image acquisition and processing is non-negligible and has to be compensated for. Otherwise, the position control loop of the surgical robot will not be able to make the robot's motions synchronized to the heart motions; instead, the robot will follow the delayed heart motions, which creates the risk of the surgical robot puncturing the heart due to a collision.

To compensate for the time delay, the delayed POI position should be predicted. Such a heart motion prediction is a problem of time series forecasting, which requires a model to predict future values of the time series based on its present and previously observed values. Various methods have been proposed to solve time series forecasting problems such as Kalman filtering, weighted moving average, and exponential smoothing. As the heart motion is quasi-periodic, in Chapter 5, an EKF was used for motion prediction. To improve the prediction accuracy, in this chapter, a NN-based heart motion prediction method is proposed. It has been demonstrated that a NN model can approximate any continuous function and it has been successfully used for forecasting of many time series in many applications [97]–[100]. Also, NN has the advantage that it can approximate nonlinear functions without any prior information of the data series, which makes it suitable for application of quasi-periodic beating-heart motion prediction.

Much of the past work [100]–[102] on using NN to predict an organ's physiological motion has focused on radiotherapy and the prediction of tumor motion under respiration. For image-guided radiotherapy applications, diagnostic X-ray imaging was used to detect the markers on the tumor. Different from these works, in this chapter, US imaging is used to obtain the POI position and no markers are implanted on the surface of the heart to reduce the harm to the human body and increase the observation accuracy of the POI position.

For the NN model, there are different architectures that can be chosen such as feedforward NN and recurrent NN (RNN) for the time series forecasting problems. The main difference between the feedforward and RNNs is the presence of feedback loops in the latter network. The presence of feedback loops in the RNN has a profound positive impact on the learning capability and on the prediction performance. Therefore, an RNN is used in the chapter. To verify its ability to predict heart motion data, two types of datasets are acquired: (a) fixed heart rate and maximum amplitude, and (b) varying heart rate and maximum amplitude. Also, different prediction horizons are tested.

A schematic of the steps of the NN-based heart motion predictor is shown in Figure 6.1. A US machine acquires images of a beating heart and a surgical instrument and passes the image sequences to the image processing algorithms to capture the POI position. The heart tissue position data is then fed to an RNN for training it to predict the heart motion. The last step involves evaluating the performance of the NN.

The trained RNN is able to predict the real-time POI positions $\mathbf{x}_e$. The summed position of the master robot $\mathbf{x}_m$ and POI $\mathbf{x}_e$ is transmitted to the slave robot as a reference signal $\mathbf{x}_r(= \mathbf{x}_m + \mathbf{x}_e)$ as shown in Figure 5.2. The main difference between this chapter and the last chapter is the heart motion predictor. The rests of the control strategy for a teleoperation system in beating-heart surgery are the same. A more detailed description of the teleoperation system control strategy can be referred to Section 5.1.
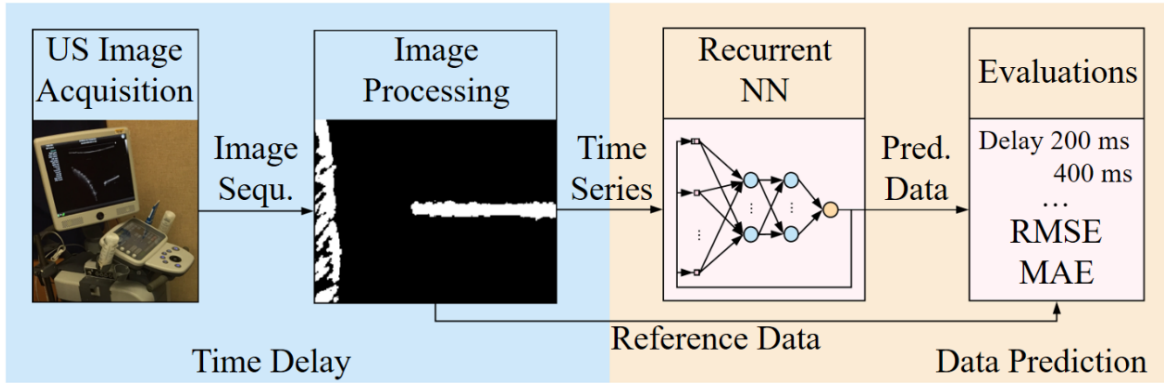
Figure 6.1. A schematic of the proposed steps for heart motion prediction.

To the best knowledge of the authors, this is the first research on using RNN to predict POI position for US image-guided beating-heart surgery. The rest of this chapter is organized as follows. Section 6.2 introduces the approach for POI motion tracking in US images and presents the NN based motion prediction method. Section 6.3 shows the results of using the NN algorithm and compares them to those of using the EKF algorithm. Section 6.4 presents the experimental results by combining the NN heart motion predictor and robot impedance control. Section 6.5 concludes the chapter.

6.2 Neural Network-based Heart Motion Predictor

The time series of beating-heart motion data can be obtained through the acquisition and processing of a sequence of US images showing the beating heart. As discussed later, the position of the POI on the beating heart is defined as the heart position along the surgical instrument's axis, and it can be calculated through feature extraction algorithms. When the surgical instrument is kept still, the POI position can be acquired directly from the measured tool-heart distance along the surgical tool's axis. To minimize the image processing time, the acquired POI position is predicted first using NN. The predicted POI position then is upsampled using cubic interpolation.

6.2.1 Heart motion tracking

The US image sequences are acquired through a 6MHz 4dl14-5/38 linear 4D transducer connected to a SonixTouch US scanner (SonixTouch from Ultrasonix, Richmond, BC, Canada) (Figure 6.2). The 2D US images are collected from the US scanner using a DVI2USB 3.0 frame grabber (Epiphan, Ottawa, ON, Canada). The frame rate of the US scanner is 25 Hz. A one-degree-of-freedom custom-built mechanical cam and a voice coil actuator (NCC20-18-020-1X from H2W Technologies Inc., Santa Clarita, CA, USA) are used to simulate the beating heart's motion. The heart simulator can produce motion signals, which temporally matched to an ECG signal [24], with a peak-to-peak amplitude of 9 mm. At the tip of the heart simulator, an artificial plastisol-based tissue is mounted on to simulate the heart tissue. A straight and rigid tool is used as the surgical instrument. Both the plastic tissue and the rigid tool are submerged in a water tank to simulate the heart's blood pool and guarantee that they are visible under the US. The depth of the US images is 5.5 cm.

To capture the heart motion data, each US image frame is first converted to a binary image by choosing a threshold of 0.3. Then, a 3×3 Sobel edge detection [90] and a Hough transform [91] are used to obtain, respectively, the edge points and the longest line (as the detected surgical tool). The extension of the longest line intersects the edge of the heart tissue, and the intersection point is considered as the POI (Figure 6.3).
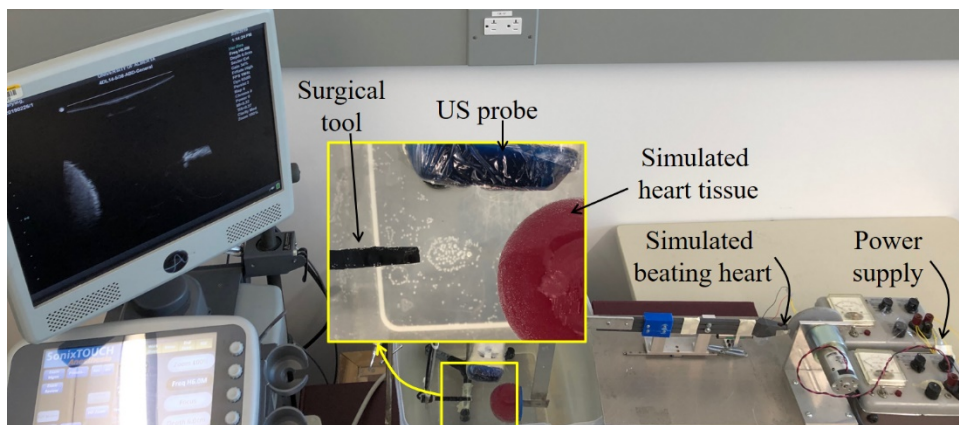
Figure 6.2. The experimental setup for US image acquisition.
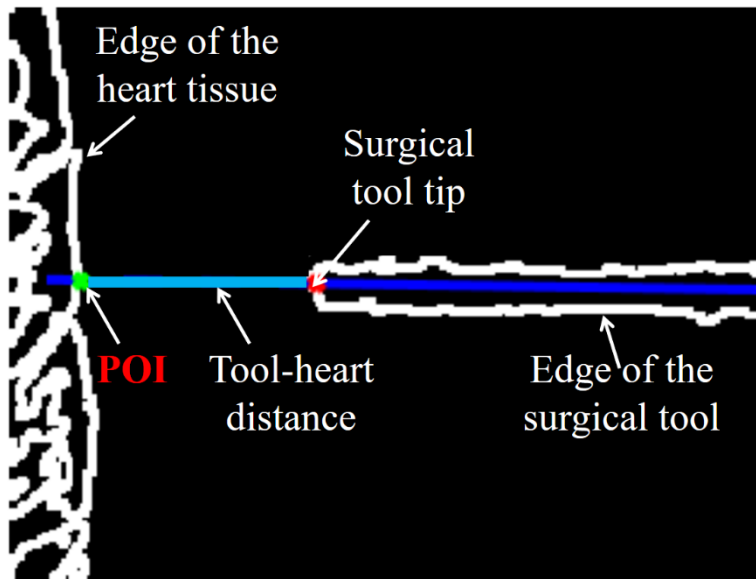
Figure 6.3. The detected tooltip, POI, and tool-heart distance.

The tracked POI position in the image frame is converted to the world coordinate by converting it from pixels into mm, and the time series of the POI position is obtained (Figure 6.4a). To compare the tracked POI position data with the simulated heart's directly measurable position, a potentiometer (LP-75FP-5K from Midori America Corp., Fullerton, CA, USA) is used to collect and record the real-time position of the beating-heart simulator. The mean absolute error between the tracked data and the directly measured data of a 1000 s-long data is 0.5697 mm, which is 0.0633 of the peak-to-peak amplitude of the heart motion and is sufficiently small.

Five US image sequences each ~ 1000 s long are recorded for the training and test of the NN. The corresponding time series of the tracked POI position data are labelled as dataset 1-5. These data are approximately periodic as the simulated heart keeps creating the same motions, which means the fundamental frequency ($f_1 = 1.12$ Hz) and the maximum amplitude of the motions are fixed (Figure 6.4b).

To further simulate more realistic and complex heart motion, the voltage applied to the voice coil actuator of the simulated heart, which is responsible for creates the back-and -forth motion, is changed. Also, the maximum amplitude of the simulated heart motion is changed by using springs of different stiffnesses in the heat simulator, thus changing how closely the simulator's end point follows the motions of the rotating cam. Five similar 1000 s long US image sequences are recorded and the time series of the acquired POI position data are labelled as dataset 6-10. The power spectral density (PSD) of the POI position data show that the dominant peaks are $f_{21} = 0.8214$, $f_{22} = 1.123$, and $f_{23} = 1.310$ Hz (Figure 6.4b).

To implement the NN, the acquired ten POI position datasets will be split into training and out-of-sampling test subsets, separately. Specifically, the first 75% of each dataset is used for training and the left is reserved for testing.

(a)   (b)
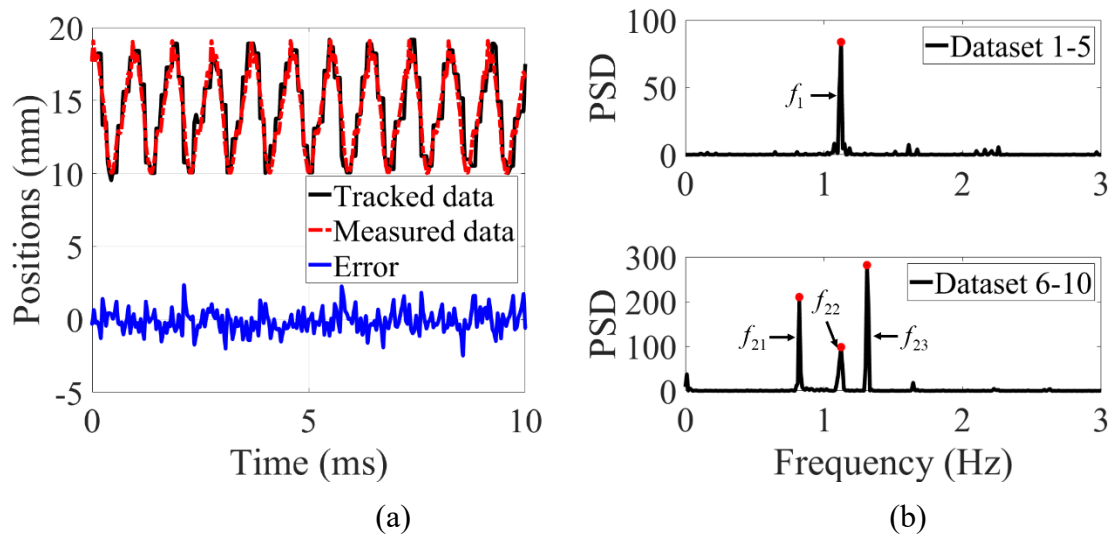
Figure 6.4. Heart position. (a) Time series of the tracked and directly measured POI position with fixed heart rate and amplitude. (b) The PSDs of the tracked POI position captured from two types of US image sequences.

6.2.2 RNN

For training the NN that will predict the heart motion, the tracked heart motion $x(n)$ serves both as the input and the output or the observation (albeit with the difference that the former is delayed with respect to the latter). The prediction problem can, therefore, be described as given an input vector $\mathbf{x}(n)$, the NN model must capture the underlying dynamics responsible for generating $x(n+1)$ as shown in Figure 6.5. For multiple-step ahead prediction of $x(n)$, namely, to predict $x(n+D)$, where D is the delay length that needs to be compensated for, a closed-loop nonlinear autoregressive (NAR) network is employed as discussed later.
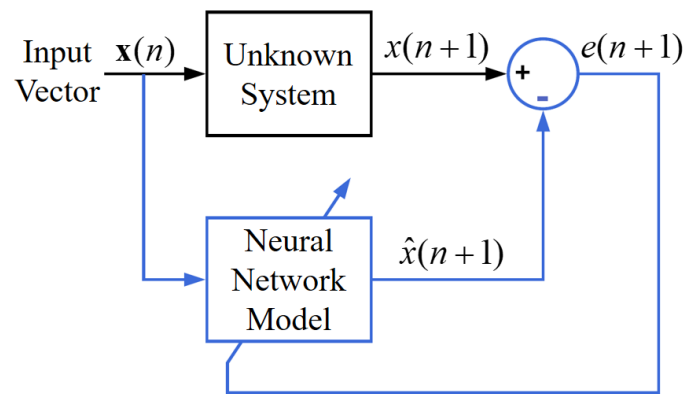
Figure 6.5. Block diagram of time series prediction using the NN model.

An RNN is a class of NN where connections between units form a directed cycle. In other words, it has at least one feedback loop. The advantage of an RNN is it can use its internal memory to process sequences of inputs. In this chapter, as the problem is to predict the quasi-periodic heart motion $x(n)$ which is a time series given the present and past values of $x(n)$, there is no external input to the network, a NAR network, therefore, is appropriate to learn and implement the recursive prediction of heart motion.

The architecture layout of a NAR is shown in Figure 6.6, which employs a generic RNN that follows naturally from a static multilayer perceptron (MLP) with two hidden layers. The NAR

model has a single output that is fed back to the input layer of the MLP via a tapped-delay-line memory of q units. The output is denoted by $x(n+1)$. The signal vector $\mathbf{x}(n)$ applied to the input layer of the MLP consists of the delayed values of the output, namely, $x(n)$, $x(n-1)$, ..., $x(n-q+1)$. The dynamic behavior of the NAR model is described by

$$x(n+1) = F(x(n), x(n-1), \ldots, x(n-q+1)) \tag{6.1}$$

where F is a nonlinear function of its arguments. The MLP is used to approximate the function F. The dimension and values of the input vector $\mathbf{x}(n)$ should be determined, which are described in the next section. In Figure 6.6, each circle represents a neuron. The model of each neuron in the 1st, 2nd, and output layers can be expressed as

$$y_j^1(n+1) = \varphi\left(b_j^1(n+1) + \boldsymbol{\omega}_j^1(n+1)\mathbf{x}(n)\right) \tag{6.2a}$$

$$y_k^2(n+1) = \varphi\left(b_k^2(n+1) + \boldsymbol{\omega}_k^2(n+1)\mathbf{y}^1(n+1)\right) \tag{6.2b}$$

$$\hat{x}(n+1) = \varphi(b^o(n+1) + \boldsymbol{\omega}^o(n+1)\mathbf{y}^2(n+1)) \tag{6.2c}$$

where $\varphi(v)$ is a nonlinear activation function. Here, a logistic function given by $\varphi(v) = \frac{1}{1+\exp(-av)}$ is used. Value a is an adjustable positive parameter. Also, $\boldsymbol{\omega}_j^1(n+1)$ and $b_j^1(n+1)$ are the weight vector and bias for the jth hidden node in the 1st layer, $\boldsymbol{\omega}_k^2(n+1)$ and $b_k^2(n+1)$ are the weight vector and bias for the kth hidden node in the 2nd layer, and $\boldsymbol{\omega}^o(n+1)$ and $b^o(n+1)$ are the weight vector and bias for the node in the output layer. Vector $\mathbf{y}^1(n+1)$ consists of all node outputs in the first layer (i.e. $y_j^1(n+1)$, $j = 1, 2, \ldots, J$), and $\mathbf{y}^2(n+1)$ consists of all node outputs in the second layer (i.e. $y_k^2(n+1)$, $k = 1, 2, \ldots, K$).

The error between the predicted time series $\hat{x}(n+1)$ and the expected time series $x(n+1)$ will be used for backward computation. The Levenberg-Marquardt backpropagation (LM BP) algorithm is employed as the training function to attain the fastest backpropagation performance.

117

The NAR network is trained to model the unknown system by using an open-loop NAR configuration. The trained network then is then switched to a closed-loop NAR configuration for multi-step-ahead prediction so that various delays can be implemented. By using the closed-loop mode, the NN can continue to predict by using internal feedback and simulate for as many predictions into the future as are desired.
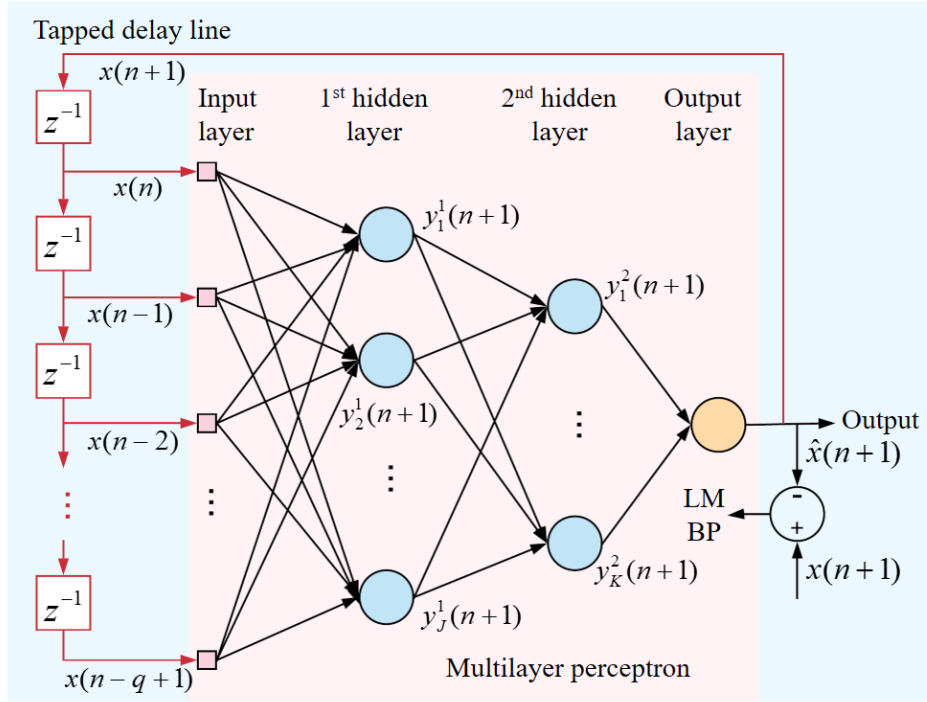
Figure 6.6. Architectural graph of a NAR network.

To identify the mapping that provides the NAR model, dynamic reconstruction is needed. A fundamental result in dynamic reconstruction theory is the delay embedding theorem developed by Takens [103], which shows that dynamic reconstruction is possible using the m-dimensional vector $\mathbf{x}(n)$ when given the observable $x(n+1)$. The vector $\mathbf{x}(n)$ is the input vector to the input layer and can be expressed as

$$x(n) = [x(n), x(n\text{-}d), \ldots, x(n\text{-}(m\text{-}1)d)]^{\mathrm{T}} \tag{6.3}$$

118

where m is the embedding dimension, and d is the normalized embedding delay.

To estimate the embedding dimension m, the method of false nearest neighbors [104] is used. By increasing m, the fraction of the false neighbors will reduce, and an appropriate embedding dimension can be determined. For the fixed and varying rate and amplitude data, the explored embedding dimensions are chosen to be 18 and 25, respectively.

The proper prescription for choosing d is to recognize that the normalized embedding delay should be large enough for $x(n)$ and $x(n\text{-}d)$ to be essentially independent of each other, but not so independent as to have no correlation with each other. This can be achieved by using the d for which the mutual information between $x(n)$ and $x(n\text{-}d)$ attains its first minimum [105]. The explored normalized embedding delays for fixed and varying rate and amplitude data are both selected to be 2.

Once the m and d are determined, the delayed inputs of the MLP $\mathbf{x}(n)$ can be determined. Each vector $\mathbf{x}(n)$ represents a point in the reconstructed state space which contains all necessary information to find the future points in the system's trajectory through state space.

To evaluate the prediction results, two evaluations are chosen [106]: root-mean-square error (RMSE) and mean absolute error (MAE), which are expressed as

$$\text{RMSE} = \sqrt{\frac{\sum_{i=1}^{N} \left(x(n_i) - \hat{x}(n_i)\right)^2}{N}} \tag{6.4a}$$

$$\text{MAE} = \frac{\sum_{i=1}^{N} |x(n_i) - \hat{x}(n_i)|}{N} \tag{6.4b}$$

where $x(n_i)$ is the desired output, $\hat{x}(n_i)$ is the actual prediction.

RMSE is a frequently used measure of the differences between values predicted by a model and the values observed; that is, it is a good measure of accuracy. MAE is well suited to compare prediction methods on a single series. Therefore, the RMSE will be used for the training data to

119

explore the NN parameters (i.e. hidden layers # and neurons # in each layer) of the NAR from 12 architecture forms (Table 6.1) by using fivefold cross-validation design. Then, both evaluations will be used for the testing data to evaluate the prediction results.

Table 6.1. Neuron Network Architecture Design

No.	Architecture	No.	Architecture	No.	Architecture
1	A-6-0-B	5	A-10-0-B	9	A-14-0-B
2	A-6-3-B	6	A-10-3-B	10	A-14-3-B
3	A-6-6-B	7	A-10-6-B	11	A-14-0-B
4	A-6-9-B	8	A-10-9-B	12	A-14-3-B

*The NN architecture form indicates the number of neurons in each layer. Here, A indicates the input number which is 18 for dataset 1-5 and 25 for dataset 6-10, and B indicates the output number which is 1.

6.2.3 The effect of the NN architecture

The aim of this study is to demonstrate the effect of the NN-based heart motion prediction algorithm. Two types of datasets (dataset 1-5: fixed heart rate and maximum amplitude, and dataset 6-10: varying heart rate and maximum amplitude) are acquired and tested. Various prediction horizons are tested to explore the prediction ability of the method. The designed NN algorithm is compared to the EKF algorithm to verify the effectiveness of the proposed method. Based on the design and methodology of the NAR network, for each architecture form, the RMSE across all five folds of cross-validation on each dataset is calculated and the mean and standard deviation across all ten datasets are presented in Figure 6.7. It is seen that with more complex NN architecture, the RMSE becomes smaller. Also, due to the increase of trainable parameters of the NN architecture, the computational capacity and the risk of overfitting increase. Considering this trade-off, the explored NN architectures for dataset 1-5 (Figure 6.7a) and dataset 6-10 (Figure 6.7b) are chosen to be 18-10-6-1 and 25-10-9-1, respectively. The summarized architecture layouts of the NAR for the two types of datasets are shown in Figure 6.8.
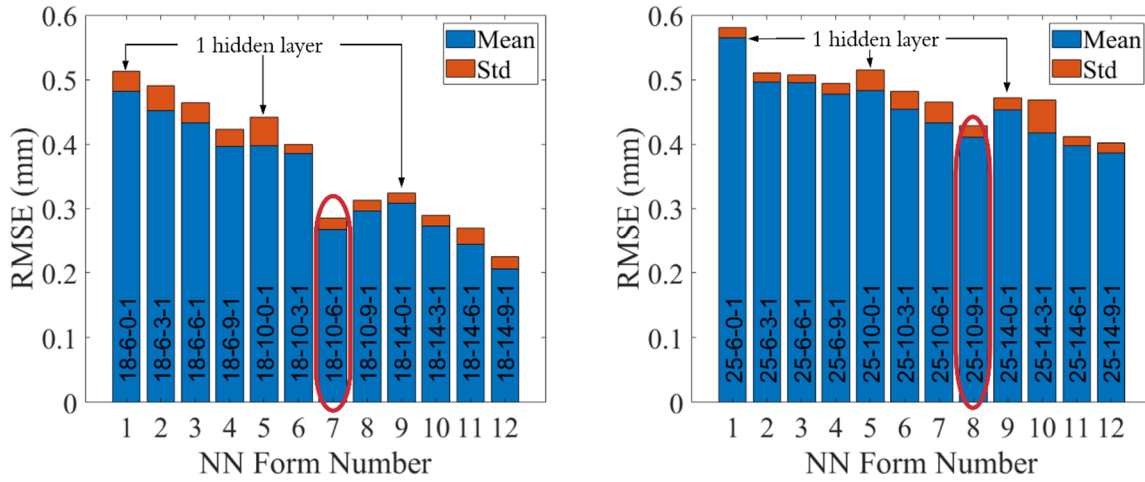
Figure 6.7. The RMSE results of the designed different NN architecture forms for (a) dataset 1-5 and (b) dataset 6-10.
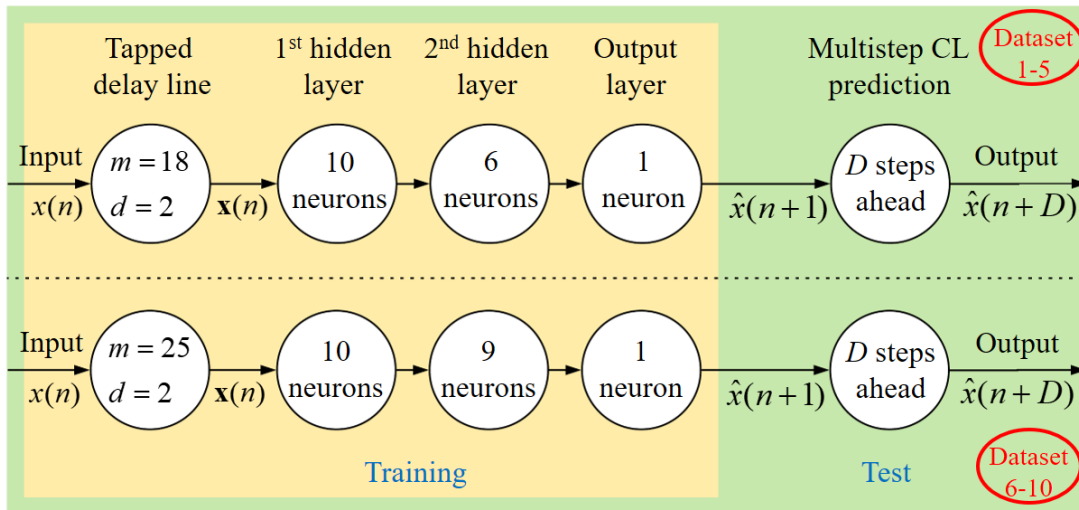
Figure 6.8. The architectural layout of the designed NAR network.

By changing the delay length D in Figure 6.8, various prediction horizons have tested. The time delay caused by US image acquisition and processing is approximately 160 ms [96]. As the frequency of the US machine is 25 Hz, the interval between two data points is 40 ms. Therefore, to compensate for a delay of 160 ms, 4 steps ahead should be predicted. In Figure 6.9, the NN-based prediction results of a ten-second fixed rate and maximum amplitude data are presented and compared to the actual tracked POI position data. The prediction results using an EKF algorithm [17] are also presented in Figure 6.9. The EKF takes advantage of the quasi-periodicity of the heart motion that is modeled as a time-varying Fourier series to compensate for the time delay. The EKF is tested with the same POI position data and compared to the results of the NN predictor. The reported errors between the predicted and the actual tracked POI position data in Figure 6.9 show that the NN prediction results are better than the EKF prediction results.

Furthermore, the NN and EKF predictors are tested for all datasets. The means and standard deviations of the two evaluations are listed in Table 6.2. For dataset 1-5, both MAE and RMSE using NN are lower than those of using EKF with reduction by 60%, while for dataset 6-10, the two evaluations using NN are roughly 70% less than those of using EKF.
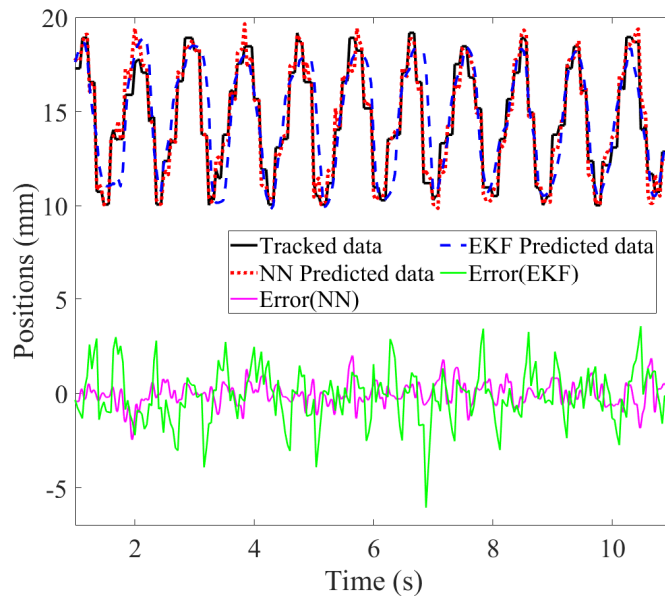
Figure 6.9. The heart motion prediction results with a time delay of 160 ms.

Table 6.2. Evaluations for a delay of 160 ms

Dataset	Algorithm	MAE (mm)	RMSE (mm)
1-5	NN	0.3757 ± 0.0536	0.5177 ± 0.0842
	EKF	0.9592 ± 0.0245	1.3442 ± 0.0346
6-10	NN	0.6305 ± 0.0440	0.7411 ± 0.0664
	EKF	1.9540 ± 0.1384	2.5871 ± 0.1176

To further explore the prediction performance of the two algorithms with respect to different datasets and time delays, the prediction horizon D is changed from 1 to 8 consecutively, which means the delay is changing from 40 ms to 320 ms with an interval of 40 ms. The means and standard deviations of MAE and RMSE for two types of datasets are shown in Figure 6.10. It is seen that the NN prediction has much lower errors compared to the EKF prediction, regardless of the types of the datasets, the evaluations, and the delayed time.

(a)   (b)
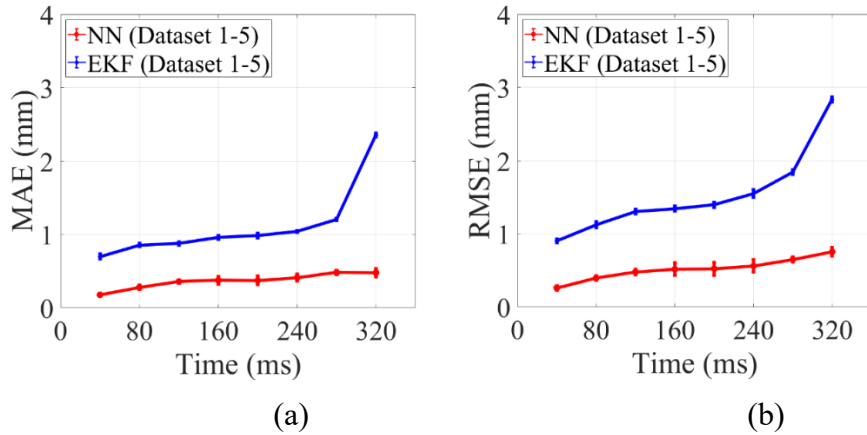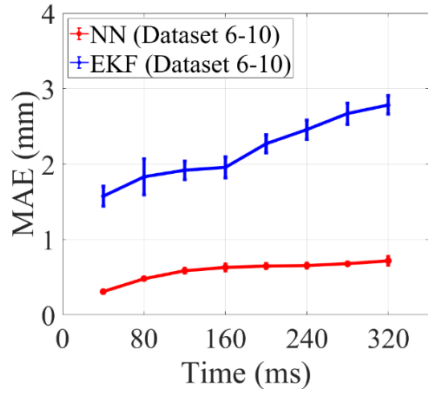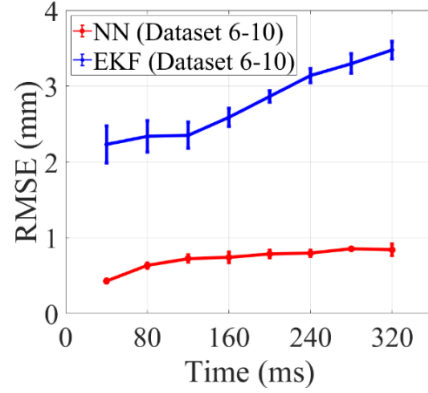
(c)   (d)

Figure 6.10. The MAE and RMSE in heart motion prediction for time delays that are changed from 40 ms to 320 ms with an interval of 40 ms, using NN and EKF. (a) and (b) are the MAE and RMSE for dataset 1-5, while (c) and (d) are the MAE and RMSE for dataset 6-10.
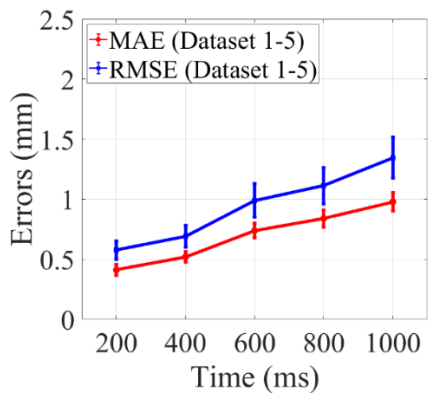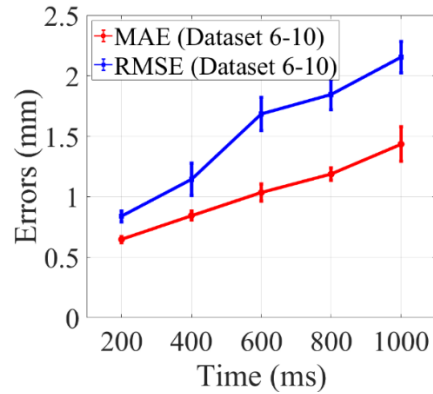
(a)   (b)

Figure 6.11. The MAE and RMSE in POI position prediction for (a) dataset 1-5 and (b) 6-10 for delays of 200, 400, 600, 800, and 1000 ms, using NN.

The NN algorithm is applied to both types of datasets to measure the prediction ability of the POI position up to 1000 ms in advance. Figure 6.11 shows the prediction performance using NN for time delays of 200, 400, 600, 800, and 1000 ms. Both MAE and RMSE increase as the

delayed time increases. The prediction for the varying rate and maximum amplitude datasets (dataset 6-10) has higher errors compared to those for the fixed rate and maximum amplitude datasets (dataset 1-5). For dataset 6-10, the prediction accuracy using NN for delay of 1000 ms is like that of using EKF for delay of 40 ms (Figure 6.10c and Figure 6.10d). This demonstrates that the NN algorithm presents significant advantages over the EKF algorithm such as higher accuracy and longer prediction horizon.

6.2.4 Data upsampling

The predicted heart position is then interpolated from its inherent measurement rate which is 25 Hz to the sampling rate of 1 kHz by using cubic interpolation. A detailed description about cubic interpolation is presented in Section 5.2.2.

6.3 Master Robot: Non-oscillatory Force Feedback

The reference impedance model for the master robot is designed as shown in (3.1). Its parameters are chosen the same as those listed in the second column of Table 3.1. The PID controllers for the master robot of $K_{p_m} = 1000$, $K_{i_m} = 200$, $K_{d_m} = 1$ and for the slave robot of $K_{p_s} = 1000$, $K_{i_s} = 0$, $K_{d_s} = 20$ are used to guarantee the robot positions follow their corresponding desired trajectories.

6.4 Experimental Results

The experimental setup employs the same robots, force sensors, US scanner, and heart simulator as shown in Section 5.4.1 (Figure 5.5) in order to compare the results to those presented in Section 5.4.2. This telerobotic system consists of a reference impedance model for the master robot and a heart motion predictor to provide heart position to the slave robot. To verify the advantage of the NN-based heart motion predictor, the comparative experiments consist of three groups: (a) teleoperation system with master impedance control and no heart motion predictor for the slave robot, (b) teleoperation system with master impedance control and EKF-based heart motion predictor for the slave robot, and (c) teleoperation system with master impedance control and NN-based heart motion predictor for the slave robot. In the experiments, the tested hypothesis is as

follows: Motion compensation and force feedback using a NN predictor are better than those using an EKF predictor or no predictor as the NN predictor has a higher accuracy and a longer prediction horizon compared to the EKF predictor or no predictor. The surgical tasks in the experiments are that human operator teleoperated a slave robot to get close to, make contact with, and break contact with the simulated beating heart tissue. During the contact, the human operator is conducted to stay still so that the slave robot can primarily synchronize with the beating heart's motion. The experiments are completed by one user (the thesis author) and repeated one time as the results are only used to verify the advantage of the NN-based heart motion predictor. As the teleoperation system was simple enough to not require trained surgeons for operating it, we only recruited the thesis author to conduct the experiments. To show the difference between the three groups of experiments, in the following, only the processes of contact are presented and calculated in the results. As discussed before, the contact duration is defined as the time when the slave-heart tissue interaction force is greater than 0.4 N.

Figure 6.12 shows the positions and forces of the three teleoperation systems for the master and slave. As seen in Figure 6.12a, a significant delay between the positions of the slave robot and the beating heart simulator is observed due to the US image acquisition and processing. By using EKF- and NN-based heart motion predictors in the teleoperation systems, this time delay is well compensated for (Figure 6.12b and Figure 6.12c). The position tracking performance of the developed system is evaluated by calculating the mean absolute synchronization error (MASE) in contact duration, $\text{MASE} = \frac{1}{n} \sum_{i=1}^{n} |e_i|$, where e_i is the position error between the surgical tool tip and its desired position when contact occurs, n is the samples number of contact duration. This position result is calculated and listed in Table 6.3. The MASEs using no heart motion predictor, EKF-based predictor, and NN-based predictor are 0.0045 mm, 0.0032 mm, and 0.0016 mm, respectively. It is clear that using a NN to predict the heart position gives the best result among the three strategies.

Additionally, in Figure 6.12, the forces of the master and slave robots during contact are shown. Because of the reference impedance model for the master robot, the force feedback

126

perceived by the human operator are all non-oscillatory regardless of the predictor type. However, the slave-tissue interaction forces are influenced by the accuracy of motion compensation. The average forces applied by the human operator on the master robot (AFM) and the average forces applied by the slave robot on the simulated heart (AFS) for three teleoperation systems are calculated and are presented in Table 6.3. The standard deviations of AFM for difference heart motion predictors are small which demonstrates that good non-oscillatory force feedback is achieved. The standard deviations of AFS for the three heart motion predictors are large due to the residual mismatch between the heart motion and the slave robot motion, and due to the internal inertia of the force sensor. However, despite that, the standard deviation of AFS for NN-based predictor is smaller than that for the other predictors as the higher motion compensation accuracy. In other words, the teleoperation system with NN-based heart motion predictor can achieve the best motion compensation performance and the smallest oscillator portion of the slave-tissue interaction force among the three experimental systems. These results have tested the hypothesis that the motion compensation and force feedback using a NN predictor performs better than using an EKF predictor or no predictor for teleoperation systems in beating-heart surgery.
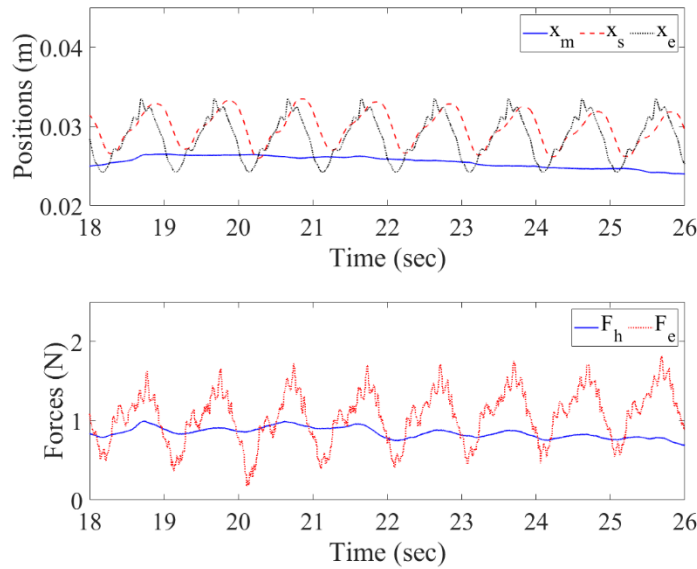
(a)
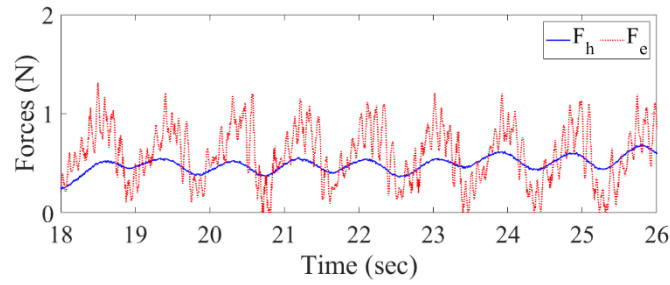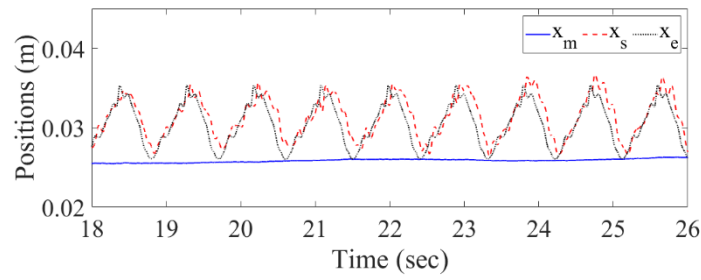
(b)
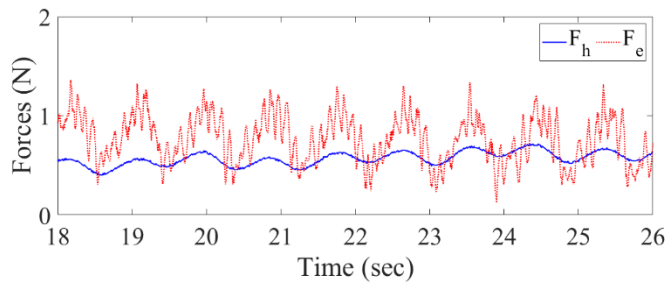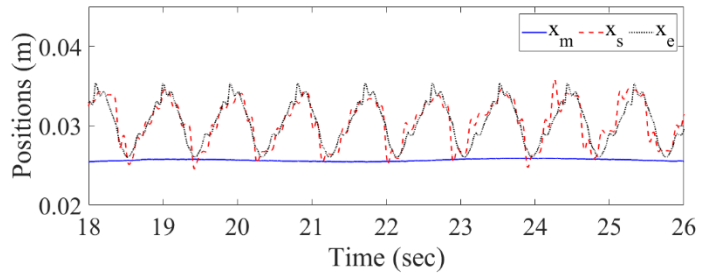
(c)

Figure 6.12. Position trajectories and interaction forces of the master and slave robots. Results for teleoperation system with master robot impedance control and (a) no heart motion predictor, (b) EKF-based heart motion predictor, and (c) NN-based heart motion predictor for the slave robot. In the upper position figure, the blue solid line is the position of the master

128

robot/human operator, the red dashed line is the position of the slave robot, and the gray dotted line is the position of the heart. In the below force figure, the blue solid line is the human-master interaction force, and the red dotted line is the slave-tissue interaction force.

Table 6.3. Experimental Results

Results	MASE (m)	AFM (N)	AFS (N)
No prediction	0.0045	0.8503 ± 0.0660	1.0568 ± 0.3282
EKF predictor	0.0032	0.4881 ± 0.0763	0.8554 ± 0.2838
NN predictor	**0.0016**	0.5674 ± 0.0679	$\mathbf{0.7622 \pm 0.2408}$

6.5 Concluding Remarks

A method of heart motion prediction was proposed to compensate for the non-negligible time delays caused by US image acquisition and processing. A nonlinear autoregressive network was used to solve the prediction problem for the datasets that consist of fixed and varying heart rate and maximum amplitude data. The neural network algorithm was compared to an extended Kalman filter algorithm. Using a neural network, mean absolute error and the root mean squared error decreased significantly compared to those of using extended Kalman filter. Also, the neural network algorithm was proved to be able to predict the heart position up to 1000 ms in advance. The results showed that the neural network algorithm has higher accuracy and prediction ability than the extended Kalman filter algorithm, which makes it possible for the neural network algorithm to be used in robotics-assisted beating-heart surgery.

The designed neural network algorithm was combined with the robot impedance control in a telerobotic system for beating-heart surgery to compensate for the beating heart's motion so that specific tasks can be operated on the beating-heart tissue. Three groups of experiments were carried out: teleoperation systems with master robot impedance control and (a) no heart motion predictor, (b) EKF-based heart motion predictor, and (c) NN-based heart motion predictor for the slave robot. The experimental results demonstrated that the motion compensation and force

feedback using a NN predictor performs better than using an EKF predictor or no predictor for teleoperation systems in beating-heart surgery.

Chapter 7

Multilateral Impedance Control for Surgical Training and Cooperation

In this chapter [6], an impedance-controlled multi-master/single-slave telerobotic system is developed for haptics-enabled surgical training and cooperation in beating-heart surgery and enabling automatically motion compensation for the beating heart's motion as well as non-oscillatory force feedback to the human operators. Multi-user shared control architecture is developed, and a multilateral impedance-controlled strategy is employed for this architecture. The desired objectives of the proposed system are (a) providing position guidance to the trainees during training procedure, (b) providing force feedback to all human operators (trainer and trainees) regardless of their levels of authority over the slave robot, (c) motion compensation for the heart's motion, and (d) reflecting only the non-oscillatory force portion of the slave-heart tissue interaction force to all human operators. To this end, virtual fixtures and a dominance factor are introduced, and a reference impedance model with adjusted parameters is designed for each master or slave robot. The proposed impedance-based control methodology is evaluated experimentally.

---

[6]Portions of this chapter were published in "L. Cheng and M. Tavakoli, "A Multilateral Impedance-Controlled System for Haptics-Enabled Surgical Training and Cooperation in Beating-Heart Surgery," *International Journal of Intelligent Robotics and Applications*, 2019, minor revision." [19]

7.1 Introduction

Various configurations of the robot-assisted system have been proposed. Position-based surgical systems obtain the physiological motions by observation [61], prediction [81], and estimation [53]. The employed sensors are varied from sonomicrometry crystals [107], high-speed cameras [36], [52], infrared radiometer [40], to US machine [17], [96]. Force-based surgical systems [42], [50], [53] employ force sensors to make the contact forces track the desired forces. Additionally, to control the dynamic behavior between the surgical robot and heart tissue, impedance-controlled systems [14], [16], [17] are presented subsequently. A detailed description of these work can be found in [108].

All the past work focused on the hand-held devices or single-master-single-slave teleoperation systems to perform surgical tasks. These systems provide the expert human operators with assistance in beating-heart surgical procedure, but they cannot provide training opportunities for the novice operators. This leads us to come up with the idea that in addition to developing advanced surgical systems for beating-heart surgery, training the novices to use such systems proficiently is equally important and necessary. Moreover, in realistic beating-heart surgery, human operators usually need to perform complex tasks within a limited workspace. Therefore, an effective expert-in-the-loop surgical training for the novice human operators plays an essential role in decreasing potential risks during operation.

In addition, the systems of the past work are only suitable for a single human operator instead of multiple human operators, which lead them cannot allow for cooperative task performance like a multi-user teleoperation system. Particularly, if a task is delicate and complex, two or more expert operators simultaneously perform the operation is necessary to minimize the risk of tissue injury and too-tissue collision. As a result, the interest of this chapter focuses on developing a multi-user teleoperation system which enables expert-in-the-loop surgical training and multiple operators cooperatively perform a physical operation on the slave robot in the remote environment (beating-heart surgery). This requires the system not only to enable automatically

motion compensation for the beating heart's motion as well as non-oscillatory force feedback to the human operators, but also to enable training and cooperation for multiple users.

The rest of this chapter is organized as follows. Section 7.2 introduces the related work about multilateral teleoperation systems incorporating control architectures and control strategies in literature. Section 7.3 describes the developed multilateral teleoperation system for surgical training and cooperation in beating-heart surgery and the desired objectives for the system. Section 7.4 presents the control methodology for the master and slave robots, which includes the proposed reference impedance model for each robot and the parameter adjustment guidelines for the models. Section 7.5 shows the experimental results and discussion. Finally, Section 7.6 contains concluding remarks.

7.2 Related Work

A most common form of multi-user systems for surgical training and cooperation is the dual-user shared control system [109], which includes two master robots manipulated by a trainer and a trainee, respectively, and one slave robot to perform tasks. This system enables both operators to interact with the environment simultaneously by providing haptic feedback to them.

Various dual-user shared control architectures have been proposed. In [109], the authors initially introduced the dominance factor for the surgical training system to provide skill levels of control authority over the task to both trainer and trainee. In this system, the trainer and trainee perceived force feedback from the master robots instead of the remote slave robot. In [110], the authors using the three-port master-slave network model proposed the complementary linear combination architecture and the masters correspondence with environment transfer architecture for haptic training. The former proposed the desired position and force commands for each robot by using the weighted sum of positions and forces of the other two robots. The latter provided half environment forces to both operators regardless of their authorities over the task. Based on [110], a six-channel dual-user shared control architecture was developed in [111]. Also, in [112], the authors developed an architecture that provides direct interaction between the operators and the

slave robot by employing two dominance factors. In addition to the authority of the trainer over the trainee, the authority of the trainer over the slave robot was designed to adjust the supremacy of teleoperators. In [113], a dual-user teleoperation surgical training architecture incorporating virtual fixtures (active constraints) was proposed. This architecture enabled novice trainee to receive haptic virtual fixtures cueing so that the trainee can follow the right gesture of the trainer. After the trainee has authority over the task, an expertise-oriented training was used providing a weighted sum of forces of the environment and the force exerted by virtual fixtures to the trainee. In [114], the authors extended the work presented in [113] and evaluated the system by employing a surgical setup consisting of the classic da Vinci surgical system and the dV-Trainer master console. Moreover, in [115], the authors proposed an architecture for cooperation by providing each operator with a force authority factor over the task and providing them with the same position commands regardless of their exerted forces.

In addition to different dual-user shared control architectures, various control strategies for these architectures are proposed. H_∞-based shared control approach for haptic training and collaboration was proposed in [109]. For the six-channel dual-user teleoperation system shown in [111], a transparency-optimized distance transfer function was introduced to compare the performance of the proposed system with that of the transparency-optimized four-channel controller. In [116], a P + D controller involving gravity compensation for all the robots was proposed to guarantee the stability of the dual-user system. In [115], an adaptive nonlinear impedance control strategy was developed for the nonlinear teleoperation system, and the stability of uncertain teleoperation system has been proven via the Lyapunov theorem. Other researches on sliding-mode-based control strategy [117], adaptive fuzzy force/motion control method [118], passivity-based approach based on the Port-Hamiltonian [119], and neural network-based control method [120] were presented successively.

As a special case of multi-user teleoperation system, dual-user shared control system has attracted extensive attention and discussion. However, to provide surgical training for a class of trainees and realize a common task performance for multiple operators, a general multi-user system is needed. Fortunately, much of the work on dual-user teleoperation systems can be

extended to multi-user systems. For instance, In [121], the authors developed a robust stability analysis framework for unconditional stability analysis of multi-master/multi-slave teleoperation systems and verified it on two dual-user shared control architectures. In [122], a multi-master/single-slave system was developed for cooperative and training applications. The proposed architecture allowed each human operator to feel the environment force for having an ideal transparent operation and provided the slave robot with the weighted sum of the position of each operator.

In this chapter, a multi-master/single-slave teleoperator system for haptics-enabled surgical training and cooperation in beating-heart surgery is developed. The desired objectives of the teleoperation system are (a) providing position guidance to the trainees during the training procedure, (b) providing force feedback to all human operators regardless of their levels of authority over the slave robot, (c) motion compensation for the heart's motion, and (d) non-oscillatory forces feedback to all human operators. Table 7.1 summarizes the above previous research and states if the desired objectives are satisfied and if the system can be extended to a multi-user system.

Table 7.1. Summary of previous research and proposed method

Previous research	Objectives			Suitable for multi-user system
	Position guidance to the trainees	Environmental force feedback	Motion compensation and non-oscillatory force feedback	
[110]	No	No	No	No
[112][113]	No	No	No	No
[114]	No	Yes	No	No
[115][116]	Yes	No	No	Yes
[117]	Yes	No	No	Yes
[123]	No	No	No	Yes
[124]	No	Yes	No	Yes
Proposed method	Yes	Yes	Yes	Yes

In [14], [16], a bilateral impedance-controlled system with two reference impedance models for the master and slave robots, respectively, was proposed such that beating-heart surgery is facilitated. The proposed bilateral teleoperation system takes advantage of the frequency range of the heart's motion to successfully realize motion compensation and non-oscillatory force feedback to the human operator. Different from [14], [16], this chapter focuses on haptics-enabled surgical training and task cooperation in beating-heart surgery. Therefore, the bilateral teleoperation systems in [14], [16] must be replaced by a multilateral teleoperation system. The new framework builds on previous work of the authors and makes use of multi-user teleoperation scenario, allowing the presence of a trainer and multiple trainees in the training and cooperation loop.

In this chapter, a reference impedance model is designed for each robot, and the corresponding parameters are adjusted to meet the requirements of motion compensation and non-oscillatory force feedback. For the sake of clarity, the operation procedure is divided into three scenarios: fundamental training, skills assessment, and task cooperation. The desired objectives for each scenario are defined and satisfied by using virtual fixtures and a dominance factor. After the trainees are sufficiently trained, the trainer and trainees collaboratively control the slave robot to perform common tasks on the beating-heart tissue. To the best knowledge of the authors, this is the first research framework for beating-heart surgical training and cooperation. In other words, this is an initial work for adapting a teleoperation system for beating-heart surgery to surgical training and cooperation purposes. The overall system not only requires motion compensation and non-oscillatory haptic feedback but should also be suitable for surgical training and task cooperation for multiple human operators simultaneously.

7.3 Multilateral Teleoperation Systems

The multilateral teleoperation system for beating-heart surgical training and cooperation involves n master robots that provide position commands and one slave robot that receives those commands and executes tasks on the beating-heart tissue. Figure 7.1 shows the developed system, human operators, and beating heart. In the master site, human operator 1 is the trainer and manipulates

master robot 1, and the other operators are trainees who manipulate their corresponding master robots. In the slave site, the slave robot works as a surgical robot and performs tasks inside or outside the beating heart.
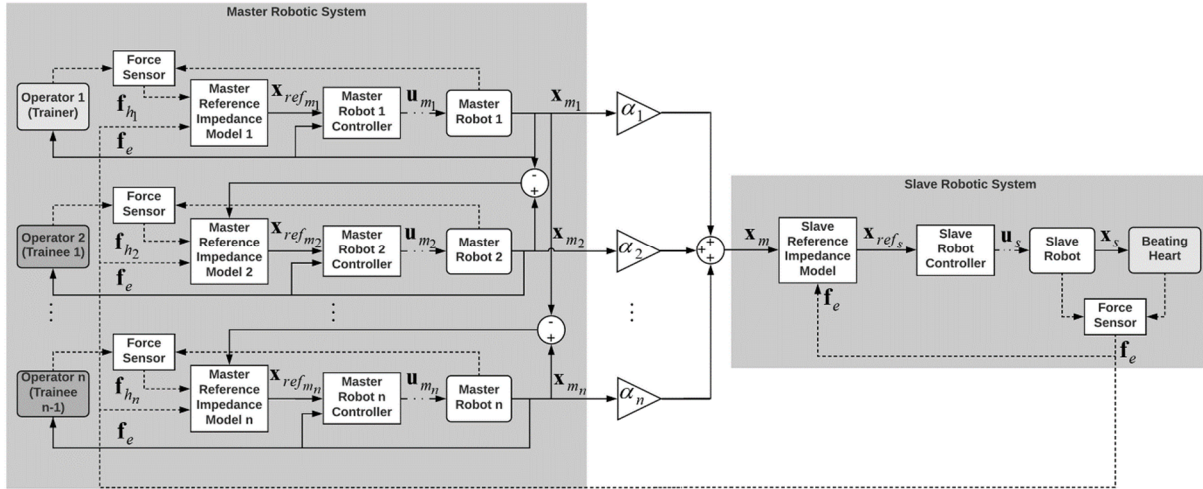
Figure 7.1. The multilateral teleoperation system for beating-heart surgical training and cooperation. The solid, dashed, and dash-dotted lines indicate the position transfer paths, force transfer paths, and control signals, respectively.

7.3.1 Desired Objectives

In the developed system (Figure 7.1), each robot is attached with a force sensor to measure the interaction force between the human operator and the master robot, $\mathbf{f}_{h_i}$ ($i = 1, \cdots, n$), or the interaction force between the slave robot and the heart tissue, $\mathbf{f}_e$. The positions of the master robots end-effectors, $\mathbf{x}_{m_i}$ ($i = 1, \cdots, n$), and the position of the slave robot end-effector, $\mathbf{x}_s$, can be measured and recorded by the robot encoders. Therefore, the measured interaction forces and end-effector positions of the robots can be transmitted through a communication channel to achieve the desired objectives for the beating-heart surgical training and cooperation system. Based on the divided three scenarios, the desired objectives for each scenario are as follows.

Scenario 1: Fundamental training. The skills levels of the trainees are assumed to be at the lowest (no skill). Only the trainer has authority over the surgical task. In other words, the trainer will teleoperate the slave robot alone and show the right gesture and exerted force to the trainees at the same time. The goals in this scenario include two parts. For the master site, the trainees should be guided to follow the position of the trainer, $\mathbf{x}_{m_1}$, to practice operation gesture. Also, all human operators should feel the (possibly scaled) non-oscillatory (low-frequency) portion of the slave-heart interaction forces. Note that the movements and applied forces by the trainees do not affect the movements and performance of the trainer and the slave robot. Therefore, there is no risk imposed by the trainees to the beating-heart tissue. Therefore, for the slave site, the movements of the slave robot, $\mathbf{x}_s$, is only affected by the trainer's motion, $\mathbf{x}_{m_1}$. At the same time, the slave robot should compensate for the motion of the beating heart, $\mathbf{x}_e$.

Scenario 2: Skills assessment. After the trainees are trained, the skills levels of the trainees will be assessed. A dominance factor, α_i ($i = 1, \cdots, n$), is defined to represent the skills level of each trainee, and it will be used for task cooperation. The dominance factor for each trainee should satisfy the equation $\sum_{i=1}^{n} \alpha_i = 1$, $\alpha_i \geq 0$. The transmitted position of the master robots to the slave robot in scenario 3 can be expressed as $\mathbf{x}_m = \alpha_1 \mathbf{x}_{m_1} + \alpha_2 \mathbf{x}_{m_2} + \cdots + \alpha_n \mathbf{x}_{m_n}$. Therefore, scenario 1 is a special case when $\alpha_1 = 1$ and $\alpha_i = 0$ ($i = 2, \cdots, n$). As the skills assessment is not the research focus of this chapter, the series dominance factors in the experiments are assigned randomly.

Scenario 3: Task cooperation. Based on the skills level of each trainee, the trainees and trainer can cooperate to accomplish one task. In this scenario, both trainer and trainees can fully feel the (possibly scaled) non-oscillatory slave-heart interaction force and have authorities over the task according to their corresponding skills levels. The main difference between scenario 1 and scenario 3 is that the former provides position guidance from the trainer to the trainees, but the latter does not. For the sake of clarity, the above objectives are summarized in Table 7.2.

Table 7.2. Objectives for the multilateral teleoperation system

Scenarios	Objectives	
	Master site	Slave site
Scenario 1: Fundamental training	**Position guidance for the trainees:** $\mathbf{x}_{m_i} = \mathbf{x}_{m_1}, (i = 2, \cdots, n)$	**Transmitted master robots' position to the slave site: $\mathbf{x}_m = \mathbf{x}_{m_1}$**
	Non-oscillatory force feedback to all operators	Motion compensation for the beating heart: $\mathbf{x}_s$ complies with $\mathbf{x}_e$ during interaction
Scenario 2: Skills assessment	Obtain dominance factor α_i such that $\sum_{i=1}^{n} \alpha_i = 1, \alpha_i \geq 0$	
Scenario 3: Task cooperation	**No position guidance for the trainees:** $\mathbf{x}_{m_i} \neq \mathbf{x}_{m_1}, (i = 2, \cdots, n)$	**Transmitted master robots' position to the slave site: $\mathbf{x}_m = \alpha_1\mathbf{x}_{m_1} + \alpha_2\mathbf{x}_{m_2} + \cdots + \alpha_n\mathbf{x}_{m_n}$**
	Non-oscillatory force feedback to all operators	Motion compensation for the beating heart: $\mathbf{x}_s$ complies with $\mathbf{x}_e$ during interaction

7.3.2 Control Strategy Overview

The control of the multilateral teleoperation system is the most important issue to perform beating-heart surgical training and tasks cooperation successfully. In Figure 7.1, a reference impedance model is proposed for each master or slave robot.

The reference impedance model for each master robot incorporates the forces applied by the corresponding human operator and the heart tissue and dictates the haptic force feedback from the heart tissue to the operator. As mentioned above, the non-oscillatory force feedback can be achieved by appropriately adjusting the parameters of the reference impedance model. The adjusted reference impedance model generates the desired position for the corresponding master robot i ($i = 1, \cdots, n$), $\mathbf{x}_{ref_{m_i}}$. A master robot controller is used for the master robot to track the desired position. The actual position of the master robot is $\mathbf{x}_{m_i}$, and $\mathbf{u}_{m_i}$ is the control signal to the master robot.

The reference impedance model for the slave robot provides the flexibility of the slave robot in tracking the master robots' position, $\mathbf{x}_m$, in response to the slave-heart interaction force.

139

By appropriately adjusting its parameters, the slave robot can compensate for the beating-heart motion perfectly. The slave robot controller receives the slave robot desired trajectories generated by the impedance model ($\mathbf{x}_{ref_s}$) and actual trajectories ($\mathbf{x}_s$), and outputs the control signal $\mathbf{u}_s$ to the slave robot. The reference impedance models and their parameter adjustments and controllers are presented in Section 7.4 in detail.

7.4 Control Methodology

7.4.1 Reference Impedance Models

The reference impedance model for each master robot in Cartesian coordinates includes the human-master interaction force, the scaled slave-heart interaction force, and the desired master response trajectory. The relationships can be expressed as

$$\mathrm{M}_{m_1}\ddot{\mathbf{x}}_{ref_{m_1}} + \mathrm{C}_{m_1}\dot{\mathbf{x}}_{ref_{m_1}} + \mathrm{K}_{m_1}\mathbf{x}_{ref_{m_1}} = \mathbf{f}_{h_1} - k_\mathrm{f}\mathbf{f}_e \tag{7.1a}$$

$$\mathrm{M}_{m_i}\ddot{\mathbf{x}}_{ref_{m_i}} + \mathrm{C}_{m_i}\dot{\mathbf{x}}_{ref_{m_i}} + \mathrm{K}_{m_i}\mathbf{x}_{ref_{m_i}} = \mathbf{f}_{h_i} - k_\mathrm{f}\mathbf{f}_e - \beta\mathbf{f}_{v_i} \tag{7.1b}$$

$$\mathbf{f}_{v_i} = \mathrm{M}_m^v\ddot{\mathbf{e}}_{m_i} + \mathrm{C}_m^v\dot{\mathbf{e}}_{m_i} + \mathrm{K}_m^v\mathbf{e}_{m_i} \tag{7.1c}$$

where M_{m_i}, C_{m_i}, and K_{m_i} are the virtual mass, damping, and stiffness of the ith master impedance model. The subscript $i = 1$ refers to the human operator 1 that is the trainer, and $i = 2, \cdots, n$ refers to the human operator $2, \cdots, n$, which are trainees. Scalars k_f and β are two force scaling factors. The interaction forces ($\mathbf{f}_{h_i} \in \mathbb{R}^{6\times1}$, $\mathbf{f}_e \in \mathbb{R}^{6\times1}$) and the desired master response ($\mathbf{x}_{ref_{m_i}} \in \mathbb{R}^{6\times1}$) are vectors. Here, $\mathbf{f}_{v_i}$ is a designed virtual force generated by a virtual fixture designed to guide the trainees along the right path of the surgery, and $\mathbf{e}_{m_i} = (\mathbf{x}_{m_i} - \mathbf{x}_{m_1})$ is the position tracking error between trainer and each trainee. Also, M_m^v, C_m^v, and K_m^v correspond to the impedance characteristics of the virtual fixture model. As the robots' accelerations are hard to measure, M_m^v is set to be 0. According to the desired objectives for the trainees, scalar β is set to be 1 for training scenario and 0 for cooperation scenario.

140

The reference impedance model for the slave robot is concerned with the slave-heart interaction force and the desired slave impedance model's response deviation from the trajectory of the master robot. The model can be expressed as

$$M_s\ddot{\tilde{\mathbf{x}}}_{ref_s} + C_s\dot{\tilde{\mathbf{x}}}_{ref_s} + K_s\tilde{\mathbf{x}}_{ref_s} = -\mathbf{f}_e \tag{7.2}$$

where $\tilde{\mathbf{x}}_{ref_s} = \mathbf{x}_{ref_s} - k_p\mathbf{x}_m$, and k_p is the position scaling factor. Here, $\mathbf{x}_m \in \mathbb{R}^{6\times1}$ is the position vector of the master robot. Also, M_s, C_s, and K_s are the virtual mass, damping and stiffness of the slave impedance model.

7.4.2 Parameter Adjustments

To illustrate the parameter adjustment guidelines for the reference impedance models clearly, damping ratios and natural frequencies of the reference impedance models are introduced. For each master robot, the damping ratio is given by $\zeta_{m_1} = C_{m_i}/2\sqrt{M_{m_i}K_{m_i}}$, and the natural frequency is given by $\omega_{n_{m_i}} = \sqrt{K_{m_i}/M_{m_i}}$. For the slave robot, the damping ratio is $\zeta_s = C_s/2\sqrt{M_sK_s}$, and the natural frequency is $\omega_{n_s} = \sqrt{K_s/M_s}$. In the following, only the damping ratios, the natural frequencies, and the stiffnesses are chosen to be adjusted.

1) Fundamental training

The reference impedance model for master robot 1 (7.1a) aims to avoid possible fatigue and exhaustion caused by the oscillatory slave-heart interaction force feedback to the trainer. Also, the reference impedance model for the other master robot (7.1b) aims to provide position guidance to all trainees from the trainer, and meanwhile all trainees should feel the non-oscillatory force feedback. Therefore, a virtual force, $\mathbf{f}_{v_i}$ (7.1c), is designed so that each trainee's motion can follow the position command of the trainer. The desired objective is $\mathbf{f}_{v_i} \rightarrow 0$ as $\mathbf{e}_{m_i} \rightarrow 0$, so the impedance characteristics of the virtual force are set to be moderate. If $\mathbf{f}_{v_i}$ equals 0 is achieved, equations (7.1a) and (7.1b) have the same expressions and goal, so the parameters of (7.1a) and (7.1b) are adjusted to be the same. To be more specific, a well-trained trainee will perfectly follow the

trainer's position commands which means $\mathbf{f}_{v_i}$ will be 0 so that the trainee can perceive the same force feedback as the trainer perceived. In other words, the virtual force $\mathbf{f}_{v_i}$ can be treated as an evaluation indicator of the trainee's skill level. Both high and low $\mathbf{f}_{v_i}$ mean the trainee is unskilled and provides the trainee with a clue to change his/her position. Therefore, firstly, ξ_{m_i} is chosen to be 0.7 to get a fast behaviour in response to the harmonic force of the human operator. Secondly, to filter out the high frequency of the slave-heart interaction force and achieve $(\mathbf{f}_{h_i} - k_\mathrm{f}\mathbf{f}_e^L) \to 0$, the natural frequencies of (7.1a) and (7.1b) $(\omega_{n_{m_1}}$ and $\omega_{n_{m_i}})$ should be several times smaller than the rate of the heart motion $(\omega_{n_{m_1}} = \omega_{n_{m_i}} \ll \omega_h)$ and the stiffnesses of models (7.1a) and (7.1b) (K_{m_i}) are chosen small.

The goal of the slave impedance model (7.2) is to make the slave robot comply with the beating heart's motion during the contact procedure. Based on (7.2), the deviation from the scaled master trajectory $(\tilde{\mathbf{x}}_{ref_s} = \mathbf{x}_{ref_s} - k_\mathrm{p}\mathbf{x}_m)$ provides the flexibility of the slave robot. As for the training scenario, only the trainer has authority over the surgical task, the position commands transmitted to the slave robot, $\mathbf{x}_m$, is $\mathbf{x}_{m_1}$. Note that the flexibility of the slave robot can neither be too small nor too large. If the slave robot is too flexible, it cannot apply enough forces on the heart surface to perform tasks. If the slave robot is too rigid, the motion compensation cannot be achieved. Therefore, the stiffness of the slave impedance model (K_s) should be adjusted to be moderate. Also, the natural frequency of (7.2) (ω_{n_s}) should be several times greater than the rate of the heart motion $(\omega_{n_s} \gg \omega_h)$. Here, ζ_s is chosen to be 0.7.

2) Task cooperation

For task cooperation, both trainer and trainee have authority over the surgical task. The goal is that all operators can feel the same non-oscillatory force feedback, but they can provide different position commands to the slave robot. The position transmitted to the slave robot is the weighted sum of every operator's position. The only difference between training and cooperation is that the virtual force for cooperation is set to be zero; that is, β is equal to 0. The rest parameters of models

(7.1a), (7.1b) and (7.2) are selected the same as those for the training scenario. Table 7.3 summarizes the parameter adjustments guidelines for the reference impedance models.

Table 7.3. Parameter adjustments for the reference impedance models

Scenarios	Objectives & Adjusted Parameters			
	Master site		Slave site	
Scenario 1: Fundamental training	Objectives	Position guidance for the trainees	Objectives	$\mathbf{x}_m = \mathbf{x}_{m_1}$
	Parameters	• $\beta = 1$	Parameters	• $\alpha_1 = 1$, $\alpha_i = 0$, $(i = 2, \cdots, n)$
	Objectives	Non-oscillatory force feedback	Objectives	Motion compensation
	Parameters	• Small K_{m_i} to achieve $\mathbf{f}_{h_i} \to k_f\mathbf{f}_e$ • Small $\omega_{n_{m_i}}$ $(\ll \omega_h)$ to filter out the high-frequency portion of $\mathbf{f}_e$	Parameters	• Moderate K_s to exert appropriate force • Large ω_{n_s} $(\gg \omega_h)$ to make the slave robot comply with the heart motion
Scenario 2: Skills assessment	Obtain dominance factor α_i such that $\sum_{i=1}^{n} \alpha_i = 1$, $\alpha_i \geq 0$			
Scenario 3: Task cooperation	Objectives	No position guidance for the trainees	Objectives	$\mathbf{x}_m = \alpha_1\mathbf{x}_{m_1} + \alpha_2\mathbf{x}_{m_2} + \cdots + \alpha_n\mathbf{x}_{m_n}$
	Parameters	• $\beta = 0$	Parameters	• $\sum_{i=1}^{n} \alpha_i = 1$, $\alpha_i \geq 0$
	Objectives	Non-oscillatory force feedback	Objectives	Motion compensation
	Parameters	• Small K_{m_i} to achieve $\mathbf{f}_{h_i} \to k_f\mathbf{f}_e$ • Small $\omega_{n_{m_i}}$ $(\ll \omega_h)$ to filter out the high-frequency portion of $\mathbf{f}_e$	Parameters	• Moderate K_s to exert appropriate force • Large ω_{n_s} $(\gg \omega_h)$ to make the slave robot comply with the heart motion

3) Controllers

The dynamics of the master and slave robots in the Cartesian space can be expressed as

$$\mathbf{M}_{\mathbf{x},m}(\boldsymbol{\theta}_m)\ddot{\mathbf{x}}_m + \mathbf{C}_{\mathbf{x},m}(\boldsymbol{\theta}_m,\dot{\boldsymbol{\theta}}_m)\dot{\mathbf{x}}_m + \mathbf{G}_{\mathbf{x},m}(\boldsymbol{\theta}_m) + \mathbf{F}_{\mathbf{x},m}(\dot{\boldsymbol{\theta}}_m) = \mathbf{f}_m + \mathbf{f}_h \qquad (7.3)$$

$$\mathbf{M}_{\mathbf{x},s}(\boldsymbol{\theta}_s)\ddot{\mathbf{x}}_s + \mathbf{C}_{\mathbf{x},s}(\boldsymbol{\theta}_s,\dot{\boldsymbol{\theta}}_s)\dot{\mathbf{x}}_s + \mathbf{G}_{\mathbf{x},s}(\boldsymbol{\theta}_s) + \mathbf{F}_{\mathbf{x},s}(\dot{\boldsymbol{\theta}}_s) = \mathbf{f}_s - \mathbf{f}_e \qquad (7.4)$$

Here $\boldsymbol{\theta}_i$ is the joint angle of the robot's end-effector, $\mathbf{f}_i$ is the control torque of the robot, and $\mathbf{M}_{\mathbf{x},i}(\boldsymbol{\theta}_i)$, $\mathbf{C}_{\mathbf{x},i}(\boldsymbol{\theta}_i,\dot{\boldsymbol{\theta}}_i)$, $\mathbf{G}_{\mathbf{x},i}(\boldsymbol{\theta}_i)$ and $\mathbf{F}_{\mathbf{x},i}(\dot{\boldsymbol{\theta}}_i)$ are the inertia matrix, the centrifugal and Coriolis term, the gravity term, and the friction torque, respectively. Note that $i = m$ for the master and $i = s$ for the slave.

To track the ideal responses of the reference impedance models for the master and slave robots, the PID controllers are employed for each master and slave robot. In the experiments, the parameters of PID controllers for the master robot 2 are $K_{p_m} = 1000$, $K_{i_m} = 200$, $K_{d_m} = 1$. The PID controller parameters for the master robot 1 and the slave robot are $K_{p_s} = 1000$, $K_{i_s} = 0$, $K_{d_s} = 20$.

7.5 Experiments

The experiments are conducted to evaluate the proposed multilateral impedance-based control method for surgical training and cooperation. Figure 7.2 shows the experimental setup, which consists of a Phantom Premium 1.5A robot (Geomagic Inc., Wilmington, MA, USA) as the master robot 1 and two Quanser robots (Quanser Consulting Inc., Markham, ON, Canada) as the master robot 2 and the slave robot, separately. Two human operators are employed to implement training and cooperation tasks. The human operator manipulating the master robot 1 is treated as the trainer, and the other operator is treated as the trainee. The beating-heart is simulated by a custom-built mechanical cam whose end is attached a plastisol-based tissue to simulate the heart tissue. This heart simulator generates continuous heart motion signals with a fundamental frequency of 64 bpm to simulate the real-heart motion [24]. To measure the human operator-master robot interaction forces and the slave robot-heart tissue interaction force, a 50M31 force/torque sensor (JR3 Inc.,

Woodland, CA, USA) and an ATI Gamma Net force/torque sensor (ATI Industrial Automation, Inc., Apex, NC, USA) are attached to the end-effectors of the master robot 1 and 2, separately. Another ATI Gamma Net force/torque sensor (ATI Industrial Automation, Inc., Apex, NC, USA) is attached to the end-effector of the slave robot. For the sake of brevity, the experiments only present the motion along x-axis to evaluate the feasibility of the proposed method. It is straightforward to extend the proposed method from 1-DOF to multiple-DOF. The adjusted parameters of the reference impedance models in (7.1) and (7.2) are listed in Table 7.4.
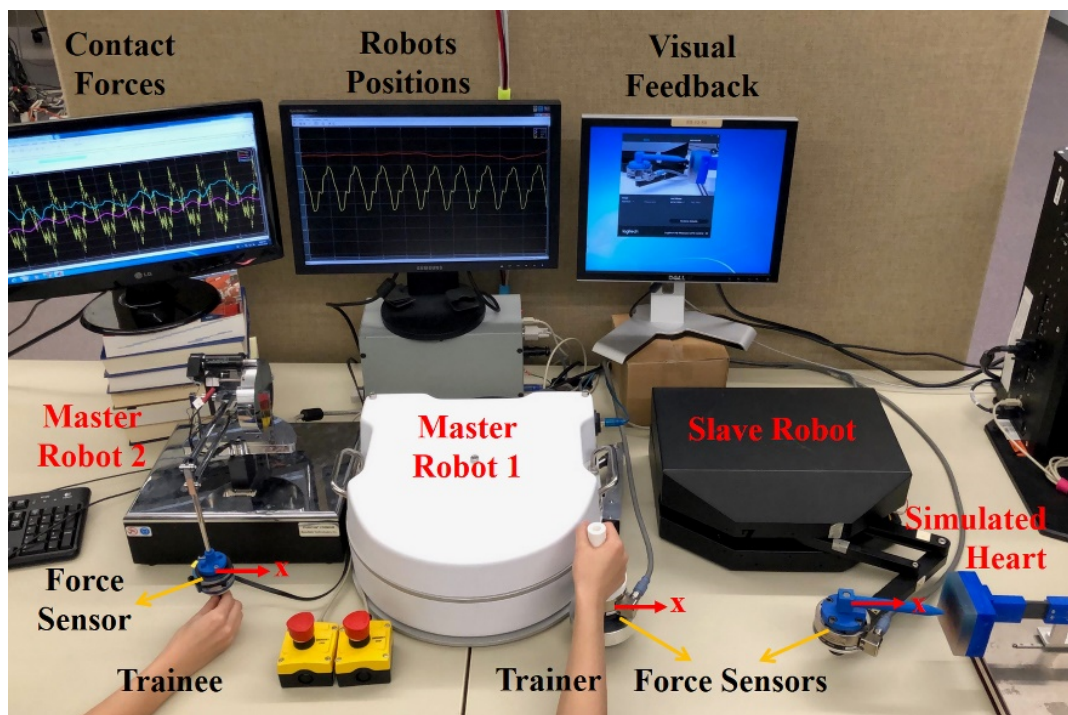

Figure 7.2. Experimental setup.

Table 7.4. Parameters of the reference impedance models

Impedance Model (7.1a)	Impedance Model (7.1b)	Impedance Model (7.1c)	Impedance Model (7.72)
$K_{m_1} = 10$ N/m	$K_{m_2} = 10$ N/m	$K_m^v = 30$ N/m	$K_s = 160$ N/m
$\omega_{n_{m_1}} = 0.5$ rad/sec	$\omega_{n_{m_2}} = 0.5$ rad/sec	$C_m^v = 0.1$ Ns/m	$\omega_{n_s} = 20$ rad/sec
$\zeta_{m_1} = 0.7$	$\zeta_{m_2} = 0.7$		$\zeta_s = 0.7$
$C_{m_1} = 28$ Ns/m	$C_{m_2} = 28$ Ns/m		$C_s = 11.2$ Ns/m
$M_{m_1} = 40$ kg	$M_{m_2} = 40$ kg		$M_s = 0.4$ kg
$k_f = 1$			$k_p = 1$

7.5.1 Training Results

The experiments include two scenarios: surgical training and task cooperation. In the surgical training scenario, three groups of experiment which consist of two unskilled-trainee cases and one skillful-trainee case are simulated. For all these experiments, only the trainer has authority over the slave robot. Based on the description in 7.4.2, the force feedback perceived by the trainee will change according to different cases. Only when the trainee follows the trainer's position commands perfectly, the trainee can perceive the same force feedback as the trainer perceived, which means the trainee is well trained.

The first unskilled-trainee case requires the trainee to keep the master robot 2 at the original point. Figure 7.3 shows the positions and contact forces of the master and slave robots in this experiment. As can be seen in Figure 7.3, the virtual force generated by virtual fixture model, $\mathbf{f}_{v_2}$, stays negative due to the distance between the two master robots. This virtual force mainly leads the force perceived by the trainee to be lower than the trainer-master1 contact force. Also, due to the designed reference impedance models for the master and slave robots, the slave robot complies with the heart's motion perfectly and the forces perceived by the human operators are both non-oscillatory, which is possible to increase the robot operability for the human operators.

The second unskilled-trainee case requires the trainee to make the master robot 2 go farther than the trainer's robot (master robot 1). The experimental results are shown in Figure 7.4. In this experiment, $\mathbf{f}_{v_2}$ keeps positive that mainly leads the force perceived by the trainee to be higher than the trainer-master (robot 1) contact force. To simulate a skillful performance for the trainee, the trainee is asked to follow the position of the trainer, and Figure 7.5 shows the results. In Figure 7.5, the virtual force is almost 0 due to the trainer's perfect position tracking. Therefore, the trainee-master (robot 2) contact force is almost the same as the trainer-master1 contact force. The above three training cases show that the advantage of the virtual fixture guidance force is to provide a position clue to the trainee when his/her position goes too far away from the trainer's position.
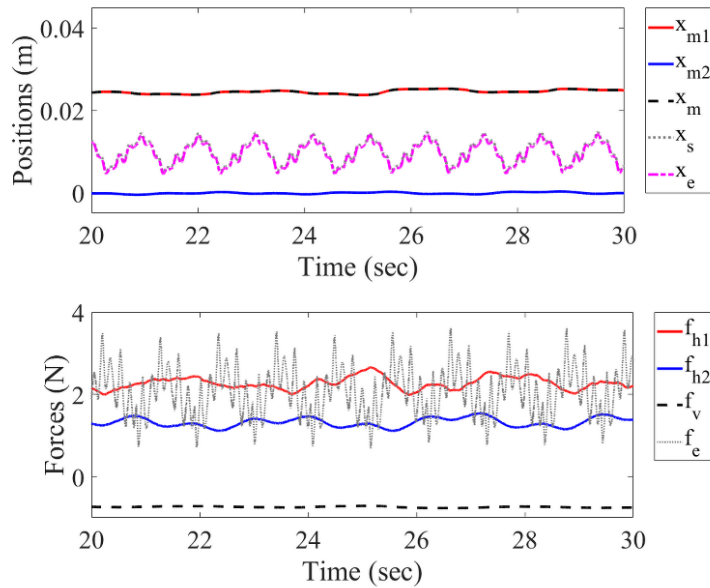

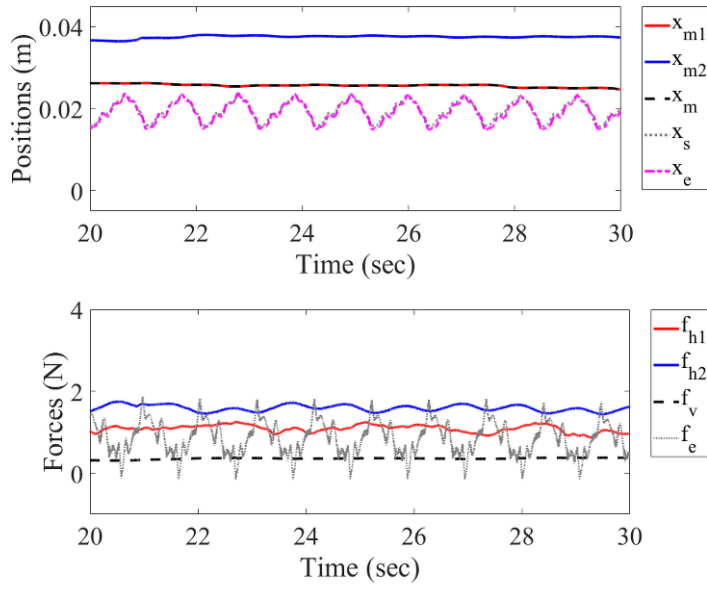**Figure 7.3. Training Results of the first unskilled-trainee case.**

Figure 7.4. Training Results of the second unskilled-trainee case.
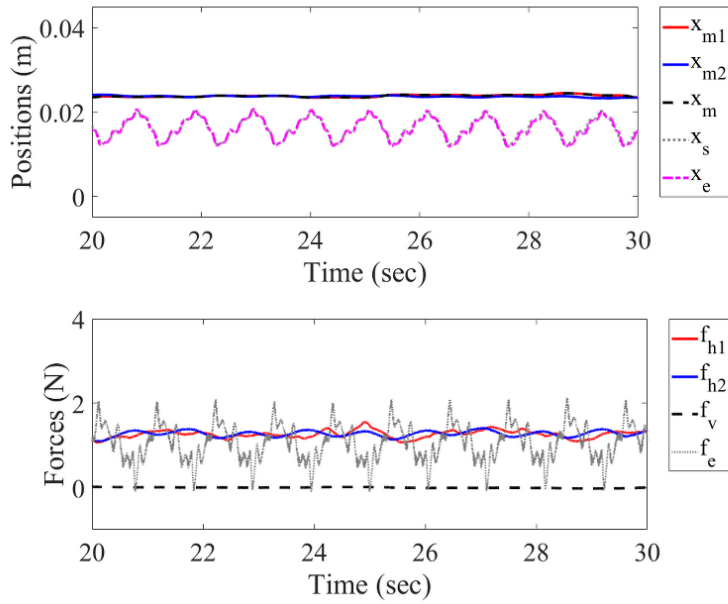

Figure 7.5. Training Results of the skillful-trainee case.

7.5.2 Cooperation results

To investigate the behavior of the system with different dominance factor, the experiments are divided into two groups to be conducted. For the experiment in each group, three phases are included. In phase I, only the master robot 1 moves and the master robot 2 is kept at the original point. In phase II, only the master robot 2 moves and the master robot 1 is kept at the original point. In phase III, both master robot 1 and 2 move cooperatively, and they are asked to take the same path. In the experiments, the task is to move in both free motion and contact motion interaction with the simulated beating-heart tissue.

Figure 7.6 shows the results of the experiment in the first group. The dominance factors are set as $\alpha_1 = \alpha_2 = 0.5$, which means the two human operators have the same level of authority over the slave robot. When the slave robot moves in free motion, it simply tracks the weighted sum of the two master robots' positions, x_m. While when the slave robot contacts the beating-heart tissue, it begins to comply with the heart's motion. Additionally, in Figure 7.6, the human-master robot contact forces are relatively steady compared to the oscillatory slave-heart contact force. Note that, in phase I and phase II, the two human-master robot contact forces are not close to each other that is caused by the reference impedance models for the two master robots (7.1a) and (7.1b). The distances between the two master robots lead to the differences between the left sides of (7.1a) and (7.1b). These differences can be reduced by decreasing the parameters of models (7.1a) and (7.1b). In this chapter, however, considering the limitation of the robots, the adjusted parameters in Table 7.3 are the optimal values. In phase III, as the two master robots have almost the same positions, the left sides of (7.1a) and (7.1b) are basically the same. Therefore, the two human-master robot contact forces are basically the same.

The experiment in the second group is conducted with dominance factors of $\alpha_1 = 0.3$ and $\alpha_2 = 0.7$. The positions and forces results are presented in Figure 7.7. In this experiment, the master robot 2 has more authority over the slave robot than the master robot 1. Therefore, in phase I, the master robot 1 must go much farther than the distance went by the master robot 2 in phase II to make the slave robot contact with the beating-heart tissue. In phase III, the position commands

transmitted from the master robots to the slave robot, x_m, are the same as the two master robots' positions. This performance is the same as that shown in phase III of Figure 7.6 although the dominance factors are different. It is concluded that as long as the positions of the two master robots are the same (phase III), x_m will be the same as the two master robots' positions regardless of the skills levels of the operators.
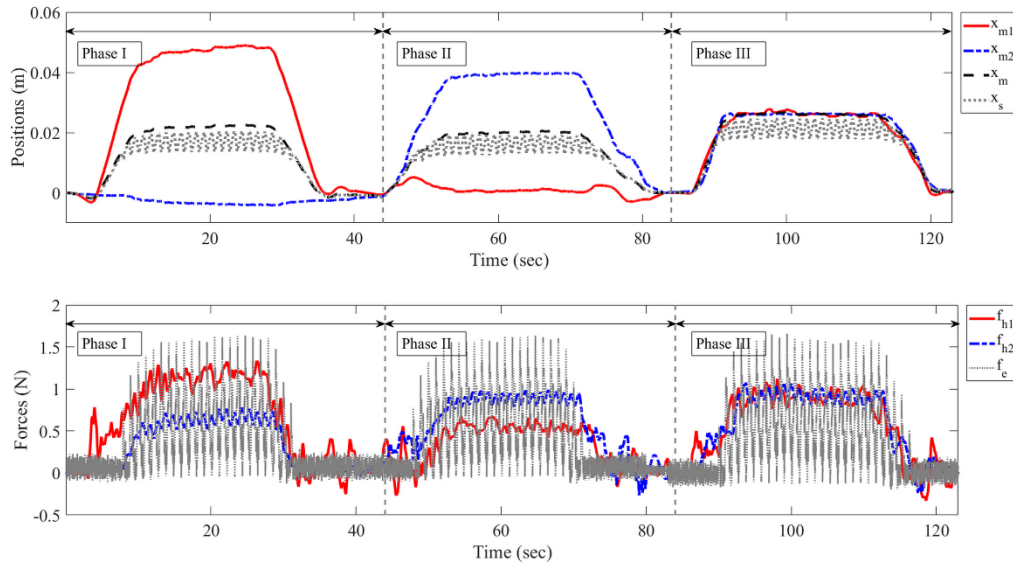
Figure 7.6. Cooperation results of the experiment in the first group. The dominance factors are set as $\alpha_1 = \alpha_2 = 0.5$.
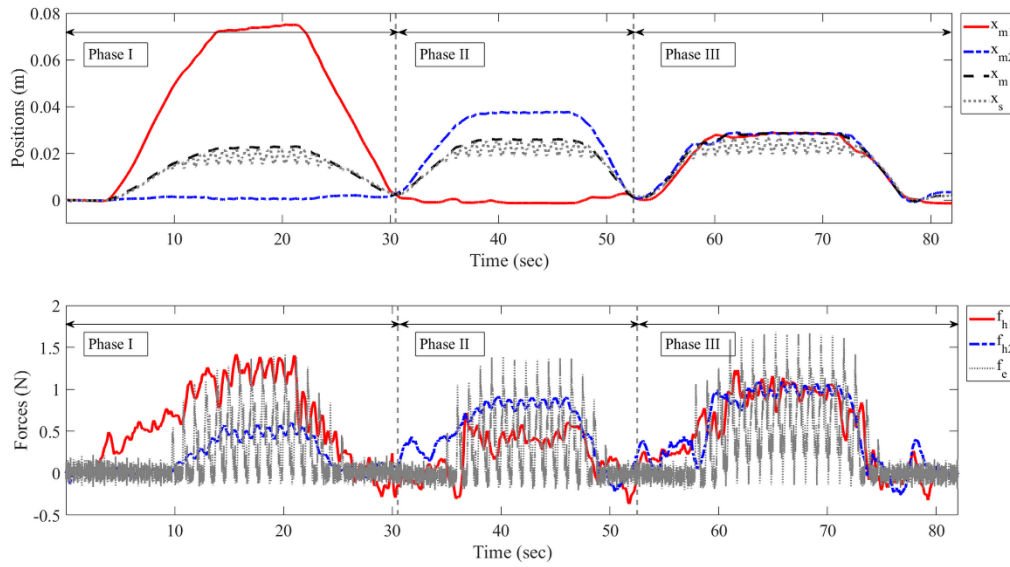
Figure 7.7. Cooperation results of the experiment in the second group. The dominance factors are set as $\alpha_1 = 0.3$ and $\alpha_2 = 0.7$.

7.6 Concluding Remarks

A multilateral impedance-controlled telerobotic system is proposed for surgical training and cooperation in beating-heart surgery. This system not only enables motion compensation and non-oscillatory haptic feedback but is also suitable for surgical training and task cooperation for multiple human operators simultaneously. By designing the reference impedance model with adjusted parameters for each master or slave robot, motion compensation and non-oscillatory haptic feedback in beating-heart surgery are achieved. In a training procedure, the virtual fixture guidance force provides each trainee with a position clue when his/her position goes too far away from the trainer's position, so that position and force tracking can be realized. The trainees can perceive full non-oscillatory force feedback and implement cooperative tasks. Difference dominance factors are set for the two human operators, and the experimental results demonstrated that the proposed method could be used for surgical training and cooperation in beating-heart

151

surgery perfectly. Future work will involve exploring the method's potential uses in real surgical robots, i.e., da Vinci surgical systems.

Chapter 8

Summary and Future Directions

This thesis develops control methods for robot-assisted master-slave teleoperation systems for beating-heart surgery in order to automatically provide compensation for the beating heart's motion and reflect non-oscillatory haptic forces to the human operator. The control methods presented in this thesis can be divided into two categories: pure impedance control and combination of impedance- and image-based control. The former employs reference impedance model for each robot in the system, whereas in the latter the reference impedance model is designed only for the master robot and combined with US image-based heart motion predictor to compensate for the beating heart's motion.

The first controller presented in Chapter 3 is a bilateral impedance-controlled telerobotic system for beating-heart surgery. The proposed method only uses the measured interaction forces without any need for vision-based heart motion estimation, active observer or motion prediction to compensate for the beating-heart motion automatically and provide the human operator with a feeling of operating on an arrested heart simultaneously. The experiments were designed to demonstrate the viability and superiority of the developed system performing 1-DOF and 3-DOF simulated surgical tasks. The 1-DOF task was performing beating-heart anchor deployment for mitral valve annuloplasty under the guidance of US images. In this experiment, the system has been shown reduce operation time, increase safety to the heart tissue, achieve lower and more

153

stable force application by the operator, and obtain high success rate of deploying anchors. The telerobotic system with an anchor driver attached to the slave robot's end-effector reduced the excess force application rate by 70% and increased the success rate of anchor deployment by 100% compared to manual attempts. The motion compensation instrument also decreased the task completion time (from the operation start to stapling) by 22% and reduced the mean absolute synchronization error by 30%. Low and stable operator forces were achieved when compared to the case of no motion compensation. As for the 3-DOF physiological motion compensation, the experimental evaluations demonstrated that the proposed method could be used in the robot with significant dynamics and achieve accurate performance for surgical applications that need low and constant contact forces during beating-heart interventions. It should be noted that due to the flexibility of the designed reference impedance model for the slave robot, the bilateral impedance control method is more suitable for surgeries that require less tool-tissue interaction forces such as mitral valve annuloplasty, blunt resection, ablation, etc.

In Chapter 4, a switched-impedance control method involves two switched reference impedance models for the master and slave robots is proposed and implemented for telerobotic beating-heart surgery. The main advantage of this method over the one presented in Chapter 3 is that during slave-heart interaction, the human operator can feel the stiffness of the heart tissue through the master robot, and the slave robot can synchronize its motions with the heart's motion and follow the commands of the human operator as closely as possible to execute the desired surgical task. Therefore, this method is more suitable for surgeries which involve large forces being applied on the heart tissue such as tissue cutting, suturing, penetration, etc. To validate the proposed telerobotic framework, two scenarios amenable to two surgical tasks including mitral valve annuloplasty and soft tissue cutting were tested in both simulations and experiments. Results of both simulations and experiments for two surgical scenarios suggested that the proposed telerobotic system achieves the stated goals. In addition, a user study involving a line drawing task, which is similar to tissue cutting, was conducted in experiments. The user study of line drawing demonstrated that the proposed switched impedance control strategy offers timesaving, perfect

lines, and easy control of the slave-heart interaction force compared to the case without motion compensation.

The robot impedance control was combined with ultrasound imaging-based control algorithms for beating heart's motion compensation in Chapter 5 and 6. To make the human operator perform the surgical procedure as if the beating heart is stationary, a reference impedance model was designed for the master robot. The ultrasound imaging was used to capture the position of the POI on the heart tissue. The slave robot was controlled to synchronize its motions with the heart's (POI) motion and follow the commands of the human operator. The presence of US imaging introduced ultrasound non-negligible time delay to the system due to image acquisition and processing. To address this issue, an EKF- and a NN-based heart motion predictors were designed in Chapter 5 and 6, respectively. The ability of the systems with two heart motion predictors was evaluated experimentally.

In Chapter 5, a cubic interpolation and an EKF was used to upsample and predict the detected POI position by US image processing. Specifically, the detected POI position was upsampled first and then predicted by EKF. The control strategy took advantage of the quasi-periodicity of the POI position, modeled the delayed POI position as a time-varying Fourier series, and predicted the POI position by EKF to compensate for the time delay. With the upsampled and predicted heart motion, the slave robot was controlled with GPC to follow the human operator's motions and synchronize with the beating-heart motion by taking advantage of the future input and output values. By comparing the proposed control method with conventional DFR teleoperation system without and with AMC, it is proved that the proposed method could be used in teleoperation beating heart surgery and achieve safer and more accurate performance.

In Chapter 6, a NAR network was used to solve the prediction problem for the datasets that consist of fixed and varying heart rate and maximum amplitude data. The NN algorithm was compared to an EKF algorithm. Using NN, the mean absolute error and the root mean squared error decreased significantly compared to those of using EKF. Also, the NN algorithm was proved to be able to predict the heart position up to 1000 ms in advance. The results showed that the NN

algorithm has higher accuracy and prediction ability than the EKF, which makes it possible for the NN algorithm to be used in robotics-assisted beating-heart surgery. Then the designed NN algorithm was combined with the robot impedance control in the telerobotic system. Three groups of experiments were carried out: teleoperation systems with master robot impedance control and (a) no heart motion predictor, (b) EKF-based heart motion predictor, and (c) NN-based heart motion predictor for the slave robot. The experimental results demonstrated that the motion compensation and force feedback using a NN predictor performs better than using an EKF predictor or no predictor for teleoperation systems in beating-heart surgery.

In Chapter 7, the impedance control method was extended to be used for haptic-enabled surgical training and cooperation in beating-heart surgery. Multi-user shared control architecture was developed, and a multilateral impedance-controlled strategy was employed for this architecture. Besides the two desired objectives for robot-assisted beating-heart surgery mentioned in Section 2.3.3, there are another two objectives for the proposed system: (a) providing position guidance to the trainees during the training procedure, (b) providing force feedback to all human operators (trainer and trainees) regardless of their levels of authority over the slave robot. To this end, virtual fixtures and a dominance factor were introduced, and a reference impedance model with adjusted parameters was designed for each master or slave robot. In a training procedure, the virtual fixture guidance force provided each trainee with a position clue when his/her position goes too far away from the trainer's position, so that position and force tracking could be realized. The trainees could perceive full non-oscillatory force feedback and implement cooperative tasks. Difference dominance factors were set for the two human operators, and the experimental results demonstrated that the proposed method could be used for surgical training and cooperation in beating-heart surgery perfectly.

8.1 Future Work

The following research can be performed in the future to improve this robot-assisted beating-heart surgical system.

- Intelligent control of the da Vinci research kit (dVRK) using the proposed methods

  - The daVinci Research Kit is a telerobotic surgical system, which consists of a surgeon's console, master tool manipulators (MTMs), and a patient side console, patient side manipulaotrs (PSMs). The proposed impedance-based control method can be utilized for MTMs and PSMs for bilateral teleoperation system. The main challenges are the parameter adjustment of the reference impedance models for the MTM and PSM given the significant dynamics of dVRK and the control of MTM and PSM.

  - To keep the PSM compensate for the heart motion during the whole procedure (both contact and no contact cases), the robot impedance control method can be combined with US imaging-based control algorithms. In other words, an impedance controller for the MTM and a US image-based position controller for the PSM can be developed for telerobotic beating-heart surgery. Both EKF- and NN-based heart motion predictors can be tested for the dVRK. Furthermore, a deep learning-based heart motion predictor can be designed to further increase the accuracy of motion compensation, and test for the dVRK.

- Control for teleoperation system with a flexible surgical robot

  - The dexterity of surgical robots in minimally invasive surgeries can be enhanced by using flexible, thin and lightweight surgical tools. Nevertheless, the requirements of such flexible surgical tools make proposed teleoperation control methods, which are for rigid robots, no longer sufficient. Based on the preliminary study and analysis presented in Appendix A, an impedance control-based method can be used for teleoperation system with a flexible surgical robot in beating-heart surgery.

  - Considering the characteristics of a flexible surgical robot, mounting position and force sensors on the end-effector may be not possible. Therefore, the first step is

modeling the flexible surgical robot for beating-heart surgery, which is generally separated into two parts: a rigid slave actuator and a flexible surgical tool. The position of the surgical tool tip can be measured by using ultrasound images. The contact force between the surgical tool tip and the heart tissue can be estimated based on the model of the flexible slave robot and image-based feedback of the flexible tool's shape under contact load.

o The designed flexible slave robot model can be combined with the proposed teleoperation system that includes robot impedance control and ultrasound image guidance. The reference trajectory for the slave actuator can be calculated based on the flexible robot model so that the surgical tool tip will compensate for the heart motion and follow the position commands of the master robot. By replacing the rigid end-effector used in the previous experimental setups with a flexible surgical tool such as an ablation catheter or a bioptome, the experimental validation is feasible.

o Much of the previous work focused on motion compensation along the primary component of heart motion (i.e., motions were considered along only one DOF) and the experimental setup was simplified compared with the real beating-heart surgeries. To further demonstrate the value of the developed systems, multi-DOF master and slave robots should be considered, and several clinically relevant applications should be selected such as tissue resection, cutting and suturing, and ablation. To begin, a new experimental setup involving surgical tools and muscular tissue with heart structures should be developed. And then the motion compensated teleoperation systems are expected to be able to perform surgical tasks outside or inside the heart tissue.

References

[1]   A. D. Greer, P. M. Newhook, and G. R. Sutherland, "Human-machine interface for robotic surgery and stereotaxy," *IEEE/ASME Trans. Mechatronics*, vol. 13, no. 3, pp. 355–361, 2008.

[2]   J. Burgner *et al.*, "A Telerobotic System for Transnasal Surgery," *IEEE/ASME Trans. Mechatronics*, vol. 19, no. 3, pp. 996–1006, 2014.

[3]   World Health Organization. *Noncommunicable Diseases Progress Monitor*. 2015.

[4]   A. Ruszkowski, O. Mohareri, S. Lichtenstein, R. Cook, and S. Salcudean, "On the feasibility of heart motion compensation on the daVinci® surgical robot for coronary artery bypass surgery: Implementation and user studies," in *IEEE International Conference on Robotics and Automation*, 2015, pp. 4432–4439.

[5]   L. J. Dacey *et al.*, "Perioperative stroke and long-term survival after coronary bypass graft surgery.," *Ann. Thorac. Surg.*, vol. 79, no. 2, pp. 532–536, 2005.

[6]   M. F. Newman, J. L. Kirchner, B. Phillips-Bute, *et al.*, "Longitudinal Assessment of Neurocognitive Function After Coronary-Artery Bypass Surgery," *N. Engl. J. Med.*, vol. 344, no. 6, pp. 395–402, 2001.

[7]   D. Paparella, T. M. Yau, and E. Young, "Cardiopulmonary bypass induced inflammation:

Pathophysiology and treatment. An update," *Eur. J. Cardio-thoracic Surg.*, vol. 21, no. 2, pp. 232–244, 2002.

[8] J. Zeitlhofer *et al.*, "Central nervous system function after cardiopulmonary bypass," *Eur. Heart J.*, vol. 14, pp. 885–890, 1993.

[9] D. C. Bellinger *et al.*, "Developmental and neurological status of children at 4 years of age after heart surgery with hypothermic circulatory arrest or low-flow cardiopulmonary bypass," *Circulation*, vol. 100, no. 5, pp. 526–533, 1999.

[10] G. M. McKhann, M. A. Grega, L. M. Borowicz, W. A. Baumgartner, and O. A. Selnes, "Stroke and encephalopathy after cardiac surgery: An update," *Stroke*, vol. 37, no. 2, pp. 562–571, 2006.

[11] G. D. Angelini, F. C. Taylor, B. C. Reeves, and R. Ascione, "Early and midterm outcome after off-pump and on-pump surgery in Beating Heart Against Cardioplegic Arrest Studies (BHACAS 1 and 2): A pooled analysis of two randomised controlled trials," *Lancet*, vol. 359, pp. 1194–1199, 2002.

[12] J. Fix *et al.*, "Do patients with less than 'echo-perfect' results from mitral valve repair by intraoperative echocardiography have a different outcome?," *Circulation*, vol. 88, no. 5 Pt 2. pp. II39-48, 1993.

[13] D. T. Kettler, R. D. Plowes, P. M. Novotny, N. V. Vasilyev, P. J. Del Nido, and R. D. Howe, "An active motion compensation instrument for beating heart mitral valve surgery," in *IEEE*

International Conference on Intelligent Robots and Systems, 2007, pp. 1290–1295.

[14] L. Cheng, M. Sharifi, and M. Tavakoli, "Towards Robot-Assisted Anchor Deployment in Beating-Heart Mitral Valve Surgery," *Int. J. Med. Robot. Comput. Assist. Surg.*, vol. 14, no. 3, p. e1900, 2018.

[15] L. Cheng, S. Member, J. Fong, and M. Tavakoli, "Semi-Autonomous Surgical Robot Control for Beating-Heart Surgery," in *IEEE 15th International Conference on Automation Science and Engineering*, 2019.

[16] L. Cheng and M. Tavakoli, "Switched-Impedance Control of Surgical Robots in Teleoperated Beating-Heart Surgery," *J. Med. Robot. Res.*, vol. 3, no. 03n04, p. 1841003, 2018.

[17] L. Cheng and M. Tavakoli, "Ultrasound image guidance and robot impedance control for beating-heart surgery," *Control Eng. Pract.*, vol. 81, pp. 9–17, 2018.

[18] L. Cheng and M. Tavakoli, "Neural - Network - Based Heart Motion Prediction for Ultrasound - Guided Beating - Heart Surgery," in *IEEE 15th International Conference on Automation Science and Engineering*, 2019.

[19] L. Cheng and M. Tavakoli, "A Multilateral Impedance-Controlled System for Haptics-Enabled Surgical Training and Cooperation in Beating-Heart Surgery," *Int. J. Intell. Robot. Appl.*, 2019. Minor revision.

[20] M. Tavakoli, R. V. Patel, M. Moallem, and A. Aziminejad, *Haptics for Teleoperated*

Surgical Robotic Systems. New Frontiers in Robotics series, World Scientific, 2008.

[21]   S. G. Yuen, D. T. Kettler, P. M. Novotny, R. D. Plowes, and R. D. Howe, "Robotic motion compensation for beating heart intracardiac curgery," *Int. J. Rob. Res.*, vol. 28, no. 10, pp. 1355–1372, 2009.

[22]   A. H. Zahraee, J. K. Paik, J. Szewczyk, and G. Morel, "Toward the development of a hand-held surgical robot for laparoscopy," *IEEE/ASME Trans. Mechatronics*, vol. 15, no. 6, pp. 853–861, 2010.

[23]   M. Bowthorpe, M. Tavakoli, H. Becher, and R. Howe, "Smith predictor-based robot control for ultrasound-guided teleoperated beating-heart surgery," *IEEE J. Biomed. Heal. Informatics*, vol. 18, no. 1, pp. 157–166, 2014.

[24]   M. Bowthorpe, V. Castonguay-siu, and M. Tavakoli, "Development of a Robotic System to Enable Beating-heart Surgery," *J. Robot. Soc. Japan*, vol. 32, no. 4, pp. 23–30, 2014.

[25]   G. S. Guthart and J. K. Salisbury, "The Intuitive telesurgery system: overview and application," in *IEEE International Conference on Robotics and Automation*, 2000, pp. 618–621.

[26]   M. Tavakoli, A. Aziminejad, R. V. Patel, and M. Moallem, "High-fidelity bilateral teleoperation systems and the effect of multimodal haptics," *IEEE Trans. Syst. Man, Cybern. Part B*, vol. 37, no. 6, pp. 1512–1528, 2007.

[27]   L. Cheng and M. Tavakoli, "Control of a mechatronics-assisted system for surgeries using

flexible tools," in *IEEE 15th International Conference on Automation Science and Engineering*, 2019.

[28] Y. Nakamura, K. Kishi, and H. Kawakami, "Heartbeat synchronization for robotic cardiac surgery," in *IEEE International Conference on Robotics and Automation*, 2001, pp. 2014–2019.

[29] R. Ginhoux, J. A. Gangloff, M. F. de Mathelin, L. Soler, M. M. A. Sanchez, and J. Marescaux, "Beating Heart Tracking in Robotic Surgery Using 500 Hz Visual Servoing, Model Predictive Control and an Adaptive Observer," in *IEEE International Conference on Robotics and Automation*, 2004, pp. 274–279.

[30] R. Ginhoux, J. Gangloff, M. de Mathelin, L. Soler, M. M. Arenas Sanchez, and J. Marescaux, "Active filtering of physiological motion in robotized surgery using predictive control," *IEEE Trans. Robot.*, vol. 21, no. 1, pp. 67–79, 2005.

[31] J. Gangloff, R. Ginhoux, M. de Mathelin, L. Soler, and J. Marescaux, "Model poredictive control for compensation of cyclic organ motions in teleoperated laparoscopic surgery," *IEEE Trans. Control Syst. Technol.*, vol. 14, no. 2, pp. 235–246, 2006.

[32] R. Richa, P. Poignet, and C. Liu, "Three-dimensional Motion Tracking for Beating Heart Surgery Using a Thin-plate Spline Deformable Model," *Int. J. Rob. Res.*, vol. 29, no. 2, pp. 218–230, 2010.

[33] R. Richa, A. P. L. Bó, and P. Poignet, "Towards robust 3D visual tracking for motion

compensation in beating heart surgery," *Med. Image Anal.*, vol. 15, no. 3, pp. 302–315, 2011.

[34]   B. Yang, C. Liu, S. Member, P. Poignet, and W. Zheng, "Motion Prediction Using Dual Kalman Filter for Robust Beating Heart Tracking," in *Engineering in Medicine and Biology Society (EMBC), 2015 37th Annual International Conference of the IEEE*, 2015, pp. 4875–4878.

[35]   W. Bachta, P. Renaud, E. Laroche, A. Forgione, and J. Gangloff, "Active stabilization for robotized beating heart surgery," *IEEE Trans. Robot.*, vol. 27, no. 4, pp. 757–768, 2011.

[36]   Y. Nakajima, T. Nozaki, and K. Ohnishi, "Heartbeat synchronization with haptic feedback for telesurgical robot," *IEEE Trans. Ind. Electron.*, vol. 61, no. 7, pp. 3753–3764, 2014.

[37]   A. Ruszkowski, C. Schneider, O. Mohareri, and S. Salcudean, "Bimanual Teleoperation with Heart Motion Compensation on the da Vinci R Research Kit : Implementation and Preliminary Experiments," in *IEEE International Conference on Robotics and Automation*, 2016, pp. 4101–4108.

[38]   W. Bachta, P. Renaud, L. Cuvillon, E. Laroche, A. Forgione, and J. Gangloff, "Motion prediction for computer-assisted beating heart surgery," *IEEE Trans. Biomed. Eng.*, vol. 56, no. 11, pp. 2551–2563, 2009.

[39]   A. Schweikard, G. Glosser, M. Bodduluri, M. J. Murphy, and J. R. Adler, "Robotic Motion Compensation for Respiratory Movement During Radiosurgery," *Comput. Aided Surg.*, vol.

5, pp. 263–277, 2000.

[40]   S. Mansouri, F. Farahmand, G. Vossoughi, and A. A. Ghavidel, "A Hybrid Algorithm for Prediction of Varying Heart Rate Motion in Computer-Assisted Beating Heart Surgery," *J. Med. Syst.*, vol. 42, no. 10, 2018.

[41]   S. G. Yuen, S. B. Kesner, N. V Vasilyev, P. J. Del Nido, and D. Howe, "3D Ultrasound-Guided Motion Compensation System for Beating Heart Mitral Valve Repair," *Med. Image Comput. Comput. Interv.*, vol. 11, no. Pt 1, pp. 711–719, 2008.

[42]   S. B. Kesner and R. D. Howe, "Robotic catheter cardiac ablation combining ultrasound guidance and force control," *Int. J. Rob. Res.*, vol. 33, no. 4, pp. 631–644, 2014.

[43]   M. Bowthorpe and M. Tavakoli, "Physiological organ motion prediction and compensation based on multirate, delayed, and unregistered measurements in robot-assisted surgery and therapy," *IEEE/ASME Trans. Mechatronics*, vol. 21, no. 2, pp. 900–911, 2016.

[44]   M. Bowthorpe and M. Tavakoli, "Ultrasound-Based Image Guidance and Motion Compensating Control for Robot-Assisted Beating-Heart Surgery," *J. Med. Robot. Res.*, vol. 1, no. 1, p. 1640002, 2016.

[45]   M. Bowthorpe and M. Tavakoli, "Generalized Predictive Control of a Surgical Robot for Beating-Heart Surgery Under Delayed and Slowly-Sampled Ultrasound Image Data," *IEEE Robot. Autom. Lett.*, vol. 1, no. 2, pp. 892–899, 2016.

[46]   P. Moreira, C. Liu, N. Zemiti, and P. Poignet, "Beating Heart Motion Compensation Using

Active Observers and Disturbance Estimation," in *IFAC Symposium on Robot Control International Federation of Automatic Control*, 2012, pp. 741–746.

[47]   P. Moreira, N. Zemiti, C. Liu, and P. Poignet, "Viscoelastic model based force control for soft tissue interaction and its application in physiological motion compensation," *Comput. Methods Programs Biomed.*, vol. 116, no. 2, pp. 52–67, 2014.

[48]   M. Dominici and R. Cortesão, "Model Predictive Control Architectures with Force Feedback for Robotic-Assisted Beating Heart Surgery," in *IEEE International Conference on Robotics and Automation*, 2014, pp. 2276–2282.

[49]   M. Dominici and R. Cortesão, "Cascade Robot Force Control Architecture for Autonomous Beating Heart Motion Compensation with Model Predictive Control and Active Observer," in *IEEE RAS & EMBS International Conference on Biomedical Robotics and Biomechatronics*, 2014, pp. 745–751.

[50]   R. Cortesão and M. Dominici, "Robot Force Control on a Beating Heart," *IEEE/ASME Trans. Mechatronics*, vol. 22, no. 4, pp. 1736–1743, 2017.

[51]   E. E. Tuna, T. J. Franke, O. Bebek, A. Shiose, K. Fukamachi, and M. C. Cavuşoğlu, "Heart Motion Prediction Based on Adaptive Estimation Algorithms for Robotic Assisted Beating Heart Surgery," *IEEE Trans. Robot.*, vol. 29, no. 1, pp. 261–276, 2013.

[52]   Ö. Bebek and M. C. Çavusoglu, "Intelligent Control Algorithms for Robotic-Assisted Beating Heart Surgery," *IEEE Trans. Robot.*, vol. 23, no. 3, pp. 468–480, 2007.

[53] S. G. Yuen, D. P. Perrin, N. V Vasilyev, P. J. Nido, R. D. Howe, and S. Member, "Force Tracking With Feed-Forward Motion Estimation for Beating Heart Surgery," *IEEE Trans. Robot.*, vol. 26, no. 5, pp. 888–896, 2010.

[54] S. B. Kesner, S. Member, R. D. Howe, and S. Member, "Force Control of Flexible Catheter Robots for Beating Heart Surgery," in *IEEE International Conference on Robotics and Automation*, 2011, pp. 1589–1594.

[55] C. R. Wagner, N. Stylopoulos, P. G. Jackson, and R. D. Howe, "The Benefit of Force Feedback in Surgery: Examination of Blunt Dissection," *Presence Teleoperators Virtual Environ.*, vol. 16, no. 3, pp. 252–262, 2007.

[56] O. Mohareri, C. Schneider, and S. Salcudean, "Bimanual telerobotic surgery with asymmetric force feedback: A daVinci® surgical system implementation," in *IEEE International Conference on Intelligent Robots and Systems*, 2014, pp. 4272–4277.

[57] N. Hogan, "Impedance Control: An Approach to Manipulation : Part I — Theory," *ASME, J. Dyn. Syst. Meas. Control*, vol. 107(1), pp. 1–7, 1985.

[58] N. Hogan, "Impedance Control : An Approach to Manipulation : Part II — Implementation," *ASME, J. Dyn. Syst. Meas. Control*, vol. 107(1), pp. 8–16, 1985.

[59] Z. Zarrouk, A. Chemori, and P. Poignet, "Adaptive Force Feedback Control for 3D Compensation of Physiological Motion in Beating Heart Surgery," in *IEEE/RSJ International Conferernce on Intelligent Robots and Systems*, 2010, pp. 1856–1861.

167

[60] K. J. Kuchenbecker and G. Niemeyer, "Induced Master Motion in Force-Reflecting Teleoperation," *J. Dyn. Syst. Meas. Control*, vol. 128, no. 4, pp. 800–810, 2006.

[61] S. G. Yuen, D. T. Kettler, P. M. Novotny, R. D. Plowes, and R. D. Howe, "Robotic Motion Compensation for 3D Ultrasound-Guided Beating Heart Surgery," *Int. J. Rob. Res.*, vol. 28, no. 10, pp. 1355–1372, 2009.

[62] R. O. Bonow *et al.*, "ACC/AHA 2006 Guidelines for the Management of Patients With Valvular Heart Disease," *Circulation*, vol. 114, pp. e84–e231, 2006.

[63] J. M. F. De Oliveira and M. J. Antunes, "Mitral valve repair: better than replacement.," *Heart*, vol. 92, no. 2, pp. 275–281, 2006.

[64] M. K. Rausch, W. Bothe, J. P. E. Kvitting, J. C. Swanson, D. C. Miller, and E. Kuhl, "Mitral valve annuloplasty: A quantitative clinical and mechanical comparison of different annuloplasty devices," *Ann. Biomed. Eng.*, vol. 40, no. 3, pp. 750–761, 2012.

[65] D. D. Glower, "Surgical approaches to mitral regurgitation," *J. Am. Coll. Cardiol.*, vol. 60, no. 15, pp. 1315–1322, 2012.

[66] M. Sharifi, H. Salarieh, S. Behzadipour, and M. Tavakoli, "Tele-echography of moving organs using an Impedance-controlled telerobotic system," *Mechatronics (A J. IFAC)*, vol. 45, pp. 1339–1351, 2017.

[67] J.-J. Slotine and W. Li, *Applied Nonlinear Control*. Englewood Cliffs, NJ: Prantice-Hall, 1991.

[68]   X. Liu, R. Tao, and M. Tavakoli, "Adaptive control of uncertain nonlinear teleoperation systems," *Mechatronics (A J. IFAC)*, vol. 24, pp. 66–78, 2014.

[69]   M. Sharifi, S. Behzadipour, and H. Salarieh, "Nonlinear Bilateral Adaptive Impedance Control with Applications in Telesurgery and Telerehabilitation," *J. Dyn. Syst. Meas. Control*, vol. 138, no. 11, pp. 111010(1–16), 2016.

[70]   M. Sharifi, H. Salarieh, S. Behzadipour, and M. Tavakoli, "Tele - echography of Moving Organs Using an Impedance - controlled Telerobotic System," *Mechronics (A J. IFAC)*, vol. 67, pp. 52–63, 2017.

[71]   S. Chiaverini, B. Siciliano, and L. Villani, "Force/position Regulation of Compliant Robot Manipulators," *Autom. Control. IEEE Trans.*, vol. 39, no. 3, pp. 647–652, 1994.

[72]   G. W. Snedecor and W. G. Cochran, "The Two-Tailed T-Test," in *Statistical Methods (The Lowa State University Press Ames)*, 1967, pp. 59–60.

[73]   S. B. Kesner and R. D. Howe, "Position control of motion compensation cardiac catheters," *IEEE Trans. Robot.*, vol. 27, no. 6, pp. 1045–1055, 2011.

[74]   S. G. Yuen, N. V Vasilyev, J. Pedro, and R. D. Howe, "Robotic Tissue Tracking for Beating Heart Mitral Valve Surgery," *Med. Image Anal.*, vol. 17, no. 8, pp. 1236–1242, 2013.

[75]   A. M. Okamura, "Methods for haptic feedback in teleoperated robot-assisted surgery," *Ind. Robot An Int. J.*, vol. 31, no. 6, pp. 499–508, 2004.

[76]   M. Kitagawa, A. M. Okamura, B. T. Bethea, V. L. Gott, and W. a Baumgartner, "Analysis of Suture Manipulation Forces for Teleoperation with Force Feedback," in 5*th International Conference on Medical Image Computing and Computer Assisted Intervention*, 2002, pp. 155–162.

[77]   S. Hara, Y. Yamamoto, T. Omata, and M. Nakano, "Repetitive control system: A new type servo system for periodic exogenous signals.pdf," *IEEE Trans. Automat. Contr.*, vol. 33, no. 7, pp. 659–669, 1988.

[78]   C. Kempf, M. Tomizuka, R. Horowitz, and W. Messner, "Comparison of Four Discrete-Time Repetitive Control Algorithms," *IEEE Control Syst.*, vol. 13, no. 6, pp. 48–54, 1993.

[79]   O. Bebek and M. C. Cavusoglu, "Model Based Control Algorithms for Robotic Assisted Beating Heart Surgery," in *Proceedings of the 28th Annual International Conference of the IEEE Engineering in Medicine and Biology Society*, 2006, pp. 823–828.

[80]   S. B. Kesner and R. D. Howe, "Discriminating Tissue Stiffness with a Haptic Catheter : Feeling the Inside of the Beating Heart," in *IEEE World Haptics Conference*, 2011, pp. 1–6.

[81]   B. Yang, C. Liu, W. Zheng, and S. Liu, "Motion prediction via online instantaneous frequency estimation for vision-based beating heart tracking," *Inf. Fusion*, vol. 35, pp. 58–67, 2017.

[82]   J. Fong and M. Tavakoli, "Kinesthetic Teaching of a Therapist's Behavior to a

Rehabilitation Robot," *Int. Symp. Med. Robot.*, 2018, pp. 1–6.

[83] C. R. Wagner, D. P. Perrin, R. D. Howe, N. Vasilyev, and P. J. Nido, "Force Feedback in a Three-Dimensional Ultrasound-Guided Surgical Task," in *HAPTICS '06 Proceedings of the Symposium on Haptic Interfaces for Virtual Environment and Teleoperator Systems*, 2005, pp. 43-48.

[84] S. B. Kesner and R. D. Howe, "Discriminating Tissue Stiffness with a Haptic Catheter : Feeling the Inside of the Beating Heart," in *IEEE World Haptics Conference*, 2011, pp. 13–18.

[85] T. Chanthasopeephan, J. P. Desai, A. C. Lau, "Study of Soft Tissue Cutting Forces and Cutting Speeds," *Stud. Health Technol. Inform.*, pp. 56–62, 2004.

[86] Z. Hu, W. Sun, and B. Zhang, "Characterization of Aortic Tissue Cutting Process: Experimental Investigation Using Porcine Ascending Aorta," *J. Mech. Behav. Biomed. Mater.*, vol. 18, pp. 81–89, 2013.

[87] M. C. Çavusoglu, D. Feygin, and F. Tendick, "A Critical Study of the Mechanical and Electrical Properties of the PHANToM Haptic Interface and Improvements for High Performance Control," *Presence*, vol. 11, no. 5, pp. 555–568, 2002.

[88] X. Liu and M. Tavakoli, "Adaptive Inverse Dynamics Four-Channel Control of Uncertain Nonlinear Teleoperation Systems," *Adv. Robot.*, vol. 25, no. 13–14, pp. 1729–1750, 2011.

[89] D. D. Matthew and M. Tavakoli, "Measuring the Dynamic Impedance of the Human Arm

Without a Force Sensor," in *IEEE International Conference on Rehabilitation Robotics*, 2013, pp. 1-8.

[90]   I. Sobel, "An isotropic 3 by 3 image gradient operator," *Mach. Vis. three-demensional Sci.*, vol. 1, no. 1, pp. 23–34, 1990.

[91]   R. O. Duda and P. E. Hart, "Use of the Hough transform to detect lines and cures in pictures," *Commun. Assoc. Comput. Mach.*, vol. 15, no. 1, pp. 11–15, 1972.

[92]   A. H. Jazwinski, *Stochastic Processes and Filtering Theory*. Courier Corporation, 2007.

[93]   J. B. Rawlings and D. Q. Mayne, *Model predictive control*. 2009.

[94]   M. Sharifi, H. Salarieh, S. Behzadipour, and M. Tavakoli, "Beating-heart robotic surgery using bilateral impedance control: Theory and experiments," *Biomed. Signal Process. Control*, vol. 45, pp. 256–266, 2018.

[95]   P. Malysz and S. Sirouspour, "Nonlinear and filtered force/position mappings in bilateral teleoperation with application to enhanced stiffness discrimination," *IEEE Trans. Robot.*, vol. 25, no. 5, pp. 1134–1149, 2009.

[96]   M. Bowthorpe and M. Tavakoli, "GPC-based Teleoperation for Delay Compensation and Disturbance Rejection in Image-guided Beating-heart Surgery," in *IEEE International Conference on Robotics and Automation*, pp. 4875-4880, 2016.

[97]   B. Doucoure, K. Agbossou, and A. Cardenas, "Time series prediction using arti fi cial

wavelet neural network and multi-resolution analysis : Application to wind speed data," *Renew. Energy*, vol. 92, pp. 202–211, 2016.

[98] J. Tang, F. Liu, Y. Zou, W. Zhang, and Y. Wang, "An Improved Fuzzy Neural Network for Traffic Speed Prediction Considering," *IEEE Transactions on Intelligent Transportation Systems*, vol. 18, no. 9, pp. 2340–2350, 2017.

[99] L. Guo, N. Li, F. Jia, Y. Lei, and J. Lin, "A recurrent neural network based health indicator for remaining useful life prediction of bearings," *Neurocomputing*, vol. 240, pp. 98–109, 2017.

[100] I. Bukovsky *et al.*, "A Fast Neural Network Approach to Predict Lung Tumor Motion during Respiration for Radiation Therapy Applications," *Biomed Res. Int.*, pp. 489679(1–13), 2015.

[101] T. P. Teo *et al.*, "Feasibility of predicting tumor motion using online data acquired during treatment and a generalized neural network optimized with of fl ine patient tumor trajectories," *Am. Assoc. Phys. Med.*, vol. 45, no. 2, pp. 830–845, 2018.

[102] V. De Luca *et al.*, "Evaluation of 2D and 3D ultrasound tracking algorithms and impact on ultrasound-guided liver radiotherapy margins," *Am. Assoc. Phys. Med.*, vol. 45, no. 11, pp. 4986–5003, 2018.

[103] F. Takens, "On the numerical determination of the dimension of an attractor," *Dynamical systems and bifurcations*, Springer, Berlin, Heidelberg, pp. 99-106, 1985.

[104] H. Abarbanel. *Analysis of oberserved chaotic data*. Springer Science & Business Media, 2012.

[105] A. M. Fraser, "Information and Entropy in Strange Attractors," *IEEE Trans. Inf. Theory*, vol. 35, no. 2, pp. 245–262, 1989.

[106] N. K. Ahmed, A. F. Atiya, N. El Gayar, and H. EI-Shishiny, "An Empirical Comparison of Machine Learning Models for Time Series Forecasting," *Econometric Reviews*, vol. 29, no. 5, pp. 594-621, 2010.

[107] T. Horiuchi, E. E. Tuna, K. Masamune, and M. C. Çavuşoğlu, "Heart motion measurement with three dimensional sonomicrometry and acceleration sensing," in *IEEE/RSJ International Conferernce on Intelligent Robots and Systems*, pp. 4143–4149, 2012.

[108] B. Fallahi, L. Cheng, and M. Tavakoli. *State Observation and Feedback Control in Robotic Systems for Therapy and Surgery*. In Control System Design of Bio-Robotics and Bio-Mechatronic with Advanced Applications, Elsevier, 2019.

[109] S. S. Nudehi, R. Mukherjee, and M. Ghodoussi, "A shared-control approach to haptic interface design for minimally invasive telesurgical training," *IEEE Trans. Control Syst. Technol.*, vol. 13, no. 4, pp. 588–592, 2005.

[110] B. Khademian and K. Hashtrudi-Zaad, "Shared control architectures for haptic training: Performance and coupled stability analysis," *Int. J. Rob. Res.*, vol. 30, no. 13, pp. 1627–1642, 2011.

[111] B. Khademian and K. Hashtrudi-Zaad, "Dual-user teleoperation systems: New multilateral shared control architecture and kinesthetic performance measures," *IEEE/ASME Trans. Mechatronics*, vol. 17, no. 5, pp. 895–906, 2012.

[112] A. Ghorbanian, S. M. Rezaei, A. R. Khoogar, M. Zareinejad, and K. Baghestan, "A novel control framework for nonlinear time-delayed Dual-master/Single-slave teleoperation," *ISA Trans.*, vol. 52, pp. 268–277, 2013.

[113] M. Shahbazi, S. F. Atashzar, H. A. Talebi, and R. V. Patel, "An expertise-oriented Training framework for robotics-Assisted surgery," in *IEEE International Conference on Robotics and Automation*, pp. 5902–5907, 2014.

[114] M. Shahbazi, S. F. Atashzar, C. Ward, H. A. Talebi, and R. V. Patel, "Multimodal Sensorimotor Integration for Expert-in-the-Loop Telerobotic Surgical Training," *IEEE Trans. Robot.*, vol. doi: 10.11, pp. 1–16, 2018.

[115] M. Sharifi, H. Salarieh, S. Behzadipour, and M. Tavakoli, "Stable Nonlinear Trilateral Impedance Control for Dual-User Haptic Teleoperation Systems with Communication Delays," *J. Dyn. Syst. Meas. Control*, vol. 139, pp. 121012, 2017.

[116] F. Hashemzadeh, M. Sharifi, and M. Tavakoli, "Nonlinear trilateral teleoperation stability analysis subjected to time-varying delays," *Control Eng. Pract.*, vol. 56, pp. 123–135, 2016.

[117] M. Shahbazi, S. Farokh Atashzar, H. A. Talebi, F. Towhidkhah, and M. J. Yazdanpanah, "A sliding-mode controller for dual-user teleoperation with unknown constant time delays,"

Robotica, vol. 31, no. 4, pp. 589–598, 2013.

[118] Z. Li, L. Ding, H. Gao, G. Duan, and C. Y. Su, "Trilateral teleoperation of adaptive fuzzy force/motion control for nonlinear teleoperators with communication random delays," *IEEE Trans. Fuzzy Syst.*, vol. 21, no. 4, pp. 610–624, 2013.

[119] F. Liu, A. Lelevé, D. Eberard, and T. Redarce, "A Dual-user Teleoperation System with Online Authority Adjustment for Haptic Training," *37th Annu. Int. Conf. IEEE Eng. Med. Biol. Soc.*, pp. 1168–1171, 2015.

[120] Z. Li, Y. Xia, D. Wang, D.-H. Zhai, C.-Y. Su, and X. Zhao, "Neural network-based control of networked trilateral teleoperation with geometrically unknown constraints," *IEEE Trans. Cybern.*, vol. 46, no. 5, pp. 1051–1064, 2016.

[121] B. Khademian and K. Hashtrudi-Zaad, "A framework for unconditional stability analysis of multimaster/multislave teleoperation systems," *IEEE Trans. Robot.*, vol. 29, no. 3, pp. 684–694, 2013.

[122] M. Shahbazi, S. F. Atashzar, H. A. Talebi, and R. V. Patel, "Novel Cooperative Teleoperation Framework: Multi-Master/Single-Slave System," *IEEE/ASME Trans. Mechatronics*, vol. 20, no. 4, pp. 1668–1679, 2015.

[123] S. A. Centenero and F. Hernández-alfaro, "3D planning in orthognathic surgery : CAD / CAM surgical splints and prediction of the soft and hard tissues results e Our experience in 16 cases," *J. Cranio-Maxillofacial Surg.*, vol. 40, no. 2, pp. 162–168, 2012.

[124] S. Gillen *et al.*, "Solo-surgical laparoscopic cholecystectomy with a joystick-guided camera device : a case – control study," *Surg. Endosc. Other Interv. Tech.*, vol. 28, pp. 164–170, 2014.

[125] M. E. Allaf *et al.*, "Laparoscopic visual field Voice vs foot pedal interfaces for control of the AESOP robot," *Surg. Endosc. Other Interv. Tech.*, vol. 12, pp. 1415–1418, 1998.

[126] J. Luo, C. Yang, and S. Dai, "Tremor attenuation for surgical robots using support vector machine with parameters optimization," *Tenth Int. Conf. Adv. Comput. Intell.*, pp. 667–672, 2018.

[127] P. Kazanzides, Z. Chen, A. Deguet, G. S. Fischer, R. H. Taylor, and S. P. Dimaio, "An Open-Source Research Kit for the da Vinci Surgical System," in *IEEE International Conference on Robotics and Automation*, pp. 6434–6439, 2014.

[128] A. J. Hung, J. Chen, A. Shah, and I. S. Gill, "Review Article Telementoring and Telesurgery for Minimally Invasive Procedures," *J. Urol.*, vol. 199, no. 2, pp. 355–369, 2018.

[129] S. K. Dwivedy and P. Eberhard, "Dynamic analysis of flexible manipulators, a literature review," *Mech. Mach. Theory*, vol. 41, no. 7, pp. 749–777, 2006.

[130] D. Moschini and P. Fiorini, "Performance of robotic teleoperation system with flexible slave device," in *IEEE International Conference on Robotics and Automation*, 2004, pp. 3696–3701.

[131] M. Mahvash and P. E. Dupont, "Bilateral Teleoperation of Flexible Surgical Robots," in

Proceedings of the New Vistas and Challenges in Telerobotics Workshop, IEEE 2008, International Conference on Robotics & Automation, 2008, pp. 19–23.

[132] M. Tavakoli and R. D. Howe, "Haptic Effects of Surgical Teleoperator Flexibility," *Int. J. Rob. Res.*, vol. 28, no. 10, pp. 1289–1302, 2009.

[133] S. F. Atashzar, M. Shahbazi, H. A. Talebi, and R. V. Patel, "Control of time-delayed telerobotic systems with flexible-link slave manipulators," in *IEEE/RSJ International Conferernce on Intelligent Robots and Systems*, pp. 3035–3040, 2012.

[134] A. Tobergte and A. Albu-Schäffer, "Direct force reflecting teleoperation with a flexible joint robot," in *IEEE International Conference on Robotics and Automation*, pp. 4280–4287, 2012.

[135] G. Zhu, S. S. Ge, and T. H. Lee, "Simulation studies of tip tracking control of a single-link flexible robot based on a lumped model," *Robotica*, vol. 17, no. 1, pp. 71–78, 1999.

[136] B. Siciliano and O. Khatib, *Springer Handbook of Robotics*. 2016.

[137] C. Pacchierotti, M. Abayazid, S. Misra, and D. Prattichizzo, "Teleoperation of steerable flexible needles by combining kinesthetic and vibratory feedback," *IEEE Trans. Haptics*, vol. 7, no. 4, pp. 551–556, 2014.

[138] S. E. Talole, J. P. Kolhe, and S. B. Phadke, "Extended-state-observer-based control of flexible-joint system with experimental validation," *IEEE Trans. Ind. Electron.*, vol. 57, no. 4, pp. 1411–1419, 2010.

Appendix A

Appendix A presents the control of a mechatronics-assisted system with link and joint flexibility and analyzes the transparency of the teleoperation system with a flexible surgical robot. As this work is not extended to beating-heart surgery, the methodology and analysis results are presented in Appendix A. This part is based on paper: L. Cheng and M. Tavakoli, "Control of a Mechatronics-Assisted System for Surgeries with Flexible Tools," IEEE 15th International Conference on Automation Science and Engineering, Vancouver, Canada, 2019.

Control of a Mechatronics-Assisted System for Surgeries with Flexible Tools

Abstract—Flexible and lightweight surgical tools have the potential to significantly increase the dexterity of mechatronics-assisted surgical systems for minimally invasive surgeries. However, the control of a mechatronics-assisted system with the link and joint flexibility is quite challenging and needs to be studied. In this paper, a bilateral impedance-controlled master-slave teleoperation system is considered, where the slave (surgical) robot is flexible. Two reference impedance models are designed for the master and slave robots to control the mechatronics-assisted system. Also, depending on different feedback and feedforward signals, four cases are distinguished. To obtain better transparency of the system, the tuning rules for the impedance parameters for each case are presented and the corresponding transparency measures are analyzed and compared. As a result, by appropriately adjusting the impedance model parameters, ideal position and force tracking can be attained for a teleoperation system with a flexible surgical robot. The theoretical findings are validated in simulations.

I.Introduction

Mechatronic-assisted robotic systems have been employed for surgery to assist the surgeon in performing a surgical procedure which may require the robotic system to have a large variety of extent of automation. Robotic systems for surgery can be classified into three main categories depending on the degree of autonomy granted to it: fully autonomous robotic system, high-level, semi-autonomous robotic system, and low-level, semi-autonomous robotic system.

A typical fully autonomous surgical robot is surgical computer aided design or computer aided manufacturing [1] which is using a computer to realize the process of building the patient model, planning, registration, execution, and follow-up. The preprogrammed robotic systems provide advantages and convenience to surgical procedures. However, not all surgical robotics are designed to replace the surgeon. In fact, most of them are designed to assist the surgeon by providing with versatile tools to extend the surgeon's operation ability. This kind of surgical robotics are semi-autonomous and can be classified by level of autonomy. The high-level semi-autonomous surgical systems generally work side-by-side with the surgeon and provide a joystick or foot pedal to permit the surgeon to control the motion of the surgical systems [2]. The low-level, semi-autonomous surgical systems are operated directly by the surgeon to extend his/her ability such as the elimination of hand tremor [3] and can be used for remote surgery. A typical example is the teleoperation surgical system [4] (e.g. the da Vinci system from Intuitive Surgical Inc., Sunnyvale, CA) where a surgeon interacts with a master robot to perform a desired task on the target tissue by a slave robot (surgical robot). This system can be used to perform minimally invasive surgeries (MIS) [5] with advantages such as small incisions reduce pain and short rehabilitation time.

The dexterity of mechatronic-assisted surgical robots for MIS can be enhanced by using flexible and lightweight tools such as needles, endoscopes, and catheters, while also reducing trauma, which is a benefit for post-operative recovery [6]. Nevertheless, the requirements of such flexible tools make traditional teleoperation control methods [7]–[9], which are for rigid robots, no longer sufficient as flexibility caused by the limited stiffness of transmission mechanisms at the robot joints and the deflection of links may lead to problems such as transient errors, vibrations, and instability [10]. Moreover, for a master-slave teleoperation system, the introduction of slave robot flexibility will inevitably affect the transparency of the system, which consequently reduces the accuracy of position and force tracking performance.

To this end, various control strategies have been proposed for teleoperation system with a flexible slave. In [11], a position-exchange controller for the bilateral teleoperation of flexible surgical robots was proposed. By assuming the master manipulator as a one-degree-of-freedom (1-DOF) rigid link and the slave manipulator as a 1-DOF elastic link and using the position of the master robot and the deformed shape of the flexible slave robot, the controller enabled the master robot to follow the position of the slave robot. In [12], the authors developed a more realistic model for slave link deflections and used the Extended Lawrence Four-Channel control architecture for the teleoperation system. In our previous work [13], to study the effect of a flexible robot on the conventional position error based (PEB) teleoperation and direct force reflection (DFR) teleoperation, the flexible slave manipulator with a flexible link was modeled as a linear joint

stiffness. In [13], we analyzed the transparency measures for the two systems and concluded that perfect position and force tracking might be possible assuming the control gains were infinity.

This paper builds on previous work of the authors [7][13] and developed a impedance-controlled mechatronic-assisted system for surgeries with flexible tools, which includes two impedance models for the master and slave robots, respectively. In the context of teleoperated bilateral impedance control, depending on different feedback and feedforward signals between the master and slave robots, the effect of slave flexibility and the impedance model parameters on the transparency of the system is studied.

II. System Control Method

For a teleoperation system in Fig. 1, bilateral impedance control can be applied by designing two reference impedance models for the master and slave robots, respectively.
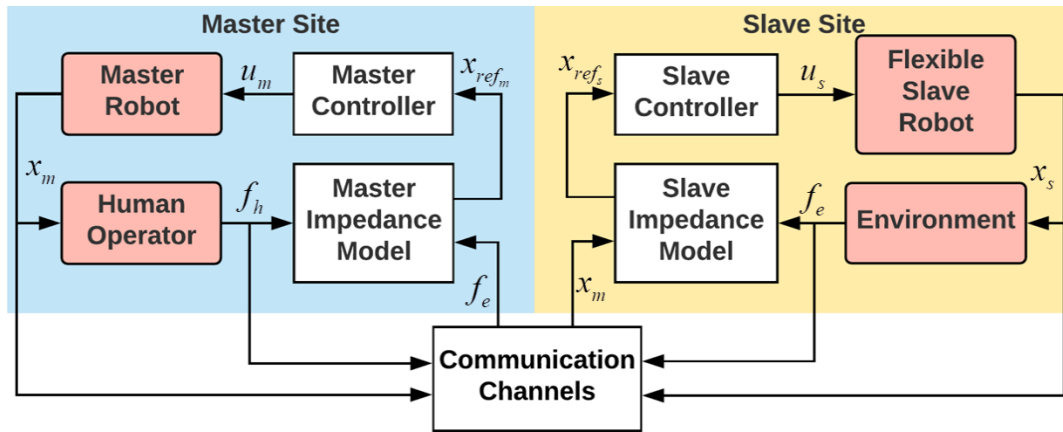

Figure 1. The bilateral impedance-controlled teleoperation system.

By adjusting the parameters of the reference impedance models appropriately, desired dynamical relations between the external forces and the robot positions can be attained. In Fig. 1, f_h is the human-master contact force, and f_e is the slave-environment contact force. Also, x_m and x_s are the positions of the master and slave robots, respectively. The reference impedance models for the master and slave robots provide desired response positions x_{ref_m} and x_{ref_s} to the master and slave position controllers, respectively, so that the robots' trajectories will follow the desired positions (ideally, $x_m = x_{ref_m}$, $x_s = x_{ref_s}$). Note that u_m and u_s are the control signals for the master and slave robots. The position controllers for the two robots are designed as proportional-derivative (PD) controllers. As the stiffness and damping terms in the dynamics of the robots would contribute to the closed-loop equations in the same way as the proportional and derivative terms of the PD position controllers, the dynamics of the robots in the following only involve the inertia terms.

181

A. Criteria for Analysis of Teleoperation Performance

For a transparent teleoperation system, the ideal goals are

$$x_m = x_s, \quad f_h = f_e \tag{1}$$

The relationship between the master the and slave quantities in (1) can be expressed in the s-domain as

$$\begin{bmatrix} F_h(s) \\ -X_s(s) \end{bmatrix} = \underbrace{\begin{bmatrix} 0 & 1 \\ -1 & 0 \end{bmatrix}}_{H} \begin{bmatrix} X_m(s) \\ F_e(s) \end{bmatrix} \tag{2}$$

where the matrix H includes the ideal hybrid parameters. We mainly consider two elements in the matrix H to analyze the teleoperation transparency:

$$h_{11} = \frac{F_h}{X_m}\Big|_{F_e = 0}, \qquad h_{21} = -\frac{X_s}{X_m}\Big|_{F_e = 0} \tag{3}$$

Here, h_{11} is the human operator perceived impedance when the slave is moving freely, and h_{21} is the position tracking fidelity when the slave is moving freely. The ideal values for these two measures are 0 and -1, respectively. Also, we consider two more measures:

$$f_{12} = \frac{F_h}{F_e}\Big|_{X_s = 0}, \qquad z_{11} = \frac{F_h}{X_m}\Big|_{X_s = \text{const}} \tag{4}$$

In the above, f_{12} is the force tracking fidelity when the slave contacts a hard environment, and z_{11} is the human operator's perceived maximum impedance. The ideal values for these two measures are 1 and ∞, respectively.

B. Flexible Slave Model

In Fig. 1, the flexible slave robot can be considered as having a flexible coupling between its motor (actuator) and end-effector (surgical tool). For a 1-DOF system, it has been proved that a flexible link and a flexible joint have similar effects on teleoperation performance [14]. The dynamics of the flexible link are identical to the dynamics of the flexible joint shown in Fig. 2 consisting of a motor and an end-effector that are coupled via a shaft with a finite stiffness. Specifically, two masses connected by a spring are used to model a rotational elastic joint (Fig. 2(a)). By using the equivalent translational model of the flexible joint, the model shown in Fig. 2(a) can be represented by the model shown in Fig. 2(b).

In Fig. 2(b), the motion equations of the flexible joint are

$$M_{sm}\ddot{x}_{sm} + k_{fs}\Delta x_s = f_s \tag{5}$$

$$M_{se}\ddot{x}_{se} - k_{fs}\Delta x_s = -f_e \tag{6}$$

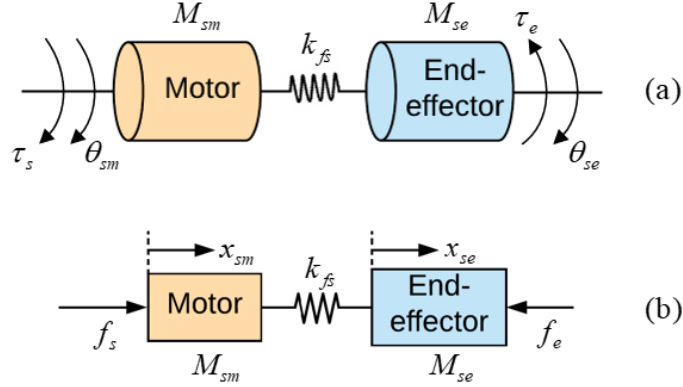$$\Delta x_s = x_{sm} - x_{se} \tag{7}$$

Figure 2. (a) Model of a flexible joint. (b) An equivalent representation of the flexible joint model. Here, M_i, θ_i, and x_i are the inertia, angle, and position. The subscript $i = sm$ is for the motor and $i = se$ is for the end-effector. Also, k_{fs} is the flexible joint's stiffness, τ_s and τ_e are the motor torque (control signal) and the torque applied by the environment, and f_s and f_e are the motor force and the force applied by the environment.

C. Models of the System with Flexible-Joint Slave Robot

The models of the bilateral impedance-controlled teleoperation system with a flexible-joint slave are presented in Fig. 3. The reference impedance models for the master and slave robots are denoted by Z_m and Z_s, respectively. The parameters m_i, c_i, and k_i are the inertia, damping, and stiffness of the reference impedance model. The subscript $i = m$ is for the master, and $i = s$ is for the slave. Also, C_m and C_s are PD position controllers for the master and slave robots, respectively. The control signals u_m and u_s are applied to the robots and result in the movements of the robots. The inertia of the master robot is denoted by M_m.
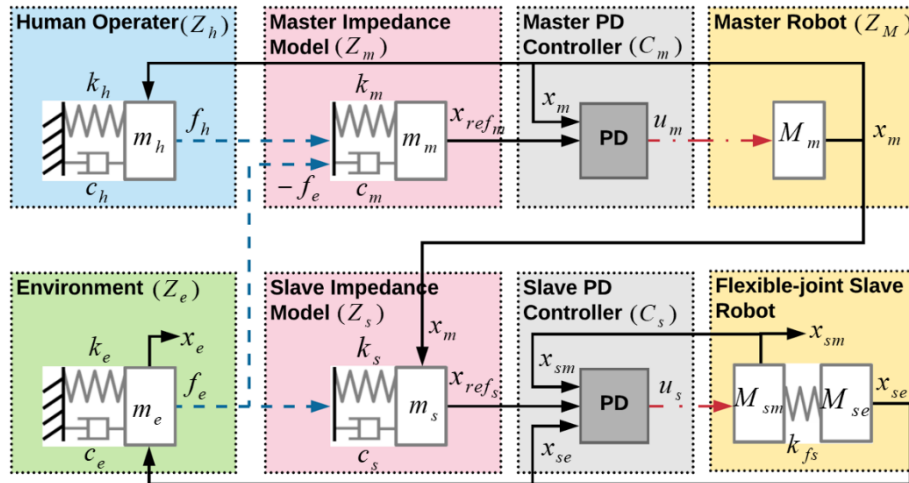

Figure 3. The models of the bilateral impedance-controlled teleoperation system with flexible-joint slave robot. The solid and dashed lines indicate the position and force transfer paths, respectively.

In Fig. 3, the human operator applies forces, f_h, on the master robot, which is an input to the reference impedance model for the master robot. This reference model also receives the slave-environment contact forces, f_e, and generates the desired position for the master robot controller which controls the master robot to track the desired position, x_{ref_m}. On the slave site, the reference impedance model for the slave robot receives the inputs of slave-environment contact forces, f_e, and the master robot position, x_m, and generates the desired position for the slave robot controller, x_{ref_s}. The desired impedance models for the master and slave robots are

$$m_m \ddot{x}_{ref_m} + c_m \dot{x}_{ref_m} + k_m x_{ref_m} = f_h - f_e \tag{8}$$

$$m_s \ddot{\tilde{x}}_{ref_s} + c_s \dot{\tilde{x}}_{ref_s} + k_s \tilde{x}_{ref_s} = -f_e \tag{9}$$

where $\tilde{x}_{ref_s} = x_{ref_s} - x_m$ is the error of the slave impedance model's response with respect to the master robot position. The objective of model (9) is decreasing the error $\tilde{x}_{ref_s}$ so that x_{ref_s} follows x_m. Here, x_{ref_s} is the reference position for the flexible slave. When x_{ref_s} is the reference position for the slave motor x_{sm}, the position of the slave end-effector x_{se} may not accurately follow the master robot position x_m. To achieve perfect position tracking between the slave end-effector x_{se} and the master robot x_m, $\tilde{x}_{ref_s}$ should be adjusted. By combining (6) and (7), x_{sm} is given by

$$x_{sm} = x_{se} + \frac{f_e}{k_{fs}} + \frac{m_{se}}{k_{fs}} \ddot{x}_{se} \tag{10}$$

Since the desired position of the slave end-effector x_{se} is x_m, the reference trajectory for x_{sm} becomes

$$x_m^* = x_m + \frac{f_e}{k_{fs}} + \frac{m_{se}}{k_{fs}} \ddot{x}_m \tag{11}$$

Therefore, the adjusted position error in (9) is

$$\tilde{x}_{ref_s} = x_{ref_s} - x_m^* \tag{12}$$

D.   Framework Overview

The s-domain representation of the impedance- controlled teleoperation system is presented in Fig. 4. With the designed impedance models for the master and slave robots, we have $C_1 = Z_s$, $C_2 = 1$, $Z_m^{-1} = \frac{1}{m_m s^2 + c_m s + k_m}$, and $Z_s^{-1} = \frac{1}{m_s s^2 + c_s s + k_s}$. Also, the master robot, the slave motor, and the slave end-effector are represented as the impedance $Z_M^{-1} = \frac{1}{M_m s^2}$, $Z_{sm}^{-1} = \frac{1}{M_{sm} s^2}$, and $Z_{se}^{-1} = \frac{1}{M_{se} s^2}$, respectively. The PD position controllers C_m and C_s (corresponding to the rigid slave) are expressed as

$$C_m = k_{d_m} s + k_{p_m}, \quad C_s = k_{d_s} s + k_{p_s} \tag{13}$$

In the present of flexible-joint slave, C_s is broke into two separate controllers C_{sm} and C_{se}. In addition, C_3 and C_4 are two position gains. The control laws for the master and slave robots are given by

$$U_m = C_3 X_{ref_m} - C_m X_m \tag{14}$$

$$U_s = C_4 X_{ref_s} - C_{sm} X_{sm} - C_{se} X_{se} \tag{15}$$

where C_{sm} and C_{se} are PD position controllers for the slave motor and the slave end-effector. Generally, $C_3 = C_m$ and $C_4 = C_s$ are designed to achieve position tracking. For simplicity, in this paper $C_m = C_s = C_{sm} = C_{se} = k_d s + k_p$ is chosen, where $k_d = 2\alpha M_{sm}$ and $k_p = \alpha^2 M_{sm}$ ($\alpha > 0$) are designed to guarantee critical damping.

Based on the possible communication signals for both feedback and feedforward, four cases are distinguished and listed in Table I. The position and the external force of the slave end-effector x_{se} and f_e may be difficult to be measured directly by sensors. Therefore, an extended state observer may be used to estimate these quantities [15][16] so that all variables are available in each case.
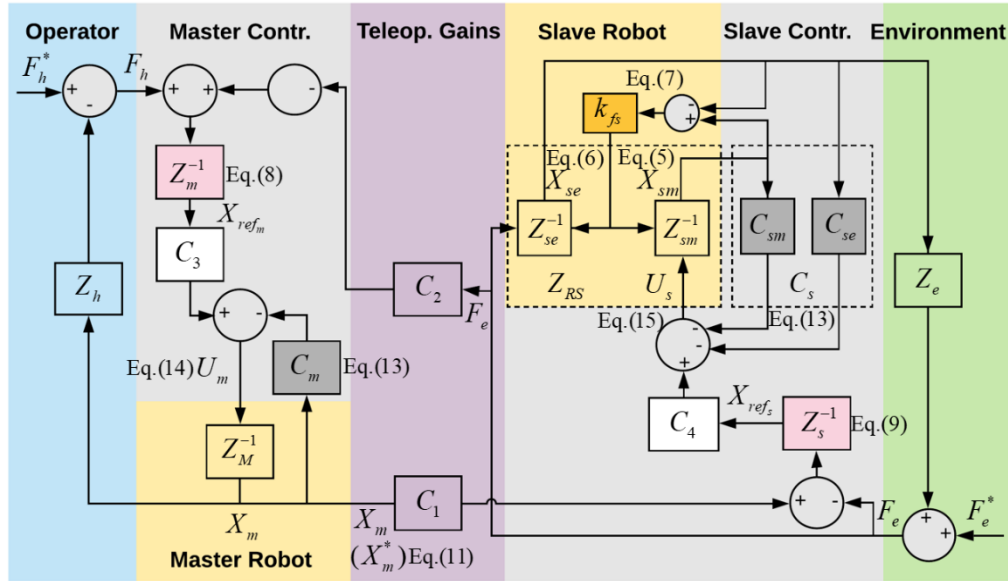

Figure 4. The bilateral impedance-controlled teleoperation architecture.

TABLE I. POSSIBLE COMMUNICATION SIGNALS

Communication Signals	Case 1	Case 2	Case 3	Case 4
Feedback	x_{sm}, f_e	x_{sm}, f_e	x_{se}, f_e	x_{sm}, x_{se}, f_e
Feedforward	x_m	x_m^*	x_m	x_m^*, x_m

III. Transparency Measures

To simplify the expressions of the results, some substitutions are introduced $\omega_0 = \sqrt{\frac{k_{fs}}{M_{se}}}$, $R_s = \frac{M_{se}}{M_{sm}}$, $r_s = \frac{m_s}{M_{sm}}$, $r_m = \frac{m_m}{M_{sm}}$. For the reference impedance models Z_m and Z_s, the natural frequencies and the damping ratios are given by $\omega_m = \sqrt{k_m/m_m}$, $\omega_s = \sqrt{k_s/m_s}$, and $\zeta_m = c_m/2\sqrt{m_m k_m}$, $\zeta_s = c_s/2\sqrt{m_s k_s}$, respectively. Assuming $\zeta_m = \zeta_{sm} = 1$, we have $Z_m = m_m(s + \omega_m)^2$ and $Z_s = m_s(s + \omega_s)^2$. Therefore, the adjustable parameters are r_m, r_s, ω_m, and ω_s.

A. Rigid Case

When the slave is rigid, to achieve better performance, $C_3 = Z_M + C_m$ and $C_4 = Z_{RS} + C_s$ are chosen, where Z_{RS} ($= \frac{1}{M_s s^2}$, where M_s is the inertia of the rigid slave robot) denotes the impedance of the rigid slave robot. As a result, the performance measures are $h_{11} = Z_m$, $h_{21} = -1$, $\frac{1}{f_{12}} = \frac{Z_s}{Z_m + Z_s}$, $z_{11} = Z_m + Z_s$. To ensure the transfer function is proper, $1/f_{12}$ is used. If the impedance models for the master and slave robots are chosen to be $Z_m = 0$ and $Z_s = \infty$, the above performance measures will equal the ideal values.

B. Flexible Case 1

For flexible case, as the slave robot includes two parts, $C_4 = \lambda_1 Z_{sm} + \lambda_2 Z_{se} + C_{sm} + C_{se}$ is chosen, where λ_1 and λ_2 are two coefficients, which can be selected as $\lambda_1 = 1$ and $\lambda_2 = 0$, for simplicity. In case 1, with feedback of x_{sm}, C_{se} is zero and $C_4 = Z_{sm} + C_{sm}$. Also, $C_3 = Z_M + C_m$ is chosen. Note that given the flexible salve model (5)-(7), the slave position X_s defined in (3) and (4) should be changed as the position of the slave end-effector x_{se}. The transparency measures are

$$h_{11} = Z_m,$$

$$h_{21} = \frac{-1}{1 + \left(\frac{s}{\omega_0}\right)^2 + R_s\left(\frac{s}{s+\alpha}\right)^2},$$

$$\frac{1}{f_{12}} = \frac{1}{1 + \frac{r_m}{r_s}\left(\frac{s+\omega_m}{s+\omega_s}\right)^2 + \frac{r_m}{R_s}\left(\frac{s+\omega_m}{\omega_0}\right)^2 + r_m\left(\frac{s+\omega_m}{s+\alpha}\right)^2},$$

$$z_{11} = Z_m + m_s \frac{(s+\omega_s)^2}{1 + \frac{r_s}{R_s}\left(\frac{s+\omega_s}{\omega_0}\right)^2 + r_s\left(\frac{s+\omega_s}{s+\alpha}\right)^2}.$$

If the stiffness of the flexible spring k_{fs} is sufficiently large and the inertia rate R_s is sufficiently small, h_{21} will equal -1, which matches the measure in the rigid case.

C. Flexible Case 2

With feedback of x_{sm} and feedforward of x_m^*, the controllers remain the same as those in Case 1. The four transparency measures are

$$h_{11} = Z_m,$$

$$h_{21} = -\frac{1+\left(\frac{s}{\omega_0}\right)^2}{1+\left(\frac{s}{\omega_0}\right)^2+R_s\left(\frac{s}{s+\alpha}\right)^2},$$

$$\frac{1}{f_{12}} = \frac{1+\left(\frac{s}{\omega_0}\right)^2}{1+\left(\frac{s}{\omega_0}\right)^2+\frac{r_m}{r_s}\left(\frac{s+\omega_m}{s+\omega_s}\right)^2+r_m\left(\frac{s+\omega_m}{s+\alpha}\right)^2},$$

$$z_{11} = Z_m + m_s\frac{(s+\omega_s)^2\left(1+\left(\frac{s}{\omega_0}\right)^2\right)}{1+r_s\left(\frac{s+\omega_s}{s+\alpha}\right)^2}.$$

D. Flexible Case 3

With feedback of x_{se}, it can be noted that C_{sm} is zero. Hence, $C_4 = Z_{sm} + C_{se}$. Also, $C_3 = Z_M + C_m$ is chosen. The four transparency measures in this case are

$$h_{11} = Z_m,$$

$$h_{21} = \frac{-1}{1+\left(R_s+\left(\frac{s}{\omega_0}\right)^2\right)\left(\frac{s}{s+\alpha}\right)^2},$$

$$\frac{1}{f_{12}} = \frac{1}{1+\frac{r_m}{r_s}\left(\frac{s+\omega_m}{s+\omega_s}\right)^2+r_m\left(\frac{s+\omega_m}{s+\alpha}\right)^2\left(1+\frac{1}{R_s}\left(\frac{s}{\omega_0}\right)^2\right)},$$

$$z_{11} = Z_m + m_s\frac{(s+\omega_s)^2}{1+r_s\left(\frac{s+\omega_s}{s+\alpha}\right)^2\left(1+\frac{1}{R_s}\left(\frac{s}{\omega_0}\right)^2\right)}.$$

E. Flexible Case 4

With feedback of x_{sm}, x_{se} and feedforward of x_m^*, x_m, the reference impedance models for the slave motor and the slave end-effector are given by

$$m_s\ddot{\tilde{x}}_{ref_{sm}} + c_s\dot{\tilde{x}}_{ref_{sm}} + k_s\tilde{x}_{ref_{sm}} = -f_e \tag{13}$$

$$m_s\ddot{\tilde{x}}_{ref_{se}} + c_s\dot{\tilde{x}}_{ref_{se}} + k_s\tilde{x}_{ref_{se}} = -f_e \tag{14}$$

where $\tilde{x}_{ref_{sm}} = x_{ref_{sm}} - x_m^*$ and $\tilde{x}_{ref_{se}} = x_{ref_{se}} - x_m$. Note that $x_{ref_{sm}}$ is the reference trajectory for the slave motor x_{sm}, and $x_{ref_{se}}$ is the reference trajectory for the slave end-effector x_{se}. In addition, C_4 is replaced by C_{4sm} and C_{4se}. The control law for the flexible slave robot is defined as $U_s = C_{4sm}X_{ref_{sm}} + C_{4se}X_{ref_{se}} - C_{sm}X_{sm} - C_{se}X_{se}$, where $C_{4sm} = Z_{sm} + C_{sm}$, and $C_{4se} = Z_{se} + C_{se}$. The resulting four measures of transparency are

$$h_{11} = Z_m,$$

$$h_{21} = -1,$$

$$\frac{1}{f_{12}} = \frac{2+(R_s-1)\left(\frac{s}{s+\alpha}\right)^2+\left(\frac{s}{\omega_0}\right)^2}{\left(1+\frac{r_m}{r_s}\left(\frac{s+\omega_m}{s+\omega_s}\right)^2\right)\left(2+(R_s-1)\left(\frac{s}{s+\alpha}\right)^2\right)+\left(\frac{s}{\omega_0}\right)^2+r_m\left(\frac{s+\omega_m}{s+\alpha}\right)^2},$$

187

$$z_{11} = Z_m + m_s \frac{(s+\omega_s)^2\left(2+\left(\frac{s}{\omega_0}\right)^2+(R_s-1)\left(\frac{s}{s+\alpha}\right)^2\right)}{2+r_s\left(\frac{s+\omega_s}{s+\alpha}\right)^2+(R_s-1)\left(\frac{s}{s+\alpha}\right)^2}.$$

IV. Transparency Analysis

A. Transparency with no Actuator Saturation

By assuming the control gain α is infinitely large, the idealized transparency measures for the four flexible cases are listed in Table II, which present that perfect free-motion position tracking can be attained. For Case 1, position tracking is satisfactory only at low frequencies ($\omega < \omega_0$), while for the other cases, position tracking is satisfactory without frequency limitations. For hard-contact force tracking ($1/f_{12}$), it can be noted that the term of $P = \frac{r_m}{r_s}\left(\frac{s+\omega_m}{s+\omega_s}\right)^2$ is involved in every denominator of the four cases. If P can be adjusted to be zero, perfect hard-contact force tracking can be achieved (For Case 1, force tracking is satisfactory at low frequencies; for other cases, force tracking is satisfactory at any frequencies).

TABLE II.   IDEALIZED TRANSPARENCY MEASURES

| Item	h_{11}	h_{21}	$1/f_{12}$	z_{11}
Case 1	Z_m	$\dfrac{-1}{1+\left(\frac{s}{\omega_0}\right)^2}$	$\dfrac{1}{1+P+\frac{r_m}{R_s}\left(\frac{s+\omega_m}{\omega_0}\right)^2}$	$Z_m+\dfrac{Z_s k_s}{Z_s+k_s}$
Case 2	Z_m	-1	$\dfrac{1+\left(\frac{s}{\omega_0}\right)^2}{1+\left(\frac{s}{\omega_0}\right)^2+P}$	$Z_m+Z_s\left(1+\left(\frac{s}{\omega_0}\right)^2\right)$
Case 3	Z_m	-1	$\dfrac{1}{1+P}$	Z_m+Z_s
Case 4	Z_m	-1	$\dfrac{2+\left(\frac{s}{\omega_0}\right)^2}{2(1+P)+\left(\frac{s}{\omega_0}\right)^2}$	$Z_m+Z_s\left(1+\frac{1}{2}\left(\frac{s}{\omega_0}\right)^2\right)$
Ideal Value	0	-1	1	∞

B. Parameter Adjustment for Robot Impedance Models

To find the effect of r_m, r_s, ω_m, and ω_s on the shape of $1/f_{12}$, as an example, the magnitudes of $1/f_{12}$ for case 3 are plotted in Fig. 5(a) when $r_m/r_s = 1, 0.5, 0.1$, $\omega_s = 100$ rad/s, $\omega_m = 1, 50, 100$ rad/s. Furthermore, when r_m/r_s is constant, small ω_m brings $1/f_{12}$ closer to the ideal value 1 (Fig. 5(b)).
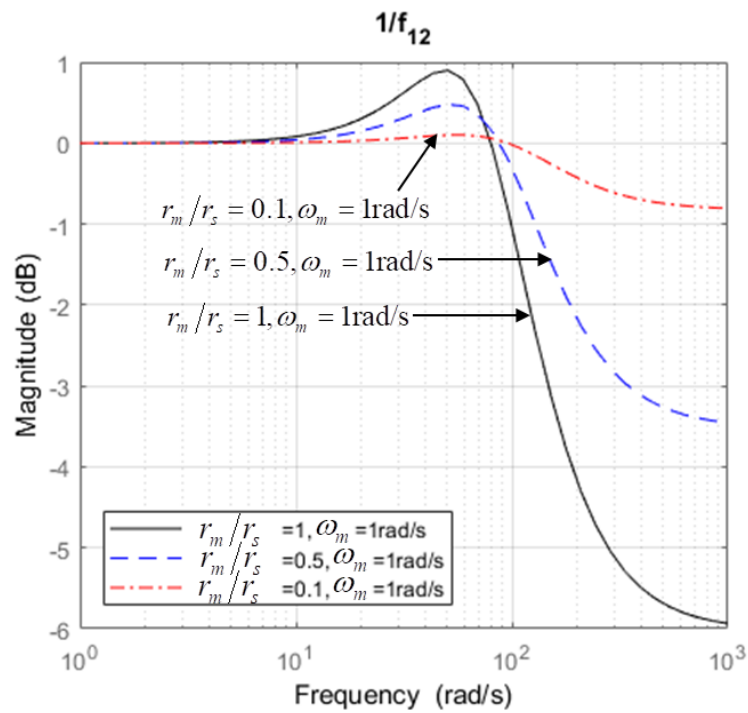
When ω_m is constant, small r_m/r_s not only brings $1/f_{12}$ closer to the ideal value 1, but also provides a wider frequency range of force tracking (Fig. 5(c)). Therefore, the frequency range of ω_m can be improved by decreasing r_m/r_s. In other words, if $\omega_m = \omega_s$ is desired, r_m/r_s has to be very small.

(a)

(b)

(c)

190
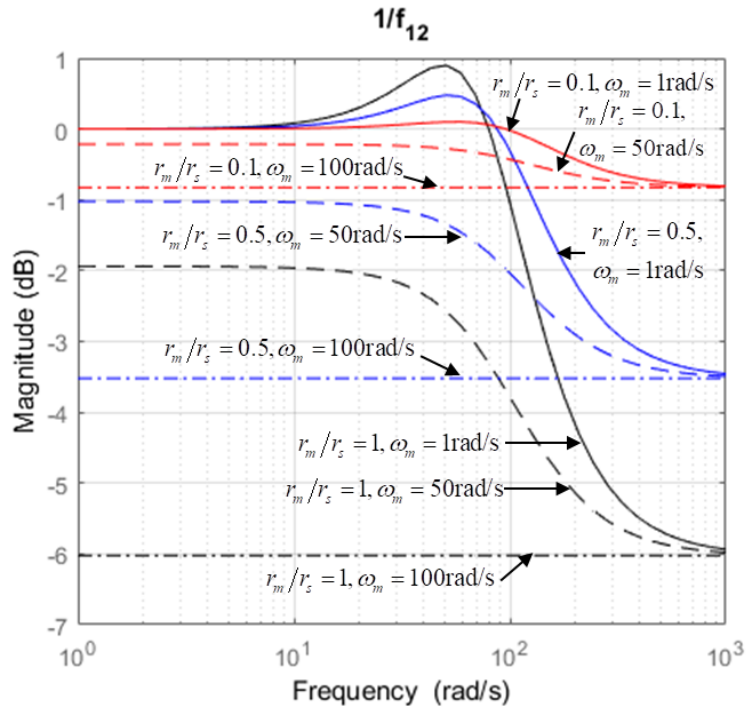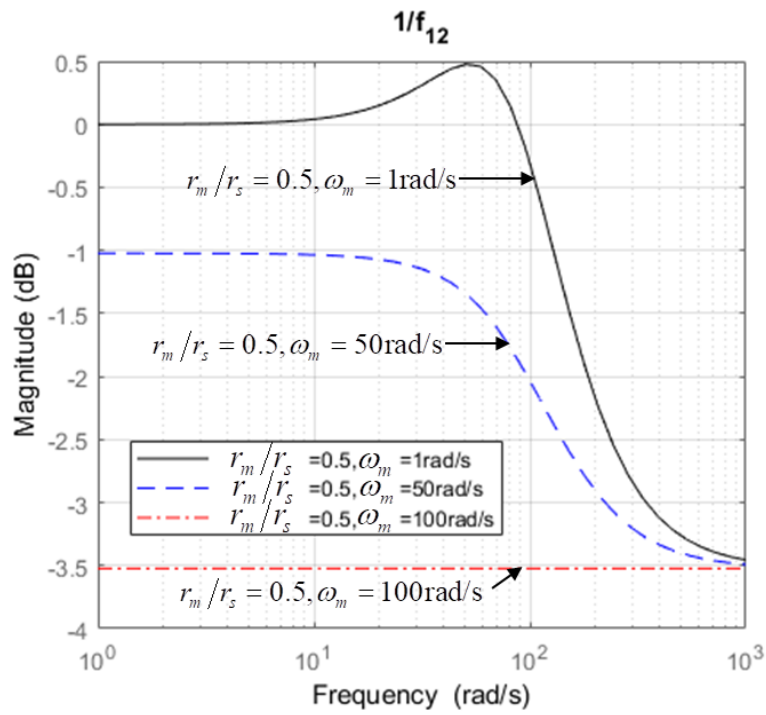
Figure 5. (a) Magnitudes of $1/f_{12}$ for case 3 (a) when $r_m/r_s = 1, 0.5, 0.1$, $\omega_s = 100$ rad/s, $\omega_m = 1$, 50, 100 rad/s. (b) When r_m/r_s is a constant (as an exapmple $r_m/r_s = 0.5$), the magnitude of $1/f_{12}$ with $\omega_m = 1, 50, 100$ rad/s. (c) When ω_m is 1 rad/s, the magnitude of $1/f_{12}$ with $r_m/r_s = 1, 0.5, 0.1$.
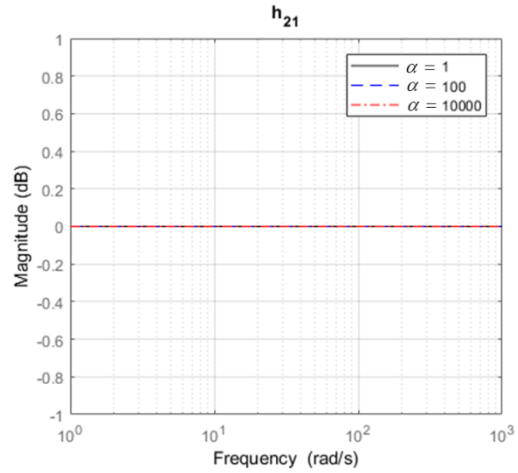
C. Position Tracking Considering Actuator Saturation

In practice, however, the control gain α cannot be infinitely large, which will inevitably influence the system's transparency measures. To investigate the effect of α on the shape of position tracking, the magnitudes of h_{21} are plotted in Fig. 6 when $\omega_0 = 100$ rad/s, $R_s = 0.1$ (lightweight slave end-effector), and $\alpha = 1, 100, 10000$. For Case 1 and 2, regardless of the control gain α, position tracking is attained only at low frequencies ($\omega < \omega_0$). Also, the frequency range of position tracking for Case 2 is a bit wider than that for Case 1. In Case 3 the position tracking performance is better than the first two cases as its maximum frequency can be improved by increasing the value of α. In Case 4, perfect position tracking is achieved at any frequencies and with any α.
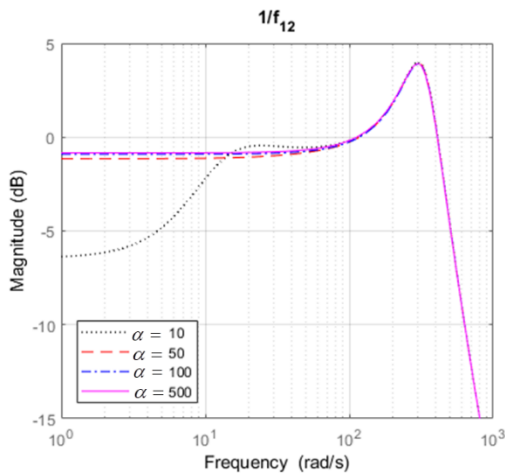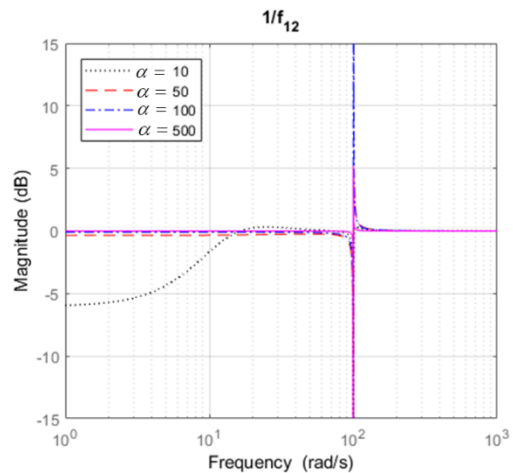

(a)

(b)
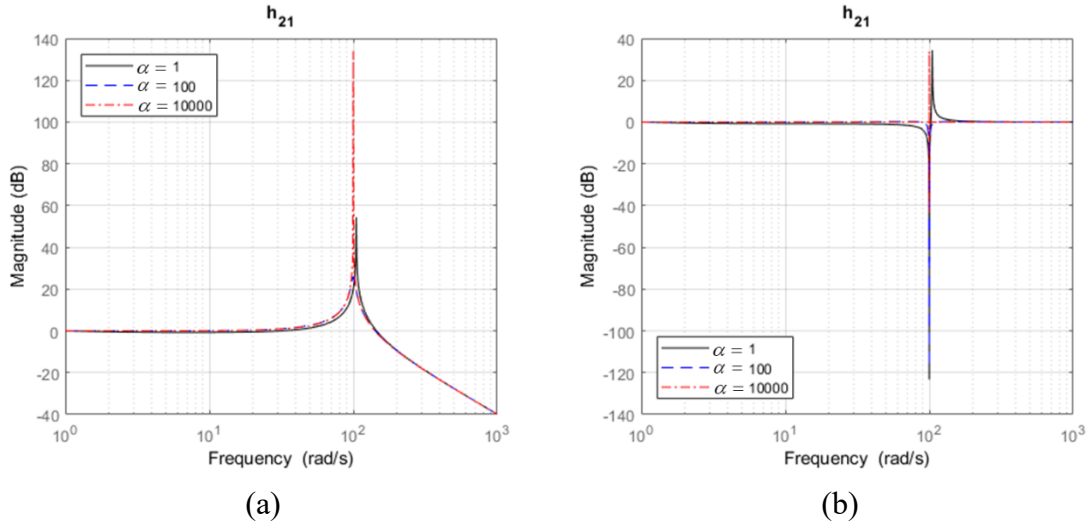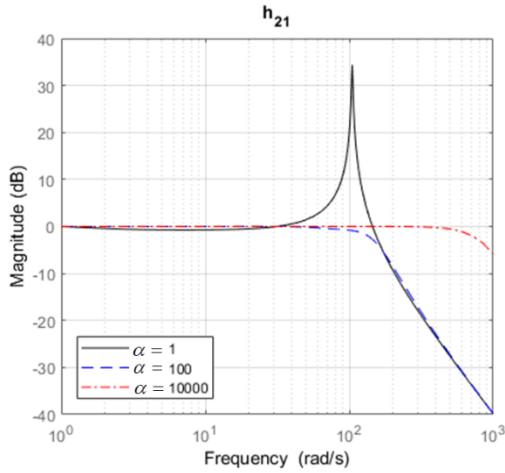
(c)　　　　　　　　　　　　　　(d)

Figure 6. Magnitudes of h_{21} for (a) Case 1, (b) Case 2, (c) Case 3, and (d) Case 4 when $\omega_0 = 100$ rad/s, $R_s = 0.1$, and $\alpha = 1, 100, 10000$.

D. Force Tracking Considering Actuator Saturation

To further investigate the effect of α on the shape of $1/f_{12}$ when r_m/r_s is very small and $\omega_m = \omega_s$, the magnitudes of $1/f_{12}$ for the four cases are plotted in Fig. 7 with $r_m = 0.01$, $R_s = 0.1$, $r_s = 10$, $\omega_m = \omega_s = \omega_0 = 100$ rad/s, $\alpha = 10, 50, 100, 500$.
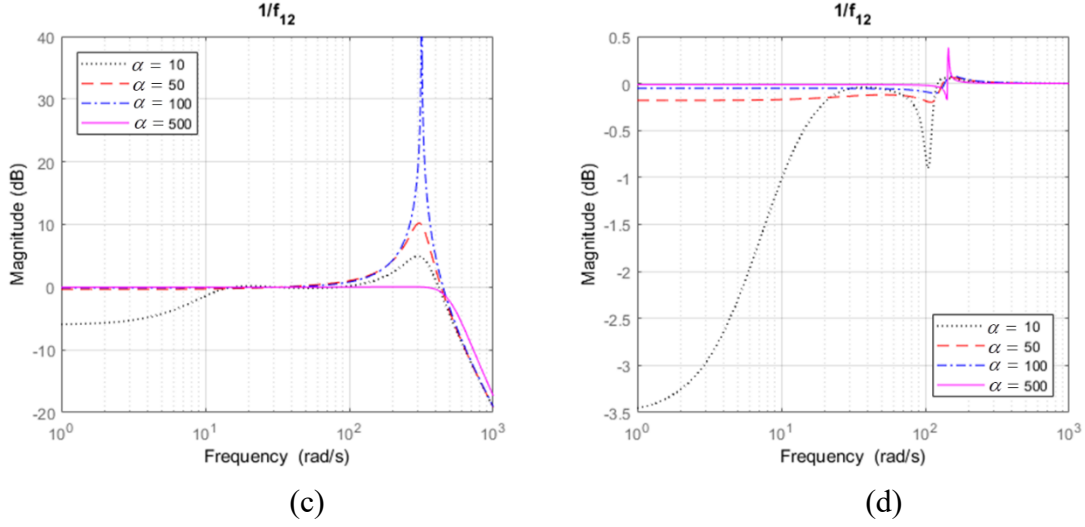

(a)　　　　　　　　　　　　　　(b)

Figure 7. Magnitudes of $1/f_{12}$ for Case (a) 1, (b) 2, (c) 3, and (d) 4 when $r_m = 0.01$, $R_s = 0.1$, $r_s = 10$, $\omega_m = \omega_s = \omega_0 = 100$ rad/s, $\alpha = 10, 50, 100, 500$.

When α is small (=10), the frequency ranges for ideal force tracking are limited for all cases, while when α is moderate or more (close to or greater than ω_m), these frequency ranges become wider and remain steady regardless of α. Moreover, in Case 1 and 2, force tracking is possible only at low frequencies (the frequency range of force tracking for Case 2 is a little wider than that for Case 1). In Case 3 (Fig. 7(c)), force tracking is satisfactory only at low frequencies, but the frequency range of $1/f_{12}$ can be improved by increasing α. In Case 4, good force tracking is achieved at any frequencies when α is not too small. Therefore, given very small r_m/r_s, perfect force tracking is possible without infinitely large α. Ideally, if $r_m = 0$ and $r_s = \infty$ are chosen, perfect free-motion transmitted impedance (h_{11}) can be attained for all cases, and perfect hard-contact transmitted impedance (z_{11}) can be achieved except for Case 1 (For Case 1, $z_{11} = k_{fs}$).

Based on the above analysis, it can be concluded that (a) for h_{11}, in all cases, the human operator will only feel the reference impedance model for the master robot (Z_m), which means decreasing m_m and ω_m in Z_m will lead to ideal free-motion transmitted impedance; (b) for h_{21}, the ideal position tracking for Case 4 can be attained at any frequencies regardless of α; for Case 3, the performance is better than those of Case 1 and 2 as the maximum frequency can be improved by increasing α. Also, regardless of α, the frequency range of position tracking for Case 2 is a bit wider than that for Case 1; (c) for $1/f_{12}$, to obtain a wider frequency range of force tracking, a moderate α (close to or greater than ω_m) is needed for all cases. Like h_{21}, the ideal force tracking is satisfactory for Case 4 at any frequencies and for the other cases at low frequencies. Moreover, the maximum frequency for Case 3 can be improved by increasing α; (d) for z_{11}, except Case 1, the human operator will only feel the impedance models for the master and slave robots. In Case 1, however, the slave flexibility will be transmitted to the human operator.

V. Simulation Study

193

The teleoperation system is simulated in MATLAB and Simulink. As an example, the results for Case 1 are presented in Fig. 8. Here, $M_m = M_{sm} = 1$ kg, $M_{se} = 0.1$ kg, $m_m = 0.01$ kg, $m_s = 10$ kg, $c_m = 2$ Ns/m, $c_s = 2 \times 10^3$Ns/m, $k_m = 100$ N/m, $k_s = 10^5$ N/m, $k_{fs} = 10^3$ N/m, and $\alpha = 100$ are chosen. Therefore, $R_s = 0.1$, $r_m = 0.01$, $r_s = 10$, $\zeta_m = \zeta_s = 1$, $\omega_m = \omega_{sm} = \omega_0 = 100$ rad/s. To achieve a rich and uniform spectrum over the frequency range of interest, the input f_h was designed to be the sum of several sinusoids evenly spaced in the frequency domain from 0 to 1000 rad/s. The simulations for free-motion and hard-contact were implemented when $k_e = 0$ N/m and $k_e = 10^6$ N/m, respectively. The recorded data from Simulink were applied spectral analysis to obtain the estimated magnitudes of the measures of transparency (Fig. 8). Without infinite α all the estimated lines (dotted) closely follow the idealized measures listed in the second row of Table II (solid).
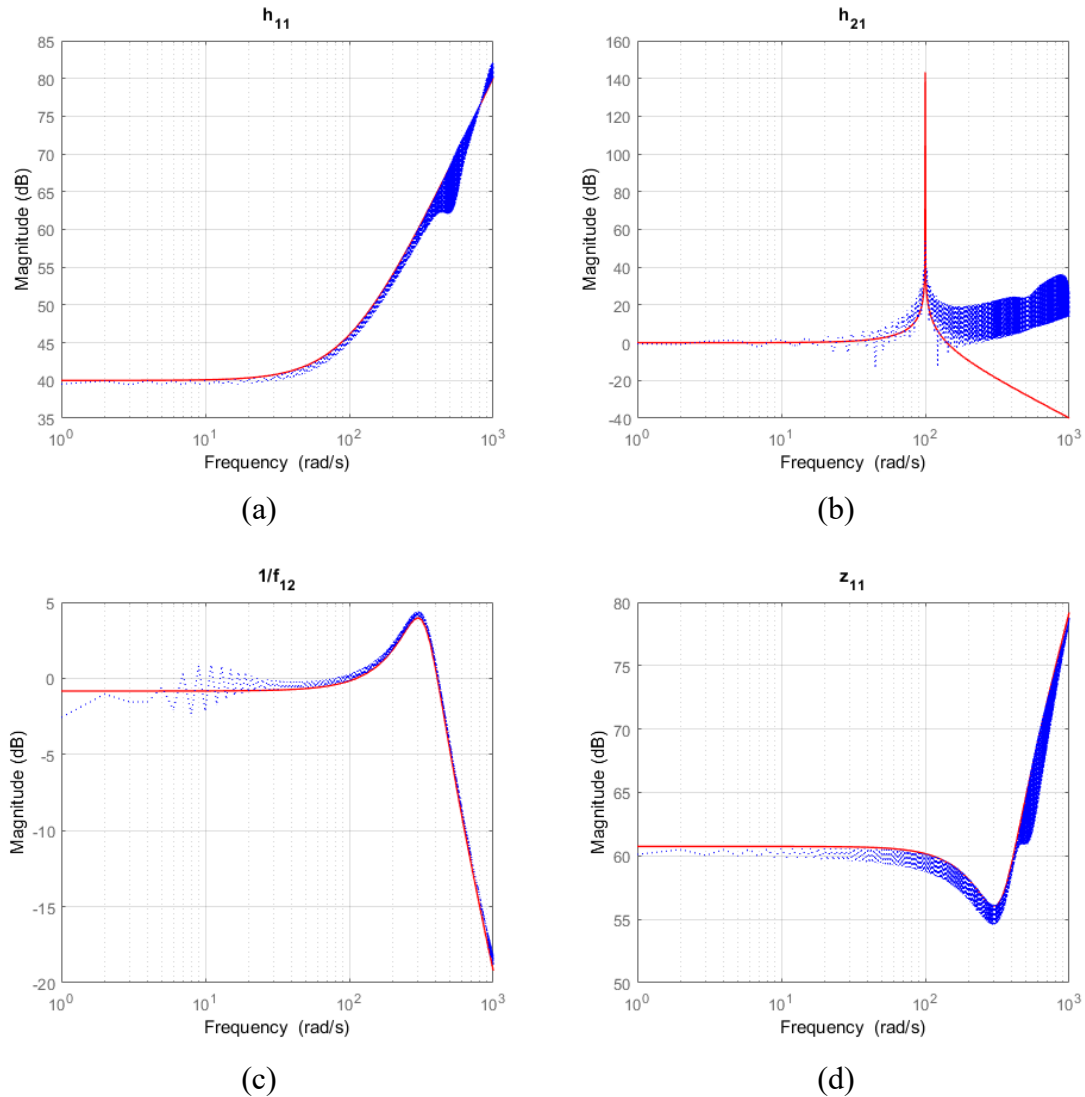

Figure 8. Magnitudes of (a) h_{11}, (b) h_{21}, (c) $1/f_{12}$, and (d) z_{11} for case 1.

VI. Conclusion

The control of a mechatronic-assisted system for surgeries with flexible tools and the effect of robot flexibility on the proposed bilateral impedance-controlled teleoperation system with different feedback and feedforward signals were studied. The parameter adjustment of the impedance models for the master and slave robots was analyzed and can be concluded that r_m/r_s should be very small if $\omega_m = \omega_s$ is desired. With the adjustment, it was shown that with the knowledge of the slave motor and tip positions (Case 4), perfect position and force tracking could be attained at any frequencies regardless of the control gain α (as long as α is not too small); otherwise, position and force tracking are possible only at low frequencies. Moreover, with the feedback of the slave tip position (Case 3), the frequency ranges of the measures can be improved by increasing the control gain. Also, regardless of the control gain, when the feedback position only involved the slave motor position, the case with accurate reference position for the slave motor (Case 2) has a bit wider frequency ranges of the measures than the other case (Case 1). By comparing the transparency measures of the proposed bilateral impedance-controlled teleoperation system with the measures of the conventional PEB and DFR teleoperation architectures presented in [13], the conclusion can be drawn that by using the adjusted parameters of the reference impedance models for the master and slave robots and considering actuator saturation, the proposed mechatronic-assisted teleoperation system can attain ideal transparency.

Acknowledgements

References

[1]   S. A. Centenero and F. Hernández-alfaro, "3D planning in orthognathic surgery : CAD / CAM surgical splints and prediction of the soft and hard tissues results e Our experience in 16 cases," *J. Cranio-Maxillofacial Surg.*, vol. 40, no. 2, pp. 162–168, 2012.

[2]   S. Gillen *et al.*, "Solo-surgical laparoscopic cholecystectomy with a joystick-guided camera device : a case – control study," *Surg. Endosc. Other Interv. Tech.*, vol. 28, pp. 164–170, 2014.

[3]   J. Luo, C. Yang, and S. Dai, "Tremor attenuation for surgical robots using support vector machine with parameters optimization," *2018 Tenth Int. Conf. Adv. Comput. Intell.*, pp. 667–672, 2018.

[4]   P. Kazanzides, Z. Chen, A. Deguet, G. S. Fischer, R. H. Taylor, and S. P. Dimaio, "An Open-Source Research Kit for the da Vinci Surgical System," *2014 IEEE Int. Conf. Robot. Autom.*, pp. 6434–6439, 2014.

[5]   A. J. Hung, J. Chen, A. Shah, and I. S. Gill, "Review Article Telementoring and Telesurgery for Minimally Invasive Procedures," *J. Urol.*, vol. 199, no. 2, pp. 355–369, 2018.

[6]   M. Tavakoli, A. Aziminejad, R. V. Patel, and M. Moallem, "High-fidelity bilateral teleoperation systems and the effect of multimodal haptics," *IEEE Trans. Syst. Man, Cybern. Part B Cybern.*, vol. 37, no. 6, pp. 1512–1528, 2007.

[7]   L. Cheng, M. Sharifi, and M. Tavakoli, "Towards robot-assisted anchor deployment in beating-heart mitral

valve surgery," *Int. J. Med. Robot. Comput. Assist. Surg.*, vol. 14, no. 3, pp. 1–10, 2018.

[8]   L. Cheng and M. Tavakoli, "Switched-Impedance Control of Surgical Robots in Teleoperated Beating-Heart Surgery," *J. Med. Robot. Res.*, pp. 1841003, 2018.

[9]   L. Cheng and M. Tavakoli, "Ultrasound image guidance and robot impedance control for beating-heart surgery," *Control Eng. Pract.*, vol. 81, pp. 9–17, 2018.

[10]   S. K. Dwivedy and P. Eberhard, "Dynamic analysis of flexible manipulators, a literature review," *Mech. Mach. Theory*, vol. 41, no. 7, pp. 749–777, 2006.

[11]   M. Mahvash and P. E. Dupont, "Bilateral Teleoperation of Flexible Surgical Robots," in *Proceedings of the New Vistas and Challenges in Telerobotics Workshop, IEEE 2008, International Conference on Robotics & Automation*, pp. 19–23, 2008.

[12]   S. F. Atashzar, M. Shahbazi, H. A. Talebi, and R. V. Patel, "Control of time-delayed telerobotic systems with flexible-link slave manipulators," in *IEEE International Conference on Intelligent Robots and Systems*, vol. 1, no. 1, pp. 3035–3040, 2012.

[13]   M. Tavakoli and R. D. Howe, "Haptic Effects of Surgical Teleoperator Flexibility," *Int. J. Rob. Res.*, vol. 28, no. 10, pp. 1289–1302, 2009.

[14]   G. Zhu, S. S. Ge, and T. H. Lee, "Simulation studies of tip tracking control of a single-link flexible robot based on a lumped model," *Robotica*, vol. 17, no. 1, pp. 71–78, 1999.

[15]   C. Pacchierotti, M. Abayazid, S. Misra, and D. Prattichizzo, "Teleoperation of steerable flexible needles by combining kinesthetic and vibratory feedback," *IEEE Trans. Haptics*, vol. 7, no. 4, pp. 551–556, 2014.

[16]   S. E. Talole, J. P. Kolhe, and S. B. Phadke, "Extended-state-observer-based control of flexible-joint system with experimental validation," *IEEE Trans. Ind. Electron.*, vol. 57, no. 4, pp. 1411–1419, 2010.